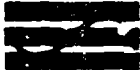


CR-171 862
C.1



 Axiomatix

(NASA-CR-171862) SPACE SHUTTLE PROGRAM
COMMUNICATION AND TRACKING SYSTEMS INTERFACE
ANALYSIS Final Report (Axiomatix, Los
Angeles, Calif.) 365 p HC A16/MP A01

N85-26841

Unclas

CSCD 22B G3/16 21198

**SPACE SHUTTLE PROGRAM
COMMUNICATION AND TRACKING SYSTEMS
INTERFACE ANALYSIS**

**Final Report
Contract NAS9-16893**

**Prepared for
NASA Lyndon B. Johnson Space Center
Houston, Texas 77058**

**Prepared by
James G. Dodds
Jack K. Holmes
Gaylord K. Huth
Richard S. Iwasaki
Peter W. Nilsen
Andreas Polydoros
Donald G. Roberts
Raimundo Sampaio
Sergei Udalov**

**Axiomatix
9841 Airport Blvd., Suite 912
Los Angeles, California 90045**

**Axiomatix Report No. 8409-2
September 30, 1984**

ADDENDUM

- 1. Performance of Solar Max Data and Tape Recorder Dumps Using the Ku-Band Channel 2 Through TDRSS**
- 2. Analysis of the Deployed Electronic Assembly Exciter Loop Drop Lock Problem**
- 3. RF Coverage Analysis**
- 4. A Toroidal Antenna Pattern for Centaur ISPM**
- 5. BER Degradation Due to Centaur Transmitted Bit Timing Jitter Noise Through the Shuttle Payload Communication System**
- 6. Performance Analyses of Using Concatenated-Coding for Centaur Signaling Through TDRSS**
- 7. Investigation of Potential Interface Between the Shuttle and the Space Station**

TABLE OF CONTENTS

	<u>Page</u>
1.0 EXECUTIVE SUMMARY	1
1.1 Contract Tasks	3
1.2 Performance of the Contract Tasks	6
2.0 KU-BAND SYSTEM IMPLEMENTATION AND PERFORMANCE EVALUATION	8
2.1 Analysis of Solar Max and Tape-Recorder Signals Through the Ku-band System	8
2.2 Analysis of the Deployed Electronic Assembly Exciter Loop Lock Problem	10
3.0 S-BAND SYSTEM ANALYSIS	11
3.1 Shuttle Orbiter S-band Antenna Activities	11
3.2 RF Coverage Analyses	12
4.0 CENTAUR INTERFACE COMPATIBILITY EVALUATION	14
4.1 Summary of Axiomatix Centaur Activities	14
4.2 Antenna Pattern Analysis	15
4.3 BER Degradation Due to Centaur Transmitted Bit Timing Jitter	15
4.4 Performance Analyses of Using Concatenated Coding For Centaur Signaling Through TDRSS	16
5.0 SHUTTLE COMMUNICATION AND TRACKING SYSTEM COMPATIBILITY ANALYSIS	18

1.0 EXECUTIVE SUMMARY

The Space Shuttle Program Communications and Tracking Systems Interface Analysis of Contract NAS 9-16893 began April 18, 1983. During this time, the Shuttle communication and tracking systems began flight testing. Two areas of analysis documented in this report were a result of observations made during flight tests. These analyses involved the Ku-band communication system. First, there was a detailed analysis of the interface between the solar max data format and the Ku-band communication system including the TDRSS ground station. The second analysis involving the Ku-band communication system was an analysis of the frequency-lock loop of the Gunn oscillator used to generate the transmit frequency. The stability of the frequency-lock loop was investigated and changes to the design were reviewed to alleviate the potential loss of data due the loop losing lock and entering the reacquisition mode. These analyses are discussed in Section 2 of this report.

Other areas of investigation were the S-band antenna analysis and RF coverage analysis. The S-band antenna system analysis involved the monitoring of the production and deliveries of the flight S-band antenna systems for the Orbiter. This area of analysis is reported in Section 3.1 and discusses the failure analyses primarily concerned with the RF switch box failures due to the lack of hermetic seals. The RF coverage analyses are presented in Section 3.2 and provide assessments of the flight tests of the Shuttle communication systems.

Two additional areas of analysis are documented in this report. The first area is the interface of the Centaur with the Shuttle. Axiomatix performed several interface compatibility analyses. First, Axiomatix proposed an biconical array antenna to meet the requirements of the Solar Polar mission. This antenna concept is reported in Section 4.2. Axiomatix analyzed the BER degradation due to transmitted bit timing jitter noise including continuous or discrete components from the Centaur Digital Computer Unit. The BER degradation was found to be only 0.04 dB. This analysis is reported in Section 4.3. Finally, since the Centaur link through the TDRSS is extremely weak, Axiomatix proposed to use the NASA standard Reed-Solomon code concatenated with currently used convolutional code. To make certain that this concatenating was practical for the Centaur environment, Axiomatix investigated the BER performance degradation due to multiple encryptors and differential coding. The results of these analyses are presented in Section 4.4

The final area of analysis was the Shuttle communication and tracking system compatibility analysis reported in Section 5. With the advent of the Space Station, the Shuttle will become part of a large number of space vehicles and spacecraft that will be linked together in a communication network. As part of the Shuttle communication and tracking system compatibility analysis, Axiomatix made a preliminary investigation into the potential interface between the Shuttle and the Space Station. In particular, an investigation was made into how to accommodate a large number of users in a multiple access communication network. The results of this investigation is presented in Section 5.

1.1 Contract Tasks

There are five major contract tasks which are related to the following Communication and Tracking (C&T) elements of the Space Shuttle Program (SSP). These SSP C&T elements are (1) the Ku-band radar/communication system, (2) the S-band network communication system, (3) the S-band antenna system, and (4) the S-band payload communication system. The detailed tasks follow.

Task 1: Ku-Band Radar/Communication Systems Analysis

Subtask 1--Ku-band Radar System Implementation and Performance Evaluation

The contractor shall provide the technical support to evaluate the Ku-band rendezvous radar implementation based on his own analytical performance predictions and test data obtained from the hardware contractor (Hughes Aircraft Company), the Orbiter contractor (Rockwell International) and NASA. The contractor shall provide NASA with the performance expected for a given rendezvous profile so that NASA may determine the best operation plan to carry out the mission. As design modifications are proposed to meet mission performance requirements, the contractor shall provide updated analytical performance predictions and recommend tests that are needed to provide an evaluation of the design modification feasibility to meet the SSP operational requirements. The contractor shall provide a performance evaluation of the test data obtained by on-orbit tests and recommend any design modifications required to meet the SSP operational requirements and to determine the operation limitations that must be imposed with the Ku-band radar system, as designed.

Subtask 2--Ku-band Communication System Implementation and Performance Evaluation

The contractor shall provide the technical support to evaluate the Ku-band communication system implementation based on his own analytical performance predictions and test data obtained from the hardware contractor (Hughes Aircraft Company), Rockwell and NASA. The contractor shall provide NASA with the acquisition and tracking performance expected of the TDRS by the Ku-band system. As part of this task, the contractor shall provide an analysis of the latest TDRSS pointing budget and the Ku-band system sidelobe rejection capability. The contractor shall provide an evaluation of overall communication system performance from the payload and Orbiter information sources through both the Ku-band system and the TDRSS. This evaluation shall be based on the contractor's analytical predictions and test data from Hughes, rockwell and NASA, including on-orbit tests. The contractor shall identify marginal system performance parameters, recommend design changes to the Ku-band system and to the interfaces with the payload and Orbiter information sources, and determine any operational limitations that must be imposed with the Ku-band communication system, as designed.

Task 2: S-Band Network Communication System Analysis

The contractor shall provide the technical support to evaluate the S-band network communication system performance through the TDRSS. This evaluation shall be based on the contractor's analytical performance

predictions and test data obtained from the hardware contractor (TRW), the Orbiter contractor (Rockwell International), and NASA. Particular attention shall be given to the spread-spectrum processor of the Orbiter network transponder to establish the performance of its current implementation. An important part of this evaluation is the on-orbit tests with the TDRSS. The contractor shall identify marginal system performance parameters, recommend design changes to the S-band system required to meet the SSP operational requirements and to determine the operational limitations that must be imposed with the S-band network communication system, as designed.

Task 3: S-band Antenna System Analysis

The contractor shall review and evaluate the S-band antenna performance and make recommendations for improvements to meet the SSP operational requirements. During this evaluation effort, the contractor shall monitor the antenna pattern measurement testing at JSC and identify areas of concern for achieving system requirements. If the measured performance is found to be marginal or inadequate, the contractor shall evaluate the design of the present Orbiter flight antennas and recommend modifications which will correct deficiencies. New techniques will be investigated to simplify the present antenna concepts which may be considered for future improved space antenna systems.

Task 4: S-band Payload Communication System Analysis

Subtask 1-- S-band Payload Communication System Implementation and Performance Evaluation

The contractor shall provide technical support to evaluate the S-band payload communication system implementation based on his based own analytical performance predictions and test data obtained from the hardware contractor (TRW), the Orbiter contractor (Rockwell International) and NASA. The contractor shall quantify nominal system operations and deviations due to variations in system performance parameters. The contractor shall evaluate the system operational scenarios expected and recommend design changes to the S-band payload system to meet the SSP operational requirements and to determine any operational limitations that must be imposed with the S-band payload communication limitations that must be imposed with the S-band payload communication system, as designed.

Subtask 2-- Payload Interface Compatibility Evaluation and Problem Area Resolution

The contractor shall provide analytical performance predictions of possible interface compatibility problems associated with interfacing payload elements such as the IUS, TDRS, PAM, Centaur, and other spacecraft command and telemetry systems with the Orbiter communications and data-handling subsystems (or elements) including the Ku-band Signal Processor, Payload Signal Processor, Payload Data Interleaver, Payload Interrogator and Payload Recorder. The contractor shall identify marginal system performance parameters that would result in the payload or Orbiter failing to meet agreed-upon interface requirements contained in the Orbiter/cargo standard interface specification (NASA JSC ICD 2-19001) and payload-unique ICD's. The contractor shall determine any design changes to the Orbiter subsystems or payload systems that must be made in order to meet the mission performance requirements and to determine the operational limitations of the Orbiter subsystems and each of the payload systems, as designed.

**Task 5: Shuttle Communication and Tracking System Compatibility
Analysis and Problem-Area Resolution**

The contractor shall analyze the overall Shuttle C&T systems and identify potential performance inadequacies in order to meet updated SSP operational requirements. These areas of updated SSP operational requirements include, but are not limited to, improvements to navigation and encryption of payload data and television. The contractor shall recommend design changes to the Shuttle C&T systems to meet these updated SSP operational requirements and provide analytical performance predictions for any changes proposed to the C&T systems.

1.2 Performance of the Contract Tasks

During the contract period from April 18, 1983 to September 30, 1984, the Shuttle communication and tracking systems began on-orbit flight testing. As a result of the on-orbit tests two distinct problems developed concerning the Ku-band communication system. First, there was a detailed analysis of the interface between the solar max data format and the Ku-band communication system including the TDRSS ground station. A similar problem to that predicted for the solar max mission was also observed during tests of dumps of the tape recorders through the Ku-band system. To analyze this problem, the complete payload communication system through the Ku-band system including the TDRSS ground system had to be modeled as was proposed as part of Task 1. The second problem that developed concerning the Ku-band communication system was the discovery that the deployed electronic assembly (DEA) exciter would drop lock and transmit random data. These two problems are presented in Section 2 of this report.

Task 3, the S-band antenna system analysis, involved the monitoring of the production and deliveries of the flight S-band antenna systems for the Orbiter. This area of analysis is reported in Section 3.1 and discusses the failure analyses primarily concerned with the RF switch box failures due to lack of hermetic seals. Task 2 was primarily concerned with the RF coverage analyses presented in Section 3.2 which provide assessments of the flight tests of the Shuttle communication systems.

The primary area of investigation of Task 4 was the Centaur interface compatibility evaluation presented in Section 4. Besides the participation in the Centaur Avionics Integration Panel, the Centaur Communications and Data System Subpanel, and the Centaur Telemetry System Interim Critical Design Review, Axiomatix performed several interface compatibility analyses. Axiomatix proposed a biconical array antenna to meet the requirements of the Solar Polar mission. This antenna concept is reported in Section 4.2. Axiomatix analyzed the BER degradation due to transmitted bit timing jitter noise including continuous or discrete components from the Centaur Digital Computer Unit. The BER degradation was found to be only 0.04 dB. This analysis is reported in Section 4.3. Finally, since the Centaur link through the TDRSS is extremely weak, Axiomatix proposed to use the NASA standard Reed-Solomon code concatenated with currently used convolutional code. To make certain that this concatenating was practical for the Centaur environment,

Axiomatix investigated the BER performance degradation due to multiple encryptors and differential coding. The results of these analyses are presented in Section 4.4

The final area of analysis was Task 5, the Shuttle communication and tracking system compatibility analysis, reported in Section 5. With the advent of the Space Station, the Shuttle will become part of a large number of space vehicles and spacecraft that will be linked together in a communication network. As part of the Shuttle communication and tracking system compatibility analysis, Axiomatix made a preliminary investigation into the potential interface between the Shuttle and the Space Station. In particular, an investigation was made into how to accommodate a large number of users in a multiple access communication network. The results of this investigation is presented in Section 5.

2.0 KU-BAND SYSTEM IMPLEMENTATION AND PERFORMANCE EVALUATION

There were two specific problems that were analyzed as part of the Ku-band System Implementation and Performance Evaluation. First, there was a detailed analysis of the interface between the solar max data format and the Ku-band communication system including the TDRSS ground station. A similar problem to that predicted for the solar max mission was also observed during tests of dumps of the tape recorders through the Ku-band system. The second problem that was analyzed was the tendency of the exciter in the deployed electronic assembly (DEA) of the Ku-band system to drop lock and transmit random data.

2.1 Analysis of Solar Max and Tape-Recorder Signals Through the Ku-band System

The analyses of the solar max data and the tape recorder dumps using the channel 2 of the Ku-band communication system are presented in Addendum 1. Channels 1 and 2 of the Ku-band communication system are in-phase quadrature on a 8.5 MHz square-wave subcarrier. That is, channel 2 is on the inphase (I) component of the QPSK signal and channel 1 is on the quadrature phase (Q) component of the QPSK signal. For the Solar Max Retrieval, computer dump data was to be transmitted to the Shuttle Orbiter at 32 kbps directly modulating the S-band carrier. The first question to be asked was whether the Transponder and Interrogator (PI) would be able to demodulate the signal without false locking. The second question to be asked was whether the demodulated signal would be completely suppressed by the hard limiter in the channel 2 modulator of the Ku-band communication system. These two questions are analyzed and favorably answered in the Technical Memorandum No. M8310-1, dated October 7, 1983 and entitled "Solar Max Retrieval Signal Structure Before and After Limiting Using the Ku-Band Channel 2 Input", which is included in Addendum 1.

Once it was determined that the solar max signal could be demodulated by the PI and would not be totally suppressed by the hard-limiter in the channel 2 modulator, it was necessary to determine the performance of the TDRSS ground station demodulation. After testing the Ku-band link including the demodulation by the TDRSS ground station in the Electronic Systems Test Laboratory (ESTL), it was found that the I and Q signals reversed at the output of the Medium-Range Demodulation (MRD). An initial evaluation of the test data and the signals transmitted through channel 2 provided some understanding of

the problem. In Addendum 1, the Technical Memorandum No. M8401-1, dated January 10, 1984 and entitled "A Possible Explanation of the Solar Max Retrieval I-Q Swapping due to Noise Filtering in the 8.5 MHz Subcarrier Demodulator" presents an analysis that shows that the power ratio of channel 2 to channel 1 out of the lowpass filters in the TDRSS ground station MRD can be as low as 1:1 when the input signal is lower than -113 dbm. Although approximations were necessary, it is shown that the noise power present in the 5-MHz PI shares the total power in channel 2 with the 32-kbps signal after hardlimiting by the channel 2 modulator but, depending on the SNR in the 5-MHz bandwidth, a good portion of the noise is filtered out in the TDRSS QPSK subcarrier demodulator arm filters. Thus, the QPSK demodulator has great difficulty in deciding whether the normally strong channel 2 or the normally weak channel 1 is in the inphase strong channel position. This could account for the tendency to lock in the wrong I-Q relationship and not be detected.

Following further testing of the Ku-band link including the demodulation by the TDRSS ground station in the ESTL, it was found that the I-Q reversal occurred during track changes when the tape recorder signal was transmitted through the channel 2 of the Ku-band communication system similar to the effect that occurred when the solar max signal was transmitted through channel 2. This result could not be explained by excess noise sharing power with the signal in the channel 2 hardlimiter. Therefore, a more detailed analysis was performed and documented in Axiomatix Report No. R8406-1, dated June 1, 1984 and entitled "Analysis of the Ku-Band Shuttle/MRD I-Q Reversal Phenomena." In this report included in Addendum 1, the I-Q flipping problem of the MRD was studied by analysis and simulation to discover why the flipping occurred. In the case of the tape-recorder dump during start-up or wraparound, it was found that the composite tape-recorder signal contained two tones increasing with frequency, plus a spectrally flat noise term. Depending on the prelimiter-filter bandwidth into the channel 2 subcarrier modulator, this composite signal determined the conditions for I-Q flipping. A 2.5 MHz, six-pole prelimiter-filter stopped the I-Q flipping completely. In the case of the solar max I-Q flipping, the small SNR at the PI caused mainly noise to be transmitted on channel 2. At the receiver, most of the noise was filtered out, greatly reducing the effective I-Q power ratio at the MRD subcarrier loop. It should be noted that observing the existence and modeling of the two tones, along with the noise output from the tape recorder start-up or wraparound, allowed Axiomatix to make very accurate performance predictions. Specifically, the

comparisons between the NASA measurements and the Axiomatix predictions based on simulations or calculations are very good for a variety of cases.

2.2 Analysis of the Deployed Electronic Assembly Exciter Loop Lock Problem

The other area of analysis of the Ku-band system is the analysis of the DEA exciter loop drop lock problem. This analysis is documented in the Axiomatix Report No. R8410-2, dated May 15, 1984 and entitled "Deployed Electronic Assembly Exciter Loop Lock Problem." This report is included in Addendum 2. The DEA provides clean signals for the transmitter TWTAs in each of the five Radar frequency channels, and for the single channel in the Communication mode of operation. In the TWTAs bypass mode of the Radar operation, the exciter output is used as the transmitter signal. In addition, the exciter provides the first and second LO signals for use in the Receiver mixer down-converters. The problem that was addressed in the report was the intermittent loss of phase lock in the exciter with the relock requiring an additional 20 μ s (which is the time for a single sweep). The occurrence of this loss of phase lock appeared to be random with a mean time between losses of about one hour. This report presents the investigation and analysis of the loss of lock problem and describes the meetings held between Hughes and Axiomatix. By changing the gains and hysteresis in the loop, the drop out and the resulting resweep were eliminated. The details of the changes are presented in the report.

3.0 S-BAND ANTENNA SYSTEM ANALYSIS

3.1 Shuttle Orbiter S-Band Antenna Activities

The primary task was to monitor the production and deliveries of the flight S-band antenna systems for the Shuttle. The major problem that arose during the contract period was the failures attributed to the RF switch, which were not hermetically sealed and therefore were vulnerable to multipaction effects characterized by high power arcing during a brief period of operation when the internal pressure within the switch reached a critical value during the slow leakage of ambient nitrogen into the space environment. Since the switches were not designed to maintain the internal nitrogen atmosphere, this partial vacuum condition conducive to multipaction was inevitable, resulting in arcing and subsequent destruction of the RF switch.

The failure analysis conducted by Rockwell International were observed during disassembly of many of the failed units. The evidence indicated that once multipaction was initiated, the resultant plasma created an electrical short which dissipated the incident RF power as thermal energy in the latching reed blade area of the switch creating charring of organic insulating materials and warping the reed blades such that electrical open circuits occurred. The extent of the damage depended on the duration of multipaction and were somewhat minimized by disrupting antenna use during this multipaction period once the cause of the failures was recognized.

The obvious cause of the multipaction was the absence of hermetic sealing of the RF switch box. Due to the extremely high cost of achieving adequate hermetic seals, an interim solution using RTV seals was devised, tested, and implemented to correct this problem, although there were no assurances of a hundred mission capability for this fix. Also, it was suggested that a more heat resistant reed blade material be substituted for the existing phosphor bronze which warped into a permanent bend under high temperatures. A high strength, high temperature metal such as stainless steel (gold plated for electrical conductivity), rather than ductile copper alloys, for example, could withstand the arcing if it occurred and yet maintain its straight shape, thereby retaining the operational capabilities of the RF switch during the remainder of the flight and subsequent flights, but it is believed no such corrective action was considered by the vendor.

Besides this RTV seal interim solution, there were other quality control fabrication problems that had to be corrected. Poor epoxy staking of

fastening screws and wiring were prominent items. It was observed that minute metallic particles resulting from machining were still present in the latching reed blade area and recommendations to fine hone the holes for insulating teflon standoffs were made. Broken connector leads resulting from loosened epoxy-staked attachment screws was another problem. The suggestion to double-nut the fastening screws was not deemed necessary; instead, more epoxy is to be used.

The quad S-band antenna patterns continue to have submarginal performance, but given the existing design, little improvement can be expected. The five horn cross configuration intended to be a possible quad upgrade has been fabricated and will be tested in the near future. Delays were encountered due to the lack of available RF switches. Other schemes to incorporate simultaneous multibeam capabilities and new low level beam switching techniques are being investigated to circumvent this dependence on electromechanical RF switches.

3.2 RF Coverage Analyses

Addendum 3 includes several technical memoranda that provide the assessment of the flight tests of the communication systems. The Technical Memorandum entitled "STS-9 Ascent RF Coverage Communication Support Formulation" provides the recommended STS-9 ascent-phase STDN support plan and the corresponding predicted Orbiter S-band PM automatic antenna switching up to and including TDRS ascent support, as derived from analysis of the STS-9 Cycle 1 reference trajectory.

STS-8 was the first Shuttle mission operation of communications via a TDRS satellite for both S-band and K-band communications. DTO 702 was an STS-8 communications flight test to exercise different operational configurations of the Orbiter's S-band communication system towards establishing flight readiness of the TDRS-mode operation. DTO 702 required exercising S-band communications through TDRS using High Data Rate, Low Data Rate, with and without spreading, with and without encryption, High Frequency and Low Frequency operation, acquisition without Doppler compensation, plus a test part to verify that antenna and beam switching occurs at the projected boundaries. The Technical Memorandum entitled "Shuttle STS-8 Mission DTO 702 Report" provides the assessment.

DTO 710 was an STS-8 communication flight test to exercise different operational configurations of the Orbiter's Ku-band communication system

towards establishing flight readiness of the Ku-band operations. The intent of DTO 710 was that Ku-band communications be exercised and verified in each of various combinations of Forward and Return modes, with and without spreading, and with and without encryption. Additionally, that K-band acquisition be demonstrated in both the automatic and the manual modes, that Ku-band failover to S-band be demonstrated and finally, a demonstration of maintaining tracking and communications during an OMS burn. The Technical Memorandum entitled "Shuttle STS-8 Mission DTO 710 Report" presents the assessment.

All parts of DTO 711 were previously verified in STS-8 DTO 710 except for exercising and verifying the Ku-band Return Link PM mode channel 3 High Data Rate at 48 Mbps. The 48 Mbps High Data Rate was exercised numerous times in STS-9, per mission reports. An assessment of the performance of the 48 Mbps High Data Rate is presented in a one page report entitled "Report on STS-9 DTO 711".

DTO's (i.e., flight tests) have been a key element of the Shuttle program since it began. The Shuttle Program Office nor anyone else has ever formulated the "life cycle" of a DTO, so the tremendous effort involved in the genesis, formulations and reformulations, reviews, scrubs, and re-reviews, and all the multiple coordinations and approvals required, have never been set down. A thorough and comprehensive description of the phases and stages of a DTO is included in Addendum 3. Also included in Addendum 3 is a note on how to analyze the STS-11 Delayed Acquisition Problem.

4.0 CENTAUR INTERFACE COMPATIBILITY EVALUATION

4.1 Summary of Axiomatix Centaur Activities

Meeting Participation

Axiomatix participated in the Centaur Avionics Integration Panel meetings and the Communications and Data System Subpanel meetings. This participation included resolution of technical problems in the areas of Centaur antenna design and performance, DCU data bit jitter, and antenna switching transients and hardline interface specification definition. These meetings were attended on the following dates:

October 20, 1983	General Dynamics
February 9-10, 1984	NASA Lewis
March 7-8, 1984	General Dynamics
June 5-6, 1984	General Dynamics
June 22, 1984	General Dynamics

Design Review Participation

Axiomatix actively participated in the Centaur Telemetry System Interim Critical Design Review on November 2, 1983. This participation entailed detailed review of all Design Review documentation and attendance at the Formal Design Review meeting. Several RIDs were generated by Axiomatix.

Analysis of Centaur Telemetry Subsystem

Axiomatix analyzed the degradation due to the data bit jitter and found that the Bit Error Rate (BER) degradation was 0.04 dB. This estimate was based on the data bit jitter plotted in the report by H. J. Choi, et al, listed below. The result was obtained assuming a 50% transition density and neglecting bit duration jitter. It has been determined that the data bit duration jitter introduces a negligible addition BER degradation.

Axiomatix initiated the bit slip rate degradation analysis and performed a comprehensive review of the literature on the subject.

Review of Reports and Papers

Axiomatix reviewed and studied the following reports and papers that pertain to the Centaur/Shuttle bit jitter issue:

- (1) C. M. Chie and C-S Tsang, "The Effects of Transmitter/Receiver Clock Time-Base Instability on Coherent Communication System Performance", IEEE Trans. on Comm., Vol. COM-30, No. 3, March 1982 (BER Degradation)
- (2) F. M. Gardner and J. F. Heck, "Angle Modulation Limits of a Noise-Free Phase Lock Loop", IEEE Trans. on Comm., Vol. COM-26, No. 8, August 1978. (Bit Slip Rate)
- (3) C. M. Chie, "Proposed Specification for Data Bit Jitter To Meet BER Requirement, January 1982, LinCom Corp., P. O. Box 2793D, Pasadena, Calif. 91105.
- (4) J. K. Holmes, "Optimum Bandwidth and Damping for the MA Bit Synchronizer Based on Linearized Tracking Error", TRW
- (5) H. J. Choi, C. M. Chie, W. C. Lindsey, and T. McKenzie, "Centaur Data Bit Jitter Test Results", LinCom Report No. TR-0384-8214-200, March 20, 1984.

4.2 Antenna Pattern Analysis

The present General Dynamics Centaur antenna design is essentially omnidirectional and therefore is not suitable for the Solar Polar mission which requires a moderate gain toroidal pattern along the Centaur vehicle axis. Axiomatix investigated a solution to this incompatibility and proposed a modified biconical array as a candidate configuration for achieving this toroidal pattern since it is readily adapted to the existing Centaur deployable antenna concept. The proposed biconical array is presented in Addendum 4.

4.3 BER Degradation Due to Centaur Transmitted Bit Timing Jitter

Axiomatix analyzed the BER degradation due to transmitted bit timing jitter noise including continuous or discrete components. The source of the

bit timing jitter originates in the Digital Computer Unit (DCU), which modulates the Centaur subcarrier and in turn, phase modulates the carrier. After S-band transmission to the Shuttle Orbiter, the PI demodulates the carrier, and the data bits are reconstructed in the PSP bit synchronizer. Frame synchronization is also done in the PSP. The detailed performance analysis is presented in the Axiomatix Report No. R8409-1, dated September 28, 1984 and entitled "BER Degradation Due to Bit Timing Jitter Noise" which is included in Addendum 5. It was determined in this report that the BER degradation due to DCU bit timing jitter, is approximately 0.04 dB. It is concluded that this is a negligible amount of degradation. Neither thermal noise, nor the discrete nature of the loop has been included in this analysis. It is felt that a full bore simulation would be needed to estimate the effects of the discrete loop. However, it is doubtful whether the discrete nature of the loop would add more than 0.1 dB. It is concluded that, due to the very involved nature of the loop, it would not be reasonable to construct such a simulation.

4.4 Performance Analyses of Using Concatenated Coding For Centaur Signaling Through TDRSS

The Centaur link through the TDRSS is extremely weak even using a $R=1/2$, $K=7$ convolutional encoding with Viterbi decoding at the TDRSS ground station. In order to improve the BER performance, Axiomatix began an investigation of concatenating a Reed-Solomon code with the convolutional code. By using a RS (255,223) code concatenated with the convolutional code, the required E_b/N_0 can be decreased by 2 dB at Probability of Bit Error (P_b) of 10^{-5} and by 2.9 dB at $P_b=10^{-7}$. The disadvantages of concatenating the convolutional code with a RS code are: added complexity, increased decoding delay, and more difficult synchronization. In Addendum 6, a viewgraph presentation is included which describes the concatenated coding scheme and presents the BER performance gain that can be obtained.

For the Centaur communication system, there are other concerns that need to be addressed in order to predict the BER performance of a concatenated coding scheme. First, the BER performance of a single-channel concatenated-coding system with multiple encryptors needed to be analyzed. This BER performance was analyzed in Technical Memorandum No. M8404-1, dated April 6, 1984 and entitled "Bit-Error Rate of the Concatenated-Coding System With Multiple

Encryptors" which is included in Addendum 6. It was found that at $P_b = 10^{-3}$, that for three encryptors in series, decryptor #1 causes a degradation of 0.14 dB, decryptor #2 causes an additional degradation of 0.023 dB and decryptor #3 causes an additional degradation of 0.01 dB. It is also worth noting that due to the steepness of the BER performance curves, a small amount of degradation in SNR still implies a large difference in BER.

A second concern is the need for differential coding to resolve the inherent ambiguity of carrier phase lock. This concern is addressed in the Technical Memorandum No. M8404-2, dated April 10, 1984 and entitled "Bit-Error Rate of the Concatenated-Coding System With Differential Encoding" which is included in Addendum 6. It was found that the best place to put the differential encoder was before the convolutional encoder but after RS encoder and the RS symbol interleaver. It is shown that the use of differential encoding when placed in its best position will cause a BER degradation of 0.02 dB over a range of BER (10^{-3} to 10^{-7}).

5.0 SHUTTLE COMMUNICATION AND TRACKING SYSTEM COMPATIBILITY ANALYSIS

With the advent of the Space Station, the Shuttle will become part of a large number of space vehicles and spacecraft that will be linked together in a communication network. As part of the Shuttle communication and tracking system compatibility analysis, Axiomatix made a preliminary investigation into the potential interface between the Shuttle and the Space Station. The results of this investigation is presented in Addendum 7. In order to accommodate a large number of users, multiple access (MA) communication was studied. Two methods of channelization were examined: frequency-division MA (FDMA) and time-division MA (TDMA). A third, code-division MA (CDMA), was not considered practical. Principal trade-offs between FDMA and TDMA are complexity versus timing requirements. FDMA has the following advantages relative to TDMA:

- (1) lower burst rate and lower user EIRP
- (2) greater MA network capacity

TDMA has the following advantages relative to FDMA:

- (1) less complex receiver hardware
- (2) less complex antenna: single-beam versus multiple simultaneous beams
- (3) does not require user power control for simultaneous near/far operations

The performance of phase-shift and frequency-shift-keying (FSK) modulation was examined. Quadrature-phase-shift-keying (QPSK) modulation is practical for the longer symbol times used in FDMA. Methods of coherent and noncoherent demodulation were discussed, including a new technique for acquiring rapid phase reference. Multiple-frequency-shift-keying (MFSK) was examined; it was shown that 4-ary MFSK is superior to higher order modulations for conserving the data bandwidth.

It was found that the FDMA system with QPSK and coherent demodulation has the performance edge over TDMA; however, the complexity of the FDMA system, particularly the antenna requirements may be the deciding factor. At this point, a clear-cut choice of multiple-access techniques (i.e., TDMA or FDMA) cannot be made. Further analyses and hardware trade-offs must be made.

ADDENDUM 1

**PERFORMANCE OF SOLAR MAX DATA AND TAPE RECORDER
DUMPS USING THE Ku-BAND CHANNEL 2 THROUGH TDRSS**



9841 Airport Boulevard • Suite 912 • Los Angeles, California 90045 • Phone (213) 641-8600

TECHNICAL MEMORANDUM NO. M8310-1

TO: P. Nilsen

DATE: October 7, 1983

FROM: J. K. Holmes

SUBJECT: Solar Max Retrieval Signal Structure Before and After Limiting
Using the Ku-Band Channel 2 Input

1.0 SUMMARY

In this memorandum, it is shown that the limiter inherent in the channel 2 input of the Ku-band QPSK subcarrier modulator does not suppress the 32-kbps baseline solar max retrieval signal at the 8.5-MHz QPSK subcarrier channel 2 output located in the TDRSS ground terminal. In fact, with the current phase-modulation indices specified for solar max, the subcarrier (16 kbps) signal is suppressed by at least 80 dB, while the baseband signal is at full power! However, since the subcarrier data is stripped off at the Shuttle payload signal processor (PSP), subcarrier suppression is not a problem. By changing the phase-modulation indices to $\theta_1 = 0.8$ radians and $\theta_2 = 0.6$ radians, it would be possible to give each signal equal power at a level of about -5 dB (0 dB is the total limiter power) if that were required.

2.0 MODEL

In Figure 1, the model for the solar max retrieval data dump is shown. The solar max 32-kbps biphase-M data is modulated onto the carrier along with the modulated 1.024-MHz subcarrier. The subcarrier has 16-kbps of biphase-M BPSK modulation on it. In the Shuttle Payload Interrogator (PI), the carrier phase-locked-loop demodulates the signal, producing the baseband 32-kbps solar max signal and the 16-kbps modulated subcarrier plus spectral components at a frequency of $n\omega_{SC}$, with $n=2,3,4,\dots$

The lowpass filter (LPF) limits the spectral extent into the Shuttle Ku-band channel 2 input*. This input acts as a limiter. After the 192-kbps NSP data (channel 1) is placed on the QPSK subcarrier, it is bandpass filtered to the fundamental and added to wideband channel 3 (mode 2) data and frequency modulated onto the Ku-band carrier to the TDRSS. After being relayed from the TDRSS to the TDRSS ground terminal, the signal is FM demodulated in order to send the baseband plus modulated subcarrier signal to the medium-rate bit synchronizer (MRBS) for data tracking and detection.

*However, we neglect this filtering in the following analysis.

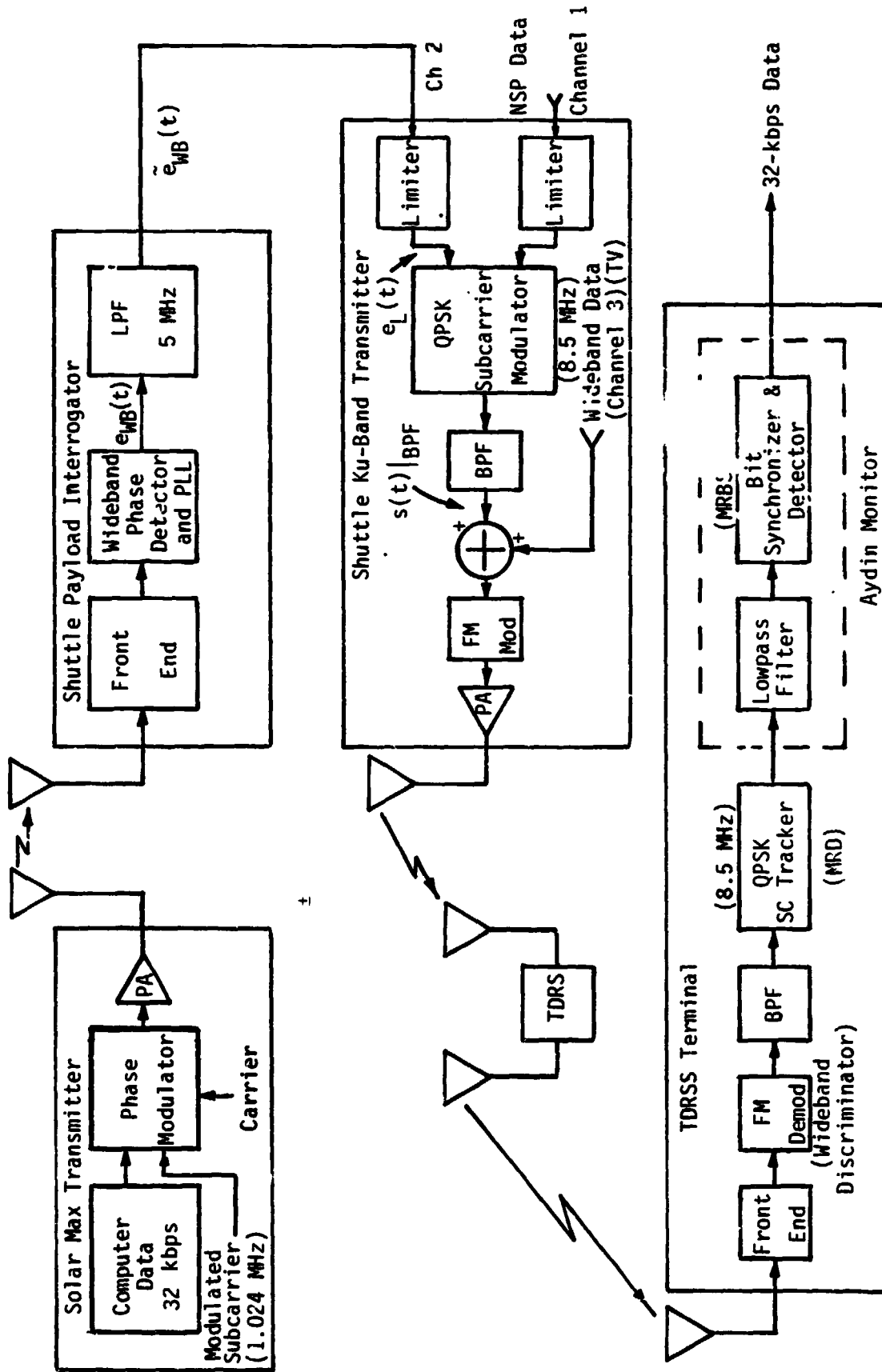


Figure 1. Model for the Solar Max Retrieval Data Dump

3.0 MODULATED SIGNAL COMPONENTS

First we consider the spectral composition of the modulated solar max retrieval signal. The waveform of the signal is given by

$$y(t) = \sqrt{2P} \sin(\omega_c t + \theta_1 d_1(t) \sin \omega_{sc} t + \theta_2 d_2(t)) \quad (1)$$

where:

P = signal power

$\omega_c = 2\pi f_c$, angular carrier frequency

$\theta_1 = 16$ -kbps phase-modulation angle ($0.8 \pm 5\%$ rad)

$\theta_2 = 32$ -kbps phase-modulation angle ($1.0 \pm 5\%$ rad)

$d_1(t)$ = 16-kbps biphase-M data

$d_2(t)$ = 32-kbps biphase-M data

Expanding, we obtain:

$$y(t) = \sqrt{2P} \cos(\theta_1 \sin \omega_{sc} t) \left[\cos \theta_2 \sin \omega_c t + d_2(t) \sin \theta_2 \cos \omega_c t \right] \\ + \sqrt{2P} d_1(t) \sin(\theta_1 \sin \omega_{sc} t) \left[\cos \theta_2 \cos \omega_c t - d_2(t) \sin \theta_2 \sin \omega_c t \right] \quad (2)$$

We have

$$\cos(\theta \sin x) = J_0(\theta) + \sum_{n=2}^{\infty} 2J_n(\theta) \cos nx ; \sin(\theta \sin x) = \sum_{n=1}^{\infty} 2J_n(\theta) \sin nx \quad (3)$$

where \sum denotes a summation over even integers and \sum denotes a summation over odd integers. Using (3) in (2), we have the result:

$$y(t) = \sqrt{2P} \left\{ J_0(\theta_1) \sum_{n=2}^{\infty} 2J_n(\theta_1) \cos n\omega_{sc} t \right\} \left[\cos \theta_2 \sin \omega_c t + d_2(t) \sin \theta_2 \cos \omega_c t \right] \\ + \sqrt{2P} d_1(t) \left\{ \sum_{n=1}^{\infty} 2J_n(\theta_1) \sin(n\omega_{sc} t) \right\} \left[\cos \theta_2 \cos \omega_c t - d_2(t) \sin \theta_2 \sin \omega_c t \right] \quad (4)$$

Now, expanding (4) for the first few terms yields

$$\begin{aligned}
 y(t) = & \overbrace{\sqrt{2P} J_0(\theta_1) \cos \theta_2 \sin \omega_c t}^{\text{carrier}} + \overbrace{\sqrt{2P} d_2(t) \sin \theta_2 J_0(\theta_1) \cos \omega_c t}^{\text{baseband data}} \\
 & + \overbrace{\sqrt{2P} d_1(t) \cos \theta_2 \left\{ J_1(\theta_1) \sin[(\omega_{sc} - \omega) t] + J_{-1}(\theta_1) \sin[(\omega_{sc} + \omega) t] \right\}}^{\text{subcarrier data}} \\
 & - \overbrace{\sqrt{2P} d_1(t) d_2(t) \sin \theta_2 \left\{ J_1(\theta_1) \cos[(\omega_{sc} - \omega) t] + J_{-1}(\theta_1) \cos[(\omega_{sc} + \omega) t] \right\}}^{\text{cross-modulation term}} \\
 & + \text{terms at } \omega_c \pm n\omega_{sc} \quad n \geq 2 \quad (5)
 \end{aligned}$$

Hence, the power distribution is given by:

(a) Carrier power

$$\frac{P_c}{P} = J_0^2(\theta_1) \cos^2(\theta_2) \quad (6)$$

(b) Baseband data

$$\frac{P_{d2}}{P} = J_0^2(\theta_1) \sin^2 \theta_2 \quad (7)$$

(c) Subcarrier data

$$\frac{P_{d1}}{P} = 2 \cos^2 \theta_2 J_1^2(\theta_1) \quad (8)$$

(d) Cross modulation

$$\frac{P_{d1d2}}{P} = 2 \sin^2 \theta_2 J_1^2(\theta_1) \quad (9)$$

Note that the cross-modulation term is in phase quadrature to the subcarrier data term. The power-level change caused by adding the baseband data to the existing subcarrier-modulation process is depicted in Table 1.

Table 1. Nominal Values of Power Levels With and Without
The Baseband Modulation Application
($\theta_1 = 0.8$ and $\theta_2 = 1.0$)

Power Ratios	Without Baseband Signal (dB)	With Baseband Signal (dB)	Change (dB)
$\frac{P_c}{P}$	-1.45	-6.80	-5.35
$\frac{P_{d1}}{P}$	-5.65	-11.0	-5.35
$\frac{P_{d2}}{P}$	-	-2.96	-
$\frac{P_{d1d2}}{P}$	-	-7.15	-

4.0 DEMODULATED SPECTRAL COMPONENTS

In this section, we evaluate the PI carrier demodulated signal, the system model of which is shown in Figure 2.

We determine the power distribution in the wideband output, denoted by $e_{WB}(t)$. To obtain the signal output, we assume that the carrier reference has an error of ϕ radians, so that the demodulated signal is of the form $y(t) \cdot \sqrt{2} \cos(\omega_c t - \phi)$, or

$$\begin{aligned}
 e_{WB}(t) = & \left[\sqrt{P} \left\{ J_0(\theta_1) + \sum_{n=2}^{\infty} 2J_n(\theta_1) \cos n\omega_{SC} t \right\} \left\{ \cos\theta_2 \sin\phi + \sin\theta_2 d_2(t) \cos\phi \right\} \right. \\
 & + \left. \sqrt{P} d_1(t) \left\{ \sum_{n=1}^{\infty} 2J_n(\theta_1) \sin n\omega_{SC} t \right\} \left\{ \cos\theta_2 \cos\phi - \sin\theta_2 d_2(t) \sin\phi \right\} \right] \\
 & + O(2\omega_c) \qquad (10)
 \end{aligned}$$

Expanding once again, we have

$$\begin{aligned}
 e_{WB}(t) = & \sqrt{P} \cos\theta_2 \sin\phi \left\{ J_0(\theta_1) + \sum_{n=2}^{\infty} 2J_n(\theta_1) \cos n\omega_{SC} t \right\} \\
 & + \sqrt{P} d_2(t) \sin\theta_2 \cos\phi \left\{ J_0(\theta_1) + \sum_{n=2}^{\infty} 2J_n(\theta_1) \cos n\omega_{SC} t \right\} \\
 & + \sqrt{P} d_1(t) \cos\theta_2 \cos\phi \left\{ \sum_{n=1}^{\infty} 2J_n(\theta_1) \sin n\omega_{SC} t \right\} \\
 & - \sqrt{P} d_1(t) d_2(t) \sin\theta_2 \sin\phi \left\{ \sum_{n=1}^{\infty} 2J_n(\theta_1) \sin n\omega_{SC} t \right\} \qquad (11)
 \end{aligned}$$

Hence, the terms at baseband and ω_{SC} are given by

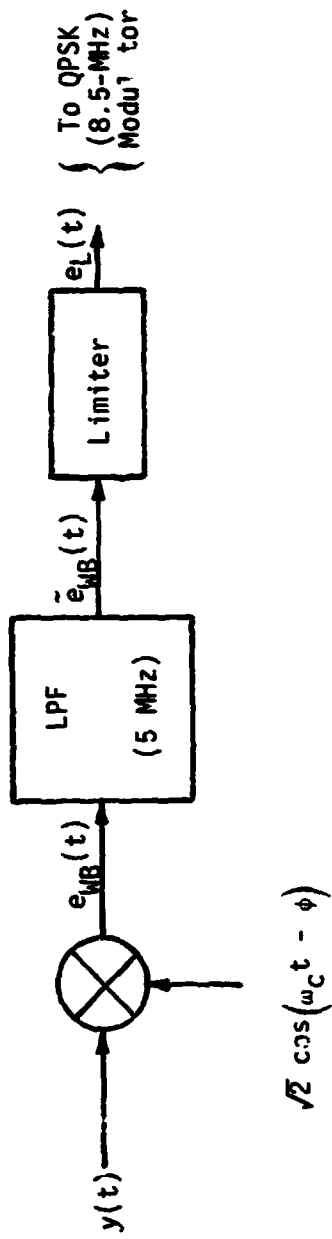


Figure 2. Shuttle PI Carrier-Demodulation Model

$$\begin{aligned}
 e_{\text{WB}}(t) = & \overbrace{\sqrt{P} J_0(\theta_1) \cos\theta_2 \sin\phi}^{\text{DC}} + \overbrace{\sqrt{P} d_2(t) \sin\theta_2 \cos\phi J_0(\theta_1)}^{\text{32-kbps data}} \\
 & + \overbrace{2\sqrt{P} J_1(\theta_1) d_1(t) \cos\theta_2 \cos\phi \sin \omega_{\text{SC}} t}^{\text{16-kbps data on 1.024-MHz subcarrier}} \\
 & - \overbrace{2\sqrt{P} d_1(t) d_2(t) J_1(\theta_1) \sin\theta_2 \sin\phi \sin \omega_{\text{SC}} t}^{\text{cross modulation on subcarrier}} \\
 & + \text{terms at } 2\omega_{\text{SC}}, 3\omega_{\text{SC}}, \text{ etc.} \tag{12}
 \end{aligned}$$

Notice from (12) that cross modulation in the desired band (baseband to above ω_{SC}) does not exist if the reference carrier is in perfect quadrature, i.e., ideal carrier tracking with $\phi = 0$. Since the solar max will be on the end of the boom in the Shuttle, the SNR should be very high and the phase error ϕ , very small; thus, cross modulation should be negligible (since it depends on $\sin\phi$, with ϕ the phase error).

5.0 DEMODULATED AND LIMITED SPECTRAL COMPONENTS

Now we consider the limited version of $e_{WB}(t)$ since that will be representative of what is demodulated out of channel 2 at the TDRSS Earth terminal QPSK subcarrier-tracking loop.

Using (1) with the reference signal we obtain, as an input to the lowpass filter (in closed form),

$$e_{WB}(t) = \sqrt{2} \cos(\omega_c t - \phi) \sqrt{2P} \sin(\omega_c t + \theta_1 d_1(t) \sin \omega_{sc} t + \theta_2 d_2(t)) \quad (13)$$

or

$$e_{WB}(t) = \sqrt{P} \sin(\theta_1 d_1(t) \sin \omega_{sc} t + \theta_2 d_2(t) + \phi) + O(2\omega_c) \quad (14)$$

After filtering the signal, the terms at $2\omega_c$ are effectively removed so that we have, to a good approximation,

$$\tilde{e}_{WB}(t) = \sqrt{P} \sin[\theta_1 d_1(t) \sin \omega_{sc} t + \theta_2 d_2(t) + \phi] \quad (15)$$

After going through the limiter, we obtain

$$e_L(t) = \text{sgn}(\tilde{e}_{WB}(t)) = \sqrt{P_L} \left[\text{in}[\theta_1 d_1(t) \sin \omega_{sc} t + \theta_2 d_2(t) + \phi] \right] \quad (16)$$

where $\left[\text{in}[x] \right]$ is given by $\text{sgn}(\sin(x))$ and $\sqrt{P_L}$ is the voltage output of the limiter.

Denote $a_1(t)$ as the binary-valued input of channel 1 to the QPSK (8.5-MHz) modulator and let $a_2(t) = e_L(t)$ the channel 2 input to the QPSK modulator. We have

$$a_1(t) = d_3(t) \quad (17)$$

and

$$a_2(t) = \left[\text{in}[\theta_1 d_1(t) \overset{(1.024 \text{ MHz})}{\downarrow} \sin \omega_{sc1} t + \theta_2 d_2(t) + \phi] \right] \quad (18)$$

Now the 8.5-MHz subcarrier is modulated in the form

$$s(t) = \sum_{n=1}^{\infty} \frac{4}{n\pi} \sin \left[n \left(\omega_{sc2} t + \phi(t) \right) \right] \quad (19)$$

where

$$\phi(t) = \theta a_1(t) a_2(t) - \frac{\pi}{2} (a_1(t) - 1) \quad (20)$$

The value of θ determines the power relationship between channels 1 and 2. A value of 26.6° provides a 4:1 power ratio (Ch2:Ch1) after lowpass filtering the 8.50-MHz subcarrier to the fundamental. Now,

$$s(t) = \sum_{n=1}^{\infty} \frac{4}{n\pi} \sin \left[n \left(\omega_{sc2} t + \phi(t) \right) \right] \quad (21)$$

or

$$s(t) = \sum_{n=1}^{\infty} \frac{4}{n\pi} \cos(n\phi) \sin(n\omega_{sc2} t) + \sum_{n=1}^{\infty} \frac{4}{n\pi} \sin(n\phi) \cos(n\omega_{sc2} t) \quad (22)$$

Now,

$$\cos(n\phi) = \cos \left\{ \left[\theta a_1 a_2 - \frac{\pi}{2} (a_1 - 1) \right] n \right\} \quad (23)$$

$$\cos(n\phi) = \cos(na_1 a_2 \theta) \cos \left[n \frac{\pi}{2} (a_1 - 1) \right] - \sin(n\theta a_1 a_2) \sin \left(n \frac{\pi}{2} (a_1 - 1) \right) \quad (24)$$

$$\sin(n\phi) = \sin \left[na_1 a_2 \theta \right] \cos \left(n \frac{\pi}{2} (a_1 - 1) \right) + \cos(na_1 a_2 \theta) \sin \left(n \frac{\pi}{2} (a_1 - 1) \right) \quad (25)$$

Also,

$$\cos(n\phi) = \cos(n\theta) \cdot a_1(t) \quad (26)$$

and

$$\sin(n\theta) = a_2(t) \cdot \sin\theta \quad (27)$$

Hence,

$$s(t) = a_1(t) \sum_{n=1}^{\infty} \frac{4}{n\pi} \cos(n\theta) \sin(n\omega_{sc2}t) + a_2(t) \sum_{n=1}^{\infty} \frac{4}{n\pi} \sin\theta \cdot \cos n\omega_{sc2}t \quad (28)$$

Now $s(t)$ is bandpass filtered (see Figure 1) so that its fundamental is passed; therefore, we obtain out of the BPF

$$s(t)|_{BPF} = a_1(t) \frac{4}{\pi} \cos\theta \sin \omega_{sc2}t + a_2(t) \frac{4}{\pi} \sin\theta \cos \omega_{sc2}t \quad (29)$$

This signal is added to channel 3 and frequency modulated onto the carrier which is sent to the TDRS, then bent piped to the TDRS ground terminal. After FM demodulation, the signal is demodulated by the 8.5-MHz QPSK subcarrier demodulator. This produces a channel 2 output at the ground terminal which is given by

$$s_2(t) = \sqrt{P_2} \sum_{n=1}^{\infty} \sin[\theta_1 d_1(t) \sin \omega_{sc1}t + \theta_2 d_2(t) + \phi] \quad (30)$$

where P_2 is the power in the demodulated channel 2. Note that

$$\sum_{n=1}^{\infty} \sin[nx] = \sum_{n=1}^{\infty} \frac{4}{n\pi} \sin[nx] \quad (x \text{ in radians}) \quad (31)$$

which is a Fourier series expansion of $\sum_{n=1}^{\infty} \sin[nx]$. Using (31) in (30) produces

$$\begin{aligned} s_2(t) &= \sqrt{P_2} \sum_{n=1}^{\infty} \frac{4}{n\pi} \sin(n\theta_1 d_1(t) \sin \omega_{sc}t) \cos(n\theta_2 d_2(t) + n\phi) \\ &+ \sqrt{P_2} \sum_{n=1}^{\infty} \frac{4}{n\pi} \cos(n\theta_1 d_1(t) \sin \omega_{sc}t) \sin(n\theta_2 d_2(t) + n\phi) \end{aligned} \quad (32)$$

where \sum again denotes summation over odd integer values. Using the relationships in (3) produces

$$\begin{aligned}
 e_L(t) = & \sqrt{P_2} \sum_{n=1}^{\infty} \frac{4}{n\pi} (\cos n\theta_2 \cos n\phi - d_2(t) \sin n\theta_2 \sin n\phi) d_1(t) \\
 & \times \left\{ \sum_{m=1}^{\infty} 2J_m(n\theta_1) \sin(m\omega_{sc}t) \right\} + \sqrt{P_2} \sum_{n=1}^{\infty} \frac{4}{n\pi} \\
 & \times (d_2(t) \sin n\theta_2 \cos n\phi + \cos n\theta_2 \sin n\phi) \left\{ J_0(n\theta_1) + \sum_{m=2}^{\infty} 2J_m(n\theta_1) \cos(m\omega_{sc}t) \right\} \quad (33)
 \end{aligned}$$

Now we determine the terms out of the limiter at baseband out to a frequency extent of slightly more than ω_{sc} . We have

$$\begin{aligned}
 E_L(t) \Big|_{LP} = & \overbrace{\frac{8}{\pi} \sqrt{P_2} d_1(t) \left\{ \sum_{n=1}^{\infty} \frac{1}{n} \cos n\theta_2 \cos n\phi J_1(n\theta_1) \right\} \sin \omega_{sc}t}^{\text{16-kbps data on 1.024-MHz subcarrier}} \\
 & - \overbrace{\frac{8}{\pi} \sqrt{P_2} d_1(t) d_2(t) \left\{ \sum_{n=1}^{\infty} \frac{1}{n} \sin n\theta_2 \sin n\phi J_1(n\theta_1) \right\} \sin \omega_{sc}t}^{\text{cross modulation on subcarrier}} \\
 & + \overbrace{\frac{4}{\pi} \sqrt{P_2} d_2(t) \left\{ \sum_{n=1}^{\infty} \frac{1}{n} \sin n\theta_2 \cos n\phi J_0(n\theta_1) \right\}}^{\text{32-kbps data at baseband}} \\
 & + \overbrace{\frac{4}{\pi} \sqrt{P_2} \left\{ \sum_{n=1}^{\infty} \frac{1}{n} \cos n\theta_2 \sin n\phi J_0(n\theta_1) \right\}}^{\text{DC term}} \quad (34)
 \end{aligned}$$

Hence, we see that the 16-kbps data modulated on the 1.024-MHz subcarrier is present, as is the 32-kbps baseband data and they are separable by filtering. A cross-modulation term is also present on the subcarrier, but its amplitude goes to zero as the PI carrier-loop phase error, ϕ , goes to zero.

6.C POWER LEVELS OUT OF THE LIMITER

The first three terms of (33) were programmed on a digital computer with parameters $\theta_1 = 0.8$ radian, $\theta_2 = 1.0$ radian and $P_2 = 1$, with the result that all the power out of the limiter was in the 32-kbps data stream. However, by computer evaluation using 5000 terms, it was observed that, when $\theta_1 = 0.8$ radian and $\theta_2 = 0.6$ radian, the subcarrier and baseband relative-power levels were given by

$$P_{SC} = -4.5 \text{ dB} \quad ; \quad P_{BB} = -5.6 \text{ dB} \\ (\theta_1 = 0.8 \quad , \quad \theta_2 = 0.6)$$

Thus, varying the modulation indices causes the relative-power levels to vary drastically. As seen at the output of channel 2 of the 8.5-MHz subcarrier demodulator, the baseband and subcarrier signal levels are plotted in Figure 3 as a function of θ_1 for $\theta_2 = 1.0$ radian. When the specification values of $\theta_1 = 0.8$ and $\theta_2 = 1.0$ are used, it is seen that all the power resides in the baseband signal; i.e., complete suppression of the subcarrier signal occurs. Figure 4 illustrates the same signal powers for the condition that $\theta_1 = 0.8$ when θ_2 is variable.

In order to check the sensitivity of the results to the modulation indices, the indices were allowed to vary $\pm 5\%$ and $\pm 10\%$ from the nominal values of $\theta_1 = 0.8$ and $\theta_2 = 1.0$. In addition, phase errors of $\phi = 0$ and 0.1 radian were used in the program. When tolerances of 15% were used with $\theta = 0.1$, all the power appeared in the baseband (32-kbps) signal out of the QPSK demodulator. When 10% tolerances were considered, it was also found that, when $\phi = 0.1$, $\theta_1 = 0.8 + 10\% = 0.88$ and $\theta_2 = 1 - 10\% = 0.9$, the subcarrier is again fully suppressed. If $\pm 15\%$ variations could occur so that $\theta_1 > \theta_2$, then some 1.024-MHz subcarrier signal would appear along with the baseband signal at the output of the subcarrier demodulator.

When the baseband signal is turned off (assuming $\theta_2 = 0$), the normalized power output in channel 2 of the QPSK demodulator is 0.81 (total power = 1 , or -0.9 dB, which is the power in the fundamental of the 1.024-MHz subcarrier. Clearly, when $\theta_2 = 0$, no power will appear at the 32-kbps data rate.

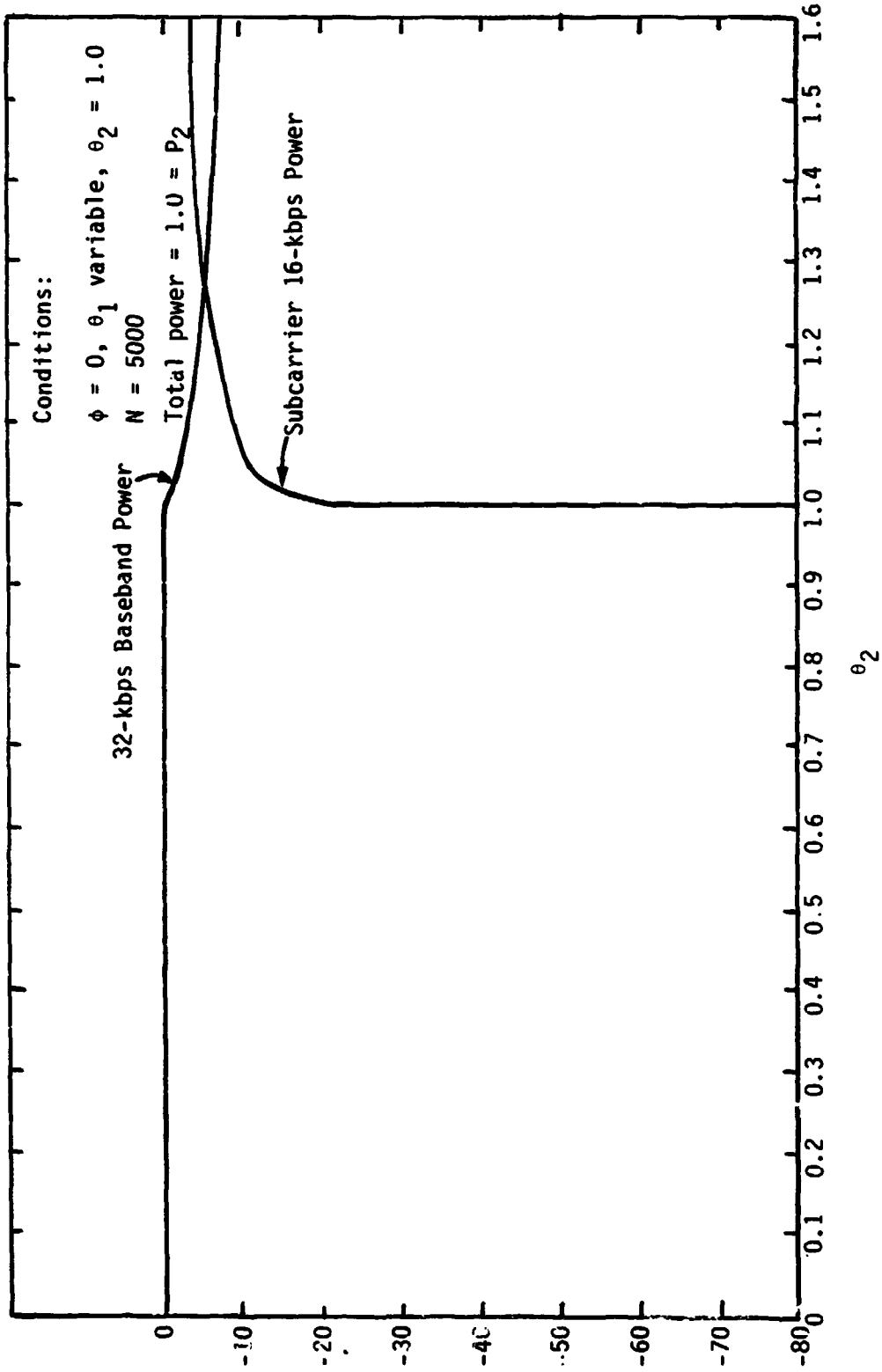


Figure 3. 32-kbps (BB) and 16-kbps (SC) Power Out of Channel 2 QPSK Demodulator

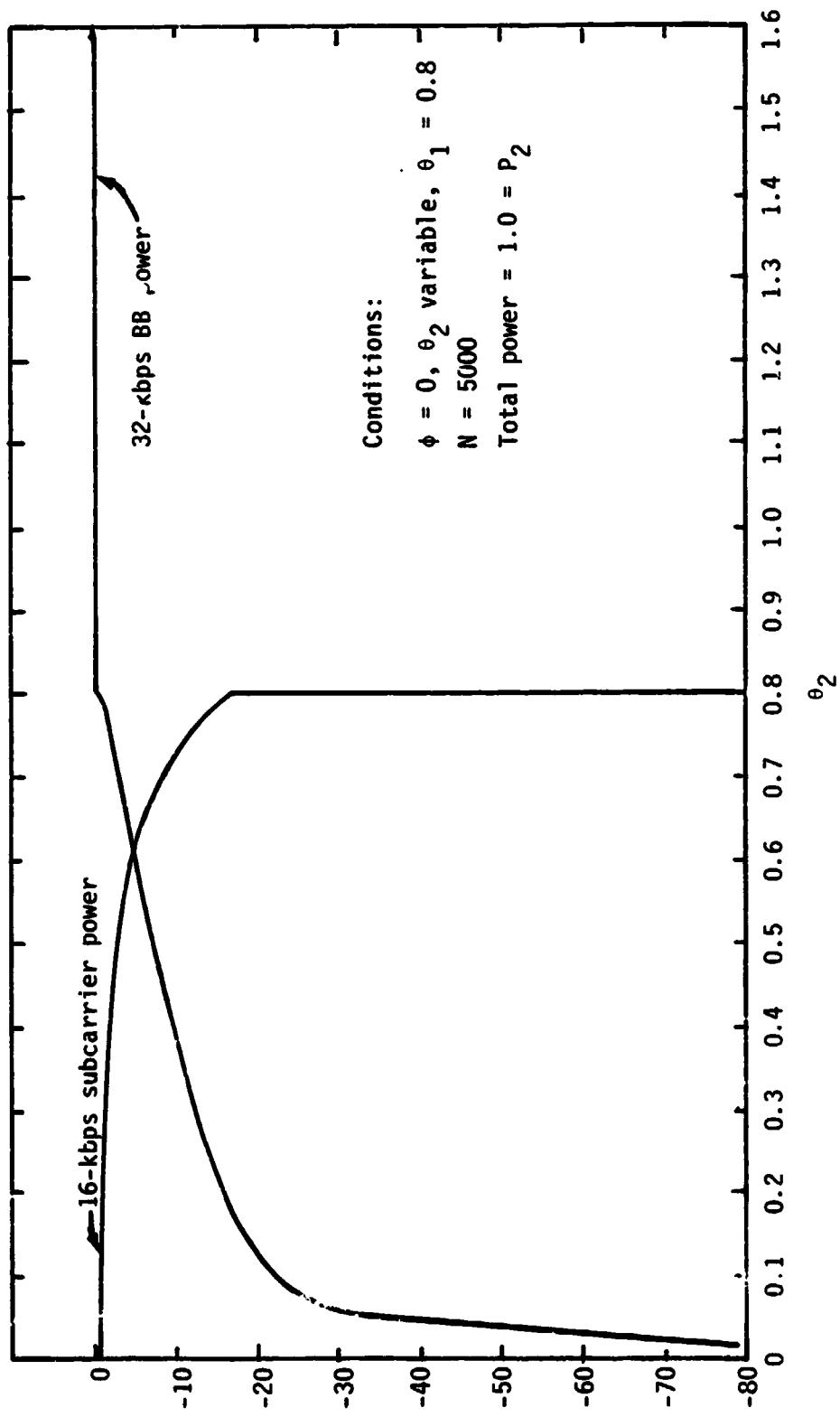


Figure 4. 32-kbps (BB) and 16-kbps (SC) Power Out of Channel 2 QPSK Demodulator

7.0 CONCLUSION

We conclude (perhaps, by good fortune) that the existing specification values of $\theta_1 = 0.8$ and $\theta_2 = 1.0$ radian fully suppress the subcarrier signal and leave the desired baseband 32-kbps at full power at the output of the QPSK subcarrier TDRSS earth terminal. Since the 5-MHz lowpass filter was not included in the analysis, the measured values of the power levels of the subcarrier and baseband signals might vary slightly from the predicted values given here.

REFERENCES

1. J. K. Holmes, "Ku-Band Bent-Pipe Mode 2 BER Performance Degradation, Axiomatix Interim Report No. R8102-4, February 18, 1981.
2. R. Cager, D. LaFlame and L. Parode, "Orbiter Ku-Band Integrated Radar and Communication Subsystems," IEEE Transactions on Communications, Volume COM-26, No. 11, November 1978.
3. S. Kindorf, private communication with TRW TDRSS engineer.



9841 Airport Boulevard • Suite 912 • Los Angeles, California 90045 • Phone (213) 641-8600

TECHNICAL MEMORANDUM NO. M8401-1

TO: Peter Nilsen Date: January 10, 1984
FROM: Jack Holmes cc: T. Costello, JSC
J. Ratliff, JSC
SUBJECT: A Possible Explanation of Solar Max Retrieval
I-Q Swapping due to Noise Filtering in the
8.5-MHz Subcarrier Demodulator

1.0 SUMMARY

In this memo, it is shown that the power ratio of channel 2 to channel 1, out of the lowpass arm filters in the TDRSS ground station subcarrier demodulator, can be as low as 1:1 when the input power is -113 dBm.

Although approximations were necessary, it seems reasonable to assume that the noise power present in the 5-MHz Shuttle Payload Interrogator shares the total power in channel 2 with the 32-kbps signal but, depending on the SNR in the 5-MHz bandwidth, a good portion of the noise is filtered out in the TDRSS QPSK subcarrier demodulator arm filters. Thus, the QPSK demodulator has great difficulty in deciding whether the strong or weak channel is phased in the strong channel position. This could account for the tendency to lock in the wrong I-Q relationship and not be detected.

2.0 APPROACH

The purpose of the calculations given in this memo is to show that, at low SNR's into the PI, the noise power contained in the 5-MHz lowpass PI filter is partly filtered out in the arm filters of the QPSK tracker (subcarrier demodulator) and therefore, the power ratio is condensed close to 1:1 out of the QPSK demodulator. To show this, we will model the system in the next section.

3.0 MODEL

A model of the complete Solar Max signal path is indicated in Figure 1. The signal transmitted from the Solar Max transmitter is of the form

$$y(t) = \sqrt{2P} \sin(\omega_c t + \theta_1 d_1(t) \sin \omega_{sc} t + \theta_2 d_2(t)) \quad (1)$$

where

- P = signal power
- $\omega_c = 2\pi f_c$, angular carrier frequency
- $\theta_1 = 16$ -kbps phase-modulation angle ($0.8 \pm 5\%$ rad)
- $\theta_2 = 32$ -kbps phase-modulation angle ($1.0 \pm 5\%$ rad)
- $d_1(t) = 16$ -kbps biphase-M data
- $d_2(t) = 32$ -kbps biphase-M data

As discussed in [1], the carrier-loop demodulated signal into the 5-MHz lowpass filter is given by

$$\begin{aligned} e_{WB}(t) = & \sqrt{P} \cos(\theta_2) \sin\phi \left\{ J_0(\theta_1) + \sum_{n=2}^{\infty} 2J_n(\theta_1) \cos n\omega_{sc} t \right\} \\ & + \sqrt{P} d_2(t) \sin \theta_2 \cos\phi \left\{ J_0(\theta_1) + \sum_{n=2}^{\infty} 2J_n(\theta_1) \cos n\omega_{sc} t \right\} \\ & + \sqrt{P} d_1(t) \cos \theta_2 \cos\phi \left\{ \sum_{n=1}^{\infty} 2J_n(\theta_1) \sin n\omega_{sc} t \right\} \\ & - \sqrt{P} d_1(t) d_2(t) \sin \theta_2 \sin\phi \left\{ \sum_{n=1}^{\infty} 2J_n(\theta_1) \sin n\omega_{sc} t \right\} + n(t) \quad (2) \end{aligned}$$

where \sum_e and \sum_o denote the summation over odd and even indices, respectively. The term $n(t)$ is a sample function of white Gaussian noise. Expanding some of the key terms, we have

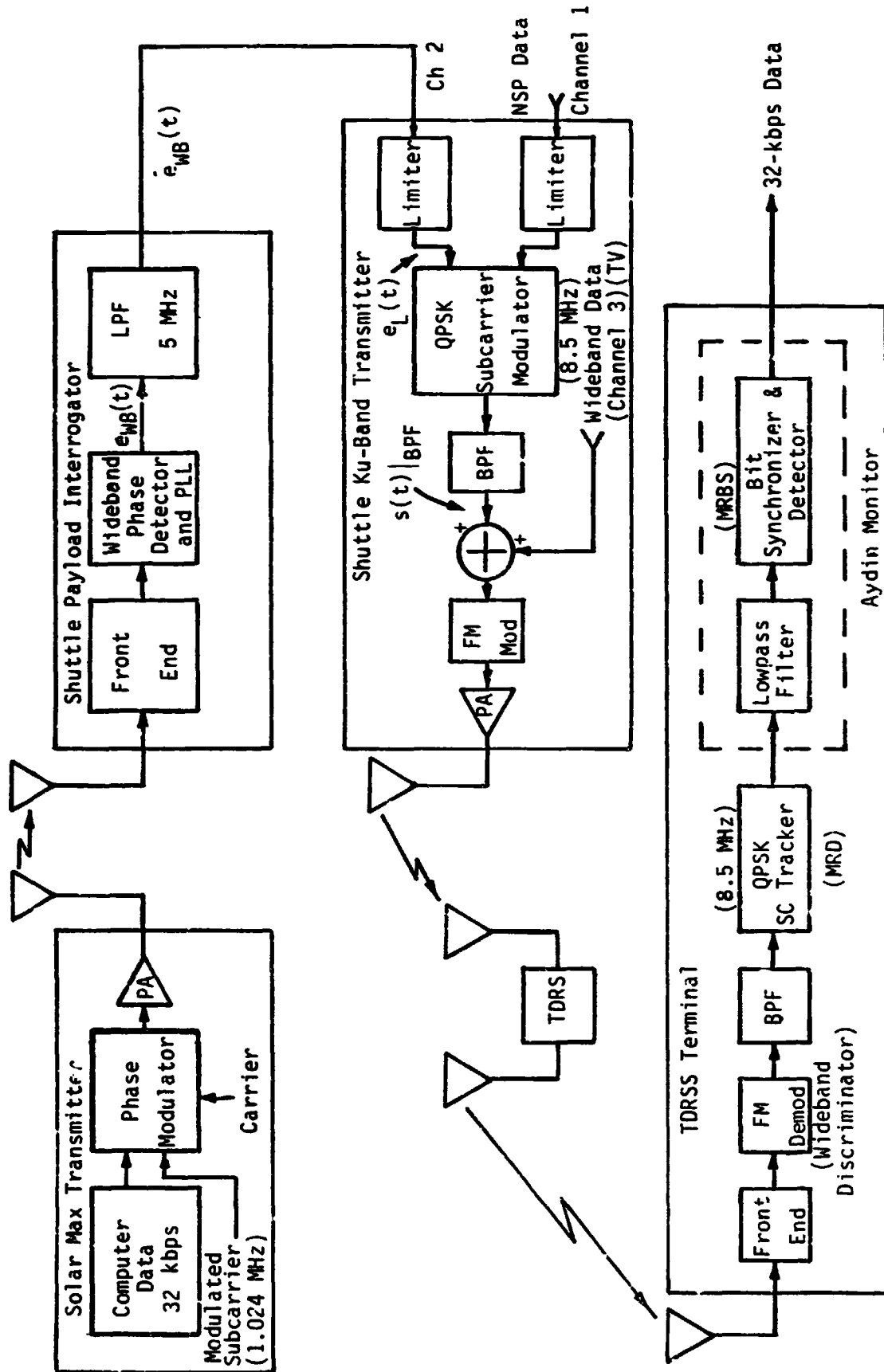


Figure 1. Mode: for the Solar Max Retrieval Data Dump

$$\begin{aligned}
 e_{\text{NB}}(t) = & \overbrace{\sqrt{P} J_0(\theta_1) \cos \theta_1 \sin \phi}^{\text{DC}} + \overbrace{\sqrt{P} d_2(t) \sin \theta_2 \cos \phi J_0(\theta_1)}^{\text{32-kbps data}} \\
 & + \overbrace{2 \sqrt{P} J_1(\theta_1) d_1(t) \cos \theta_2 \cos \phi \sin \omega_{\text{SC}} t}^{\text{16-kbps data on 1.024-MHz subcarrier}} \\
 & - \overbrace{2 \sqrt{P} d_1(t) d_2(t) J_1(\theta_1) \sin \theta_2 \sin \phi \sin \omega_{\text{SC}} t}^{\text{cross modulation on subcarrier}} \\
 & + \overbrace{2 \sqrt{P} J_2(\theta_1) \sin \theta_2 d_2(t) \cos(2 \omega_{\text{SC}} t) \cos \phi}^{\text{second harmonic of subcarrier}} + n(t) \\
 & + \text{terms at } 3\omega_{\text{SC}}, 4\omega_{\text{SC}}, \text{ etc.} \tag{3}
 \end{aligned}$$

When the phase error, ϕ , is assumed to be small, we have that the dominant term out of the carrier demodulator is

$$e_{\text{NB}}(t) \approx \overbrace{\sqrt{P} d_2(t) \sin \theta_2 J_0(\theta_1)}^{\text{32-kbps data}} + n(t) + 2\sqrt{P} J_1(\theta_1) d_1(t) \cos \theta_2 \sin \omega_{\text{SC}} t \tag{4}$$

When the modulation indices are $\theta_1 = 0.8$ and $\theta_2 = 1.0$, the relative power levels out of the 5-MHz lowpass filter, following the carrier demodulator, is given by

$$\begin{aligned}
 P_{\text{NB}} = & \underbrace{0.507 P}_{d_2(t)} + \underbrace{0.0794 P}_{\text{modulated subcarrier}} + \underbrace{0.00814 P}_{d_2(t)@2\omega_{\text{SC}}} + \dots + \underbrace{P_n}_{\text{noise}} \tag{5}
 \end{aligned}$$

with P_n being the power out of the 5-MHz lowpass filter. In order to size the thermal noise power, we note that, with the 3.5-dB noise figure of the PI receiver, the P/N_0 ratio is given by

$$\frac{P}{N_0} = P \text{ dBm} + 170.5 \text{ dBm/Hz} \tag{6}$$

So that, for a -98 dBm signal level in a noise bandwidth of $5 \times 10^6 \times \pi/2$ Hz (from the 5-MHz LPF), we have

$$\frac{P}{N_0B} = 170.5 - 10 \log\left(5 \times \frac{\pi}{2} \times 10^6\right) - 98 \quad (7)$$

or

$$\frac{P}{N_0B} = 3.5 \text{ dB} \quad (8)$$

Hence, the three significant components plus noise from (5) are given by

$$P_{WB} = 0.507P + 0.0794P + 0.00814P + 0.44P \quad (9)$$

Note that the thru, and remaining, signal-type components are negligible since the second signal term is 8 dB down from the 32-kbps baseband data term. Since the analysis with both a baseband Manchester signal and a Manchester-modulated subcarrier signal into a limiter is not available in the literature, we will modify the model slightly so that known results can be used. Hence, we will model the input to the limiter terminal* of the QPSK subcarrier as a baseband signal (32 kbps) plus thermal noise. Our model is illustrated in Figure 2.

In Appendix A, it is shown that the signal plus noise out of the (conceptual) limiter is given by

$$y(t) = d(t) \operatorname{erf}\left(\sqrt{\frac{S}{2N}}\right) + N(t) \quad (10)$$

where

$$\operatorname{erf}(x) = \frac{2}{\sqrt{\pi}} \int_0^x e^{-t^2} dt \quad (11)$$

*The limiter is inherent in the QPSK modulator.



Figure 2. Model of Signal Plus Noise into the Multiplexer (Modulator)

with $d(t)$ representing the 32-kbps baseband data stream and $N(t)$ is the resulting noise. The limiter is modeled as outputting a value of ± 1 for convenience. In Appendix B, the autocorrelation function of y is given by

$$R_y(\tau) = R_d(\tau) \operatorname{erf}^2 \left[\sqrt{\frac{S}{2N}} \right] + 4 R_d(\tau) \sum_{m=0}^{\infty} \left[z^{(2m+1)} \left(\sqrt{\frac{S}{N}} \right) \right] \left[\frac{R_n(\tau)}{\sigma^2} \right]^{2m+2} / (2m+2)! \quad (12)$$

$$+ 4 \sum_{m=0}^{\infty} \left[z^{(2m)} \left(\sqrt{\frac{S}{N}} \right) \right]^2 \left[\frac{R_n(\tau)}{\sigma^2} \right]^{(2m+1)} / (2m+1)! \quad (13)$$

where

$$z^{(n)}(x) = \frac{d^n}{dx^n} \left\{ \frac{1}{\sqrt{2\pi}} e^{-x^2/2} \right\} \quad (14)$$

The first term is the $S \times S$ term, second is the $S \times N$ terms, and the last term is the $N \times N$ terms. Notice that, at high SNR,

$$R_y(\tau) \cong R_d(\tau) \quad (15)$$

where $R_d(\tau)$ is the autocorrelation function of the 32-kbps data stream. At low SNR, it is shown in Appendix B that the autocorrelation function converges to

$$R_y(\tau) = \frac{2}{\pi} \arcsin \left[\frac{R_n(\tau)}{\sigma^2} \right] \quad (16)$$

where $R_n(\tau)$ is the input autocorrelation function of the noise and $\sigma^2 = R_n(0)$, the variance of the input noise process.

Expanding (12) produces

$$\begin{aligned}
R_y(\tau) = & R_d(\tau) \operatorname{erf}^2\left(\sqrt{\frac{S}{2N}}\right) + 2R_d(\tau) \left[z^{(1)}\left(\sqrt{\frac{S}{N}}\right)\right]^2 \left[\frac{R_n(\tau)}{\sigma^2}\right]^2 \\
& + \frac{1}{6} R_d(\tau) \left[z^{(3)}\left(\sqrt{\frac{S}{N}}\right)\right]^2 \left[\frac{R_n(\tau)}{\sigma^2}\right]^4 + \frac{1}{180} R_d(\tau) \left[z^{(5)}\left(\sqrt{\frac{S}{N}}\right)\right]^2 \left[\frac{R_n(\tau)}{\sigma^2}\right]^6 \\
& + 4 \left[z^{(0)}\left(\sqrt{\frac{S}{N}}\right)\right]^2 \left[\frac{R_n(\tau)}{\sigma^2}\right] + \frac{2}{3} \left[z^{(2)}\left(\sqrt{\frac{S}{N}}\right)\right]^2 \left[\frac{R_n(\tau)}{\sigma^2}\right]^3 \\
& + \frac{1}{30} \left[z^{(4)}\left(\sqrt{\frac{S}{N}}\right)\right]^2 \left[\frac{R_n(\tau)}{\sigma^2}\right]^5 + o\left(R_n^7(\tau)\right)
\end{aligned} \tag{17}$$

So that the first term is signal x signal and the rest are either signal x noise or noise x noise terms. As can be seen the terms tend to diminish in size assuming that $z^{(i)}(\sqrt{S/N})$ does not increase too fast with i . For each SNR evaluation we will determine the significant terms. Once the spectral density of the noise is known, the power loss at the receiver 1.8 MHz demod arm filters can be computed.

4.0 DEMODULATED POWER RATIO AT P = -98 dBm

From (8) and (9) we see that the signal to noise ratio S/N is given by

$$\frac{S}{N} = 3.5 - 10 \log(0.507) = 0.56 \text{ dB} = 1.14 \tag{18}$$

Hence by evaluating the z parameters we have

$$\begin{aligned}
z^{(0)}(1.07) &= 0.225 & z^{(3)}(1.07) &= 0.446 \\
z^{(1)}(1.07) &= -0.241 & z^{(4)}(1.07) &= -0.57 \\
z^{(2)}(1.07) &= 0.032 & z^{(5)}(1.07) &= -1.18
\end{aligned} \tag{19}$$

From (17) we can write

$$R_y(\tau) = R_d(\tau) \operatorname{erf}\left(\sqrt{\frac{S}{2N}}\right) + R_N(\tau) \tag{20}$$

with $R_N(\tau)$ defined to be equal to all the terms in $R_y(\tau)$ except

$$R_d(\tau) = \text{erf}\left(\sqrt{\frac{S}{2N}}\right)$$

Combining only the non-negligible terms from (17) we have

$$R_N(\tau) \cong 0.1 R_d(\tau) \left[\frac{R_n(\tau)}{\sigma^2} \right]^2 + 0.033 R_d(\tau) \left[\frac{R_n(\tau)}{\sigma^2} \right]^4 + 0.2 \left[\frac{R_n(\tau)}{\sigma^2} \right] \quad (21)$$

We see that the spectral density (with the help of Appendix B) is given by (neglecting $R_d(\tau)$ since $d(t)$ is much narrower banded than $n(t)$)

$$\begin{aligned} \mathcal{S}_N(f) \cong \frac{0.05}{B} \left(1 - \frac{|f|}{2B} \right) U_{2B}(f) + \frac{0.0083}{B^2} \left(\frac{4}{3} B - \frac{f^2}{2B} + \frac{|f^3|}{8B^2} \right) + \frac{0.1}{B} U_B(f) \\ 0 \leq |f| \leq 2B \end{aligned} \quad (22)$$

or

$$\mathcal{S}_N(f) \cong \frac{0.0083}{B^2} \left(\frac{8}{3} B - 2|f| + \frac{f^2}{2B} - \frac{|f^3|}{24B^2} \right) \quad 2B \leq |f| \leq 4B$$

with

$$\begin{aligned} U_B(f) &= 1 \quad |f| \leq B \\ &= 0 \quad |f| \geq B \end{aligned} \quad (23)$$

The spectral density is sketched in Figure 3.

From (10), when $S/N = 1.14$ (eq. (18)), we have, out of our apparent limiter, the signal structure

$$y_L(t) = 0.711 d_2(t) + N(t) \quad (24)$$

with the spectral density of $N(t)$ being given by (21) and (22) and is plotted in Figure 3. Now, as shown in [1], we have that at the subcarrier demodulator the signal is filtered to 1.8 MHz which reduces the power in the strong channel

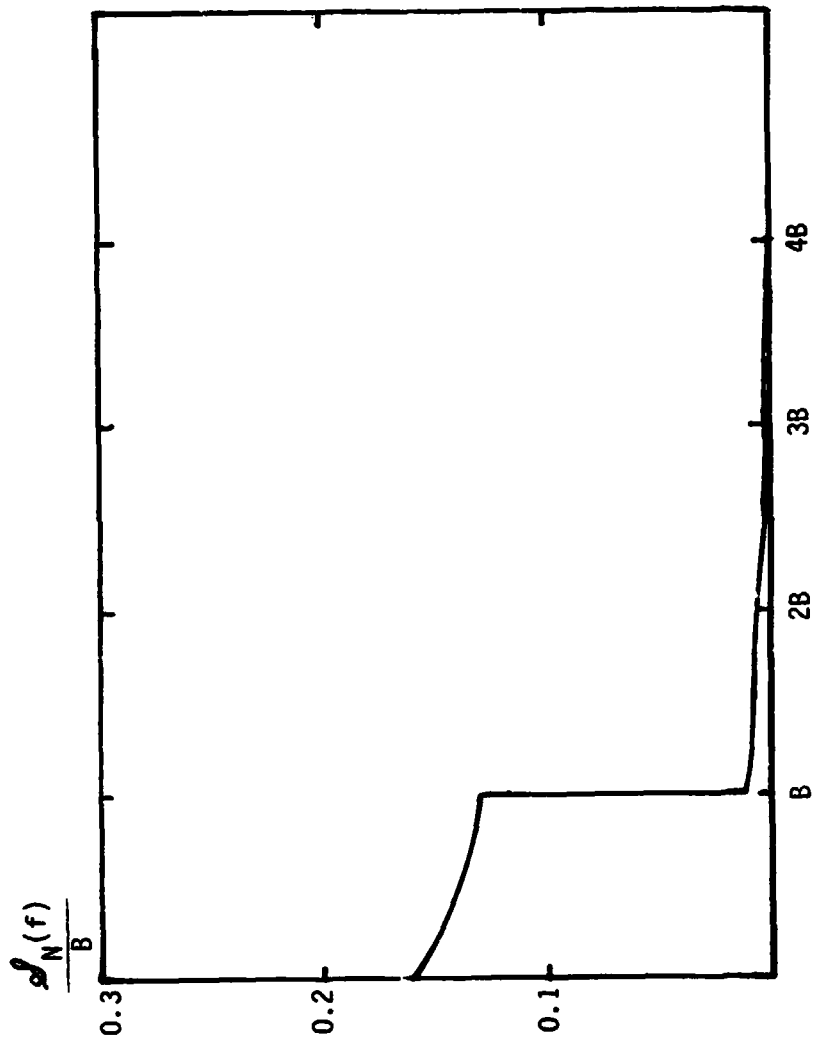


Figure 3. Sketch of Spectral Density of the Noise at $P = -98$ dBm

from the original ratio of 4:1 to something less. Since channel 1 is a 192 kbps data stream without additive thermal noise, the weak channel is not affected by the 1.8 MHz filter. The power ratio after filtering is approximately

$$PR \cong \frac{0.51 + (0.145)\left(\frac{1.8}{5.0}\right)^2}{0.25} = 2.46 \quad (25)$$

Hence in the subcarrier loop the power ratio is approximately 2.46:1.

4.0 DEMODULATED POWER RATIO AT P = -103 dBm

Now the S/N is given by

$$S/N = -4.44 \text{ dB} \quad (26)$$

The signal suppression factor

$$\alpha = \text{erf}\left(\sqrt{\frac{S}{2N}}\right) \quad (27)$$

is then given by

$$\alpha = \text{erf}(0.42) = 0.45 \quad (28)$$

so that the voltage out of the (apparent) limiter is given by

$$y_L(t) = 0.45 d_2(t) + N(t) \quad (29)$$

We can evaluate the z parameters by using the fact that $\sqrt{S/N} = 0.6$ so that

$$\begin{aligned} z^{(0)}(0.6) &= 0.33 & z^{(3)}(0.6) &= 0.53 \\ z^{(1)}(0.6) &= -0.2 & z^{(4)}(0.6) &= 0.32 \\ z^{(2)}(0.6) &= -0.21 & z^{(5)}(0.6) &= -2.31 \end{aligned} \quad (30)$$

Combining all the non-negligible terms we obtain

$$R_N(\tau) \approx 0.08 R_d(\tau) \left[\frac{R_n(\tau)}{2} \right]^2 + 0.047 R_d(\tau) \left[\frac{R_n(\tau)}{2} \right]^4 + 0.44 \left[\frac{R_n(\tau)}{2} \right] \quad (31)$$

Hence, the noise power spectral density is given by (using Appendix B)

$$\mathcal{S}_N(f) = \frac{0.04}{B} \left(1 - \frac{|f|}{2B} \right) U_{2B}(f) + \frac{0.012}{B^2} \left(\frac{4}{3} B - \frac{f^2}{2B} + \frac{|f|^3}{8B^2} \right) + \frac{0.22}{B} U_B(f) \quad (32)$$

$$0 < |f| \leq 2B$$

and

$$\mathcal{S}_N(f) = \frac{0.012}{B^2} \left(\frac{8}{3} B - 2|f| + \frac{f^2}{2B} - \frac{|f|^3}{24B^2} \right), \quad 0 \leq |f| \leq 2B \quad (33)$$

Hence, we have

$$y_L(t) = 0.45 d_2(t) + N(t), \quad (34)$$

with $N(t)$ having the spectral density of equations (32) and (33). The spectral density is plotted in Figure 4. Again filtering to 1.8 MHz yields a power ratio of

$$PR \approx \frac{0.203 + 2(0.265)\left(\frac{1.8}{5}\right)}{0.25} = 1.58 \quad (35)$$

Therefore, in the subcarrier loop, the power ratio is approximately 2.15:1.

Now consider the $P = -108$ dBm case.

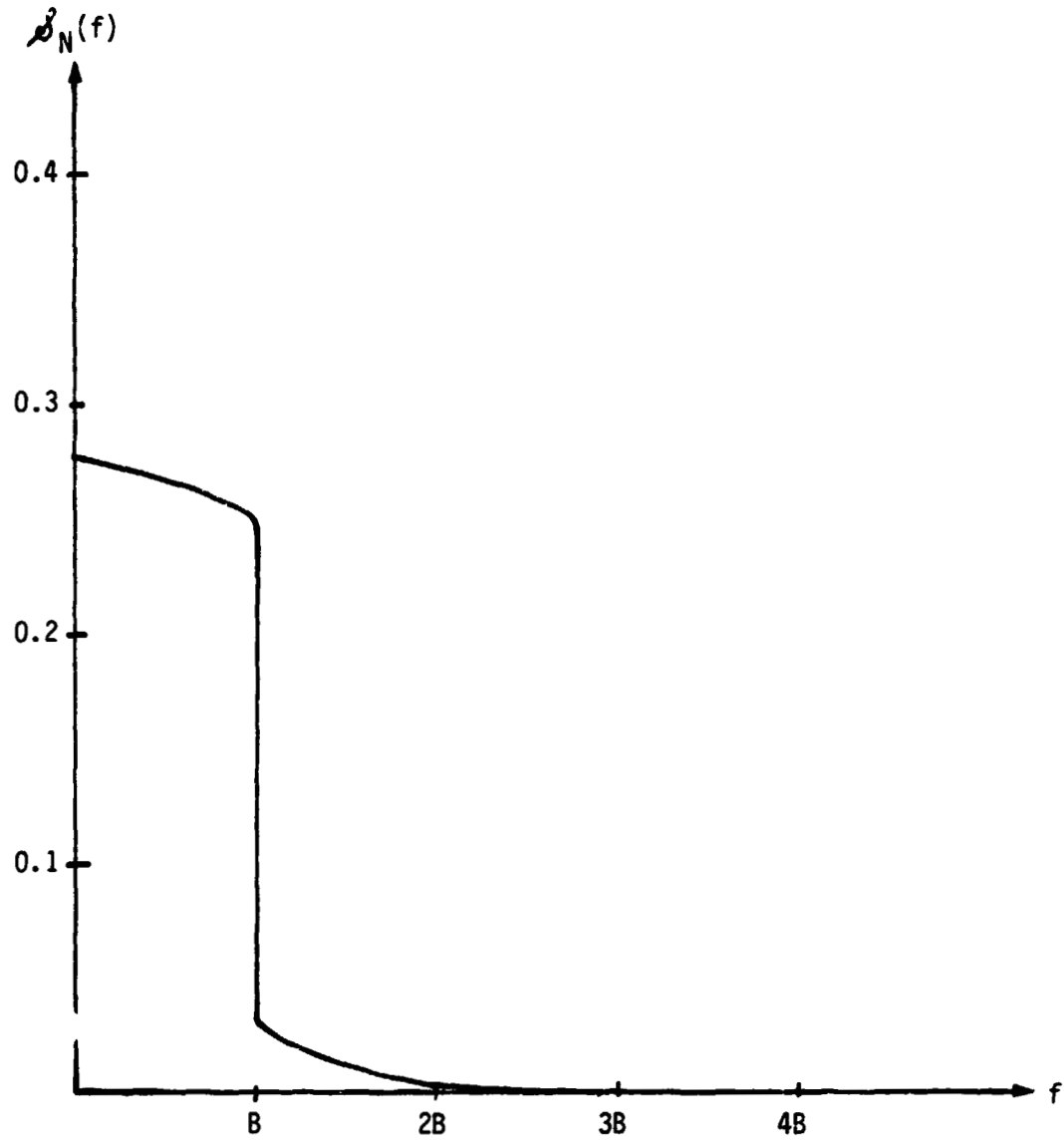


Figure 4. Power Spectral Density of the Noise When $P = -103$ dBm

5.0 DEMODULATED POWER RATIO AT P = -108 dBm

In this case, the S/N is 5 dB lower than in the previous case, hence

$$S/N = -9.44 \text{ dB} \quad (36)$$

The signal suppression factor is given by

$$\alpha = \text{erf}(0.238) = 0.265 \quad (37)$$

Hence, the voltage out of the limiter can be written as

$$y_L(t) = 0.265 d_2(t) + N(t) \quad (38)$$

In order to estimate the noise spectral density we must compute the z parameters again with argument $\sqrt{S/N} = \sqrt{0.114} = 0.337$

$$\begin{aligned} z^{(0)}(0.337) &= 0.376 & z^{(3)}(0.337) &= 0.3693 \\ z^{(1)}(0.337) &= -0.128 & z^{(4)}(0.337) &= 0.873 \\ z^{(2)}(0.337) &= -0.333 & z^{(5)}(0.337) &= -1.774 \end{aligned} \quad (39)$$

It follows that the noise autocorrelation function is given by

$$R_N(\tau) \cong 0.033 R_d(\tau) \left[\frac{R_n(\tau)}{2} \right]^2 + 0.566 \left[\frac{R_n(\tau)}{2} \right] + 0.074 \left[\frac{R_n(\tau)}{2} \right]^3 \quad (40)$$

Hence, from Appendix B, we have that the noise power spectral density is given by

$$\mathcal{S}_N(f) = \frac{0.0165}{B} \left(1 - \frac{|f|}{2B} \right) U_{2B}(f) + 0.283 U_B(f) + \frac{0.0093}{B} \left(3 - \left(\frac{f}{B} \right)^2 \right), \quad 0 < |f| < B \quad (41)$$

$$= \frac{0.0165}{B} \left(1 - \frac{|f|}{2B} \right) U_{2B}(f) + 0.0047 \left(3 - \frac{|f|}{B} \right)^2, \quad B < |f| < 3B \quad (42)$$

By adding up the total noise power and the signal power, assuming statistical independence, we see that the power totals much less than unity (~ 0.7 instead of 1.0), indicating that more terms should be taken to represent the noise waveform. However, since this analysis is only meant to imply feasibility of the I-Q switching problem, we continue on with our three term approximation. The power spectral density is plotted in Figure 5.

After filtering to 1.8 MHz we obtain a power ratio of

$$PR = \frac{0.07 + (0.32)^2 \frac{1.8}{5}}{0.25} = 1.2 \quad (43)$$

Hence we see that the power ratios are near unity at $P = -108$ dBm within the limits of our approximation.

6.0 DEMODULATED POWER RATIO AT $P = -113$ dBm

From (36), we have

$$S/N = -14.45 \text{ dB} \quad (44)$$

The signal suppression factor is given by

$$\alpha = \text{erf}(0.134) = 0.145 \quad (45)$$

It follows that the voltage out of the limiter can be written as

$$y_1(t) = 0.145 d_2(t) + N(t) \quad (46)$$

The z parameters for $\sqrt{S/N} = 0.19$ are

$$\begin{aligned} z^{(0)}(0.19) &= 0.3915 & z^{(4)}(0.19) &= 1.09 \\ z^{(1)}(0.19) &= -0.074 & z^{(3)}(0.19) &= 0.22 & z^{(5)}(0.19) &= -1.09 \\ z^{(2)}(0.19) &= -0.377 & z^{(6)}(0.19) &= -5.25 \end{aligned} \quad (47)$$

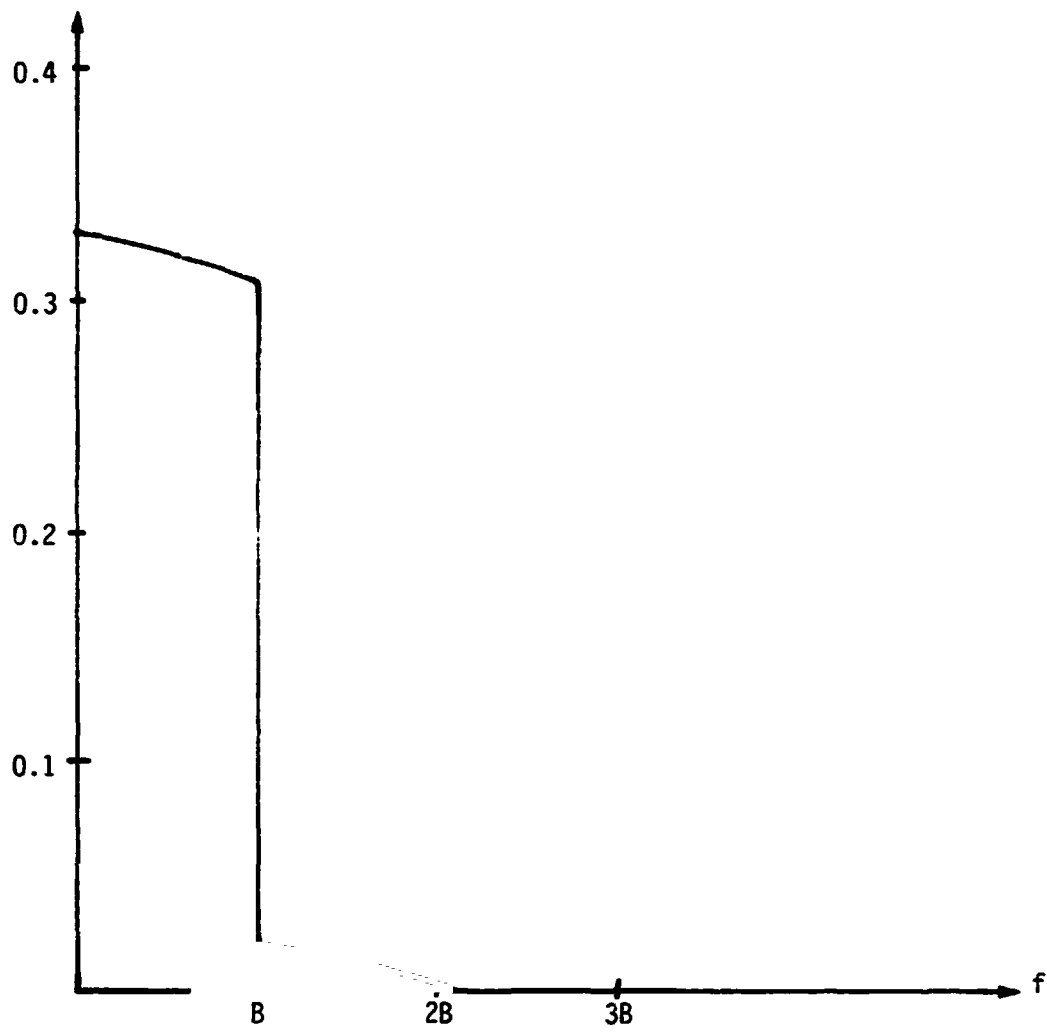


Figure 5. Sketch of Spectral Density of the Noise at $P = -106$ dBm

The noise autocorrelation function is given by

$$R_N(\tau) = 0.613 \left[\frac{R_n(\tau)}{\sigma^2} \right] + 0.09 \left[\frac{R_n(\tau)}{\sigma^2} \right]^3 \quad (48)$$

Using just the dominant term we obtain

$$S_N(f) \cong \frac{0.307}{B} U_B(f) \quad (49)$$

Hence, the power ratio after the 1.8 MHz arm filtering is

$$PR = \frac{0.021 + 0.307(2) \left(\frac{18}{5} \right)}{0.25} \quad (50)$$

which is unity! Hence, we conclude that filtering at the receiver could cause I-Q interchange in the vicinity of $P = -113$ dBm since the ratio of powers is about equal.

The channel power detector is illustrated in Figure 6. Basically it measures the voltage in the I and Q channels and forms the difference which is then filtered.

7.0 CONCLUSION

Based on some calculations which required certain approximations, it appears that the filtering of the channel signal pulse noise in the arm filters of the QPSK subcarrier demodulator can cause the power ratio out of the arm filters (what the QPSK loop "sees") is near 1:1 rather than 4:1 at an input power of about -113 dBm. Since the calculations involved important approximations, the results can only be described in approximate.

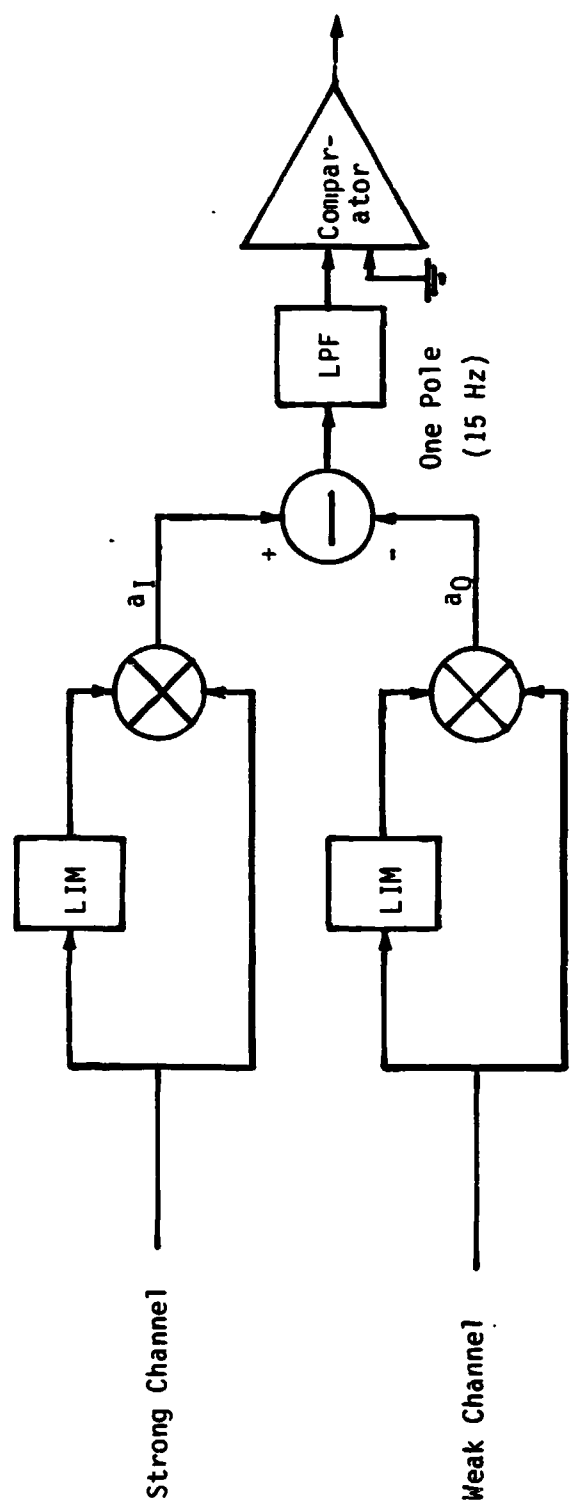


Figure 6. Channel Power Ratio Detector-Decision Circuit

REFERENCES

1. J. K. Holmes, "Solar Max Retrieval Signal Structure Before and After Limiting Using the Ku-Band Channel 2 Input," Axiomatix Technical Memorandum No. M8310-1, October 1, 1983.
2. J. K. Holmes, "Ku-Band Bent-Pipe Mode 2 BER Performance Degradation," Axiomatix Report No. R8102-4.
3. J. K. Holmes, Coherent Spread Spectrum Systems, Chapter 5, Wiley Interscience, 1982.
4. Operation and Maintenance Instructions, KSAR Medium-Range Demodulator For TDRSS Tracking, Return, and Modulation Equipment (TRAM)

APPENDIX A

BASEBAND DIGITAL SIGNAL-PLUS-NOISE THROUGH A HARD LIMITER

In this appendix, we determine the output spectral density of a baseband digital signal plus bandlimited Gaussian noise. This calculation allows one to determine the output C/N_0 value as a function of the input C/N_0 value. The derivation of the autocorrelation function follows that of Painter [1] with minor corrections in the final results. The model is shown in Figure A.1 below.

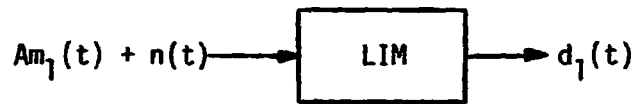


Figure A.1. Baseband Limiter Model

where $m_1(t)$ is an NRZ or Manchester binary-valued digital waveform, $n(t)$ is bandlimited, white Gaussian noise, and $d_1(t)$ is the output binary-valued waveform. Let

$$x(t) = Ad(t) + n(t) \quad (\text{A-1})$$

$$y(t) = \text{sgn}[x(t)] \quad (\text{A-2})$$

The first- and second-order density functions are given by

$$p_x(x_t, t) = \frac{1}{\sqrt{2\pi}} \exp\left[-\frac{1}{2\sigma^2} (x_t - \mu_t)^2\right] \quad (\text{A-3})$$

$$p_x(x_t, x_\tau) = \frac{1}{2\pi\sigma^2\sqrt{1-\rho^2}} \exp\left[-\frac{1}{2(1-\rho^2)} \left\{ \frac{(x_\tau - \mu_\tau)^2}{\sigma^2} - \frac{2\rho(x_\tau - \mu_\tau)(x_t - \mu_t)}{\sigma^2} + \frac{(x_t - \mu_t)^2}{\sigma^2} \right\}\right] \quad (\text{A-4})$$

where

$$x_t = x(t)$$

$$x_\tau = x(t+\tau)$$

$$\mu_t = E[x(t)] = Ad(t) \triangleq s(t)$$

$$\mu_\tau = E[x(t+\tau)] = Ad(t+\tau) \triangleq s(t+\tau)$$

$$\sigma^2 = E[(x_t - \mu_t)^2] = E[(x_\tau - \mu_\tau)^2]$$

$$\rho = \frac{1}{\sigma^2} E[(x_\tau - \mu_\tau)(x_t - \mu_t)]$$

or

$$\rho = \frac{1}{\sigma^2} E[n(t+\tau)n(t)] = \frac{R_n(\tau)}{\sigma^2} \quad (\text{A-5})$$

First let us compute the mean value of our process. We will temporarily drop the time subscript.

$$\mu = \int_{-\infty}^{\infty} \text{sgn}(x) p_x(x) dx \quad (\text{A-6})$$

which can be expressed as

$$\mu = \int_0^{\infty} \frac{1}{\sqrt{2\pi}\sigma} \exp\left[-\frac{1}{2\sigma^2}(x-s)^2\right] dx - \int_{-\infty}^0 \frac{1}{\sigma\sqrt{2\pi}} \exp\left[-\frac{1}{2\sigma^2}(x-s)^2\right] dx \quad (\text{A-7})$$

where $s = s(t) = Ad(t)$. Letting $\frac{x-s}{\sqrt{2}\sigma} = v$ produces

$$\mu = \frac{2}{\sqrt{\pi}} \int_0^{2/\sqrt{2}\sigma} e^{-v^2} dv = \text{erf}\left[\frac{s(t)}{\sqrt{2}\sigma}\right] \quad (\text{A-8})$$

Now let us determine the output autocorrelation function defined by

$$R_y(t+\tau, t) = E[y(t+\tau)y(t)] = \int_{-\infty}^{\infty} \int_{-\infty}^{\infty} \text{sgn}[x_t] \text{sgn}[x_\tau] p_x(x_t, x_\tau) dx_t dx_\tau \quad (\text{A-9})$$

Equation (A-9) can be written

$$R_y(t+\tau, \tau) = \int_0^\infty \int_0^\infty p_x(x_t, x_\tau) dx_t dx_\tau + \int_{-\infty}^0 \int_{-\infty}^0 p_x(x_t, x_\tau) dx_t dx_\tau \\ - \int_0^\infty \int_{-\infty}^0 p_x(x_t, x_\tau) dx_t dx_\tau - \int_{-\infty}^0 \int_0^\infty p_x(x_t, x_\tau) dx_t dx_\tau \quad (\text{A-10})$$

Letting $x_t - \mu_t = u\sigma$, $x_\tau - \mu_\tau = v\sigma$ produces

$$R_y(t+\tau, \tau) = \int_{-\frac{\mu_t}{\sigma}}^\infty \int_{-\frac{\mu_\tau}{\sigma}}^\infty g(u, v, \rho) dudv + \int_{-\infty}^{-\frac{\mu_t}{\sigma}} \int_{-\infty}^{-\frac{\mu_\tau}{\sigma}} g(u, v, \rho) dudv \\ - \int_{-\frac{\mu_t}{\sigma}}^\infty \int_{-\infty}^{-\frac{\mu_\tau}{\sigma}} g(u, v, \rho) dudv - \int_{-\infty}^{-\frac{\mu_t}{\sigma}} \int_{-\frac{\mu_\tau}{\sigma}}^\infty g(u, v, \rho) dudv \quad (\text{A-11})$$

where $g(u, v, \rho)$ is the density function of the random variables u and v induced from the variables x_t and x_τ .

Let

$$h = \frac{\mu_t}{\sigma} \quad k = \frac{\mu_\tau}{\sigma}$$

then

$$R_{yy}(\tau, t) = L(-h, -k, \rho) + L(h, k, \rho) - L(-h, k, -\rho) - L(h, -k, -\rho) \quad (\text{A-12})$$

so using [2]

$$L(h, k, \rho) = Q(h)Q(k) + \sum_{n=0}^{\infty} \frac{z^{(n)}(h)z^{(n)}(k)}{(n+1)!} \rho^{n+1} \quad (\text{A-13})$$

and

$$Q(h) = \frac{1}{\sqrt{2\rho}} \int_h^\infty e^{-t^2/2} dt \quad (A-14)$$

we arrive at

$$\begin{aligned} R_{yy}(t, \tau) &= Q(-h)Q(-k) + \sum_{n=0}^{\infty} \frac{z^{(n)}(-h)z^{(n)}(-k)\rho^{n+1}}{(n+1)!} \\ &+ Q(h)Q(k) + \sum_{n=0}^{\infty} \frac{z^{(n)}(h)z^{(n)}(k)\rho^{n+1}}{(n+1)!} \\ &- Q(-h)Q(k) - \sum_{n=0}^{\infty} \frac{z^{(n)}(-h)z^{(n)}(k)(-\rho)^{n+1}}{(n+1)!} \\ &- Q(h)Q(-k) - \sum_{n=0}^{\infty} \frac{z^{(n)}(h)z^{(n)}(-k)(-\rho)^{n+1}}{(n+1)!} \end{aligned} \quad (A-15)$$

where

$$z^{(n)}(x) = \frac{d^n}{dx^n} \left\{ \frac{1}{\sqrt{2\pi}} e^{-x^2/2} \right\} \quad (A-16)$$

Now

$$\begin{aligned} R_y(\tau, t) &= [Q(h) - Q(-h)][Q(k) - Q(-k)] \\ &+ \sum_{n=0}^{\infty} \frac{\rho^{n+1}}{(n+1)!} \left\{ z^{(n)}(-h)z^{(n)}(-k) + z^{(n)}(h)z^{(n)}(k) \right. \\ &\quad \left. - (-1)^{n+1} [z^{(n)}(-h)z^{(n)}(k) + z^{(n)}(h)z^{(n)}(-k)] \right\} \end{aligned} \quad (A-17)$$

Now note that

$$Q(-x) - Q(x) = \operatorname{erf}\left(\frac{x}{\sqrt{2}}\right) \quad (\text{A-18})$$

Also note that

$$\begin{aligned} z^{(n)}(x) &= z^n(-x) \quad , \quad n \text{ even} \\ z^{(n)}(x) &= -z^n(-x) \quad , \quad n \text{ odd} \end{aligned} \quad (\text{A-19})$$

So

$$\begin{aligned} R_y(t, \tau) &= \operatorname{erf}\left(\frac{h}{\sqrt{2}}\right) \operatorname{erf}\left(\frac{k}{\sqrt{2}}\right) + \sum_{\substack{n=0 \\ n \text{ even}}}^{\infty} 4 \frac{z^{(n)}(h) z^{(n)}(k) \rho^{n+1}}{(n+1)!} \\ &+ 4 \sum_{n=1}^{\infty} \frac{z^{(n)}(h) z^{(n)}(k) \rho^{n+1}}{(n+1)!} \end{aligned} \quad (\text{A-20})$$

where \sum denotes sums over n odd and \sum_{even} denotes sums over n even. Changing indices yields

$$\begin{aligned} R_y(t, \tau) &= \operatorname{erf}\left(\frac{\mu_t}{\sqrt{2}\sigma}\right) \operatorname{erf}\left(\frac{\mu_\tau}{\sqrt{2}\sigma}\right) + 4 \sum_{m=0}^{\infty} z^{(2m+1)}\left(\frac{\mu_t}{\sigma}\right) z^{(2m+1)}\left(\frac{\mu_\tau}{\sigma}\right) \frac{\rho^{2m+2}}{(2m+2)!} \\ &+ 4 \sum_{m=0}^{\infty} \frac{\rho^{2m+1}}{(2m+1)!} z^{(2m)}\left(\frac{\mu_t}{\sigma}\right) z^{(2m)}\left(\frac{\mu_\tau}{\sigma}\right) \end{aligned} \quad (\text{A-21})$$

We have, since $s(t) = \operatorname{Ad}(t)$,

$$\begin{aligned}
R_y(t, \tau) &= d(t)d(t+\tau) \operatorname{erf}^2 \left[\sqrt{\frac{S}{2N}} \right] \\
&+ 4 d(t+\tau) d(t) \sum_{m=0}^{\infty} \left[z^{(2m+1)} \left(\sqrt{\frac{S}{N}} \right) \right]^2 \left[\frac{R_n(\tau)}{\sigma^2} \right]^{2m+2} / (2m+2)! \\
&+ 4 \sum_{m=0}^{\infty} \left[z^{(2m)} \left(\sqrt{\frac{S}{N}} \right) \right]^2 \left[\frac{R_n(\tau)}{\sigma^2} \right]^{2m+1} / (2m+1)!
\end{aligned} \tag{A-22}$$

where we have let

$$\frac{A^2}{\sigma^2} = \frac{S}{N} \tag{A-23}$$

Now consider $d(t)$,

$$d(t) = \sum_{i=-\infty}^{\infty} d_i p(t-iT)$$

where $p(t) = 1, t \in (0, T)$ and $d_i = \pm 1$ with equal likelihood. Hence, the time and ensemble average of $d(t)d(t+\tau)$ yields

$$R_d(\tau) = \langle \overline{d(t)d(t+\tau)} \rangle = \left\langle \sum_{i=-\infty}^{\infty} p(t-iT) p(t+\tau-iT) \right\rangle$$

or

$$R_d(\tau) = \left[1 - \frac{|\tau|}{T} \right], \quad \text{NRZ waveforms,}$$

so that we have

$$\begin{aligned}
 R_y(\tau) = & R_d(\tau) \operatorname{erf}^2 \left[\sqrt{\frac{S}{2N}} \right] + 4 R_d(\tau) \sum_{m=0}^{\infty} \left[z^{(2m+1)} \left(\sqrt{\frac{S}{N}} \right) \right]^2 \left[\frac{R_n(\tau)}{2} \right]^{2m+2} / (2m+2)! \\
 & + 4 \sum_{m=0}^{\infty} \left[z^{(2m)} \left(\sqrt{\frac{S}{N}} \right) \right]^2 \left[\frac{R_n(\tau)}{2} \right]^{(2m+1)} / (2m+1)! \quad (A-24)
 \end{aligned}$$

The first term is the SxS term, second is the SxN terms, and the last term is the NxN term. Notice at high SNR

$$R_y(\tau) \cong R_d(\tau) \quad (A-25)$$

At low SNR

$$\begin{aligned}
 \lim_{\frac{S}{N} \rightarrow 0} \operatorname{erf} \left(\sqrt{\frac{S}{N}} \right) &= 0 \\
 \lim_{\frac{S}{N} \rightarrow 0} \left[z^{(2m)} \left(\sqrt{\frac{S}{N}} \right) \right]^2 &= \frac{1}{2\pi} \left(\frac{1}{2} \right)^{2m} \left[\frac{(2m)!}{m!} \right]^2 \\
 \lim_{\frac{S}{N} \rightarrow 0} \left[z^{2m+1} \left(\sqrt{\frac{S}{N}} \right) \right]^2 &\rightarrow 0 \quad (A-26)
 \end{aligned}$$

Therefore, (A-24) converges at S/N = 0 to

$$\lim_{\frac{S}{N} \rightarrow 0} R_y(\tau) = 4 \sum_{m=0}^{\infty} \left(\frac{1}{2\pi} \right) \left(\frac{1}{2} \right)^{2m} \left[\frac{(2m)!}{m!} \right]^2 \frac{1}{(2m+1)!} \left[\frac{R_{nn}(\tau)}{2} \right]^{2m+1} \quad (A-27)$$

or

$$R_y(\tau) = \frac{2}{\pi} \arcsin \left[\frac{R_n(\tau)}{\sigma^2} \right] \quad (A-28)$$

which is a well-known result. It is easy to show that $R_d(\tau)$ is given by

$$R_d(\tau) = \begin{cases} \left[1 - \frac{|\tau|}{T} \right] & |\tau| \leq T \\ 0 & |\tau| > T \end{cases} \quad \left. \vphantom{R_d(\tau)} \right\} \text{NRZ} \quad (\text{A-29})$$

$$R_d(\tau) = \begin{cases} \left[1 - \frac{3|\tau|}{T} \right] & |\tau| \leq \frac{T}{2} \\ \left[\frac{|\tau|}{T} - 1 \right] & \frac{T}{2} \leq |\tau| \leq T \end{cases} \quad \left. \vphantom{R_d(\tau)} \right\} \text{Manchester} \quad (\text{A-30})$$

Therefore, at the input to the FM summer due to channels 1 and 2, we have

$$s(t) = A \frac{4}{\pi} d_2(t) \cos\theta \sin(\omega_{sc} t) + A \frac{4}{\pi} d_1(t) \sin\theta \cos(\omega_{sc} t) \quad (\text{A-31})$$

where $d_2(t)$ has the spectral density given by

$$\begin{aligned} \mathcal{S}d_2(f) = & \mathcal{S}d(f) \left[\text{erf} \left(\sqrt{\frac{S_2}{N_2}} \right) \right]^2 + 4 \mathcal{F} \left\{ R_d(\tau) \sum_{m=0}^{\infty} \left[z^{(2m+1)} \left(\sqrt{\frac{S_2}{N_2}} \right) \right]^2 \left[\frac{R_n(\tau)}{\sigma_2^2} \right]^{2m+2} / (2m+2)! \right\} \\ & + 4 \mathcal{F} \left\{ \sum_{m=0}^{\infty} \left[z^{(2m)} \left(\sqrt{\frac{S_2}{N_2}} \right) \right]^2 \left[\frac{R_n(\tau)}{\sigma_2^2} \right]^{2m+1} / (2m+1)! \right\} \end{aligned} \quad (\text{A-32})$$

with $\mathcal{F}(\cdot)$ the Fourier transform and where $d_1(t)$ has the spectral density given by

$$\begin{aligned} \mathcal{S}d_1(f) = & \mathcal{S}d(f) \left[\text{erf} \left(\sqrt{\frac{S_1}{N_1}} \right) \right]^2 + 4 \mathcal{F} \left\{ R_d(\tau) \sum_{m=0}^{\infty} \left[z^{(2m+1)} \left(\sqrt{\frac{S_1}{N_1}} \right) \right]^2 \left[\frac{R_n(\tau)}{\sigma_1^2} \right]^{2m+2} / (2m+2)! \right\} \\ & + 4 \mathcal{F} \left\{ \sum_{m=0}^{\infty} \left[z^{(2m)} \left(\sqrt{\frac{S_1}{N_1}} \right) \right]^2 \left[\frac{R_n(\tau)}{\sigma_1^2} \right]^{2m+1} / (2m+1)! \right\} \end{aligned} \quad (\text{A-33})$$

and where $\mathcal{S}_d(\omega)$ denotes the data spectrum of that respective channel.

Evaluation of the S_xN and N_xN spectral densities is made in Appendix B.

References--Appendix A

1. J. H. Painter, "Ideal Limiting of Digital Signals in Gaussian Noise," IEEE Transactions on Information Theory, Vol. IT-16, #1, Jan. 1970.
2. M. Abramowitz and I. A. Stegar, Handbook of Mathematical Functions, Dover Publications, Inc., New York, 1965.

APPENDIX B
SPECTRAL DENSITY ASSOCIATED WITH

$$\left[\frac{R_n(\tau)}{\sigma^2} \right]^j, \quad j=1,2,3,4$$

In this appendix, we summarize the power spectral density associated with the j th power of

$$\left[\frac{R_n(\tau)}{\sigma^2} \right]$$

for $j=1,2,3,4$.

First consider the Fourier transform of $R_n(\tau)/\sigma^2$:

$$\mathcal{S}_n^{(1)}(\tau) = \int_{-\infty}^{\infty} \frac{R_n(\tau)}{\sigma^2} e^{-i2\pi f\tau} dt \quad (B-1)$$

For convenience, we assume that the lowpass filter of Figure 2 is an ideal low-pass filter. Hence, $R_n(\tau)$ is given by

$$R_n(\tau) = \int_{-B}^B \frac{N_0}{2} e^{i2\pi f\tau} df = N_0 B \frac{\sin(2\pi B\tau)}{(2\pi B\tau)} \quad (B-2)$$

The corresponding spectral density is given by

$$\mathcal{S}_n^{(1)}(f) = \int_{-\infty}^{\infty} \frac{R_n(\tau)}{\sigma^2} e^{-t2\pi f\tau} d\tau = \int_{-\infty}^{\infty} \frac{\sin(2\pi B\tau)}{2\pi B\tau} e^{-12\pi f\tau} d\tau \quad (B-3)$$

or

$$\mathcal{S}_n^{(1)}(f) = 2 \int_0^{\infty} \frac{\sin x}{x} \cos\left(\frac{f}{B} x\right) \frac{dx}{2\pi B} \quad (B-4)$$

$$S_n^{(1)}(f) = \frac{1}{2B} U_B, \quad (B-5)$$

where

$$U(B) = 1, \quad |f| < B \quad ; \quad U(B) = 0, \quad f > B \quad (B-6)$$

Now consider the second power of $R_n(\tau)/\sigma^2$. We have that the spectral density is given by

$$S_n^{(2)}(f) = \int_{-\infty}^{\infty} \frac{\sin^2 2\pi B\tau}{(2\pi B\tau)^2} \cos(2\pi f\tau) d\tau \quad (B-7)$$

Changing variables, we have

$$S_n^{(2)}(f) = 2 \int_0^{\infty} \frac{\sin^2 x}{x^2} \cos\left(\frac{f}{B} x\right) \frac{dx}{2\pi B} \quad (B-8)$$

Using [1, p. 450, §3.828 #5), we have

$$\begin{aligned} S_n^{(2)}(f) &= \frac{1}{2B} \left(1 - \frac{|f|}{2B}\right) \quad |f| < 2B \\ &= 0 \quad |f| \geq 2B \end{aligned} \quad (B-9)$$

Now consider the cube term which is given by

$$S_n^{(3)}(f) = \int_{-\infty}^{\infty} \frac{\sin^3(2\pi B\tau)}{(2\pi B\tau)^3} e^{-2\pi f\tau} d\tau \quad (B-10)$$

Letting $x = 2\pi B\tau$ yields

$$S_n^{(3)}(f) = 2 \int_0^{\infty} \frac{\sin^3 x}{x^3} \cos\left(\frac{f}{B} x\right) \frac{dx}{2\pi B} \quad (11)$$

$$\begin{aligned} \mathcal{J}_n^{(3)}(f) &= \frac{1}{8B} \left(3 - \left(\frac{f}{B}\right)^2 \right) & 0 < |f| < B \\ \mathcal{J}_n^{(3)}(f) &= \frac{1}{16B} \left(3 - \frac{|f|}{B} \right)^2 & B < |f| < 3B \end{aligned} \quad (B-12)$$

Now consider the fourth power term:

$$\mathcal{J}_n^{(4)}(f) = \int_{-\infty}^{\infty} \frac{\sin^4(2\pi B\tau)}{(2\pi B\tau)^4} e^{-i2\pi f\tau} d\tau \quad (B-13)$$

$$= \mathcal{F} \left\{ \frac{\sin^2(2\pi B\tau)}{(2\pi B\tau)^2} \right\} * \mathcal{F} \left\{ \frac{\sin^2(2\pi B\tau)}{(2\pi B\tau)^2} \right\} \quad (B-14)$$

$$\mathcal{J}_n^{(4)}(f) = \left\{ \frac{1}{2B} \left(1 - \frac{|f|}{2B} \right) U_B\left(\frac{f}{2}\right) \right\} * \left\{ \frac{1}{2B} \left(1 - \frac{|f|}{2B} \right) U_B\left(\frac{f}{2}\right) \right\} \quad (B-15)$$

Hence,

$$\mathcal{J}_n^{(4)}(f) = \frac{1}{4B^2} \int_{-2B+|f|}^{2B} \left(1 - \frac{|f'|}{2B} \right) \left(1 - \frac{|f-f'|}{2B} \right) U\left(\frac{f'}{2}\right) U\left(\frac{f-f'}{2}\right) df' \quad (B-16)$$

$$\mathcal{J}_n^{(4)}(f) = \frac{1}{4B^2} \left[\frac{4}{3} B - \frac{f^2}{2B} + \frac{|f|^3}{24B^2} \right] \quad 2B \leq |f| \leq 4B \quad (B-17)$$

$$\mathcal{J}_n^{(4)}(f) = \frac{1}{4B^2} \left[\frac{8}{3} B - 2|f| + \frac{f^2}{2B} - \frac{|f|^3}{24B^2} \right] \quad 2B \leq |f| \leq 4B \quad (B-18)$$

References--Appendix B

1. I. S. Gradshteyn and I. M. Ryzhik, Table of Integrals, Series, and Products, Academic Press, 1965.

ANALYSIS OF THE KU-BAND SHUTTLE/MRD

I-Q REVERSAL PHENOMENA

Interim Report

Contract NAS9-16893

Prepared for

NASA/Lyndon B. Johnson Space Center

Houston, Texas 77058

Prepared by

Jack K. Holmes

and

Raimundo Sampaio

With contributions by

G. Huth

P. Nilsen

A. Polydoros

Axiomatix

9841 Airport Blvd., Suite 912

Los Angeles, California 90045

Axiomatix Report No. R8406-1

June 1, 1984

TABLE OF CONTENTS

	<u>Page</u>
LIST OF FIGURES	ii
1.0 INTRODUCTION TO THE PROBLEM	1
2.0 SYSTEM MODEL	1
3.0 MRD TRACKING-LOOP DESCRIPTION	1
4.0 CONDITIONS REQUIRED TO INDUCE I-Q SWAPPING	22
5.0 TAPE-RECORDER-SIGNAL MODEL	30
6.0 CONCEPTUAL BASIS FOR THE TAPE-RECORDER-INDUCED I-Q FLIPPING	30
7.0 SIMULATION OF THE I-Q FLIPS	34
8.0 SOLAR MAX WEAK-SIGNAL-CASE I-Q FLIPPING	37
9.0 SUMMARY OF THE NASA LABORATORY TESTS AND THE AXIOMATIX MODULE SIMULATION	41
10.0 CONCLUSIONS	41
REFERENCES	43

APPENDICES

- A Model of the HAC Subcarrier Modulator
- B Lock-Detector Analysis
- C S-Curve of a Modified Four-Phase Costas Loop For a Particular
Quadrature Signal Input
- D Impulse Response of an Nth-Order Butterworth Filter
- E Simulation of the MRD Modified Four-Phase Costas Loop

LIST OF FIGURES

		<u>Page</u>
1.1	Model for the Solar Max Retrieval Data Dump and the OPS Data Dump	2
3.1	Modified Four-Phase Costas Loop	3
3.2	S-Curve $P_2:P_1 = 4:1$; $A_V = 2$; $SNR = \infty$	5
3.3	S-Curve $P_2:P_1 = 1:1$; $A_V = 2$; $SNR = \infty$	6
3.4	S-Curve $P_2:P_1 = 1/2:1$; $A_V = 2$; $SNR = \infty$	7
3.5	S-Curve $P_2:P_1 = 1/4:1$; $A_V = 2$; $SNR = \infty$	8
3.6	S-Curve when $P_2:P_1 = 1/8:1$; $A_V = 2$, $SNR = \infty$	9
3.7	S-Curve when $P_2:P_1 = 1/16:1$; $SNR = \infty$	10
3.8	S-Curve when $A_V = 2$, Channel 2 Drops Out (Strong Channel); $P_2:P_1 = 0:1$; $SNR = \infty$	11
3.9	S-Curve when $A_V = 2$, Channel 1 Drops Out (Weak Channel Drops Out); $P_2:P_1 = 1:0$; $SNR = \infty$	12
3.10	S-Curve; Sine Wave on Channel 2, Biphase-L Random on Channel 1; One-Pole 1.8-MHz Filter Bandwidth; $f_{SW} = 1$ MHz; $P_2:P_1 = 2.48:1$	15
3.11	S-Curve; Sine Wave on Channel 2; Biphase-L Random on Channel 1; One-Pole 1.8-MHz Bandwidth; $f_{SW} = 2$ MHz; $P_2:P_1 = 1.45:1$	16
3.12	S-Curve; Sine Wave on Channel 2, Biphase-L Random on Channel 1; One-Pole 1.8-MHz Bandwidth; $f_{SW} = 3$ MHz; $P_2:P_1 = 0.86:1$	17
3.13	S-Curve with One-Pole 1.8-MHz Bandwidth; Sine Wave on Channel 2; Biphase-L Random on Channel 1; $f_{SW} = 4$ MHz, $P_2:P_1 = 0.55:1$	18
3.14	S-Curve with One-Pole 1.8-MHz Bandwidth; $f_{SW} = 5$ MHz, $P_2:P_1 = 0.37:1$; Sine Wave on Channel 2; Biphase-L Random on Channel 1	19
3.15	S-Curve with One-Pole 1.8-MHz Bandwidth; $f_{SW} = 6$ MHz, $P_2:P_1 = 0.27:1$; Sine Wave on Channel 2; Biphase-L Random on Channel 1	20
3.16	S-Curve with One-Pole 1.8-MHz Bandwidth; $f_{SW} = 7$ MHz; $P_2:P_1 = 0.2:1$, Sine Wave on Channel 2; Biphase-L Random on Channel 1	21

3.17	S-Curve; Random Data on Channel 1; Sine Wave on Channel 2; f = 2.5 MHz	23
3.18	S-Curve; Random Data on Channel 1; Sine Wave on Channel 2; f = 3.0 MHz	24
3.19	S-Curve; Random Data on Channel 1; Sine Wave on Channel 2; f = 3.2 MHz	25
3.20	S-Curve; Random Data on Channel 1; Sine Wave on Channel 2 f = 3.4 MHz	26
3.21	S-Curve; Random Data on Channel 1; Sine Wave on Channel 2; f = 3.5 MHz	27
3.22	S-Curve; Random Data on Channel 1; Sine Wave on Channel 2; f = 3.6 MHz	28
3.23	S-Curve; Random Data on Channel 1; Sine Wave on Channel 2; f = 4.0 MHz	29
3.24	(a) Normal Playback Spectra; (b) Transient Start-Up Spectra . . .	31
3.25	Simulation of I-Q Inversion with the 5-MHz Prelimiter LPF Plotted Against Time and the Lowest Frequency Value	33
3.26	Simulation of Unsuccessful I-Q Inversion Using a 2.5-MHz LPF Plotted Against Time and the Lowest Frequency Value	35
7.1	Plot of Phase Errors Versus Time and Lowest Tone Frequency at Channel $E_b/N_0 = 2$ dB	38

SUMMARY

In this report, the I-Q flipping problem of the MRD is studied by analysis and simulation to discover why the flipping occurred. In the case of the tape-recorder dump during start-up or wraparound, it was found that the composite tape-recorder signal contained two tones increasing with frequency, plus a spectrally flat noise term. According to the prelimiter-filter bandwidth into the subcarrier modulator, this mixture determined the conditions for I-Q flipping. The narrower filter bandwidth (2.5 MHz, six-pole) stopped the I-Q flipping completely,

In the case of the Solar Max I-Q flipping, the small SNR at the Shuttle PI caused mainly noise to be transmitted on channel 2. At the receiver, most of the noise is filtered out, greatly reducing the effective I-Q ratio at the MRD subcarrier loop.

Table 9.1 summarizes the NASA laboratory measurements and Axiomatix predictions for a variety of cases with excellent agreement. It should be noted that observing the existence and modeling of two tones, along with the noise output from the tape recorder start-up or wraparound, allowed Axiomatix to make very accurate performance predictions. Specifically, the comparisons between the NASA measurements and Axiomatix predictions based on simulations or calculations are very good for a variety of cases, as can be depicted in Table 9.1.

1.0 INTRODUCTION TO THE PROBLEM

Figure 1.1 illustrates the Shuttle Ku-band transmitter, TDRSS terminal, Shuttle Payload Interrogator (PI) and Solar Max transmitter. The problem we address is the I-Q interchange which occurs in the medium-rate demodulator (MRD) under the following conditions: during bent-pipe acquisition of the 8.5-MHz subcarrier at low SNR, and during playback operation when the recorder either starts up or changes tracks (wrap-around). It should be noted that, in addition to the above sources of I-Q inversion, a square-wave data sequence on channel 2 will induce I-Q inversion if the frequency of the square wave is high enough. In the following sections, we will elaborate on the different mechanisms of this I-Q flipping.

2.0 SYSTEM MODEL

Figure 1.1 illustrates the system block diagram under study. First, we consider the Solar Max signal which is sent from the transmitter to the Shuttle receiver (PI), where it is demodulated to baseband, filtered and QPSK modulated onto an 8.5-MHz square-wave subcarrier. The modulator intrinsically limits both of the channel inputs in the modulation process. However, the bandpass filter following the QPSK modulator restores the QPSK signal to the standard QPSK sine wave and cosine wave format, being the fundamental of the square-wave rate. This process is discussed in Appendix A. This subcarrier is added to the channel 3 data, frequency modulated, and transmitted through the TDRS to the TDRSS terminal. At this ground terminal, the FM demod demodulates the carrier and produces the QPSK 8.5-MHz subcarrier which contains both channel 1 and channel 2 data. The medium-rate demodulator (MRD) is a QPSK tracking loop which produces, at its output, channel 1 and channel 2 baseband data. The problem we are addressing in this report is the flipping, or interchanging of channel 1/channel 2 data in the MRD.

3.0 MRD TRACKING-LOOP DESCRIPTION

Figure 3.1 illustrates the MRD tracking loop which is capable of tracking QPSK signals having an I-Q power ratio of either 4:1 or 1:1 in the two phases of the transmitted signal. The gain (or attenuation in the opposite arm) is set at the ratio of $A_V = \sqrt{P_2/P_1}$, where P_1 and P_2 are the respective channel powers. Basically, the loop forms an orthogonal set of sinusoids

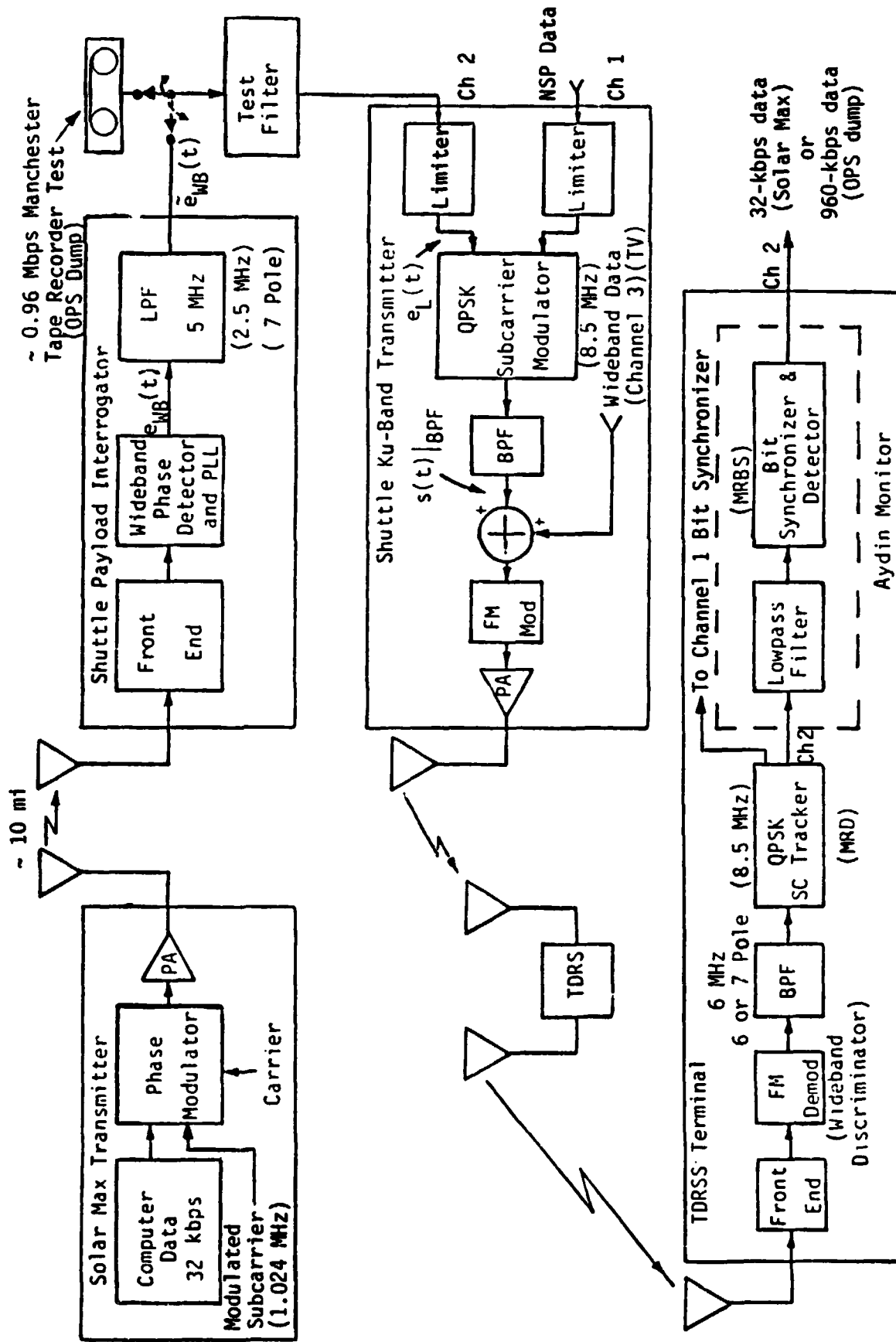


Figure 1.1. Model for the Solar Max Retrieval Data Dump and the OPS Data Dump

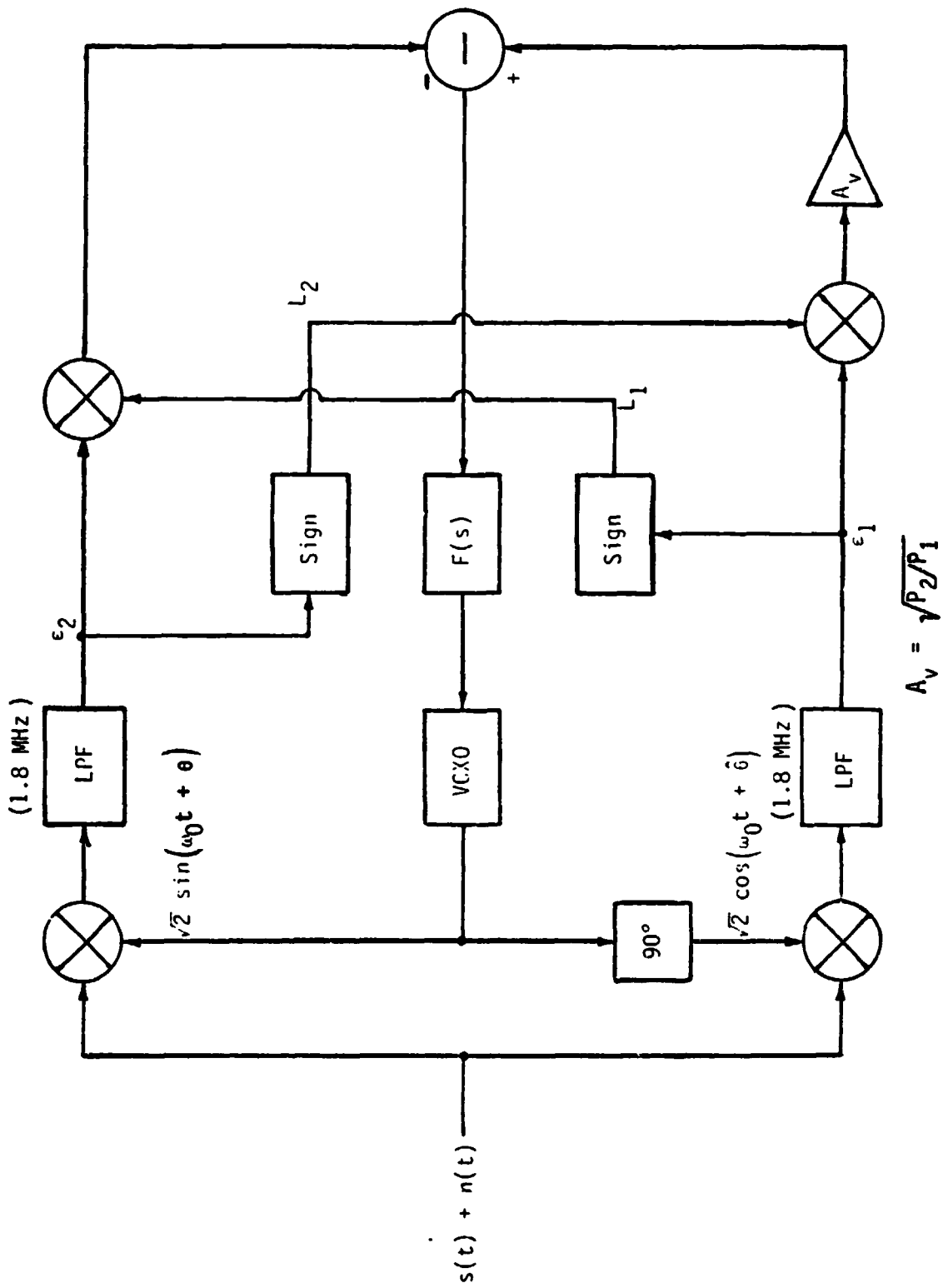


Figure 3.1. Modified Four-Phase Costas Loop

that attempt to demodulate the respective data streams which are filtered and processed through data-removal processing to yield an error-control signal. This error-control signal drives the loop filter and, in turn, controls the VCO. Normally, there are four stable lock points: 0° , 90° , 180° and 270° ; however, the angles can change according to SNR and the amount of distortion present, as well as the power ratio. Figures 3.2 through 3.9 depict the S-curves (average control signals, given ϕ) for various channel 1/channel 2 power ratios, assuming no distortion in the data signals and no additive thermal noises in the channel.

The S-curves are based on the average value of the error-control signal given a particular value of ϕ . Here the quadriphase signal is given by

$$s(t) = \sqrt{2} \sqrt{(1-\alpha)S} m_2(t) \sin(\omega_0 t + \theta_0) + \sqrt{2} \sqrt{\alpha S} m_1(t) \cos(\omega_0 t + \theta_0) \quad (1)$$

where $m_1(t)$ is the data signal in channel 1, $m_2(t)$ is the data signal in channel 2, ω_0 is the radian carrier frequency, and θ_0 is the carrier phase. From Figure 3.1, we can write

$$\begin{aligned} \epsilon_2(t) &= \sqrt{(1-\alpha)S} \tilde{m}_2(t) \cos\phi - \sqrt{\alpha S} \tilde{m}_1(t) \sin\phi \\ \epsilon_1(t) &= \sqrt{(1-\alpha)S} \tilde{m}_2(t) \sin\phi + \sqrt{\alpha S} \tilde{m}_1(t) \cos\phi \end{aligned} \quad (2)$$

where αS is the power in channel 1, $(1-\alpha)S$ is the power in channel 2, $\tilde{m}_1(t)$ is the arm-filtered channel 1 data signal, and $\tilde{m}_2(t)$ is the arm-filtered channel 2 data signal. Combining the signal as in Figure 3.1 produces the control

$$\begin{aligned} C(\phi) &= A_V [\sqrt{(1-\alpha)S} \tilde{m}_2(t) \sin\phi + \sqrt{\alpha S} \tilde{m}_1(t) \sin\phi] \\ &\quad \times \text{sgn}[\sqrt{(1-\alpha)S} \tilde{m}_2(t) \cos\phi - \sqrt{\alpha S} \tilde{m}_1(t) \sin\phi] \\ &\quad - [\sqrt{(1-\alpha)S} \tilde{m}_2(t) \cos\phi - \sqrt{\alpha S} \tilde{m}_1(t) \sin\phi] \\ &\quad \times [\sqrt{(1-\alpha)S} \tilde{m}_2(t) \sin\phi - \sqrt{\alpha S} \tilde{m}_1(t) \cos\phi] \end{aligned} \quad (3)$$

Since the channel 1 data rate is low compared to the arm-filter bandwidth (1.8 MHz), we may assume that $\tilde{m}_1(t)$ takes on the values ± 1 . For convenience, we also initially assume that $\tilde{m}_2(t) = \pm 1$ independent of $\tilde{m}_1(t)$. Hence, assuming that both $\tilde{m}_1(t)$ and $\tilde{m}_2(t)$ are random 1's or -1's, the average value of $C(\phi)$ becomes

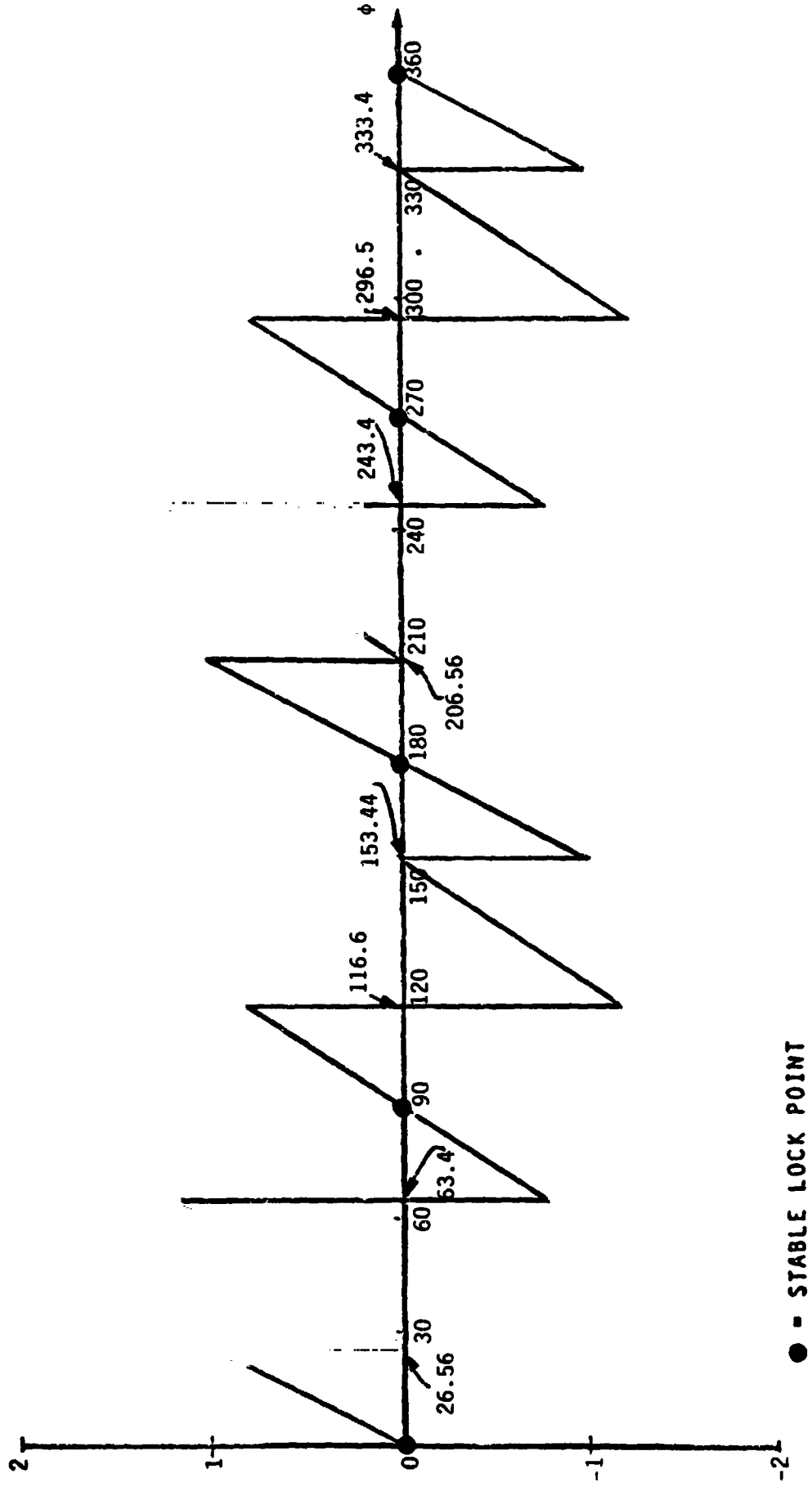
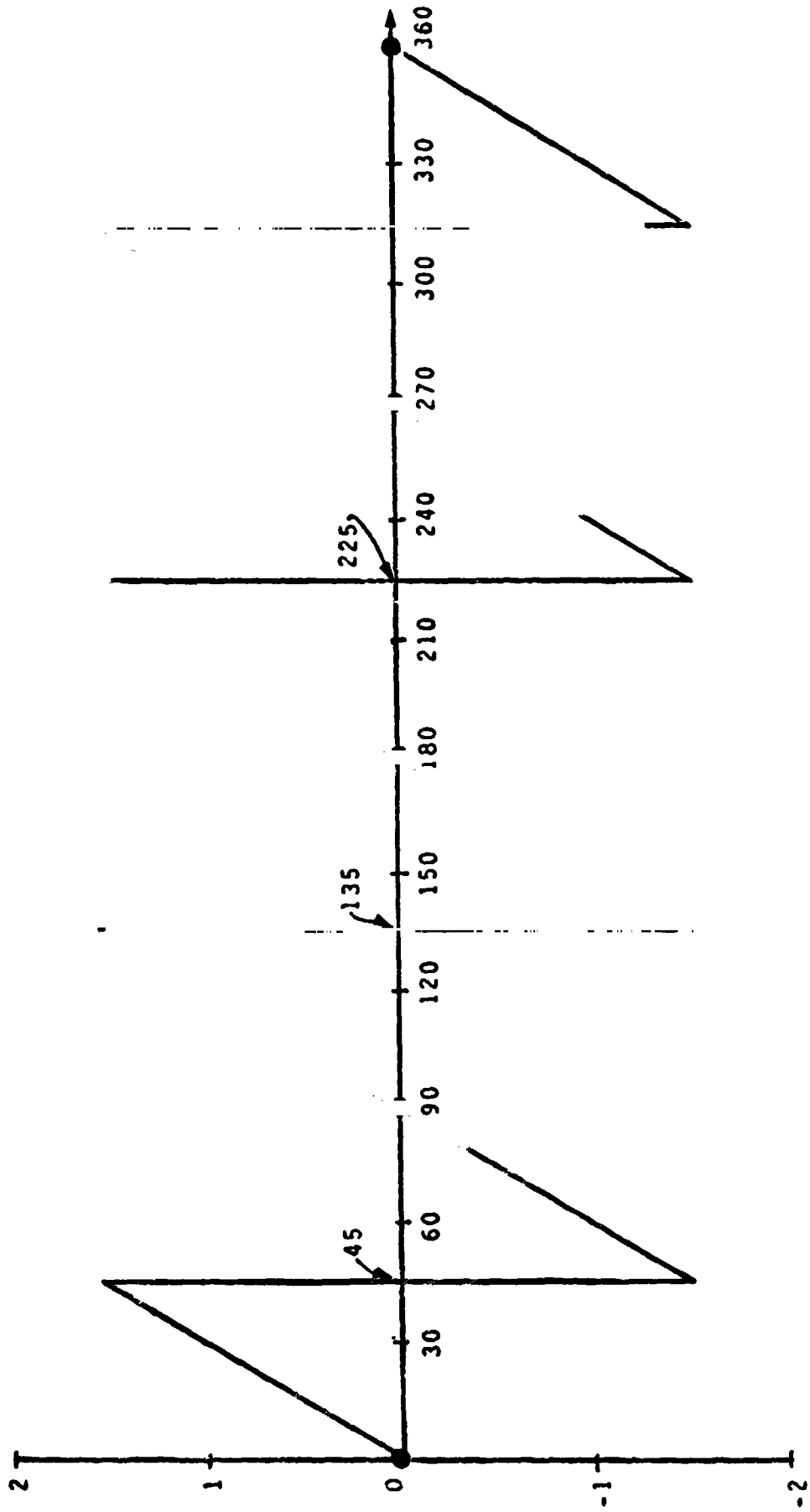
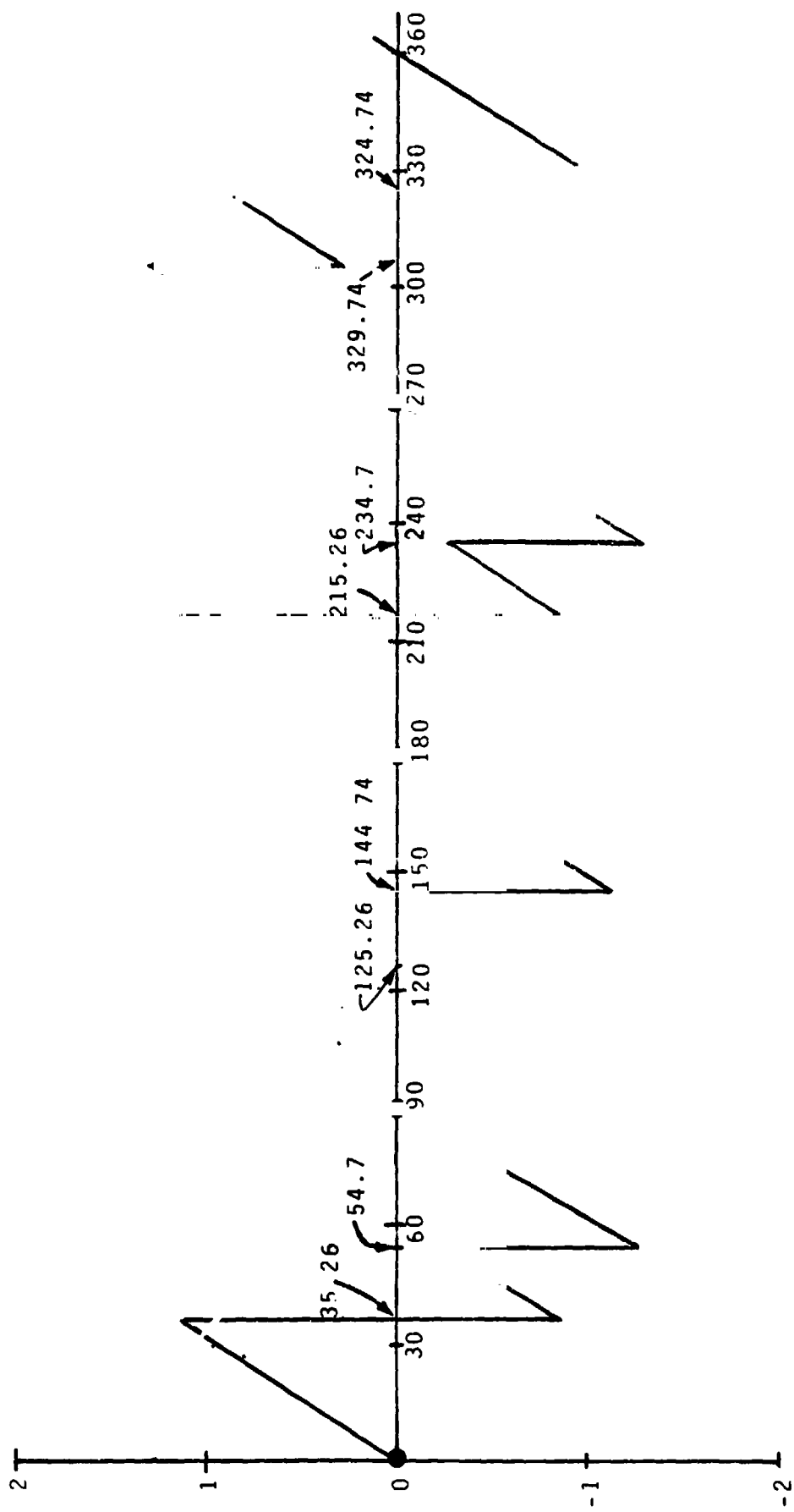


Figure 3.2. S-Curve $P_2:P_1 = 4:1$; $A_V = 2$; ∞ SNR



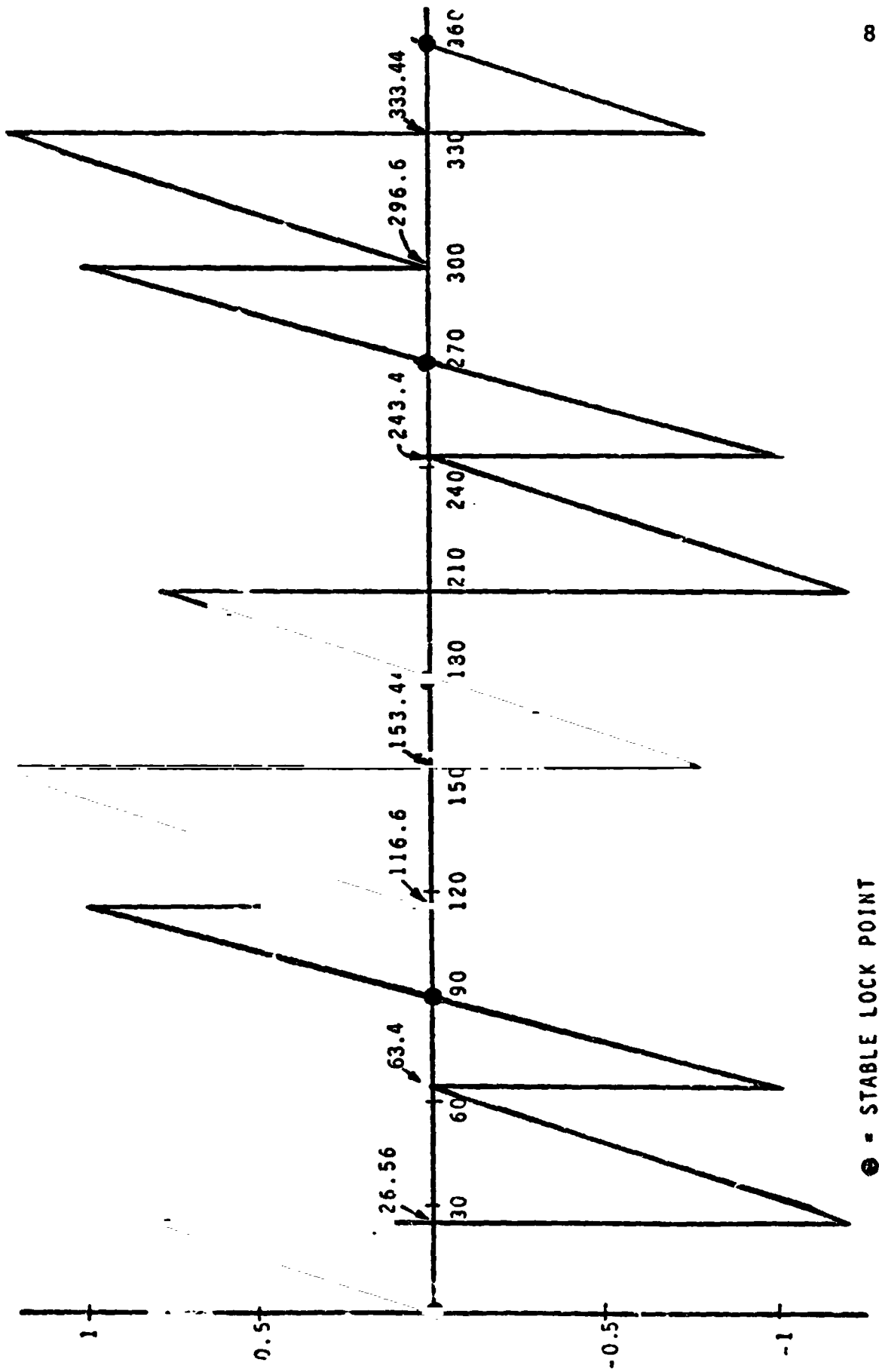
● = STABLE LOCK POINT

Figure 3.3. S-Curve $P_2:P_1 = 1:1$; $A_V = 2$; ∞ SNR



● = STABLE LOCK POINT

Figure 3.4. S-Curve $P_2:P_1 = 1/2:1$; $A_V = 2$; ∞ SNR



● = STABLE LOCK POINT

Figure 3.5. S-Curve $P_2:P_1 = 1/4:1$; $A_V = 2$; ∞ SNR

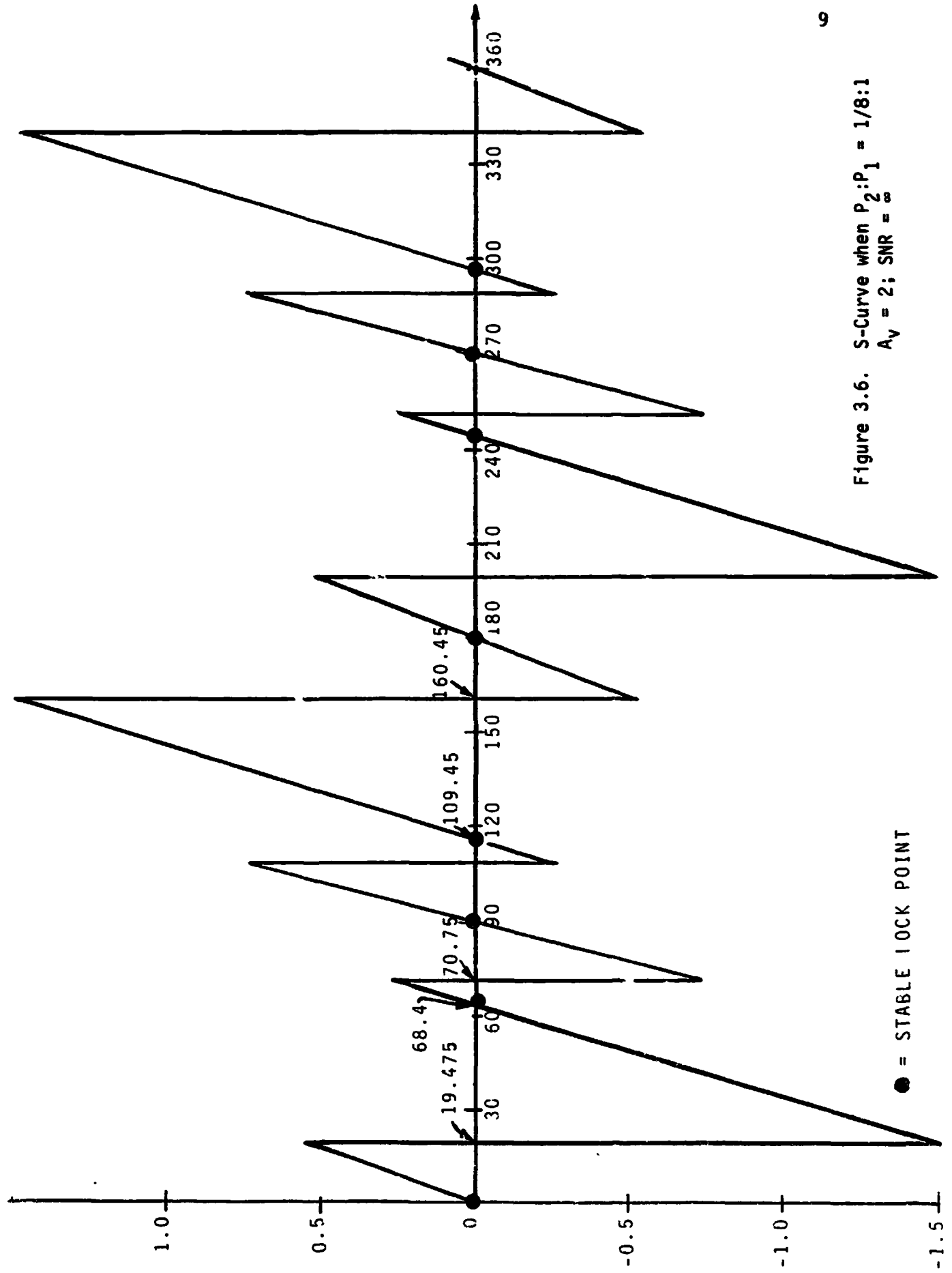


Figure 3.6. S-Curve when $P_2:P_1 = 1/8:1$
 $A_V = 2$; $SNR = \infty$

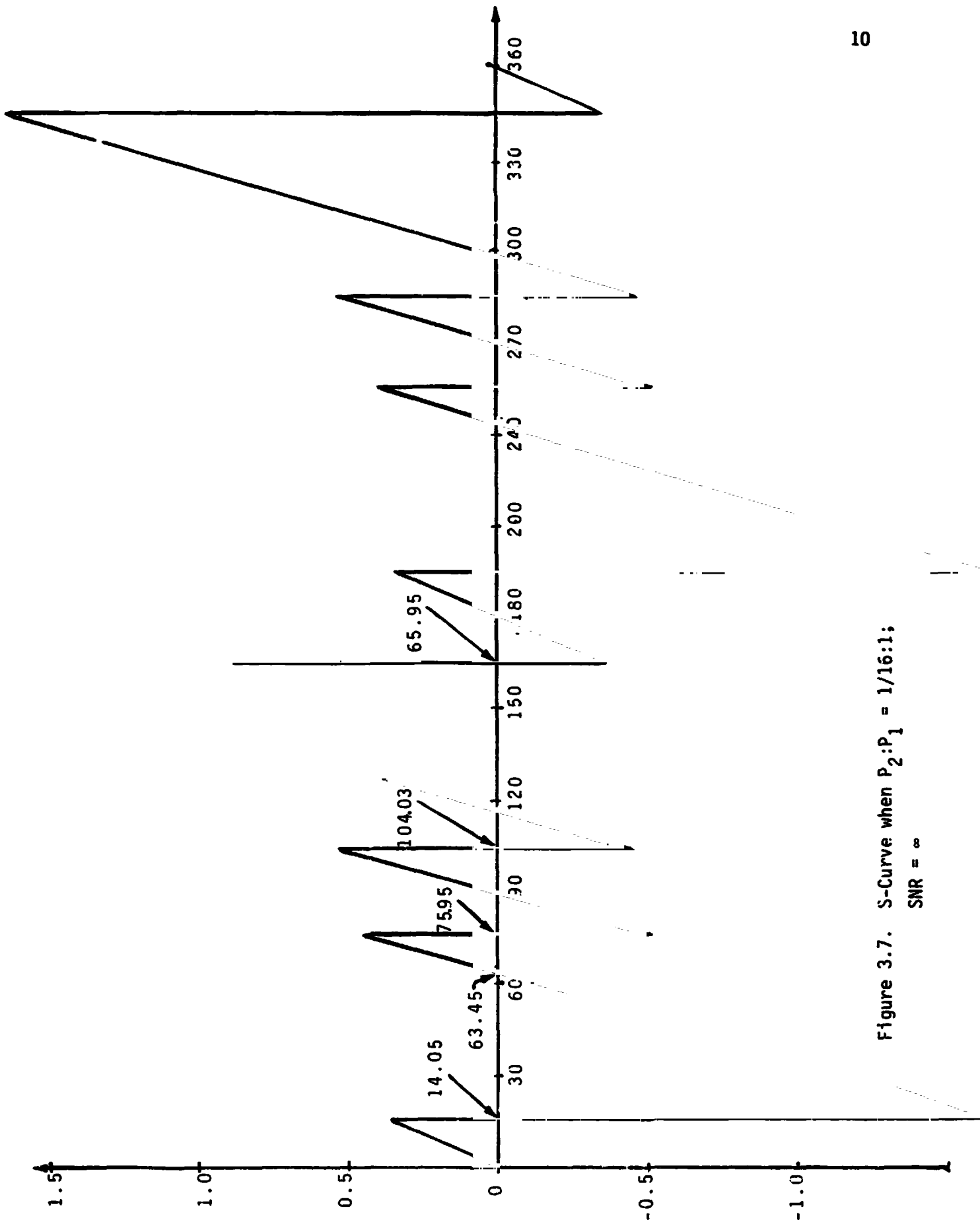
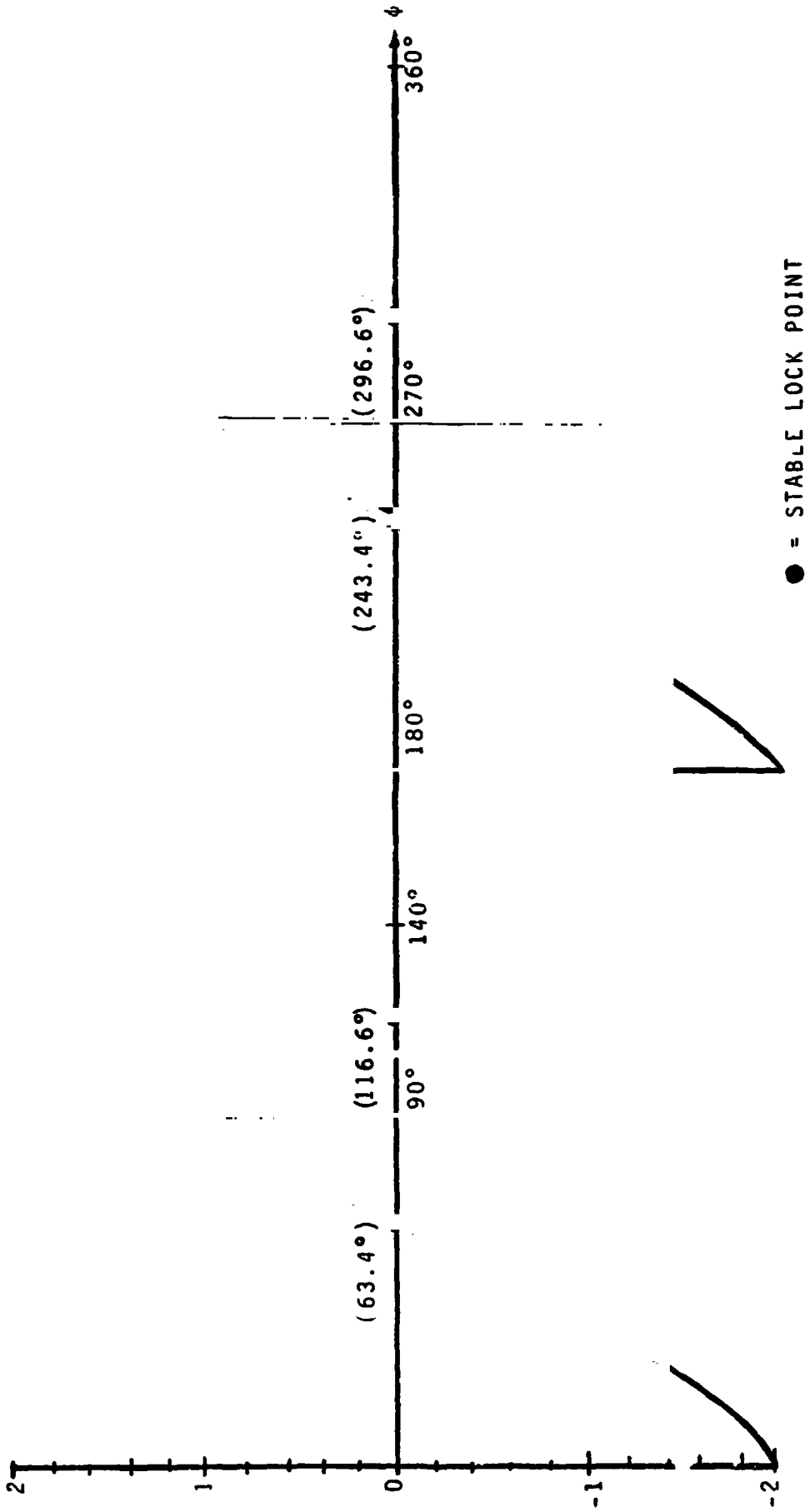


Figure 3.7. S-Curve when $P_2:P_1 = 1/16:1$;
 $SNR = \infty$



NOTE: $f(\phi) = f(\phi + \pi)$

Figure 3.8. S-Curve When $A_y = 2$, Channel 2 Drops Out (Strong Channel); $P_2:P_1 = 0:1$; $SNR = \infty$

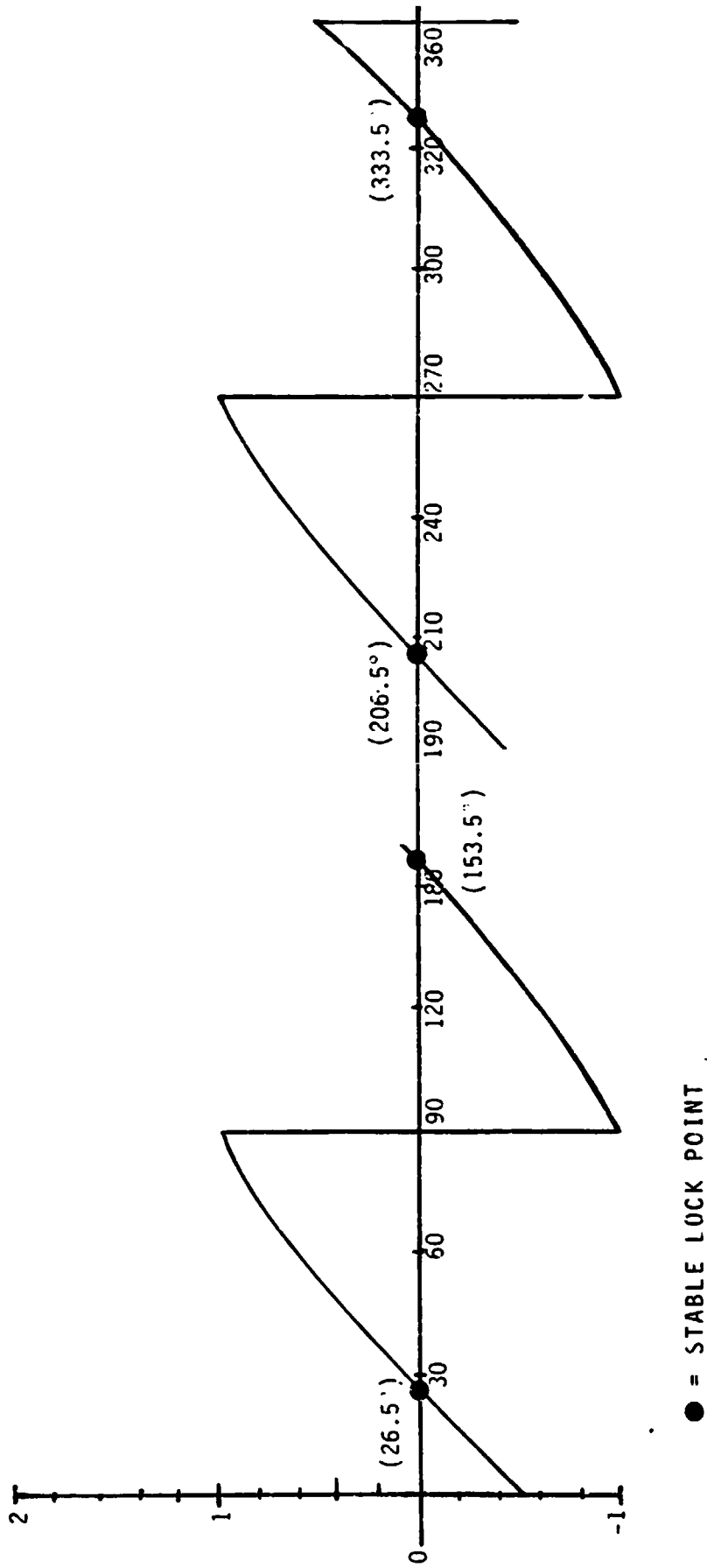


Figure 3.9. S-Curve when $A_v = 2$, Channel 1 Drops Out (Weak Channel Drops Out); $P_2:P_1 = 1:0$; $SNR = \infty$

$$\begin{aligned}
\bar{C}(\phi) = & \frac{1}{2} A_V [\sqrt{(1-\alpha)S} \sin\phi + \sqrt{\alpha S} \cos\phi] \operatorname{sgn}[\sqrt{(1-\alpha)S} \cos\phi - \sqrt{\alpha S} \sin\phi] \\
& - \frac{1}{2} [\sqrt{(1-\alpha)S} \cos\phi - \sqrt{\alpha S} \sin\phi] \operatorname{sgn}[\sqrt{(1-\alpha)S} \sin\phi + \sqrt{\alpha S} \cos\phi] \\
& + \frac{1}{2} A_V [\sqrt{(1-\alpha)S} \sin\phi - \sqrt{\alpha S} \cos\phi] \operatorname{sgn}[\sqrt{(1-\alpha)S} \cos\phi + \sqrt{\alpha S} \sin\phi] \\
& - \frac{1}{2} [\sqrt{(1-\alpha)S} \cos\phi + \sqrt{\alpha S} \sin\phi] \operatorname{sgn}[\sqrt{(1-\alpha)S} \sin\phi - \sqrt{\alpha S} \cos\phi] \\
& + \frac{A_V}{2} [-\sqrt{(1-\alpha)S} \sin\phi - \sqrt{\alpha S} \cos\phi] \operatorname{sgn}[-\sqrt{(1-\alpha)S} \cos\phi + \sqrt{\alpha S} \sin\phi] \\
& - \frac{1}{2} [-\sqrt{(1-\alpha)S} \cos\phi + \sqrt{\alpha S} \sin\phi] \operatorname{sgn}[-\sqrt{(1-\alpha)S} \sin\phi - \sqrt{\alpha S} \cos\phi] \\
& + \frac{1}{2} A_V [-\sqrt{(1-\alpha)S} \sin\phi + \sqrt{\alpha S} \cos\phi] \operatorname{sgn}[-\sqrt{(1-\alpha)S} \cos\phi - \sqrt{\alpha S} \sin\phi] \\
& - \frac{1}{2} [-\sqrt{(1-\alpha)S} \cos\phi - \sqrt{\alpha S} \sin\phi] \operatorname{sgn}[-\sqrt{(1-\alpha)S} \sin\phi + \sqrt{\alpha S} \cos\phi] \quad (4)
\end{aligned}$$

Equation (4) as the basis of Figures 3.2 through 3.9. The lock points are shown as large dots. In all of these curves, notice that the lock points are stable at 0° , 90° , 180° and 270° . When the power ratio is 1/8:1 or less, additional lock points occur, yielding eight admissible lock points.

We now consider the case when filtering of channel 2 is severe and is based on a one-pole LPF and when channel 1 has negligible filtering. We also assume a square-wave signal on channel 2 for mathematical convenience rather than a random-data sequence. The results are developed in Appendix C. From this appendix, the S-curve is given by

$$S(\phi) = -A_V G(\phi) - G(\phi + \pi/2) \quad (5)$$

where

$$G(\phi) = \text{sgn}[\sin\phi]\cos\phi$$

$$-K(\phi)\frac{2}{\pi} \left[(\cos\phi)\text{sgn}(\sin\phi)\cos^{-1}\left(\frac{|\tan(\phi)|}{A}\right) + \sin(\phi)\text{sgn}(\cos\phi)A\sqrt{1 - \left(\frac{\tan(\phi)}{A}\right)^2} \right] \quad (6)$$

with

$$K(\phi) = \begin{cases} 1 & , \quad |\sin\phi| \leq A |\cos\phi| \\ 0 & , \quad \text{otherwise} \end{cases} \quad (7)$$

and

$$\text{sgn } x = \begin{cases} 1 & , \quad x > 0 \\ 0 & , \quad x = 0 \\ -1 & , \quad x < 0 \end{cases} \quad (8)$$

and

$$A = \sqrt{\frac{1-\alpha}{\alpha}} \gamma(f_0) \quad (9)$$

with

$$\gamma(f_0) = \frac{(4/\pi)}{\sqrt{1 + \left(\frac{f_0}{1.8}\right)^2}} \quad , \quad f_0 \text{ in MHz} \quad , \quad (10)$$

the sine-wave attenuation to the tone at f_0 . It should be noted that the hard limiter illustrated in Figure 1.1 at the 8.5-MHz subcarrier converts the sine wave into a square wave but, at the TDRSS terminal, all the harmonics of the square wave are filtered out when the tone is greater than about 1.2 MHz.

Thus, the peak fundamental is $4/\pi$ of the peak square wave. Figures 3.10 through 3.16 illustrate the S-curve for various sine-wave (or square-wave) frequencies and the channel-2-to-channel-1 power ratio. Note that, when the sine wave is at 6 MHz, the S-curve is almost flat at $\phi=0$ and 180° . At 7 MHz, the curve has negative slope at 0° and 180° . Thus, if the loop is at 0° or 180° , it would move to either $\pm 90^\circ$ or $\pm 270^\circ$ if the channel 2 data changed from random Manchester to sine wave at 7 MHz. These graphs illustrate the fact that severe distortion has a marked influence on the S-curve. The previous case of negligible distortion yielded no unstable S-curves at $\phi=0^\circ$ or 180° .

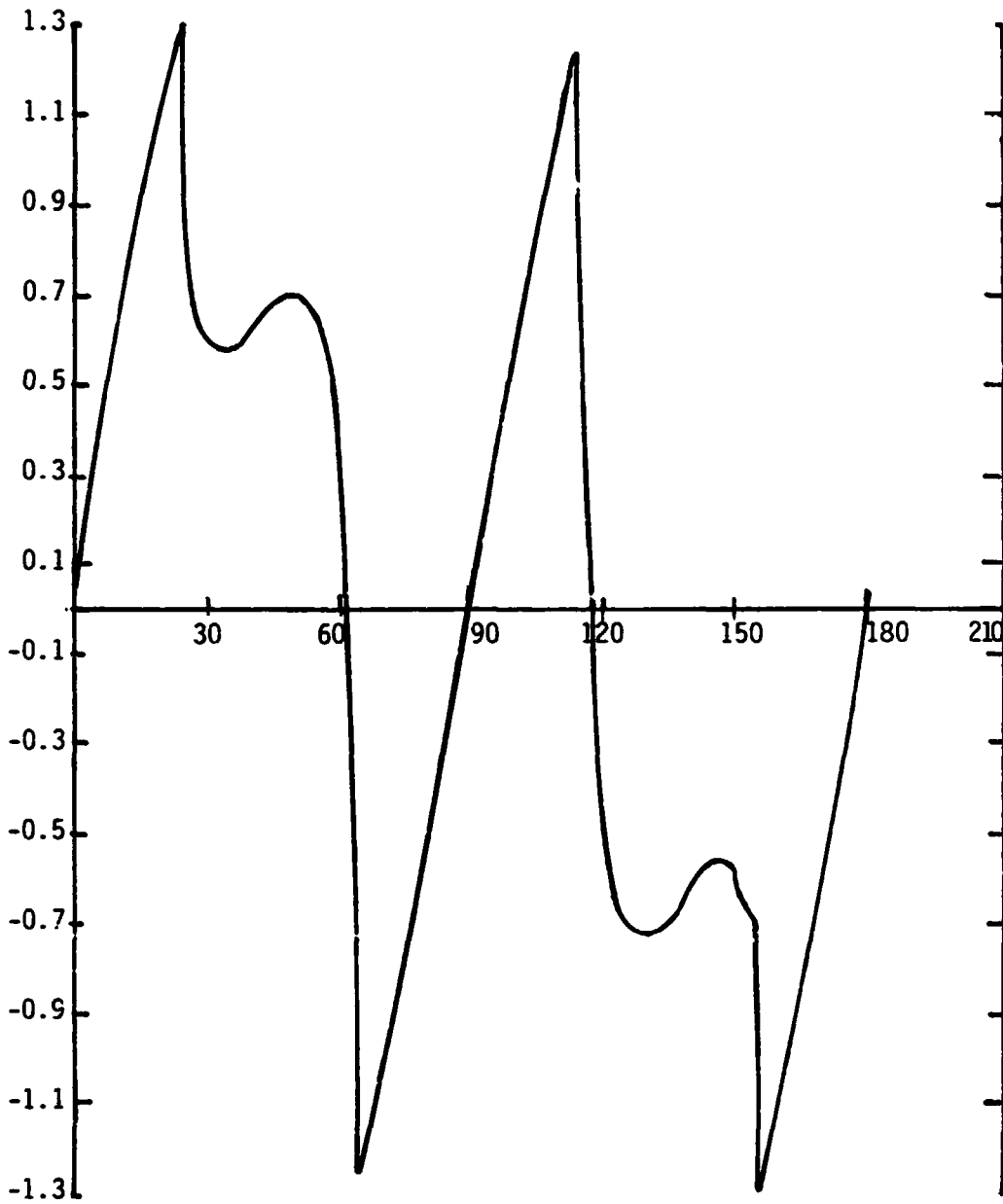


Figure 3.i0. S-Curve; Sine Wave on Channel 2, Biphase-L Random on Channel 1; One-Pole 1.8-MHz Filter Bandwidth; $f_{SW} = 1$ MHz; $P_2:P_1 = 2.48:1$

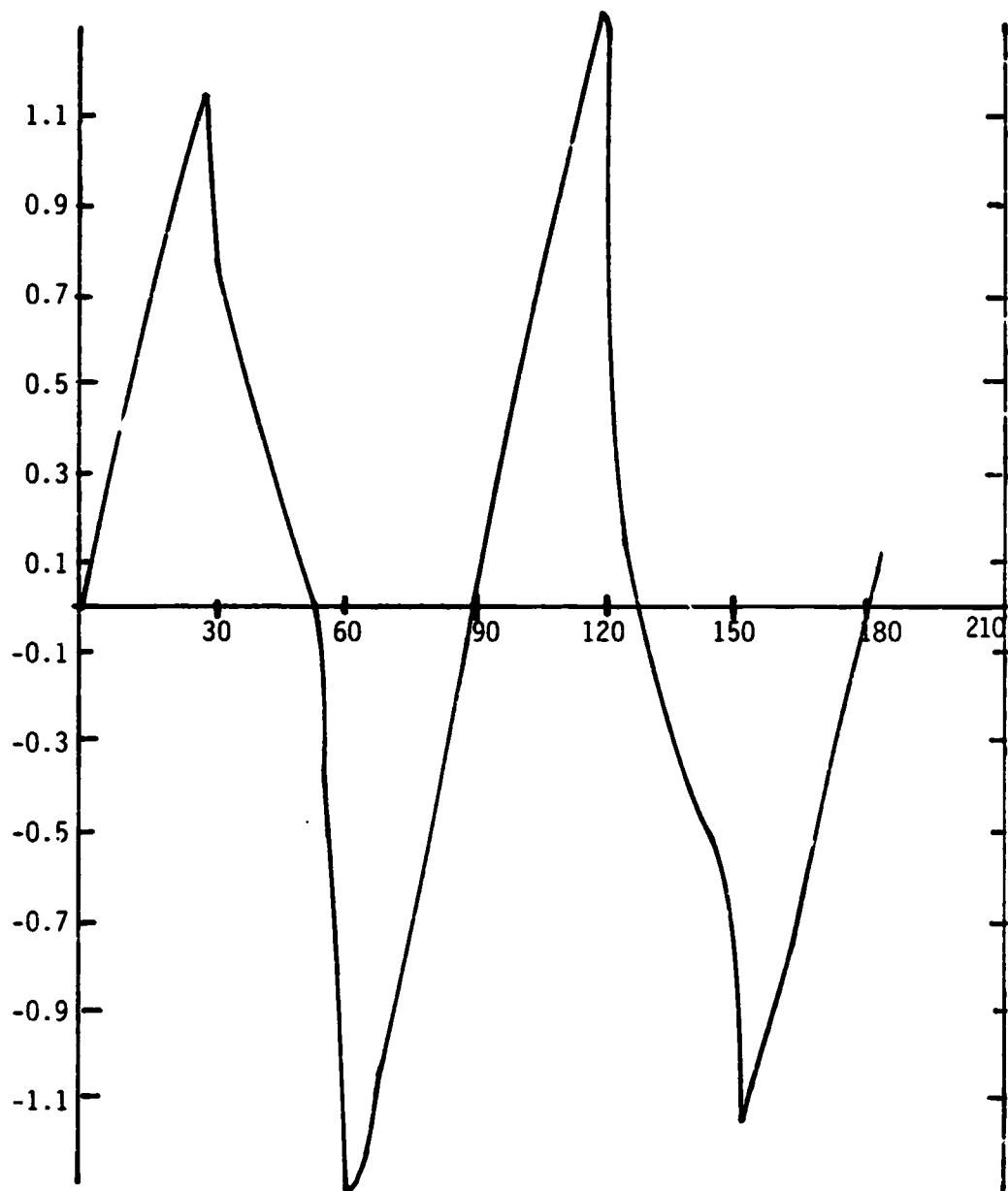


Figure 3.11. S-Curve; Sine Wave on Channel 2, Biphase-L Random on Channel 1; One-Pole 1.8-MHz Bandwidth; $f_{SW} = 2$ MHz; $P_2:P_1 = 1.45:1$

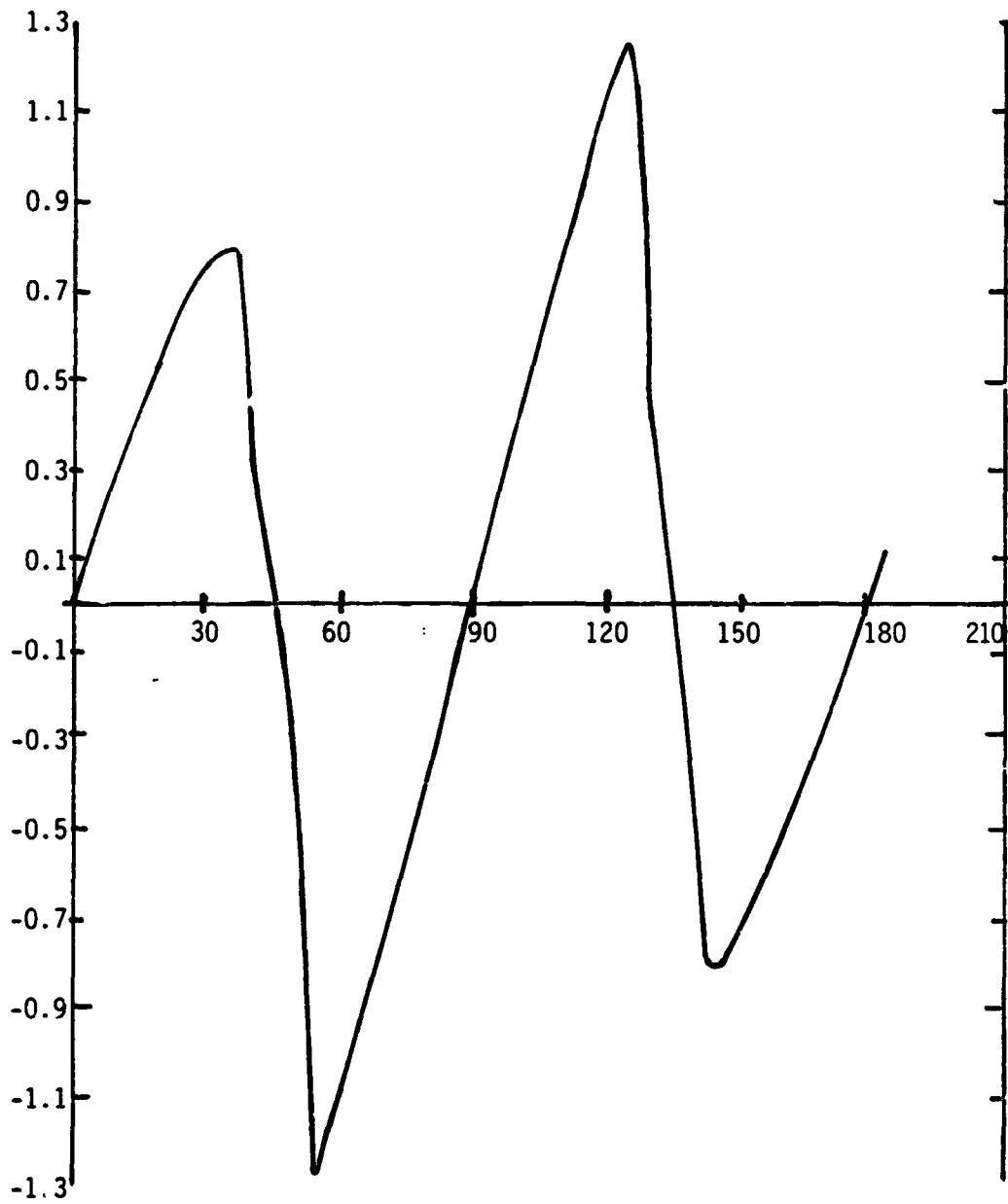


Figure 3.12. S-Curve; Sine Wave on Channel 2, Biphase-L Random on Channel 1; One-Pole 1.8-MHz Bandwidth; $f_{SW} = 3$ MHz; $P_2:P_1 = 0.86:1$

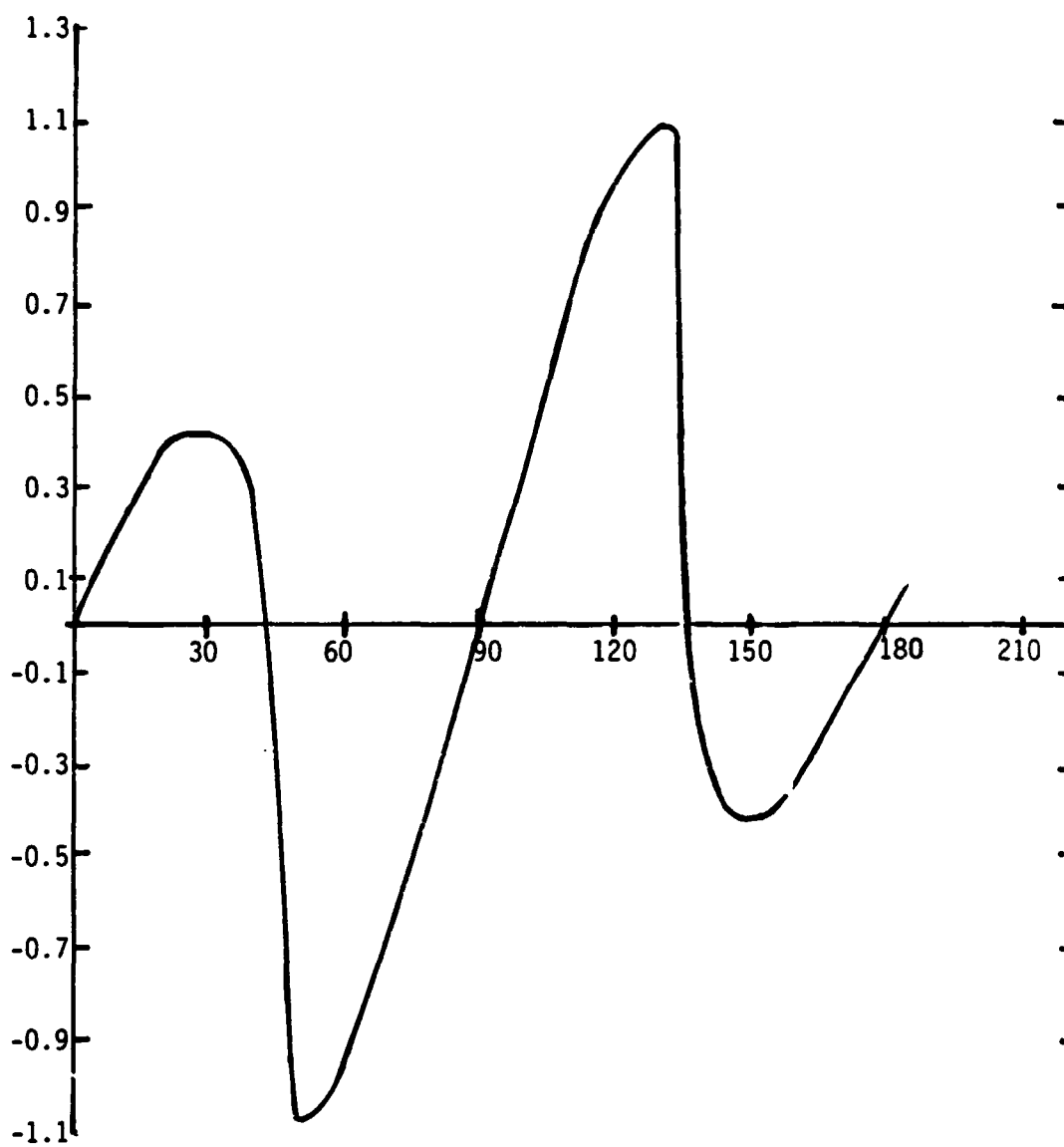


Figure 3.13. S-Curve with One-Pole 1.8-MHz Bandwidth; Sine Wave on Channel 2; Riphase-L Random on Channel 1; $f_{SW} = 4$ MHz, $P_2:P_1 = 0.55:1$

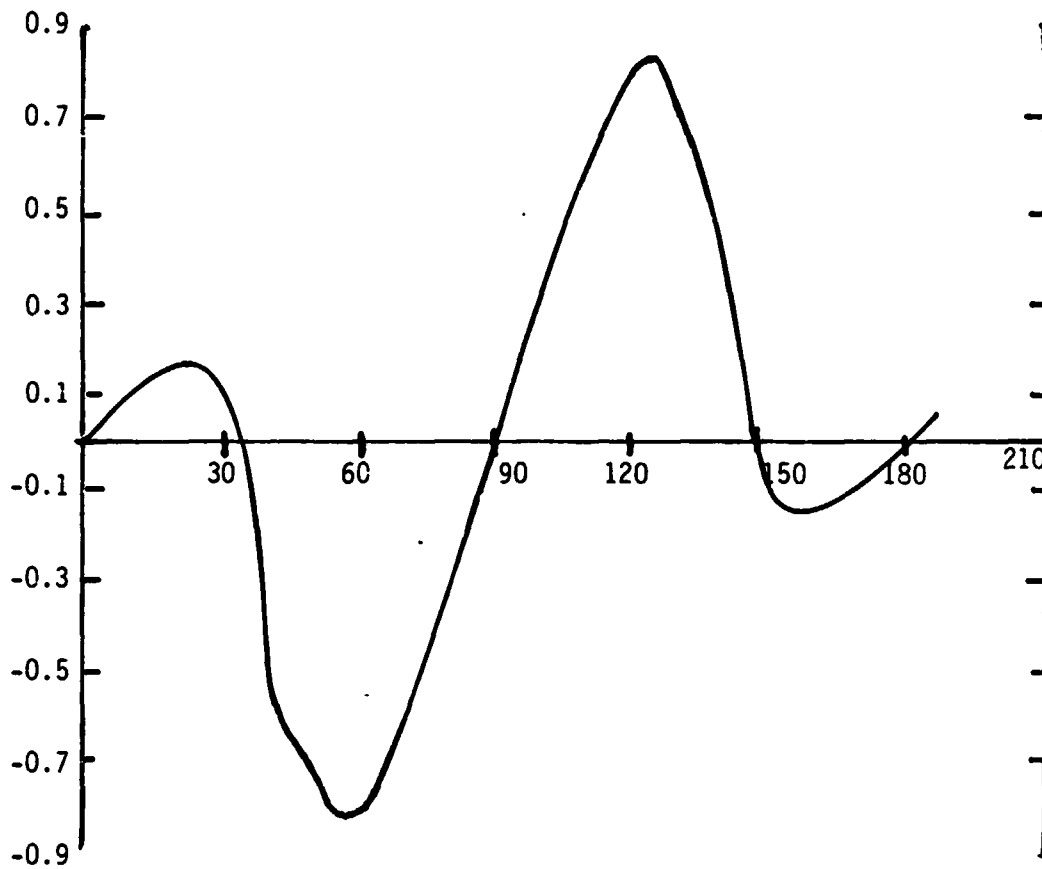


Figure 3.14. S-Curve with One-Pole 1.8-MHz Bandwidth; $f_{SW} = 5$ MHz, $P_2:P_1 = 0.37:1$; Sine Wave on Channel 2, 3phase-L Random on Channel 1

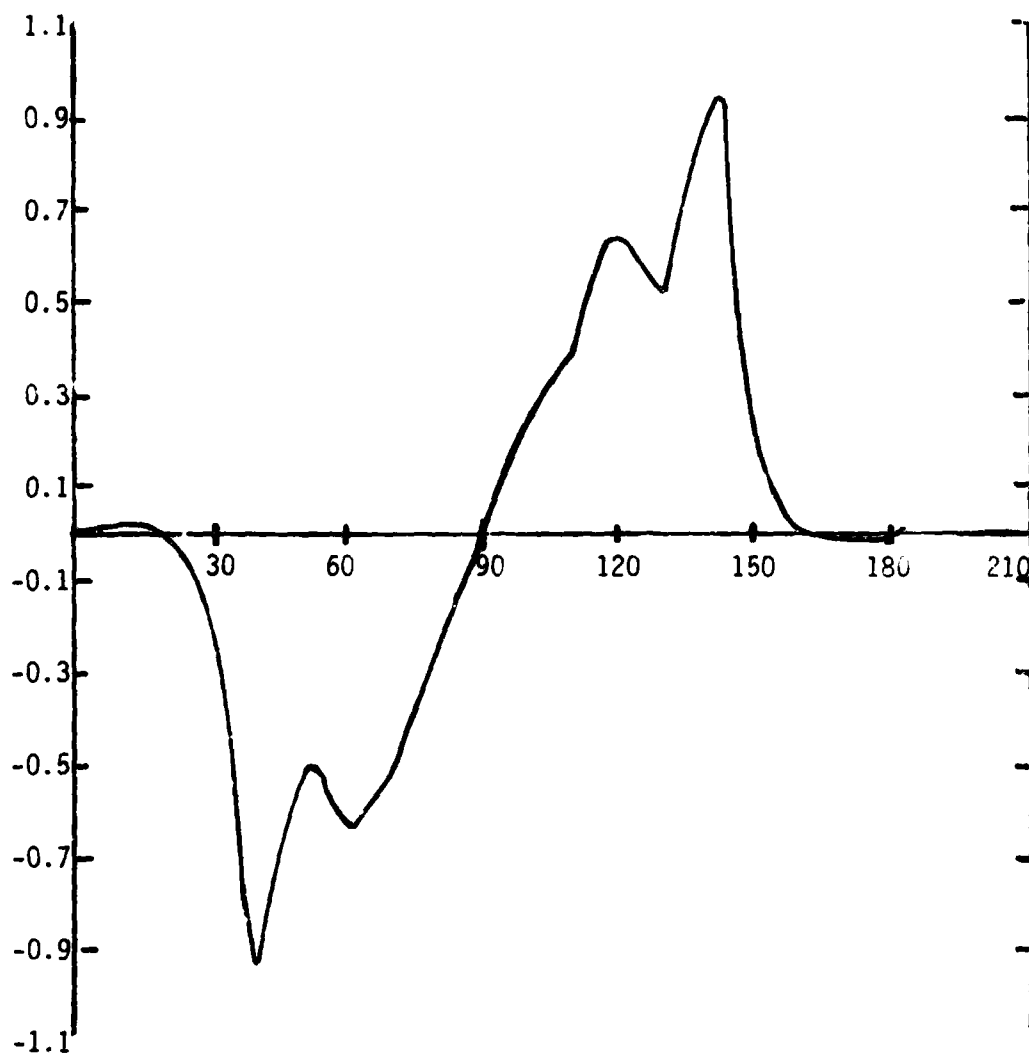


Figure 3.15. S-Curve with One-Pole 1.8-MHz Bandwidth; $f_{SW} = 6$ MHz, $P_2:P_1 = 0.27:1$; Sine Wave on Channel 2; Biphase-L Random on Channel 1

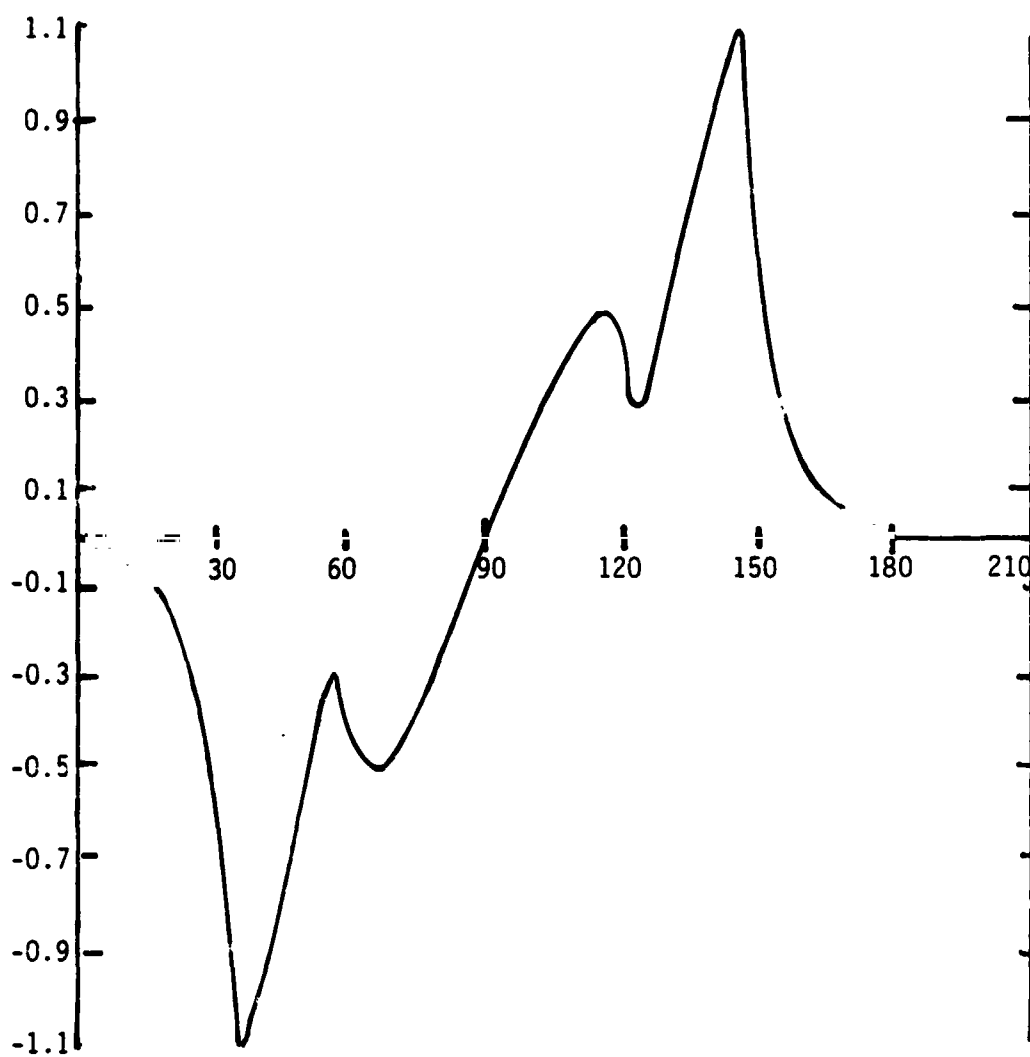


Figure 3.16. S-Curve with One-Pole 1.8-MHz Bandwidth; $f_{SW} = 7$ MHz; $P_2:P_1 = 0.2:1$, Sine Wave on Channel 2, Biphase Random on Channel 1

The final S-curve case is based on an attempt to accurately model the filters in the system. Again, a tone was used on channel 2 and random data on channel 1. A six-pole LPF of 5 MHz was employed to model the filter prior to the channel 2 limiter; a six-pole 6-MHz bandpass filter was used to model the bandpass filter prior to the QPSK tracking loop. Details of this filter are discussed in Appendix D. Figures 3.17 through 3.23 depict the resulting S-curves. These differ somewhat from the case of one-pole filtering (Figures 3.10 through 3.16). In particular, when the tone is at 3.2 MHz (Figure 3.23), the S-curve possesses a slightly positive slope at 0° or 180° . While at 3.5 MHz, a stable lock point near $\phi = 63.4^\circ$ appears with a weak lock point at 90° and 270° . At $f = 3.6$ MHz and greater, the only lock point is at $\phi = 63.4^\circ$ and 116.6° . Also, at 3.6 MHz, the power ratio of channel 2 to channel 1 at the QPSK tracking loop is about 0.4:1 while, at 4 MHz, it is about 0.12:1.

4.0 CONDITIONS FOUND TO INDUCE I-Q SWAPPING

There were basically three methods of testing which caused I-Q swapping. The first was noticed during bent-pipe operation with the Solar Max during the medium-rate demodulator (MRD) acquisition of the 8.5-MHz subcarrier. As the received signal power at the MRD is reduced, the probability of locking with the correct I-Q relationship decreases. This problem is inherently an acquisition problem; hence, it is due to a power loss of channel 2 in the MRD and the error induced in the power-ratio detector (see Appendix B).

The second means by which the MRD loop interchanges channels 1 and 2 occurs when the tape recorder driving channel 2 starts up or changes tracks (wraps around). During this start-up or wrap-around time, the tape recorder puts out a noise-like burst rather than data, which causes channels 1 and 2 to interchange.

The third way the channel interchange was observed was when a sine wave was used as the modulation input of channel 2. When the sine-wave frequency reached 2.1 MHz by stepping from 2 MHz, the MRD would interchange channels 1 and 2. This was not a random phenomena but, rather, a precise deterministic process.

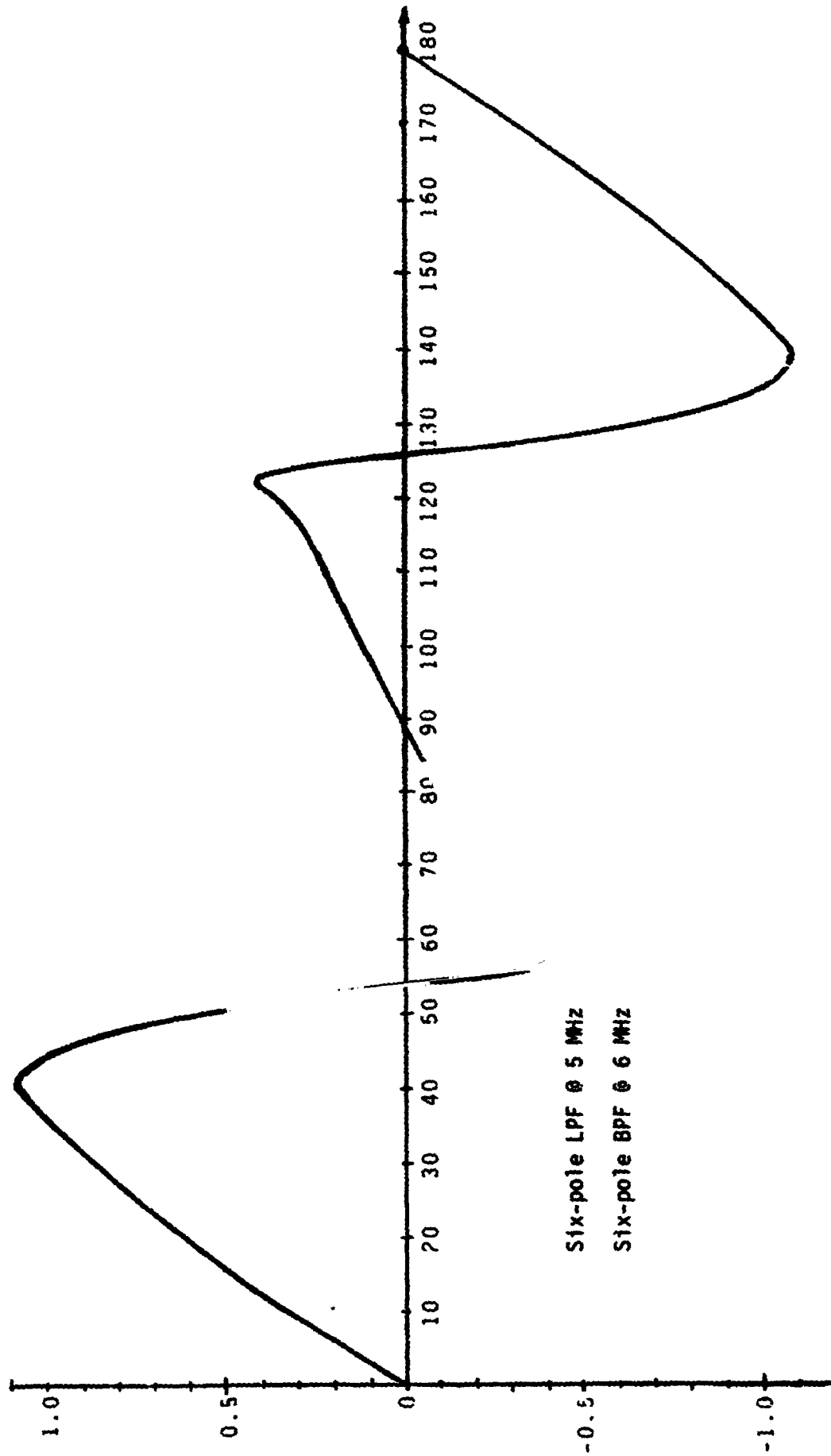


Figure 3.17. S-Curve; Random Data on Channel 1; Sine Wave on Channel 2; $f = 2.5$ MHz

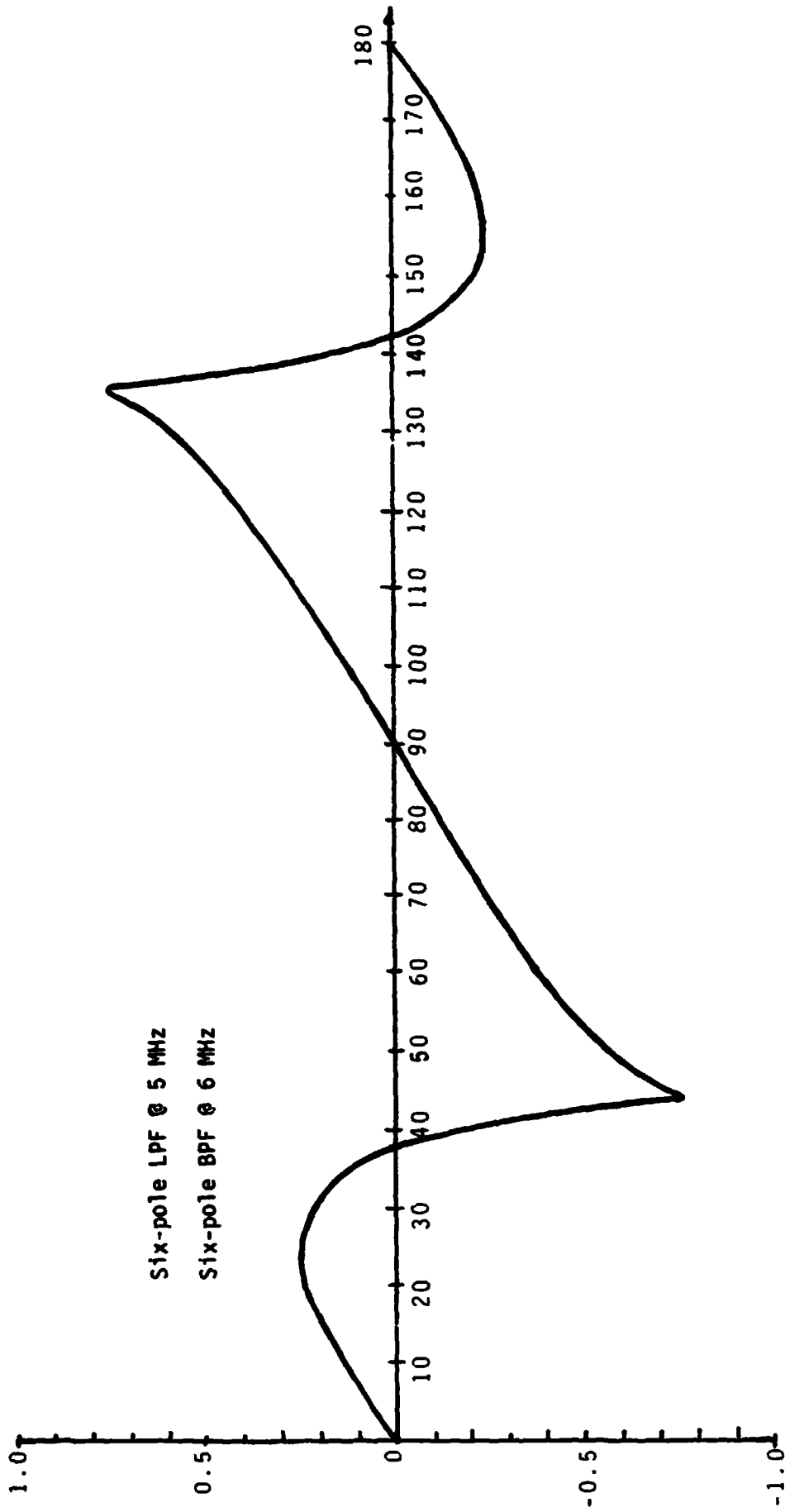


Figure 3.18. S-Curve; Random Data on Channel 1; Sine Wave on Channel 2; $f = 3.0$ MHz

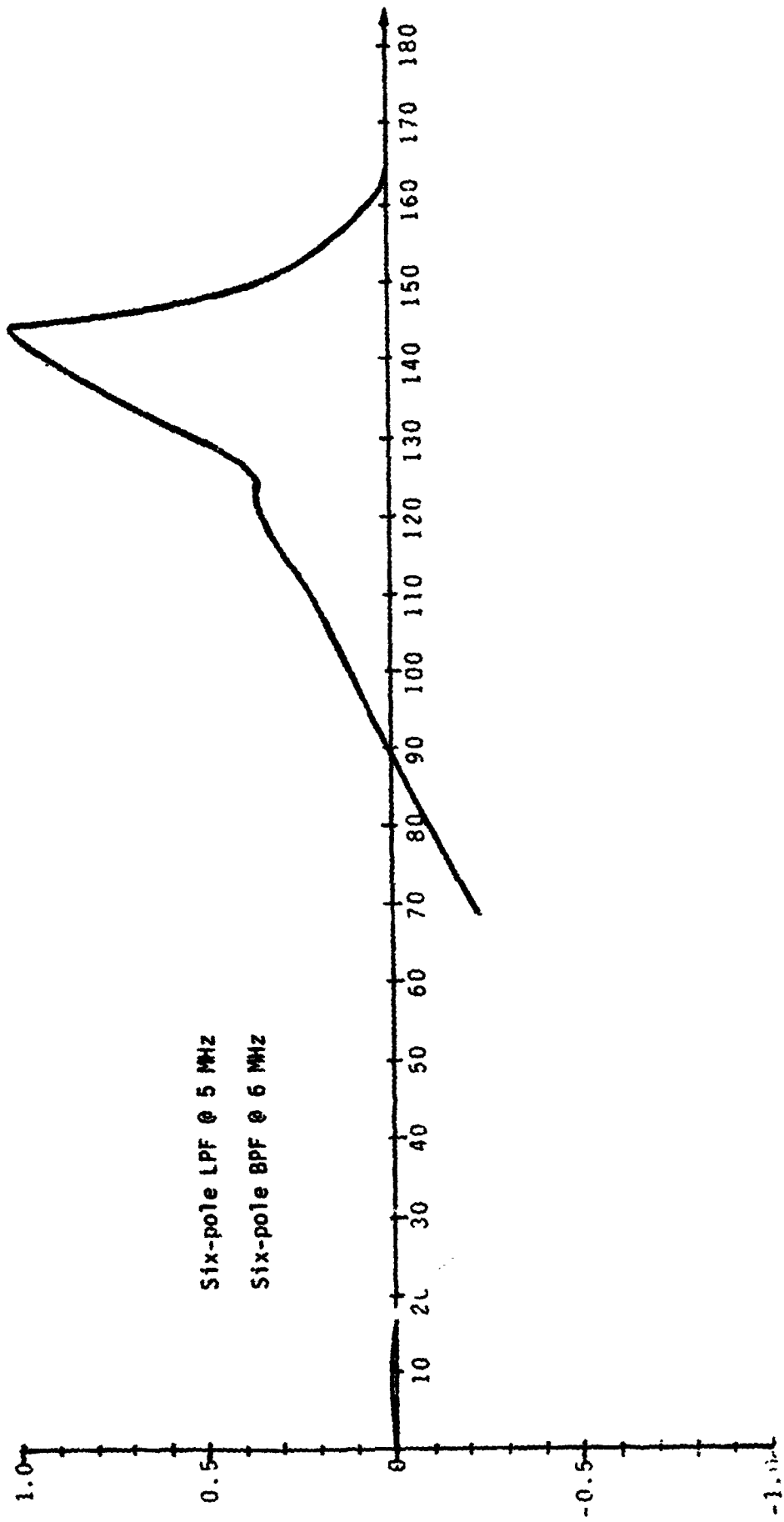


Figure 3.19. S-Curve; Random Data on Channel 1; Sine Wave on Channel 2; $f = 3.2$ MHz

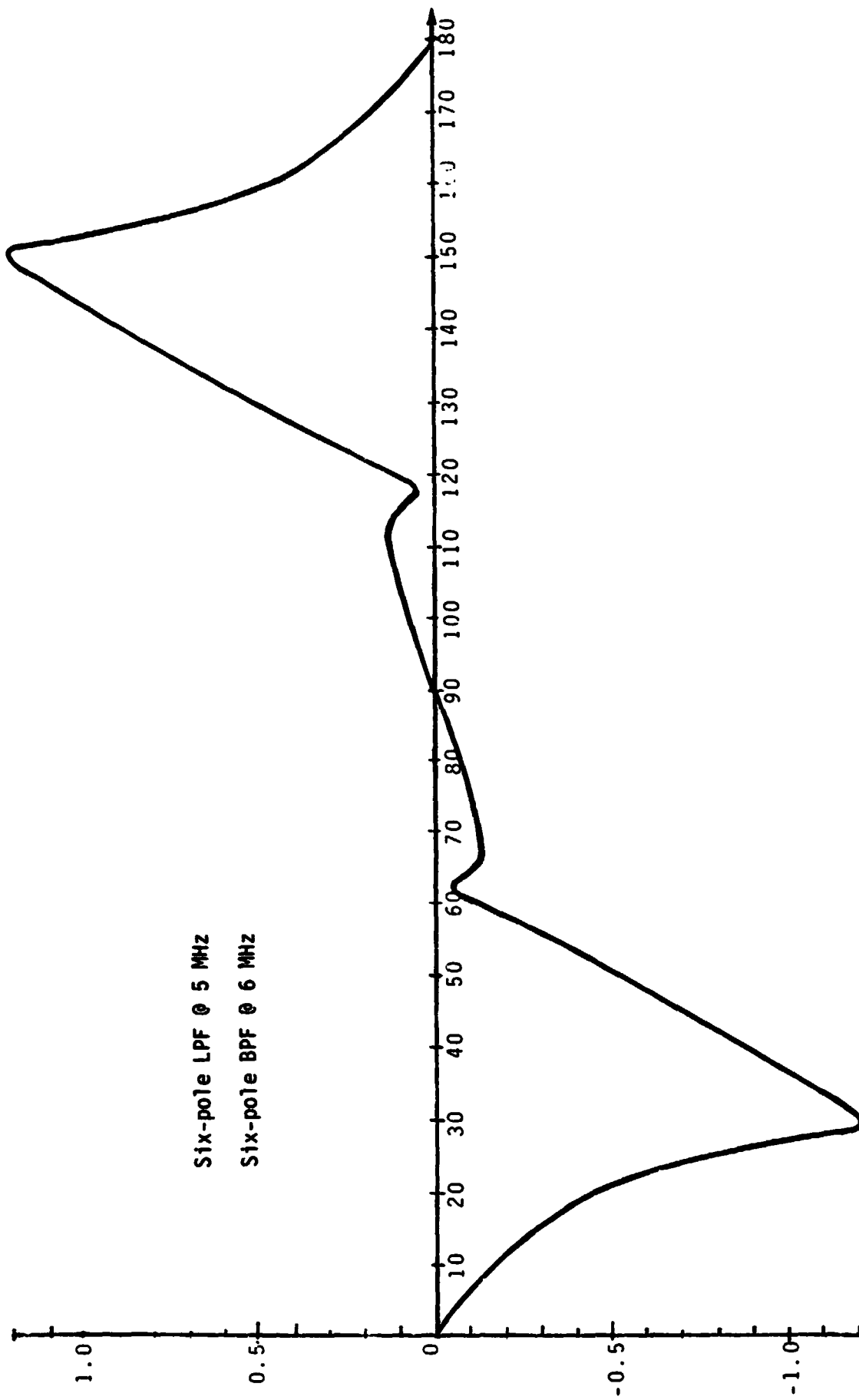


Figure 3.20. S-Curve; Random Data on Channel 1; Sine Wave on Channel 2; $f = 3.4 \text{ MHz}$

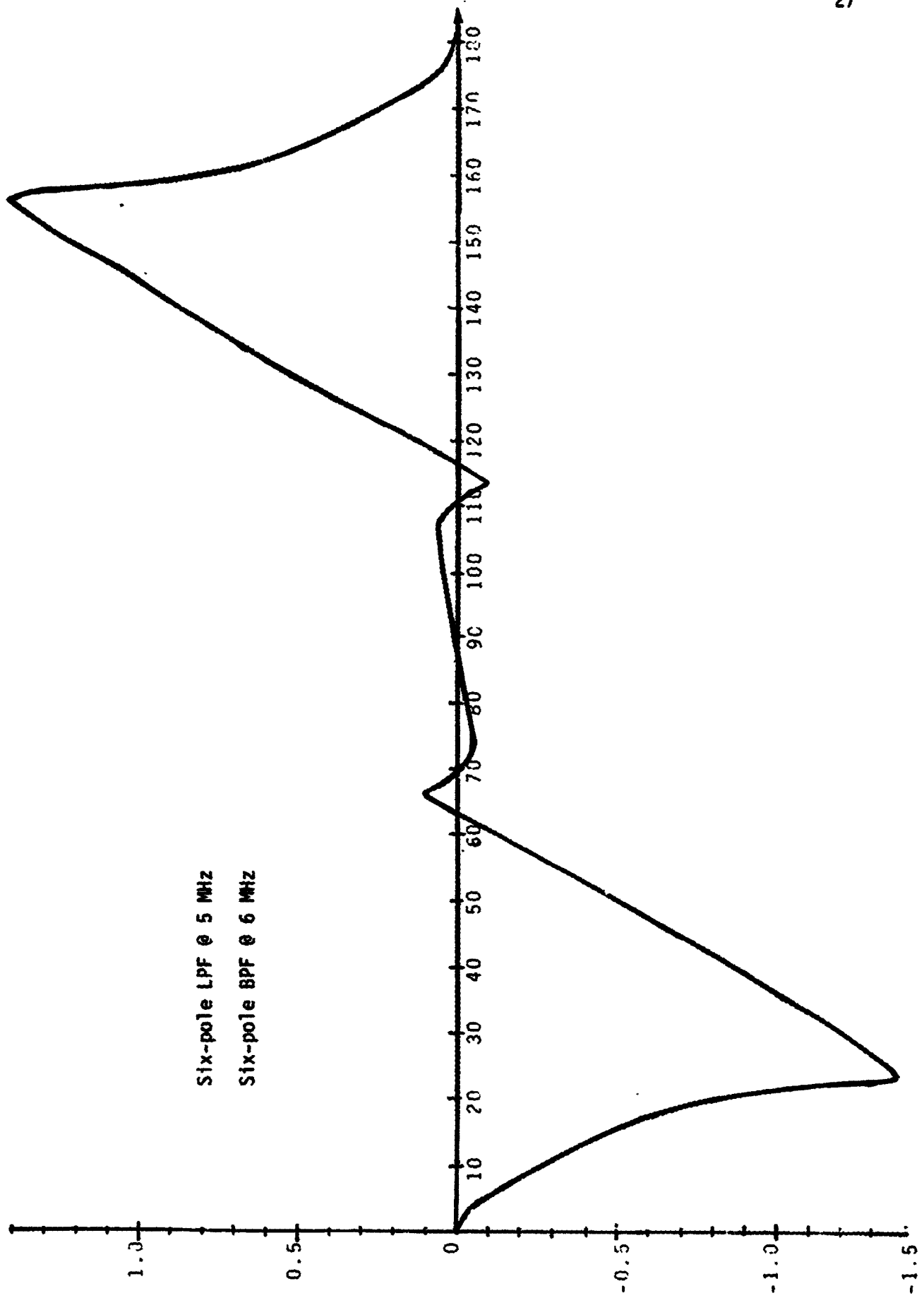
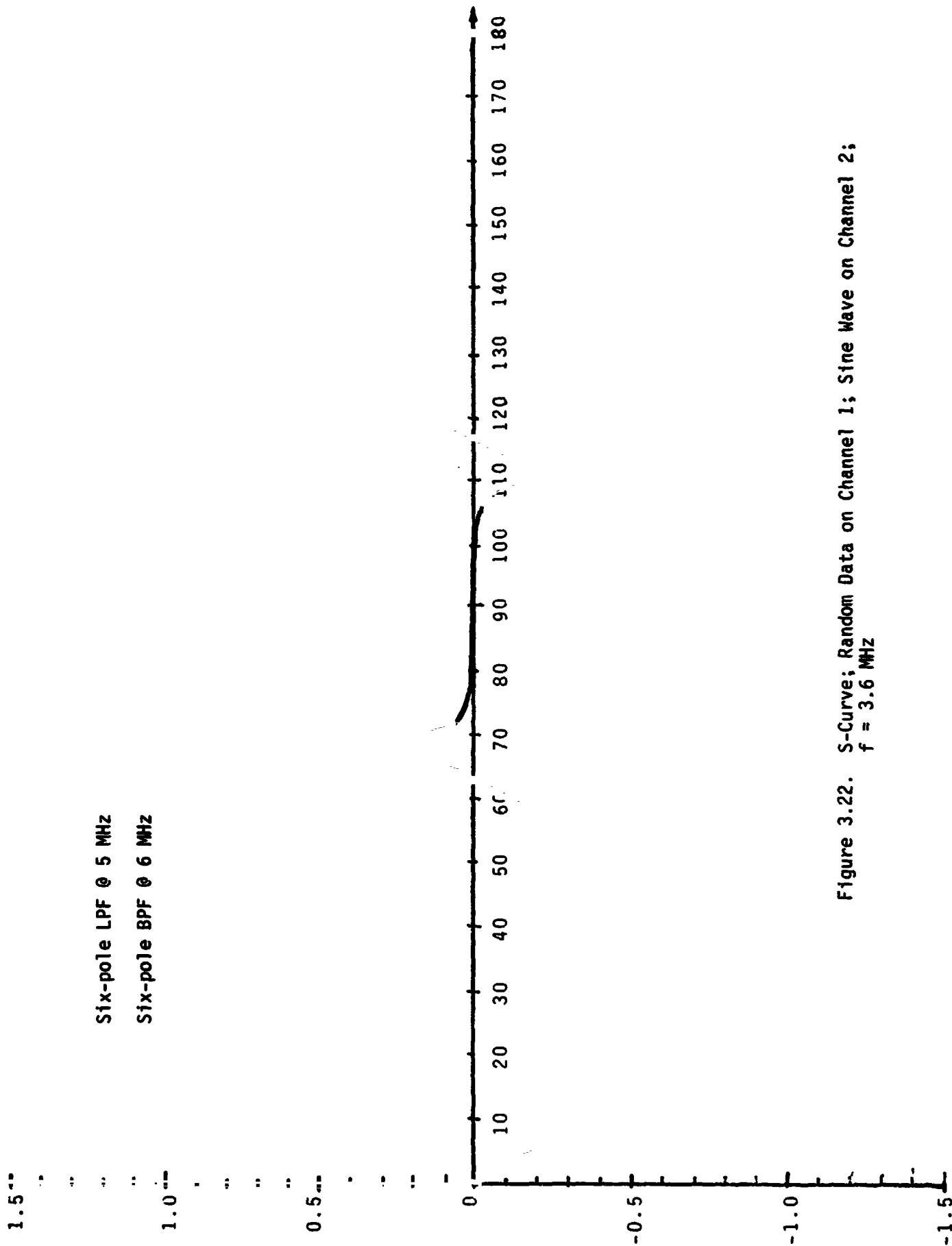


Figure 3.21. S-Curve; Random Data on Channel 1; Sine Wave on Channel 2; $f = 3.5$ MHz



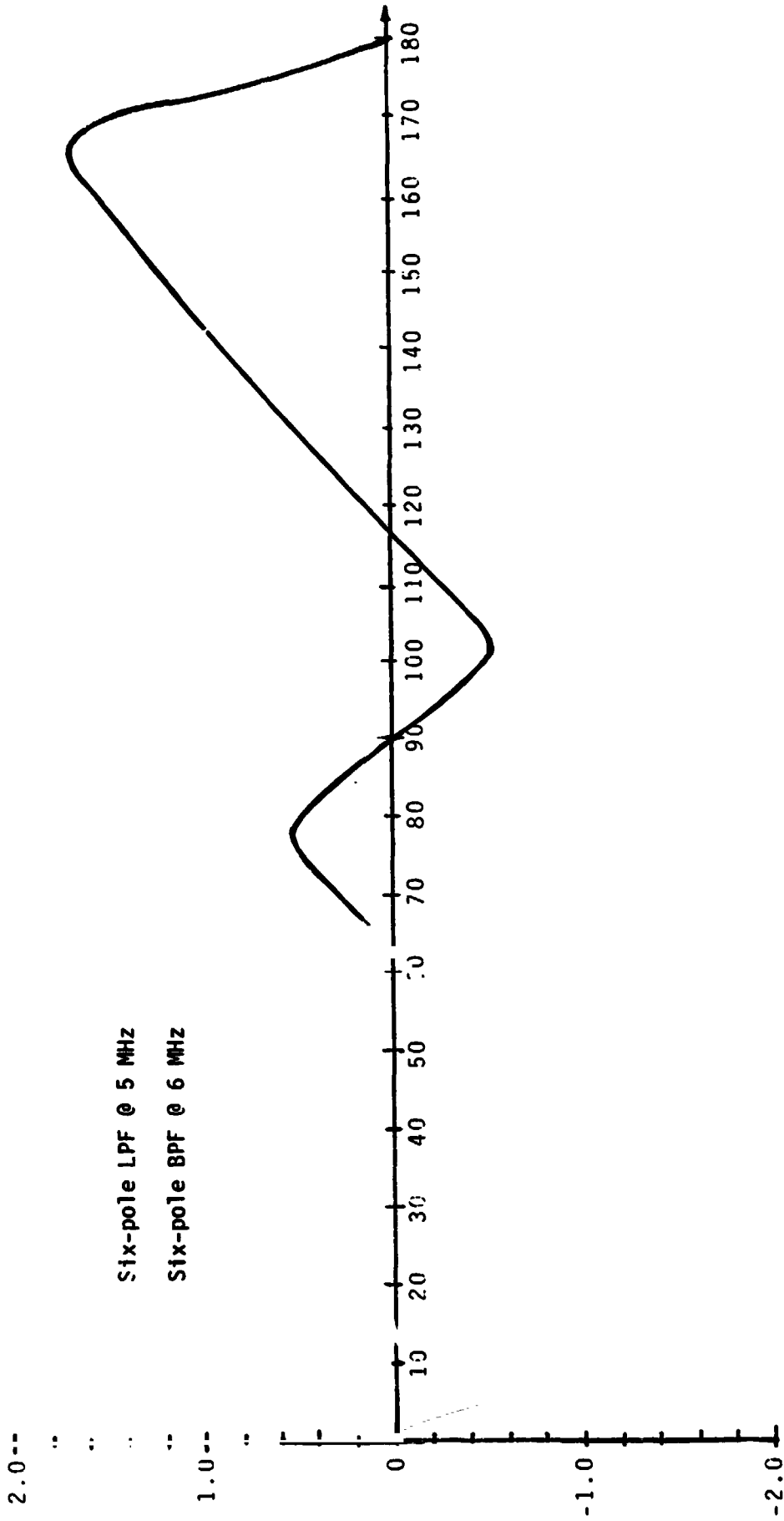


Figure 3.23. S-Curve; Random Data on Channel 1; Sine Wave on Channel 2; $f = 4.0$ MHz

5.0 TAPE-RECORDER-SIGNAL MODEL

The tape recorder was observed to produce a "noise-like" burst during the tape recorder startup or turnaround which was viewed by NASA/JSC personnel to be the source of the I-Q flipping. In Figure 3.24(a)/(b) [2, page 145] are the spectral densities of both the steady-state and start-up transient conditions. In the steady-state case, the spectral density appears to be the usual Manchester-encoded data, whereas the start-up spectral density appears to be the sum of flat noise plus two sine-wave tones that start at about 2.5 MHz and 3.8 MHz. However, since the spectral plot occurs only at a given time, as time progresses, the lines move farther out in frequency, then essentially disappear (when the data spectral density shows itself at the steady state). Observations by NASA/JSC engineers have noted that the lines do move out as time progresses.

Thus, our model for the output of the tape recorder startup or turnaround is given by (for up to one second or more)

$$V(t) = n(t) + A_1 \cos \left[\omega_1 \left(t + \frac{a}{2} t^2 \right) \right] + A_2 \cos \left[\omega_2 \left(t + \frac{a}{2} t^2 \right) \right] \quad (11)$$

where A_1 and A_2 are the tone peak amplitudes and ω_1 and ω_2 are the radian frequencies corresponding to 2.5 MHz and 4 MHz when a 5-MHz prefilter bandwidth was used and 1.25 MHz and 2 MHz when a 2.5-MHz prefilter bandwidth was used. The rate of change of frequency coefficient, a , was modeled as 1.2. The first term $n(t)$ is modeled as bandlimited white Gaussian noise. The power ratios of tone power to noise power is made a variable in the computer simulation program. It will shortly be shown that the existence of these tones accounts for the I-Q flipping phenomena in a well determined way.

6.0 CONCEPTUAL BASIS FOR THE TAPE-RECORDER-INDUCED I-Q FLIPPING

In this section, we discuss the reason why the tape recorder being turned on or wrapping around caused the I-Q inversion. During the tape-recorder startup, both a noise burst and the two sweeping tones are generated. Assume that a 5-MHz LPF (prelimiting) is used first. We can view Figures 3.17 through 3.23 to see what happens. Since the second tone (the higher frequency) will be filtered first, we neglect it and concern ourselves with the lower frequency tone only. From Figures 3.17 through 3.23, we see that, as

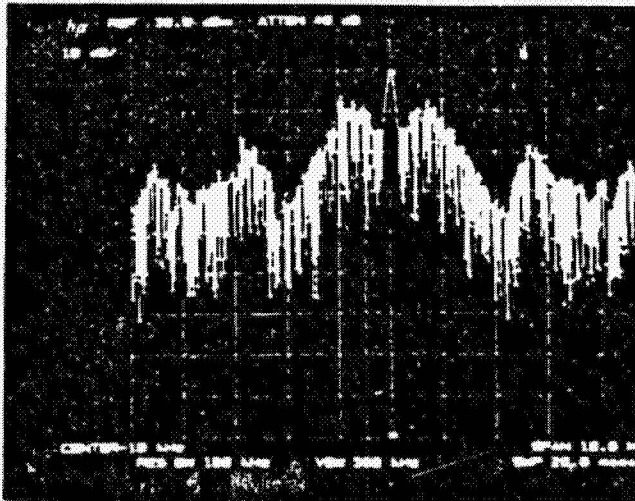


Photo of Normal Tape Playback

Center Connector of Breakout
Box Used

- 960-kbps playback
- No filter

Figure 3.24(a). Normal Playback Spectra

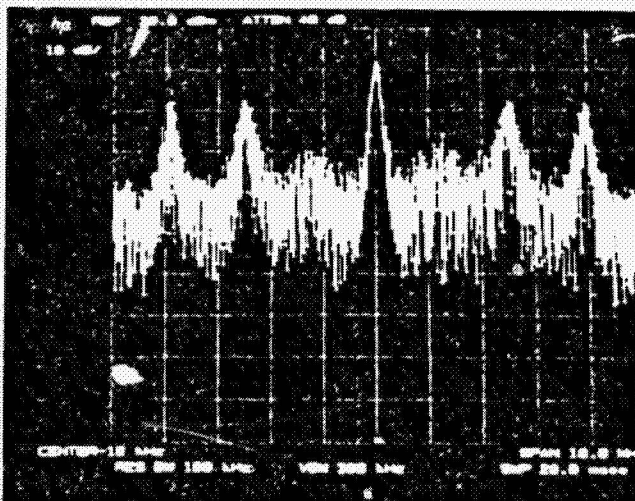


Photo at Tape Start-Up

Center Connector of Breakout
Box Used

- 960 kbps playback
- No filter

Figure 3.24(b). Transient Start-Up Spectra

the tone frequency (the value of f in these figures) increases, the S-curve lock point at $\phi=0$ starts to diminish. By the time $f= 3.2$ MHz, the S-curve has a very weak lock at $\phi=0$ while, at $f = 3.4$ MHz, the lock point disappears (the slope at $\phi=0$ is negative). Hence, at this point, the loop attempts to push the phase error towards either $+90^\circ$ or -90° . As the tape recorder continues to increase its tape speed, the two tones continue to increase in frequency leading to Figure 3.22, which shows a lock point at 63.4° . The loop will remain locked at this phase error until the tone frequency goes beyond the 5-MHz cutoff of the channel 2 lowpass prelimiter. The noise in the tape system will then be the dominant power term and the S-curves will revert to those of Figures 3.2 through 3.9. However, since the power in channel 2 is based essentially on thermal noise and enters a limiter (at the transmitter), the bandwidth is greater than 5 MHz but the 6-MHz BPF of Figure 1.1 removes some noise power, as does the 1.8-MHz arm filters of the loop. So, instead of a 4:1 power ratio, a smaller ratio (say, 1:1) occurs initially in the loop. But, from Figure 3.3, we see that a phase error of 63.4° will be carried into 90° (or -63.4° into -90°). Thus, I-Q swapping has occurred. Figure 3.25 shows a simulation of this phenomena, while Appendix E discusses the simulation model. In Figure 3.25, we see that, within a few tenths of a millisecond, the phase reaches about 63.4° and hangs there as discussed above, then slowly reaches 90° .

Now let us consider what happens when the 2.5-MHz LPF is employed prior to the channel 2 limiter. Recall that the BPF located prior to the sub-carrier demodulator (MRD) has a baseband bandwidth of 3 MHz. Now, as the tape recorder is turned on, the recorder noise starts and the two previously discussed tones start increasing their frequencies. Again, we will concern ourselves with only the lower frequency tone since it is the dominant one in terms of I-Q flipping. As the lower frequency tone reaches 2.5 MHz, it starts getting filtered by the 2.5-MHz LPF in front of the channel 2 limiter. When it gets to 3 MHz, it is down about 10 dB; hence, the dominant term is the tape-recorder noise--not the tone. But, when only noise is present, it passes through the channel 2 limiter and looks like a data stream with heavy phase or time modulation. Hence, the S-curves for data modulation are applicable. Since the prefilter is set to 2.5 MHz, the limiter-output bandwidth is increased somewhat to, say, 4 MHz. But the arm filter "captures" most of this energy so that Figure 3.3 applies (or maybe Figure 3.4--it doesn't matter).

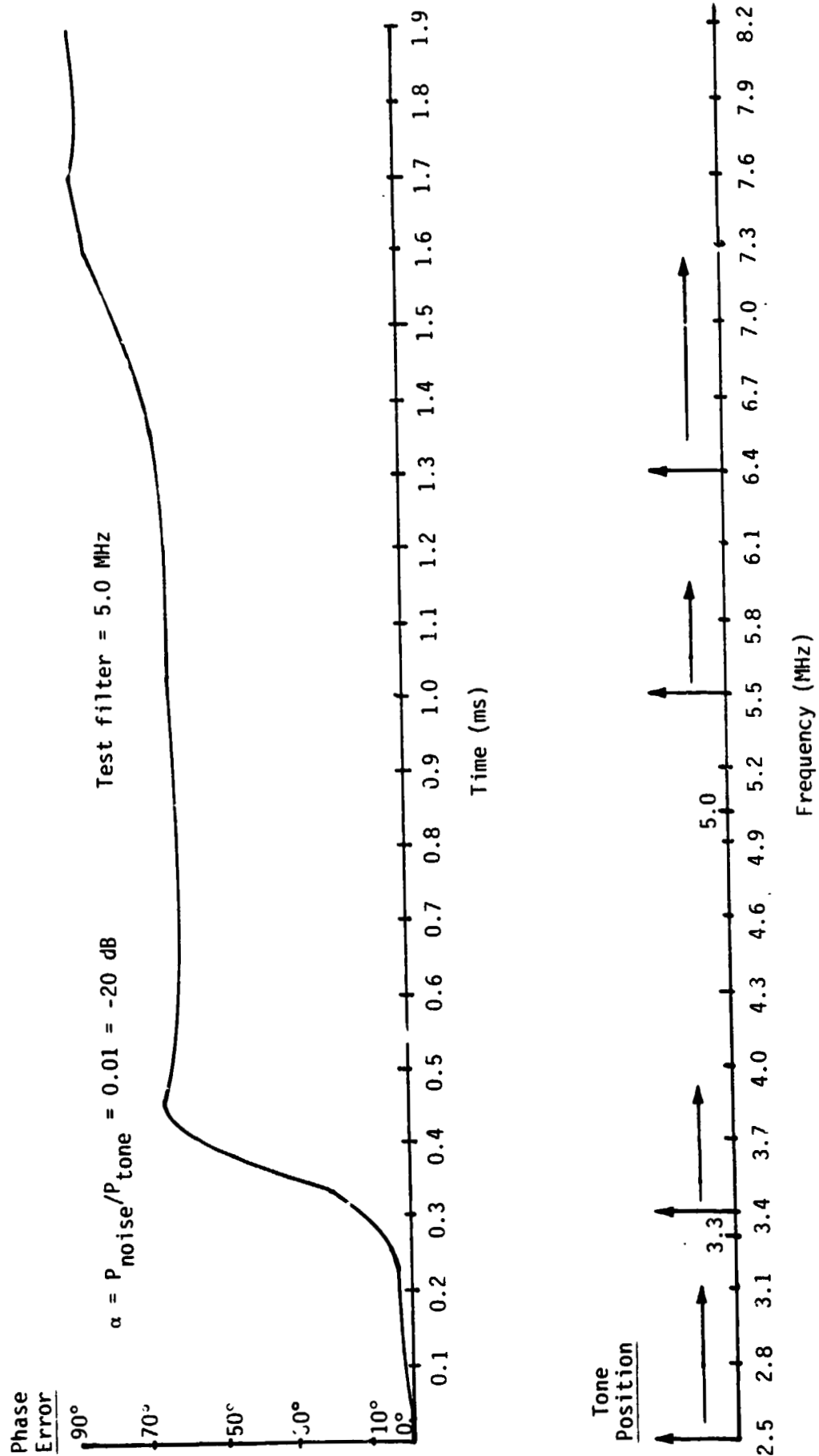


Figure 3.25. Simulation of I-Q Inversion with the 5-MHz Prelimiter LPF Plotted Against Time and the Lowest Frequency Value

From these S-curves, we see that there is no force to push the loop away from the lock point. From this discussion, it is clear that both the bandwidth and the number of poles are important since they determine how much attenuation is present to the lowest frequency tone.

Figure 3.26 illustrates the results of a simulation of the system when a 2.5-MHz prelimiter LPF was used. We see that, when the tone (which is now attenuated by about 6.5 dB at 2.9 MHz) reaches the point of the skirt of the 6-MHz bandpass filter, it is much weaker than the case when the 5-MHz LPF was used; hence, the mixture of noise-like energy to tone energy is not great enough to push the loop 90° away from the correct lock point. From Figure 3.26, the peak deviation from the lock point is about 5°.

We can now see why the square-wave test caused the loop to lose lock. Since this test was composed of only one square-wave signal, we see from Figures 3.19 and 3.20 that, at about 3.2 MHz, the S-curve has a negative slope at $\phi=0$; hence, the loop is pushed towards the lock point at 90°. Note that, once at the 90° point, the loop will not slip again if the square wave is applied when $\phi = 90^\circ$ since 90° is a stable lock point. Hence, once the loop I-Q flipped, it would not flip again on turnaround.

The measured value of square-wave-induced I-Q interchange was 2.1 MHz, whereas our theory predicts 3.2 MHz. Since we did not make a precise estimate of the tone-to-tape-noise power, we should not expect an exact agreement between the experimental measurement and theory.

7.0 SIMULATION OF THE I-Q FLIPS

In this section, we compare the NASA measurements with the simulation results performed at Axiomatix. In Table 7.1, simulation results are given for the case when no channel noise was present.

In the first two rows of Table 7.1, the individual tone-to-recorder noise spectral density was set at 87 dB-Hz which, for the two prelimiter LPF bandwidths considered, yielded SNR's of 20 and 23 dB (tone-to-noise-power ratio). The initial frequencies of the recorder tones are set so that the loop has time to respond to them before they are "outside" the LPF bandwidth. The loop bandwidth of the simulation was set to 18 kHz in order to reduce computer computation time and cost. The result shown in the last column of Table 7.1 was that, with a 5-MHz LPF prior to the limiter, it I-Q flipped whereas, with the 2.5-MHz LPF, it did not flip. This result is compatible with the observed measurements at NASA.

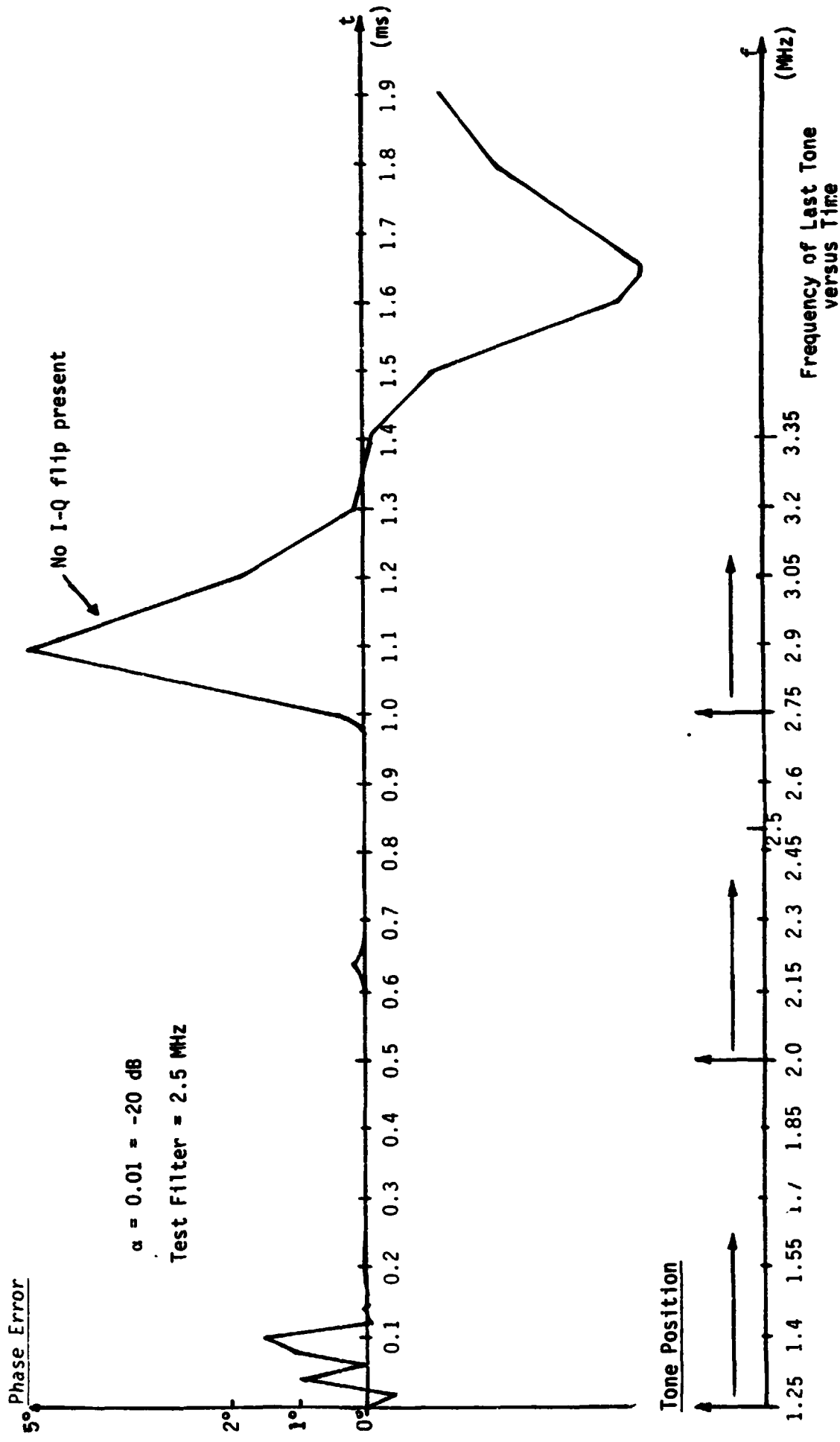


Figure 3.26. Simulation of Unsuccessful I-Q Inversion Using a 2.5-MHz LPF Plotted Against Time and the Lowest Frequency Value

Table 7.1. No Channel Noise

Tone-to-Noise PSD (Recorder Model) (dB-Hz)	Test Filter Cut-Off Frequency (MHz)	In-Band Tone-to-Noise Ratio (dB)	Initial Frequency of the Tones (MHz)	Loop BW (kHz)	Description of Simulation Result
$\beta = 87$	(6-pole) 5	20.0	2.5 & 4.0	18	FLIPPED Moved to 63.4°, then to 90° (noise takes over)
	2.5	23.0	1.25 & 2.0	18	DID NOT FLIP
$\beta = 77$	5	10.0	2.5 & 4.0	18	FLIPPED Less tendency to stay at 63.4° (noise takes over sooner than previously)
	2.5	13.0	1.0 & 2.0	18	DID NOT FLIP
$\beta = 72$	5	4.8	2.5 & 4.0	18	FLIPPED Faster than previously
	2.5	—	—	—	—
$\beta = 67$	5	0.0	2.5 & 4.0	18	FLIPPED Takes more time to take off, then flips faster
	2.5	3.0	1.0 & 2.0	18	DID NOT FLIP
$\beta = -\infty$ (Only white noise as recorder output)	5	$-\infty$	—	18	DID NOT FLIP
	2.5	$-\infty$	—	18	—

The same comparison was made in the second, third and fourth rows of Table 7.1, except that the tone-to-recorder noise spectral density was reduced by 10 dB. Again, the results agreed with NASA's observations. This test was repeated twice more, each time with a 10-dB lower tone-to-noise power spectral density with the same flipping results. Finally, recorder noise only without a tone was tried and the I-Q loop did not flip. Later, we will see that, when channel noise was added to the receiver, the loop would not I-Q flip except at very low E_b/N_0 values.

Next, channel noise (white Gaussian thermal noise) was added to the receiver in order to simulate receiver front-end noise in the usual high E_b/N_0 level that this link displays (see Table 7.2). Again, it is seen that the loop flips only with the 5-MHz LPF--not with the 2.5-MHz filter.

In the data of Table 7.3, we considered the case when the channel E_b/N_0 was low. The purpose was to try to simulate the observed I-Q flip and return at the low SNR noted by NASA/JSC. Using the 5-MHz filter, the first test was simulated with a $B_L = 18$ kHz. It appeared that the loop SNR was too low, so this bandwidth was reduced to 4.5 kHz. At 20-dB tone-to-tape-recorder noise power ratio and E_b/N_0 of 2 dB, a flip occurred, then returned to $\phi = 0$, similar to what NASA had described. Removing the tone in the recorder-output model prevented this I-Q flip and return from happening. A plot of this phenomena is depicted in Figure 7.1. Note initially that the lowest frequency tone causes the loop to start to I-Q flip ($\phi = \pm 90^\circ$), then the error gradually returns to zero phase error, that is, the I-Q flip corrects itself.

8.0 SOLAR MAX WEAK-SIGNAL-CASE I-Q FLIPPING

Even though the Solar Max case was not analyzed extensively, it is believed that the basic reason why the I-Q flipping occurred in the Solar Max case was due to the weak signal conditions near 10-nmi ranges, along with the fact that the SNR in the 5-MHz filter at these ranges was low; hence, most of the power transmitted in channel 2 was due to thermal noise. This noise was bandwidth expanded in the limiter of channel 2; hence, when this signal was captured by the four-phase loop, only a small fraction of the original amount of power remained in the arm filters. Therefore, as the SNR in channel 2 decreased, the I-Q power-ratio detector would cause the probability of I-Q flipping to increase because the captured channel 2 power decreases as the Solar Max SNR decreases (range increases). In other words, it is believed that this problem is basically one of the effective I-Q power ratio diminishing as the range of the Solar Max from the Shuttle increases.

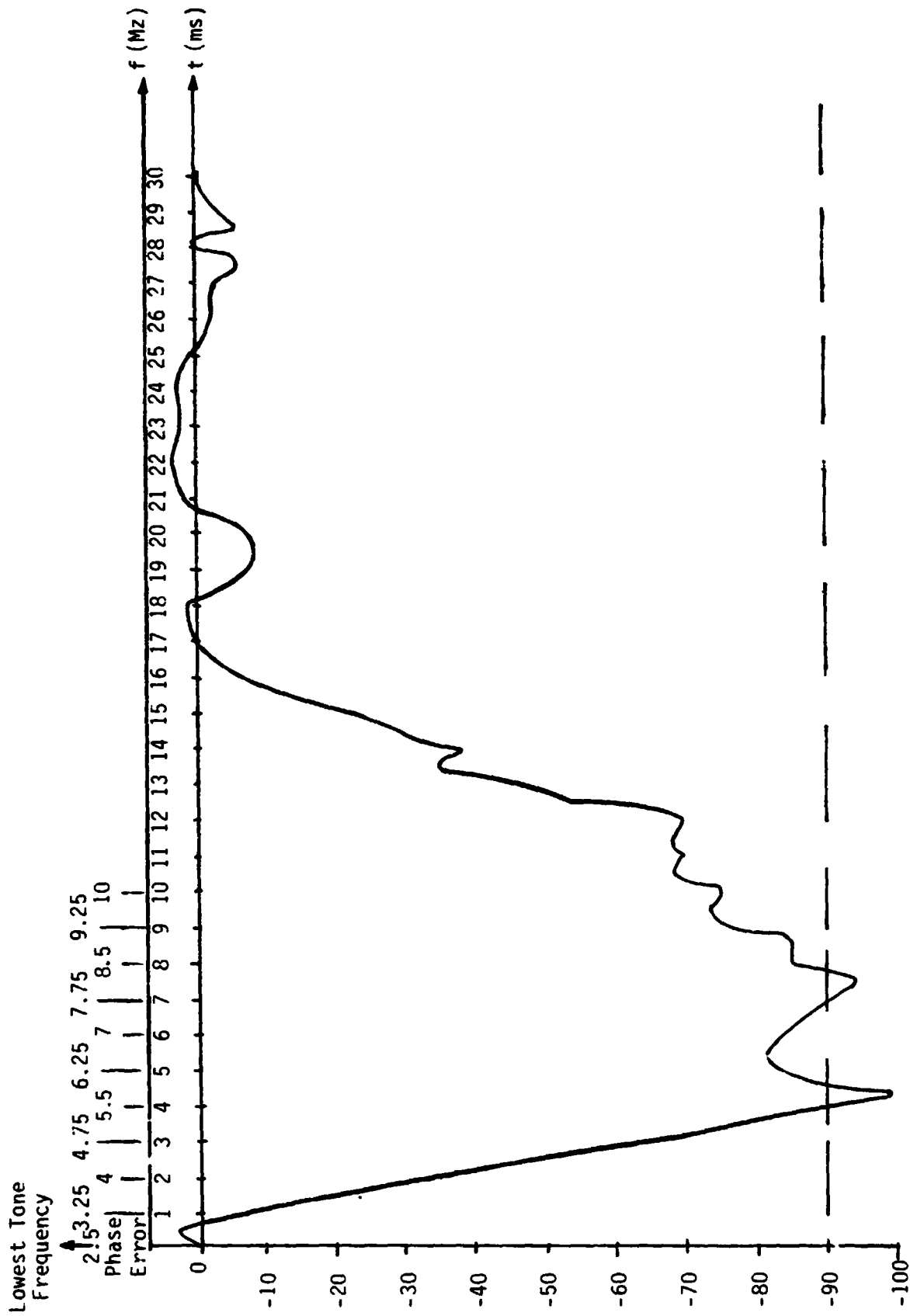


Figure 7.1. Plot of Phase Error Versus Time and Lowest Tone Frequency at Channel $E_b/N_0 = 2$ dB

Table 7.2 Weak Noise Added to the Link

Tone-to Noise PSD dB-Hz	Test Filter (MHz)	In-Band Tone-to Recorder Noise Ratio (dB)	Initial Frequency of the Tones	Loop BW (kHz)	E_b/N_0 (dB)	Description of Simulation Results
$\beta = 77$	5	10.0	2.5 & 4.0	18	16	FLIPPED
	2.5	13.0	1.25 & 2.0	18	16	DID NOT FLIP
$\beta = \infty$ (Only white noise as recorder output)	5	∞	—	18	16	DID NOT FLIP
	2.5	∞	—	18	16	—

Table 7.3. Strong Noise in the Link

$$E_b/N_0 \leq 6 \text{ dB}$$

Test Filter (MHz)	In-Band Tone-to-Recorder Noise (dB)	Initial Frequency of the Tones (MHz)	Loop BW (kHz)	E_b/N_0	
5	10.0	2.5 & 4.0	18.0	6.0	FLIPPED*; did not return to 0° (it might have needed more time)
5	10.0	2.5 & 4.0	18.0	4.0	FLIPPED*; returned to 0°, but did not stay in lock

*	5	10.0	2.5 & 4.0	4.5	4.0	FLIPPED*; did not return to 0° (more running time?)
	5	10.0	2.5 & 4.0	4.5	2.0	DID NOT FLIP (?) (More running time)
*	5	20.0	2.5 & 4.0	4.5	2.0	FLIPPED; returned to 0° and stayed in lock
	Only noise at recorder output	5	∞	---	4.5	4.0

NOTES:

- (1) Reduced sampling rate
- (2) Loop bandwidth reduced by a factor of 4
- (3) Rate of change of tone instantaneous frequency also reduced by a factor of 4 ($a = 3/10 \text{ kHz/s}$)

9.0 SUMMARY OF THE NASA LABORATORY TEST AND THE AXIOMATIX MODEL SIMULATION

In this section, we summarize some of the pertinent tests made by NASA and compare them to Axiomatix's model simulation described in Table 9.1.

First, in the NASA test, the tape recorder was turned on in channel 2 and the MRD loop flipped with a 15-MHz prelimiter LPF, but did not flip with a 2.5-MHz filter. Then, as a comparison, the Axiomatix model was utilized with a simulated tape-recorder input with a 5-MHz prelimiter LPF and the loop I-Q flipped. With a 2.5-MHz LPF, the MRD loop would not flip, agreeing with the NASA measurement.

Next, noise was introduced by NASA into channel 2 as a possible model of the tape-recorder start-up transient; it was found that, with both 15 MHz and 2.5 MHz, the MRD loop would not I-Q flip. This test was simulated on the Axiomatix simulation and found to agree.

At NASA, it was found that a 2.1-MHz square-wave signal injected into the channel 2 input would cause I-Q inversion when a 15-MHz LPF was used prior to the limiter, but it would not flip at a lower frequency. Axiomatix's model would I-Q flip with a 5-MHz filter with a 3.6-MHz square wave, but not at a lower frequency. Finally, NASA reported that, when the SNR was reduced, the I-Q flipping could be prevented. (Actually, the flip would occur, 90° change, then return back to 0°.) This apparently occurred at about $E_b/N_0 = 5$ dB at NASA whereas, for the Axiomatix model, it occurred at $E_b/N_0 \approx 2$ dB.

10.0 CONCLUSIONS

It is believed that the tape-recorder model developed herein allows us to predict or replicate the actual MRD hardware performance of I-Q flipping quite well, as noted in Table 9.1. Furthermore, we believe that it is the only theory presented which can explain all the known tests made by NASA at Johnson Space Center.

We wish to emphasize that it is our view that the tape-recorder start-up transient I-Q flipping problem is not just a noise-burst problem but, in fact, tones are also generated along with the noise in the tape recorder during start-up or wraparound. The Axiomatix theory also predicts the square-wave I-Q flipping problem which a noise-only theory does not.

Table 9.1. NASA Measurements Compared to the Axiomatix Model/Simulation

NASA Test or Axiomatix Model	Test Conditions	E_b/N_0 (dB)	LPF Band- Width (MHz)	Data (kbps)		I-Q Flip?	Axiomatix versus NASA Data Agreement ?
				Ch 1	Ch 2		
NASA	Tape recorder turned on in Channel 2	16	15	192	N/I	Yes	Yes
Axiomatix	Tape recorder turned on in Channel 2	16	5	192	N/I	Yes	
NASA	Tape recorder turned on in Channel 2	16	2.5	192	N/I	No	Yes
Axiomatix	Tape recorder turned on in Channel 2	16	2.5	192	N/I	No	
NASA	Lab noise injected into Channel 2	16	15	192	N/I	No	Yes
Axiomatix	Noise injected into Channel 2	16	5	192	N/I	No	
NASA	Lab noise injected into Channel 2	16	2.5	192	N/I	No	Yes
Axiomatix	Noise injected into Channel 2	16	2.5	192	N/I	No	
NASA	2.1-MHz square wave injected into Ch 2*	∞	15	192	N/I	Yes	Yes
Axiomatix	3.6-MHz square wave injected in Ch 2*	∞	5	192	N/I	Yes	
NASA	Lower channel SNR with recorder	6	15	192	992	Yes	Yes
Axiomatix	Lower channel SNR with recorder	4.0	5	192	960	Yes	
NASA	Lower channel SNR with recorder	4.5	15	192	992	No**	Yes
Axiomatix	Lower channel SNR with recorder	2.0	5	192	960	No**	

NOTE: N/I = not important.

*Minimum frequency that causes I-Q flips.

**Flips, then returns to 0°.

REFERENCES

1. J. K. Holmes, Coherent Spread-Spectrum Systems, Wiley Interscience, 1982.
2. Electronic Systems Test Laboratory, NASA Task 501, KSA TDRS Ground Station Medium-Rate Demod I-Q Channel-Reversal Investigation, February 1984.
3. "Ku-Band Return-Link Subcarrier Demodulator Data Reversal (I/Q Reversal)," J. E. Ratliff viewgraph presentation, Lyndon B. Johnson Space Center, March 1984.
4. "MDR I-Q Channel-Flipping Problem Status Report," Axiomatix viewgraph presentation by J.K. Holmes, G. Huth, P. Nilsen, R. Sampaio and A. Polydoros, March 15, 1984.

ADDENDUM 2

**ANALYSIS OF THE DEPLOYED ELECTRONIC ASSEMBLY
EXCITER LOOP DROP LOCK PROBLEM**

**DEPLOYED ELECTRONIC ASSEMBLY
EXCITER LOOP DROP LOCK PROBLEM**

**Prepared by
Jack K. Holmes
Gaylord Huth
Jim Dodds**

**Axiomatix
9841 Airport Blvd., Suite 912
Los Angeles, California 90045**

**Axiomatix Report No. R8410-2
May 15, 1984**

TABLE OF CONTENTS

	<u>Page</u>
LIST OF FIGURES.	i
SUMMARY	ii
1.0 PROBLEM.	1
2.0 POSSIBLE SOURCES OF THE PROBLEM.	1
3.0 SOLUTION TO THE LOSS OF LOCK PROBLEM	1
4.0 MEETINGS ATTENDED	4
5.0 ZERO BEAT DETECTOR FREQUENCIES.	4
6.0 WHAT FREQUENCIES ARE PRESENT AT THE PHASE DETECTOR.	8

LIST OF FIGURES

	<u>Page</u>
Figure 1	Exciter Functional Block Diagram 2
Figure 2	Exciter System Model 3
Figure 3	ZBD Comparator Hysteresis Design Changes 5
Figure 4	ZBD Gain/BW Design Changes 6

SUMMARY

The Deployed Electronic Assembly phase locked loop exciter drop lock problem was investigated, meetings with HAC were held, and some preliminary analysis was completed. By changing gains and adding hysteresis to the zero beat detector, the drop out and resulting resweep were eliminated. More details are contained within this report.

1.0 PROBLEM

The Deployed Electronic Assembly (DEA) provides clean signals for the transmitter TWTAs in each of the five Radar frequency channels, and for the single channel in the COMM mode of operation. In the TWTAs bypass mode of Radar operation, the exciter output is used as the transmitter signal. In addition, the exciter provides the first and second LO signals for use in the Receiver mixer downconverters.

The problem that was addressed was the intermittent loss of phase lock in the exciter with the relock requiring an additional 20 μ s (which is the time for a single sweep). The occurrence of this loss of phase lock appeared to be random with a mean time between losses of about one hour.

A block diagram model of the exciter is shown in Figure 1. When the exciter loop is locked up, the zero beat detector (ZBD) output occasionally would drop below the threshold initiating the sweep circuit. Figure 2 illustrates a system loop model for the exciter.

2.0 POSSIBLE SOURCES OF THE PROBLEM

The following reasons were suggested as a source of the problem. First, it was suggested that the noise or transients coupled onto the 156 MHz signal could cause the drop out. Secondly, the power supply noise or the transients generated external to the DEA could cause the problem. Phase noise generated internal to the exciter could be the problem source. Also, the power supply noise or transients generated within the DEA, but external to the exciter, could be the cause. Finally, too low of a threshold in the ZBD could be a basis for the problem.

3.0 SOLUTION TO THE LOSS OF LOCK PROBLEM

The proposed solution to prevent the intermittent re-sweeping is as follows:

1. Reduce the zero beat detector gain.

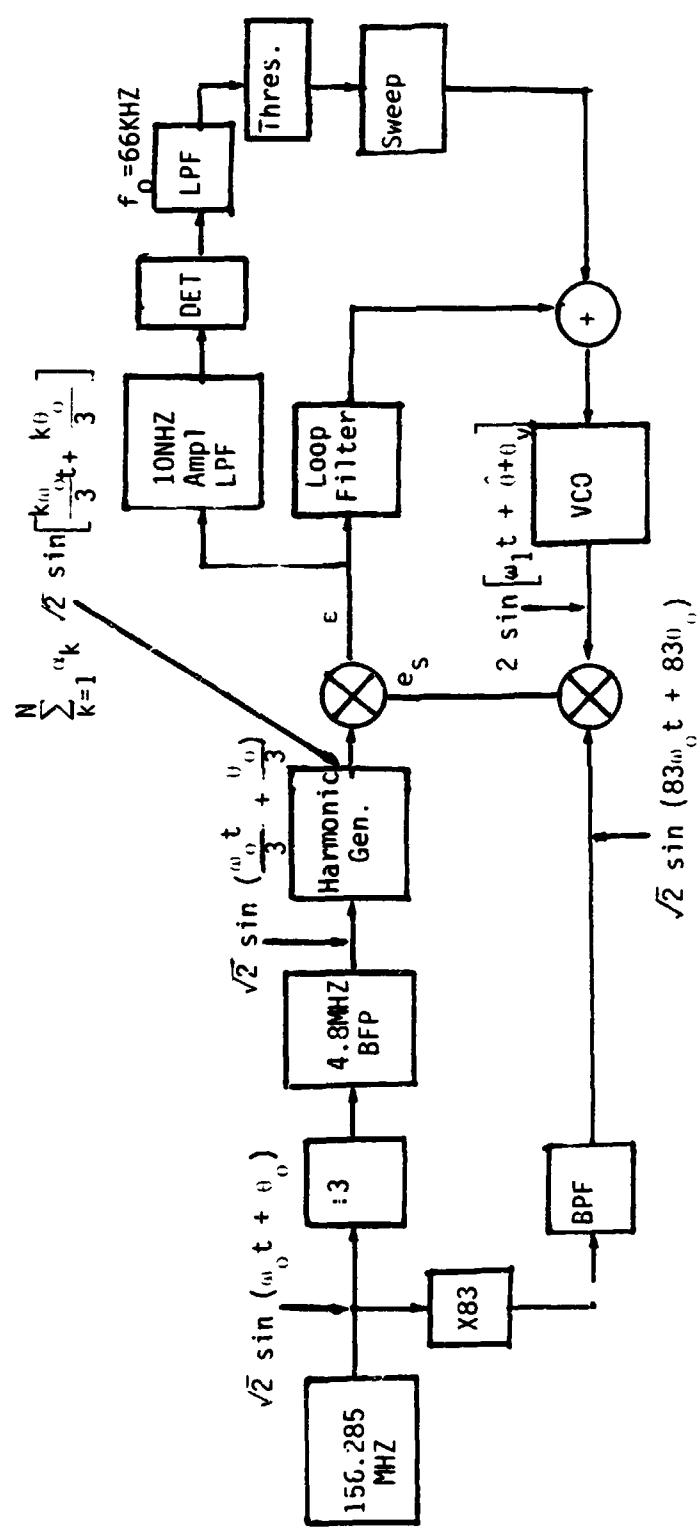


FIGURE 2: EXCITER SYSTEM MODEL

2. Increase the zero beat detector post amplifier high pass filter cutoff to 3 MHz.
3. Add hysteresis to the re-sweep comparator.

The proposed changes are illustrated in Figures 3 and 4. These combined changes stopped the occurrence of the occasional drop out and the resulting resweep.

4.0 MEETINGS ATTENDED

Axiomatix attended two meetings at Hughes Aircraft Company in building S-13, on March 16th and March 29th, 1984, to familiarize ourselves with the problem. Lance Mohler discussed the nature of the problem, and some planned tests.

We, also, attended the Ku Band MPR held at the Hacienda Hotel on April 3rd and 4th, 1984. In addition, we were in attendance at the Exciter Design Review held April 24, 1984.

Sections 5.0 and 6.0 are preliminary analyses that were completed.

5.0 ZERO BEAT DETECTOR FREQUENCIES

Consider Figure 2 for the following analysis:

We have,

$$e_s = \sqrt{2} \sqrt{2} \sin [\omega_1 t + \hat{\theta} + \theta_v] \cdot \sqrt{2} \sin [83\omega_0 t + 83 \theta_0(t)] \quad (1)$$

or neglecting the sum frequency we have,

$$e_s = \sqrt{2} \cos [(83\omega_0 t - \omega_1 t) + 83\theta_0 - \hat{\theta} - \theta_v] \quad (2)$$

so that the error signal and the signal to the ZBD is,

$$\epsilon = \sqrt{2} \cos [(83\omega_0 t - \omega_1 t) + 83\theta_0 - \hat{\theta} - \theta_v] \cdot \sum_{k=1}^N a_k \sqrt{2} \sin \left[\frac{k\omega_0}{3} t + \frac{k\theta_0}{3} \right] \quad (3)$$

k=3 common char.

which becomes,

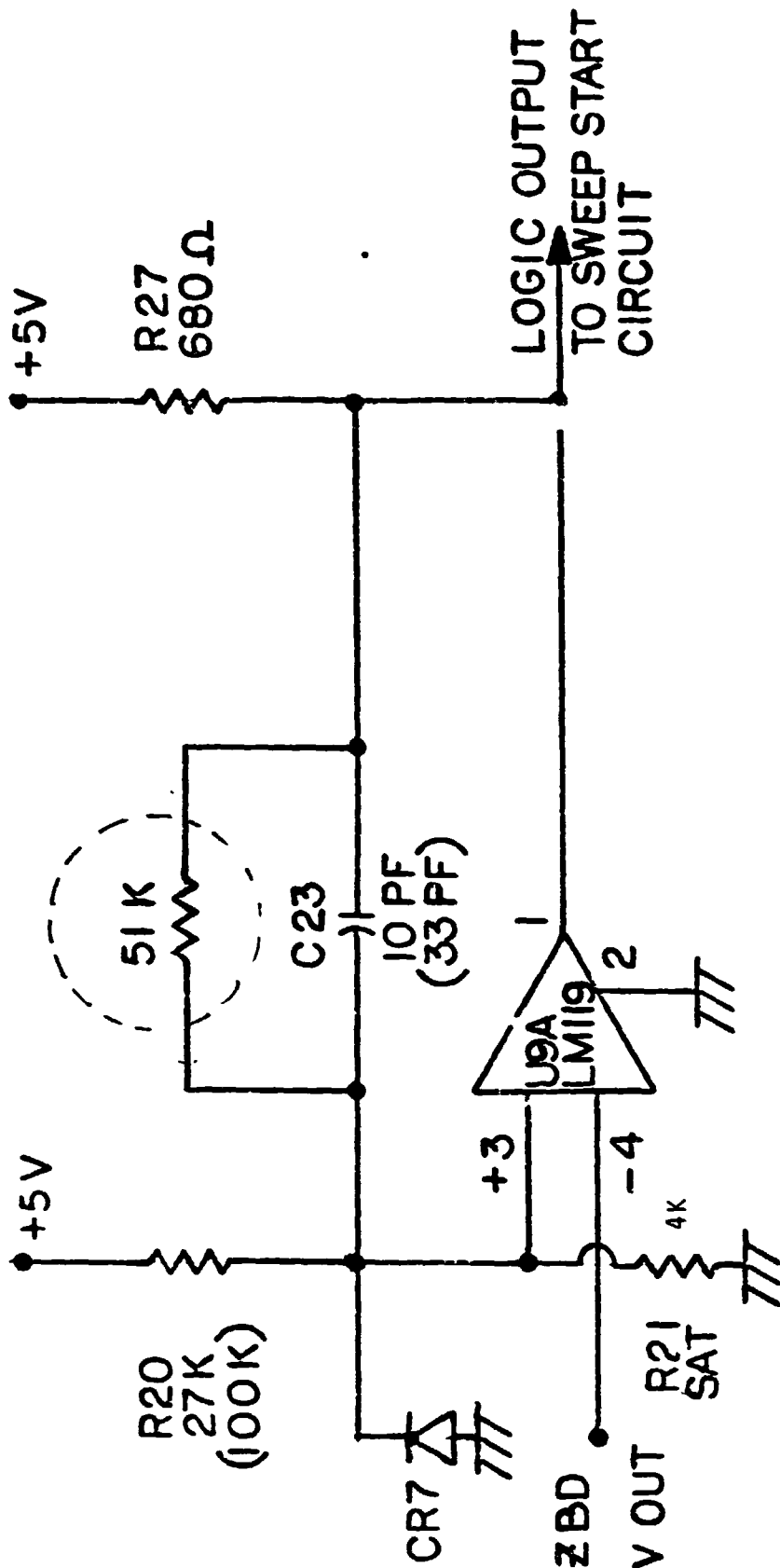


FIGURE 3:

ZBD COMPARATOR HYSTERESIS DESIGN CHANGES
 (THE RESISTOR ADDS HYSTERESIS TO THE THRESHOLD (3 CHANGES))

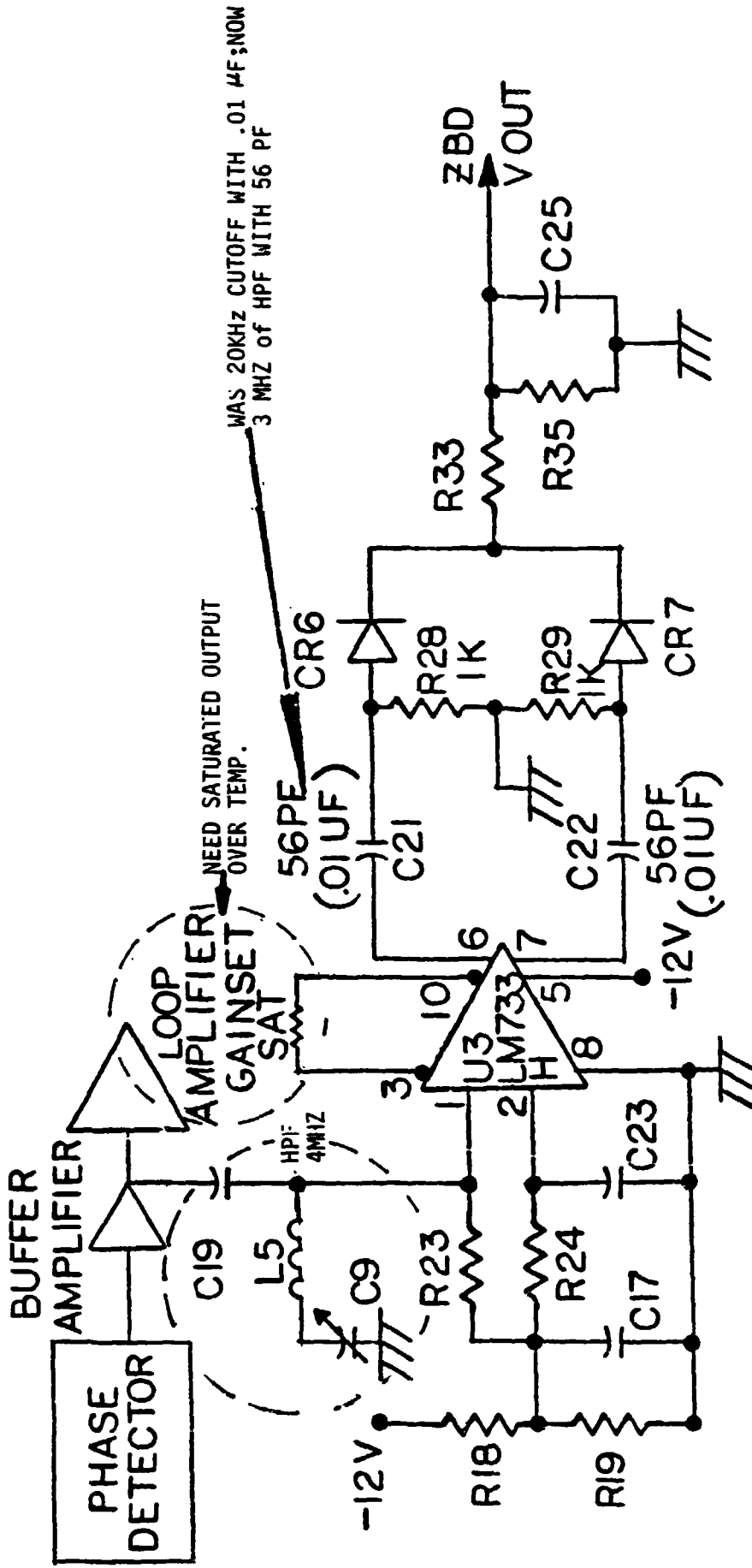


FIGURE 4:
ZBD GAIN/BW DESIGN CHANGES

(A + B)

7

$$\epsilon = \sum_{k=1}^N \alpha_k \sin \left[\frac{k\omega_o t}{3} + 83\omega_o t - \omega_1 t + 83\theta_o - \hat{\theta} - \theta_v + \frac{k\theta_o}{3} \right]$$

(A - B)

$$\sum_{k=1}^N \alpha_k \sin \left[\frac{k\omega_o t}{3} + \frac{k\theta_o}{3} - 83\omega_o t + \omega_1 t - 83\theta_o + \hat{\theta} + \theta_v \right] \quad (4)$$

and

$$(\dot{A} - \dot{B}) = \frac{k\omega_o}{3} - 83\omega_o + \omega_1 \quad (\text{neglecting } \hat{\theta}) \quad (5)$$

now

$$(\omega_1)_{\min} = 84\omega_o \Rightarrow \dot{A} - \dot{B} = \frac{k\omega_o}{3} + \omega_o$$

so that

$$\min \frac{k\omega_o}{3} + \omega_o = \frac{4}{3}\omega_o \quad (6)$$

Hence, we can neglect the $(\dot{A} - \dot{B})$, since $\frac{4}{3} \frac{\omega_o}{2\pi} \gg 100 \text{ MHz filter cutoff}$.

We, then have as the error signal,

$$\epsilon = \sum_{k=1}^N \alpha_k \sin \left[\frac{k\omega_o t}{3} + 83\omega_o t - \omega_1 t + 83\theta_o - \hat{\theta} - \theta_v + \frac{k\theta_o}{3} \right] \quad (7)$$

when lock occurs ($k_1 = 3$, or greater) so

$$\frac{k_1\omega_o}{3} + 83\omega_o - \omega_1 = 0 \quad (8)$$

or

$$\omega_1 = 83\omega_o + \frac{k_1\omega_o}{3} \quad (9)$$

Now the signal to the filter detector bank has frequency,

$$\omega_{\text{DET}} = \omega_1 - 83\omega_o \quad (10)$$

hence,

$$\omega_{\text{DET}} = \frac{k_1 \omega_0}{3} \quad (11)$$

when $k = 3$

$$\omega_{\text{DET}} = \omega_0 = 2\pi \cdot 156 \text{ MHz}$$

$$k = 4 \quad \omega_{\text{DET}} = \frac{4}{3} \omega_0 = 2\pi \cdot 208 \text{ MHz}$$

$$k = 5 \quad \omega_{\text{DET}} = \frac{5}{3} \omega_0 = 2\pi \cdot 260 \text{ MHz}$$

$$k = 6 \quad \omega_{\text{DET}} = \frac{6}{3} \omega_0 = 2\omega_0 = 2\pi \cdot 312 \text{ MHz}$$

$$k = 7 \quad \omega_{\text{DET}} = \frac{7}{3} \omega_0 = 2\pi \cdot 364 \text{ MHz} \quad (12)$$

so $k = 3$ through 7 are important.

6.0 WHAT FREQUENCIES ARE PRESENT AT THE PHASE DETECTOR?

From 7 we write,

$$\epsilon = \sum_{k=1}^N a_k \sin \left[\frac{k \omega_0}{3} t + 83 \omega_0 t - \omega_1 t + 83 \theta_0 - \hat{\theta} - \theta_v + \frac{k \omega_0}{3} \right] \quad (13)$$

$$\text{when } k_1 = 3 \text{ (CH 1 lock), we have } \omega_1 = 84 \omega_0 \quad (14)$$

so,

$$\epsilon_1 = \sum_{k=1}^N a_k \sin \left[\left(\frac{k \omega_0}{3} + 83 \omega_0 - 84 \omega_0 \right) t + 83 \theta_0 - \hat{\theta} - \theta_v + \frac{k \omega_0}{3} \right] \quad (15)$$

or,

$$\epsilon_1 = \sum_{k=1}^N a_k \sin \left[\left(\frac{k}{3} - 1 \right) \omega_0 t + 83 \theta_0 - \hat{\theta} - \theta_v + \frac{k \omega_0}{3} \right] \quad (16)$$

At lock

$$84\theta_0 - \hat{\theta} - \theta_V \approx 0 \quad (17)$$

so that

$$\epsilon_1 = \sum_{k=1}^N \alpha_k \sin \left[\left(\frac{k}{3} - 1 \right) \omega_0 t - \theta_0 + \frac{k\theta_0}{3} \right] \quad (18)$$

or

$$\begin{aligned} \epsilon_1 = & \alpha_1 \sin \left(-\frac{2}{3} \omega_0 t - \frac{2}{3} \theta_0 \right) + \alpha_2 \sin \left(-\frac{1}{3} \omega_0 t - \frac{1}{3} \theta_0 \right) \\ & + 0 + \alpha_4 \sin \left[\frac{\omega_0}{3} t + \frac{\theta_0}{3} \right] + \alpha_5 \sin \left[\frac{2\omega_0}{3} t + \frac{2\theta_0}{3} \right] \\ & + \alpha_6 \sin \left[\omega_0 t + \theta_0 \right] + \alpha_7 \sin \left[\frac{4}{3} \omega_0 t + \theta_0 \right] \end{aligned} \quad (19)$$

Hence, the following frequencies are present at the output of the phase detector in the channel 1 mode:

$$f_1 = \frac{2}{3} \cdot 156 \text{ MHz} = 104 \text{ MHz (two components combine)}$$

$$f_2 = \frac{1}{3} \cdot 156 \text{ MHz} = 52 \text{ MHz (two components combine)}$$

$$f_3 = 156 \text{ MHz}$$

$$f_4 = \frac{4}{3} \cdot 156 \text{ MHz} = 208 \text{ MHz}$$

$$f_5 = \frac{5}{3} \cdot 156 \text{ MHz} = 244 \text{ MHz}$$

$$f_6 = \frac{6}{3} \cdot 156 \text{ MHz} = 312 \text{ MHz}$$

$$f_7 = \frac{7}{3} \cdot 156 \text{ MHz} = 364 \text{ MHz} \quad (20)$$

APPENDIX A

MODEL OF THE HAC SUBCARRIER MODULATOR

By

Jack K. Holmes

May 1984

In this appendix, we discuss the Hughes Aircraft Company (HAC) implementation of the quadriphase modulator. A digital subcarrier oscillator (SCO) running at 8.5 MHz supplies a clock and its complement. Both clocks are passed through a fixed-time delay (τ) corresponding to a fixed-phase delay $2\theta_0$ in the square-wave fundamental. When not filtered, the result is a constant-envelope four-phase signal, as shown on the I-Q diagram of Figure A.1, which has an I-Q ratio of 4:1. The actual signal wave is filtered so that only the first harmonics are applied to the FM modulator.

In order to understand the power relationships of the I and Q channels, we establish the form of the filtered quadriphase signal following the work of Cager [1] in the case of no noise. The digital subcarrier phase modulator is described by

$$s(t) = \int \sin(\omega_{sc}t + \phi(t)) \quad (A-1)$$

where

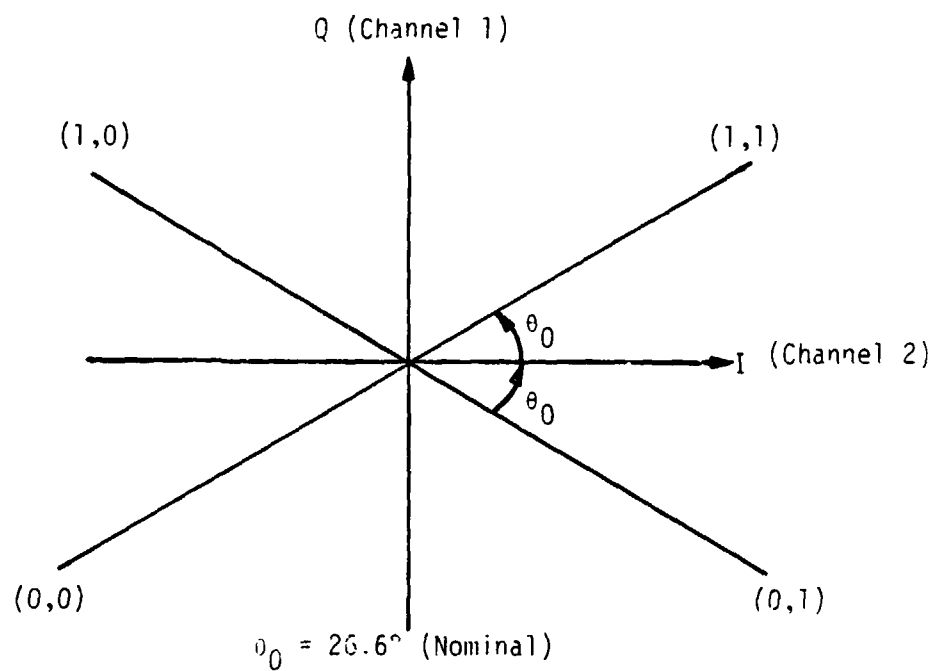
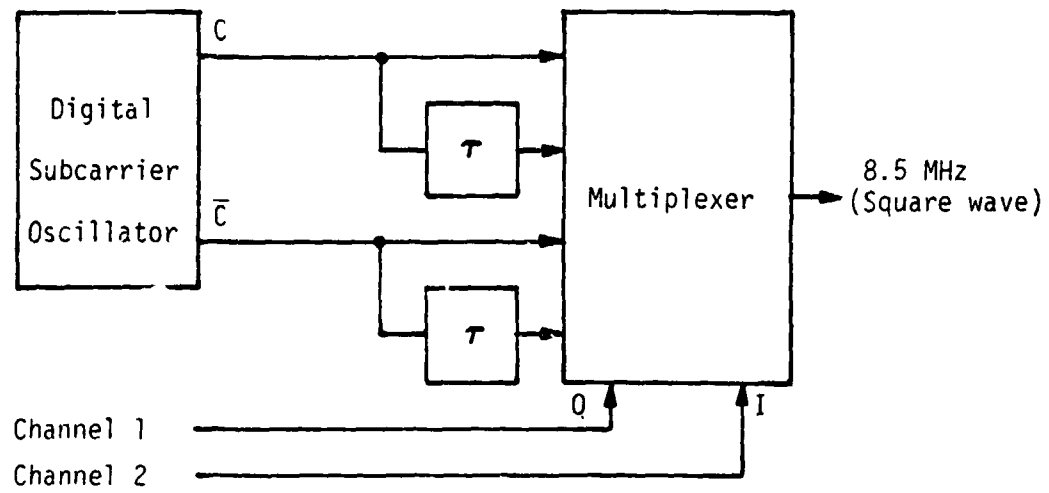
$$\phi(t) = \theta d_1(t) d_2(t) - \pi/2 (d_2(t) - 1) \quad (A-2)$$

with $d_1(t)$ the channel 1 baseband modulation and $d_2(t)$ the channel 2 baseband modulation, so that the four phases of $\phi(t)$ are described by Table A.1 below.

Table A.1. Square-Wave Oscillator Phase Relationships

$\phi(t)$	$d_1(t)$	$d_2(t)$
θ	1	1
$-\theta + \pi$	1	-1
$\theta + \pi$	-1	-1
$-\theta$	-1	1

The value of θ_0 is the value of θ such that the I and Q relationship yields a power ratio of 4:1 in the first harmonic. Expanding (A-1) in a sine-Fourier series yields



Time Delay τ \longleftrightarrow Phase Delay $2\theta_0$

Figure A.1. QPSK Subcarrier Oscillator Modulator for Mode 2 Ku-Band Return Link

$$s(t) = \sum_{n=1}^{\infty} \frac{4}{n\pi} \sin[n(\omega_{SC}t + \phi(t))] \quad (A-3)$$

where \sum denotes summation on the odd terms. Expanding (A-3) yields

$$s(t) = \sum_{n=1}^{\infty} \frac{4}{n\pi} \cos[n\phi(t)] \sin n\omega_{SC}t + \sum_{n=1}^{\infty} \frac{4}{n\pi} \sin[n\phi(t)] \cos n\omega_{SC}t \quad (A-4)$$

Using (A-2) for $\phi(t)$ yields

$$\cos[n\phi(t)] = \cos[n d_1 d_2 \theta] \cos[n(d_2-1) \pi/2] \quad (A-5)$$

and

$$\sin[n\phi(t)] = \sin[n d_1 d_2 \theta] \sin[n(d_2-1) \pi/2] \quad (A-6)$$

since $\sin[n(d_2-1) \pi/2]$ equals zero. Simplifying (A-5) and (A-6) yields

$$\cos[n\phi(t)] = d_2 \cos n\theta \quad n \text{ odd} \quad (A-7)$$

$$\sin[n\phi(t)] = d_1 \sin n\theta \quad n \text{ odd} \quad (A-8)$$

Therefore, the quadriphase signal is of the form

$$s(t) = d_2(t) \sum_{n=1}^{\infty} \frac{4}{n\pi} \cos(n\theta) \sin(n\omega_{SC}t) + d_1(t) \sum_{n=1}^{\infty} \frac{4}{n\pi} \sin(n\theta) \cos(n\omega_{SC}t) \quad (A-9)$$

Let

$$U(t) = \sum_{n=1}^{\infty} \frac{4}{n\pi} \cos n\theta \sin(n\omega_{SC}t) \quad (A-10)$$

and

$$V(t) = \sum_{n=1}^{\infty} \frac{4}{n\pi} \sin n\theta \cos(n\omega_{SC}t) \quad (A-11)$$

then

$$s(t) = d_2(t)U(t) + d_1(t)V(t) \quad (A-12)$$

To identify the waveforms expressed by (A-9), note that

$$U(t) = \sum_{n=1}^{\infty} \frac{4}{n\pi} \cos(n\theta) \sin(n\omega_{SC}t) = \frac{\int \sin(\omega_{SC}t - \theta) + \int \sin(\omega_{SC}t + \theta)}{2} \quad (A-13)$$

where $\sum \text{in}(\omega_{SC}t+\theta)$ is a hard-limited sine wave of the argument $(\omega_{SC}t+\theta)$.

Since

$$\begin{aligned} \sum \text{in}(\omega_{SC}t-\theta) + \sum \text{in}(\omega_{SC}t+\theta) &= \sum_{n=1}^{\infty} \frac{4}{n\pi} \cos(-n\theta) \sin(n\omega_{SC}t) + \sin(-n\theta) \cos(n\omega_{SC}t) \\ &\quad + \sum_{n=1}^{\infty} \frac{4}{n\pi} \cos(n\theta) \sin(n\omega_{SC}t) + \sin(n\theta) \cos(n\omega_{SC}t) \end{aligned} \quad (\text{A-14})$$

In the same manner, it can also be shown that

$$V(t) = \sum_{n=1}^{\infty} \frac{4}{n\pi} \sin n\theta \cos(n\omega_{SC}t) = \frac{\sum \text{in}(\omega_{SC}t+\theta) - \sum \text{in}(\omega_{SC}t-\theta)}{2} \quad (\text{A-15})$$

Now the right-hand sides of (A-13) and (A-15) can easily be plotted as shown in Figure A.2. Thus, we see that the digital quadriphase signal can be broken down into two orthogonal basis functions that span the space of periodic functions. Note that the sum of $U(t)$ and $V(t)$ yields a square-wave signal that is early (from $t=0$) by $2\theta/\omega_{SC}$ seconds, whereas $U(t) - V(t)$ generates a square wave with a delay of θ/ω_{SC} seconds, etc.

Note that the total power in the waveform of (A-9) is given by

$$P_S = 1/2 \sum_{n=1}^{\infty} \frac{16}{n^2\pi^2} (\cos^2(n\theta) + \sin^2(n\theta)) = \frac{8}{\pi^2} \sum_{n=1}^{\infty} \frac{1}{n^2} = 1 \quad (\text{A-16})$$

Furthermore, the power in channel 1 is given by

$$P_V = P_1 = \sum_{n=1}^{\infty} \frac{1}{2} \frac{16}{n^2\pi^2} \cos^2 n\theta = (2\theta/\pi) \quad \pi/2 \geq \theta \geq 0 \quad (\text{A-17})$$

and the power in channel 2 is given by

$$P_U = P_2 = \sum_{n=1}^{\infty} \frac{1}{2} \frac{16}{n^2\pi^2} \cos^2 n\theta = 1 - (2\theta/\pi) \quad \pi/2 \geq \theta \geq 0 \quad (\text{A-18})$$

Notice that, when $\theta = 0.464$ radians (26.58°), the power split is

$$P_1 = 0.295 \quad (\text{A-19})$$

and

$$P_2 = 0.705 \quad (\text{A-20})$$

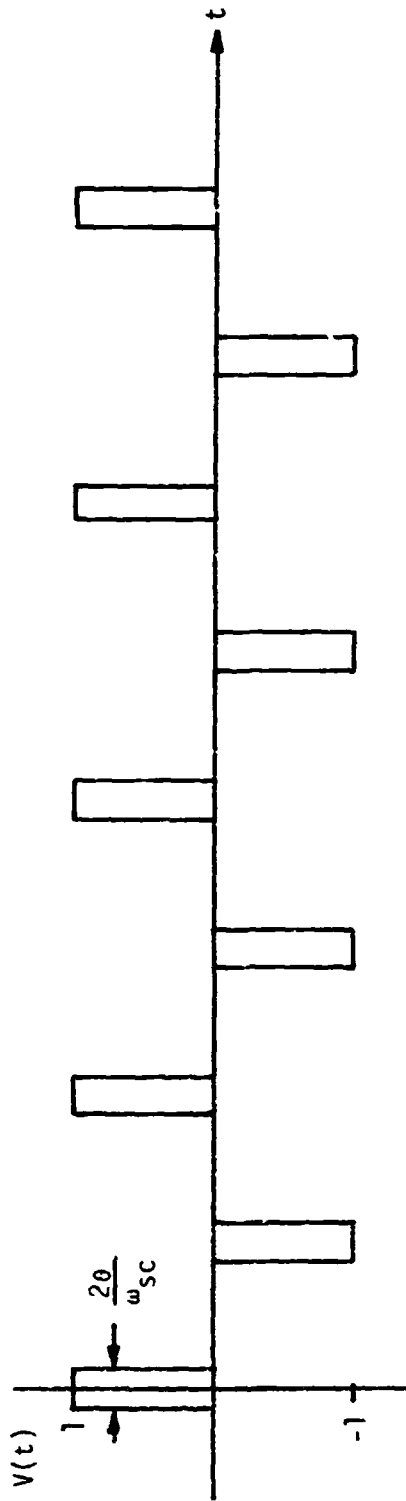
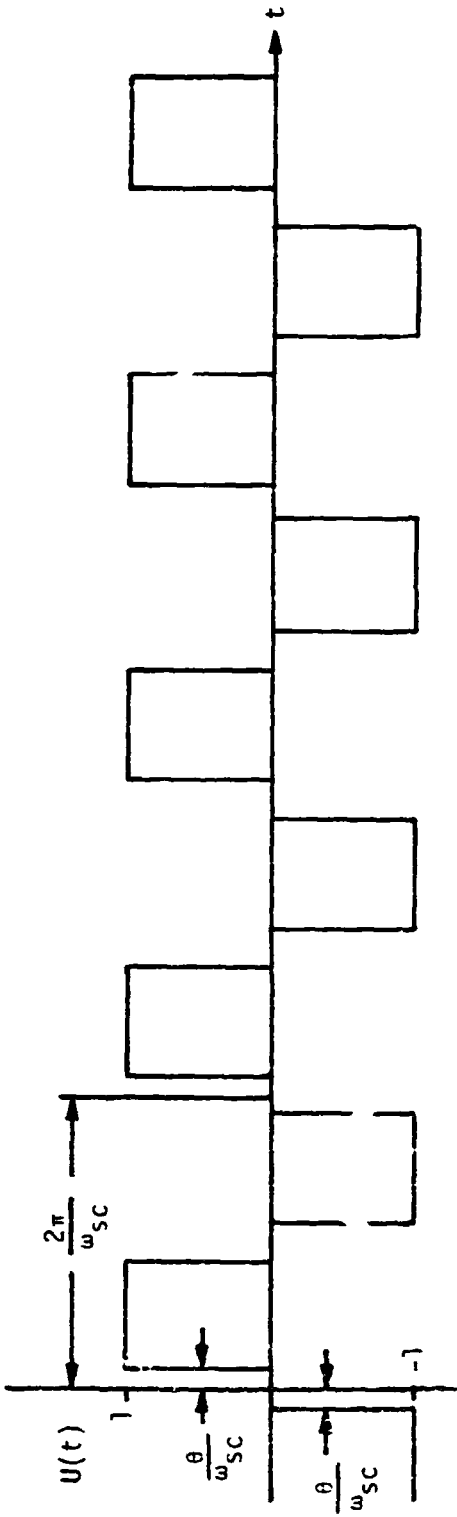


Figure A.2. Two Basis Functions for QPSK Channels 1 and 2 Signal

and P_2/P_1 is 2.38:1. However, since the BPF at the output of the MUX (quadrature modulator) passes only the fundamental, the expressions for the respective channel powers become

$$P_1 = 8/\pi^2 \sin^2\theta, \quad (\text{A-21})$$

and

$$P_2 = 8/\pi^2 \cos^2\theta \quad (\text{A-22})$$

and, for $\theta = 0.464$, we have that P_2/P_1 is 4:1, as desired.

We note from (A-9), using only the first harmonics, that the signal can be expressed as

$$s_f(t) = (4/\pi)d_1(t) \sin\theta \cos(\omega_{sc}t) + (4/\pi)d_2(t) \cos\theta \sin(\omega_{sc}t) \quad (\text{A-23})$$

where $d_1(t)$ is the output of the channel 1 limiter and $d_2(t)$ is the output of channel 2. Thus, we see that we can model the bandpass process in terms of its baseband processes.

Reference

1. R. H. Cager, "Phase-State Division Relationships in the Return-Link Baseband Modulator," Hughes IOC No. HS237-782, June 14, 1977.

APPENDIX B

LOCK-DETECTOR ANALYSIS

By

Andreas Polydoros

May, 1984

Consider the detector for the unbalanced-QPSK carrier-tracking loop, as shown in Figure B.1. Here $P_i, R_i; i=1,2$ represent the power and the data rate in the weak (1) and strong (2) channels, respectively.

Let the received waveform be

$$r(t) = \sqrt{2P_1} m_1(t) \cos(\omega_0 t + \theta) + \sqrt{2P_2} m_2(t) \sin(\omega_0 t + \theta) + n(t) \quad (B-1)$$

where $m_i(t); i=1,2$ is the baseband, ± 1 -valued data stream for each channel, $\omega_0 = 2\pi f_0$ is the carrier radian frequency, θ is the phase to be tracked and $n(t)$ is additive white Gaussian noise with the usual bandpass representation

$$n(t) = \sqrt{2} [n_c(t) \cos(\omega_0 t + \hat{\theta}) + n_s(t) \sin(\omega_0 t + \hat{\theta})] \quad (B-2)$$

In (B-2), $n_c(t), n_s(t)$ is a pair of baseband, independent, identically distributed Gaussian processes, with zero mean and flat (one-sided) power spectral density (PSD) of N_0 W/Hz. Note that the expansion of (B-2) is conveniently done around the loop (estimator) phase $\hat{\theta}$.

Upon baseband conversion (see Figure B.1), the lowpass portions (LP) of the prefiltered waveforms $e_i(t); i=1,2$ (i.e., neglecting double-frequency terms) become

$$e_1(t) \Big|_{LP} = \sqrt{P_1} m_1(t) \cos \phi + \sqrt{P_2} m_2(t) \sin \phi + n_c(t) \quad (B-3a)$$

and

$$e_2(t) \Big|_{LP} = \sqrt{P_2} m_2(t) \sin \phi - \sqrt{P_1} m_1(t) \cos \phi + n_s(t) \quad (B-3b)$$

where

$$\phi \triangleq \theta - \hat{\theta} \quad (B-4)$$

is the loop phase error, assumed to be slowly varying with respect to the data.

After lowpass filtering (LPF) by the 1.8-MHz arm filters, we get

$$\varepsilon_1(t) = \sqrt{P_1} \alpha_1 m_1(t) \cos \phi + \sqrt{P_2} \alpha_2 m_2(t) \sin \phi + \tilde{n}_c(t) \quad (B-5a)$$

and

$$\varepsilon_2(t) = \sqrt{P_2} \alpha_2 m_2(t) \cos \phi - \sqrt{P_1} \alpha_1 m_1(t) \sin \phi + \tilde{n}_s(t) \quad (B-5b)$$

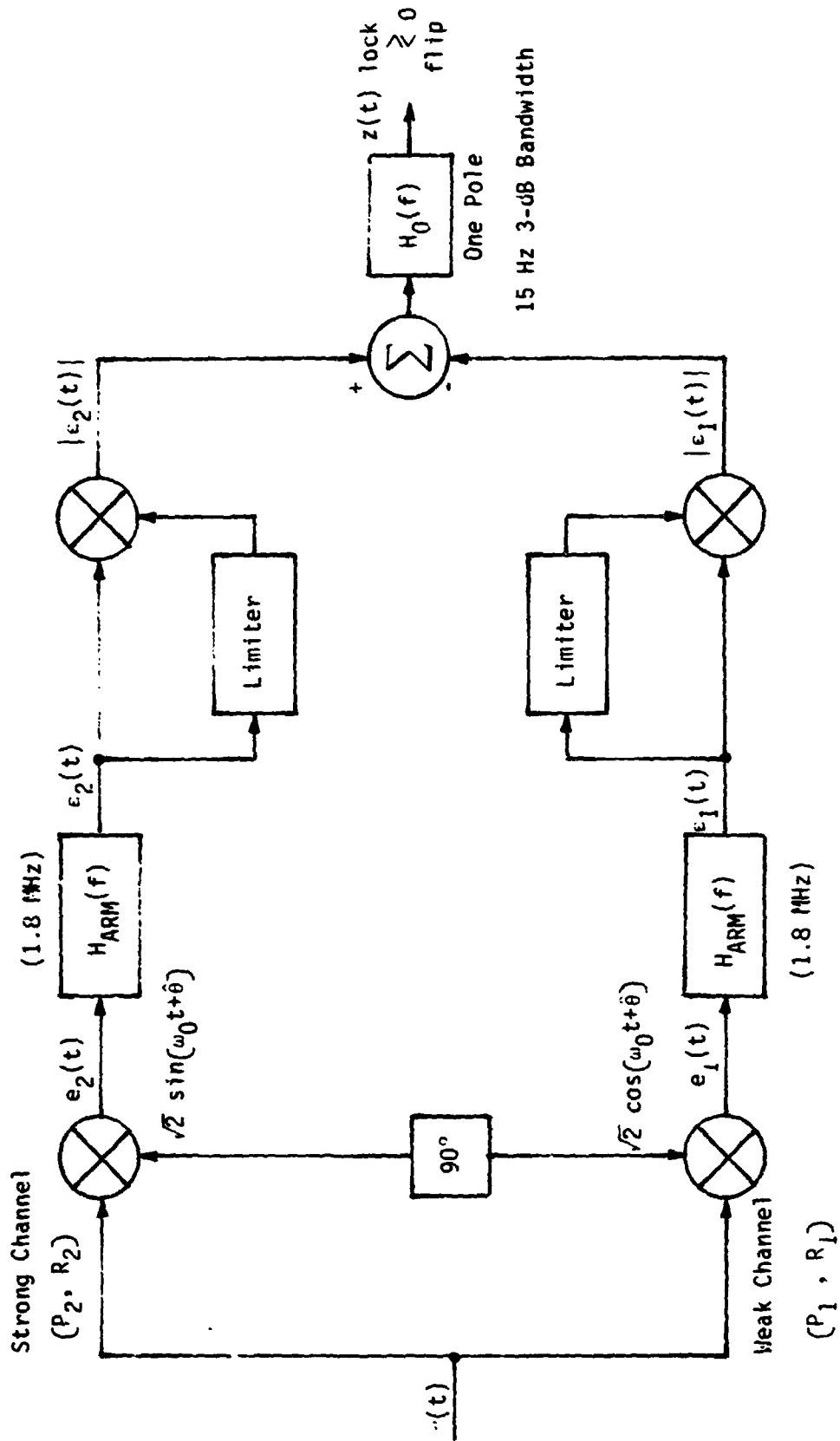


Figure B.1. Unbalanced QPSK Loop Lock Detector

where $n_i(t); i=1,2$ represents the filtered noise in each arm and

$$\alpha_i^2 = \int_{-\infty}^{\infty} |H_{ARM}(f)|^2 S_{m_i}(f) df \quad (B-6)$$

is the power-reduction coefficient for the i th data stream due to filtering (here, $S_{m_i}(f)$ represents the i th data stream PSD). Note that the effect of filtering is accounted for by a reduction in power, but not pulse-shape distortion. This is a reasonable assumption since the arm filter bandwidth (1.8 MHz) is approximately twice the data rate of the strong channel ($R_2 = 0.96$ Mbits/s), which is Manchester encoded. Thus, the pulse distortion which results from filtering is insignificant.

The waveforms $\epsilon_i(t)$ then go through an envelope detector, whose output is $|\epsilon_i(t)|$, prior to subtraction. Since the signal-to-noise ratio (SNR) in each waveform is sufficiently large, the envelope detectors can be approximated by square-law detectors, as shown in Figure B.2, whose analysis is much more tractable. Such a substitution should have a negligible effect on the overall conclusions.

Within this approximation, the inputs to the subtractor are

$$\begin{aligned} \epsilon_1^2(t) &= \alpha_1^2 P_1 \cos^2 \phi + \alpha_2^2 P_2 \sin^2 \phi + \tilde{n}_c^2(t) \\ &+ 2 \sqrt{P_1} \alpha_1 m_1(t) \tilde{n}_c(t) \cos \phi + 2 \sqrt{P_2} \alpha_2 m_2(t) \tilde{n}_c(t) \sin \phi \\ &+ (1/2) \sqrt{P_1 P_2} \alpha_1 \alpha_2 m_1(t) m_2(t) \sin 2\phi \end{aligned} \quad (B-7a)$$

and

$$\begin{aligned} \epsilon_2^2(t) &= \alpha_2^2 P_2 \cos^2 \phi + \alpha_1^2 P_1 \sin^2 \phi + \tilde{n}_s^2(t) \\ &+ 2 \sqrt{P_2} \alpha_2 m_2(t) \tilde{n}_s(t) \cos \phi - 2 \sqrt{P_1} \alpha_1 m_1(t) \tilde{n}_s(t) \sin \phi \\ &- (1/2) \sqrt{P_1 P_2} \alpha_1 \alpha_2 m_1(t) m_2(t) \sin 2\phi \end{aligned} \quad (B-7b)$$

Each of the above quantities can be divided into a mean value μ_i and a remainder noise $\eta_i(t)$, i.e.,

$$\epsilon_i^2 = \mu_i + \eta_i(t) \quad (B-8)$$

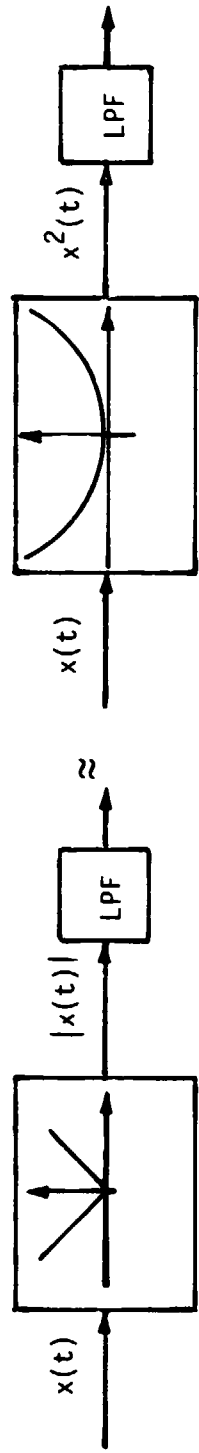


Figure B.2. Substituting an Envelope Detector with a Square-Law Detector in the Analysis

where

$$\mu_1 = \alpha_1^2 P_1 \cos^2 \phi + \alpha_2^2 P_2 \sin^2 \phi + \mathcal{E} \left\{ \tilde{n}_c^2(t) \right\} \quad (\text{B-9a})$$

$$\mu_2 = \alpha_2^2 P_2 \cos^2 \phi + \alpha_1^2 P_1 \sin^2 \phi + \mathcal{E} \left\{ \tilde{n}_s^2(t) \right\} \quad (\text{B-9b})$$

and

$$\begin{aligned} \eta_1(t) = & \left(\tilde{n}_c^2(t) - \mathcal{E} \left\{ \tilde{n}_c^2(t) \right\} \right) + 2 \sqrt{P_1} \alpha_1 m_1(t) n_c(t) \cos \phi \\ & + 2 \sqrt{P_2} \alpha_2 m_2(t) \tilde{n}_c(t) \sin \phi \\ & + (1/2) \sqrt{P_1 P_2} \alpha_1 \alpha_2 m_1(t) m_2(t) \sin 2\phi \end{aligned} \quad (\text{B-10a})$$

$$\begin{aligned} \eta_2(t) = & \left(\tilde{n}_s^2(t) - \mathcal{E} \left\{ \tilde{n}_s^2(t) \right\} \right) + 2 \sqrt{P_2} \alpha_2 m_2(t) \tilde{n}_s(t) \cos \phi \\ & - 2 \sqrt{P_1} \alpha_1 m_1(t) \tilde{n}_s(t) \sin \phi \\ & - (1/2) \sqrt{P_1 P_2} \alpha_1 \alpha_2 m_1(t) m_2(t) \sin 2\phi \end{aligned} \quad (\text{B-10b})$$

Although the exact statistical nature of $\eta_1(t)$ and $\eta_2(t)$ is complicated, certain facts can be assessed, particularly in connection with the bandwidth of the output filter $H_0(f)$ (see Figure B.1). This is a one-pole RC filter with cut-off frequency $f_c = 15$ Hz and transfer function

$$H_0(f) = \frac{1}{1 + j(f/f_c)} \quad (\text{B-11})$$

Since the 3-dB bandwidth of 75 Hz is much smaller than that of each noise term in (B-10), $\eta_1(t)$ is essentially "white" with respect to $H_0(f)$. Furthermore, by a central-limit argument on the integration effects of $H_0(f)$, its output $z(t)$ is approximately Gaussian. Thus, we may model the input noises $\eta_1(t)$ as zero-mean Gaussian processes, each with a constant PSD equal to N_i W/Hz, to be evaluated below.

Further, it can easily be shown that each term constituting the noise $\eta_1(t)$ (and similarly for $\eta_2(t)$) is statistically uncorrelated from the others. Except for the very last term in (B-10a) and (B-10b), which is identical, the same is true between any one component of $\eta_1(t)$ and any other of $\eta_2(t)$. Since the contribution of the last term is small compared to the rest, we conclude that $\eta_1(t)$ and $\eta_2(t)$ are approximately uncorrelated. Furthermore, the total PSD N_i equals the sum of the PSD's of the individual components.

The final output $z(t)$ is the difference

$$z(t) = z_2(t) - z_1(t) \quad (\text{B-12})$$

where $z_i(t); i=1,2$ is the output of H_0 due to $\epsilon_i^2(t)$. Within the Gaussian assumption, performance is uniquely determined by the mean and variance of $z(t)$.

- Mean of $z(t)$

We have that

$$\{z(t)\} = \{z_2(t)\} - \{z_1(t)\} = H_0(0) \left[\mathcal{E}\{\epsilon_2^2(t)\} - \mathcal{E}\{\epsilon_1^2(t)\} \right]$$

or

$$\mathcal{E}\{z(t)\} = \mu_z = \mu_2 - \mu_1 \quad (\text{B-13})$$

since $H_0(0) = 1$ (see (B-11)). But

$$\mathcal{E}\{n_c^2(t)\} = \mathcal{E}\{n_s^2(t)\} = \left(\frac{N_0}{2}\right) \int_{-\infty}^{\infty} |H_{ARM}(f)|^2 df \quad (\text{B-14})$$

Therefore, from (B-9), (B-13) and (B-14), we have that

$$\mu_z = \left(\alpha_2 P_2 - \alpha_1 P_1\right) \cos^2 \phi + \left(\alpha_1 P_1 - \alpha_2 P_2\right) \sin^2 \phi \quad (\text{B-15})$$

- Variance of $z(t)$

From (B-8) and (B-12), it follows that

$$\text{var}\{z(t)\} \triangleq \sigma_z^2 = \int_{-\infty}^{\infty} |H_0(f)|^2 S(f) df \quad (\text{B-16})$$

where $S(f)$ is the PSD of the difference $n_2(t) - n_1(t)$. However, due to the wideband nature of this difference (see previous discussion), it follows that

$$\sigma_z^2 = S(0) \int_{-\infty}^{\infty} |H_0(f)|^2 df \quad (\text{B-17})$$

From the functional expression of $H_0(f)$ in (B-11), it is easily shown that (B-17) reduces to

$$\sigma_z^2 = S(0) \cdot (\pi f_c) \eta_2^{-\eta_1} \quad (\text{B-18})$$

In order to derive the value of $S(f)$ at the original $f = 0$, we write the difference $\eta_2(t) - \eta_1(t)$ as

$$\eta_2(t) - \eta_1(t) = n_1(t) 2 \cos \phi \cdot n_2(t) - 2 \sin \phi \cdot n_3(t) - \sin 2\phi \cdot n_4(t) \quad (\text{B-19})$$

where the (uncorrelated) noises $n_i(t); i=1,2,3,4$ are given by

$$n_1(t) = \tilde{n}_s^2(t) - \mathcal{E}\{\tilde{n}_s^2(t)\} + \tilde{n}_c^2(t) - \mathcal{E}\{\tilde{n}_c^2(t)\} \quad (\text{B-20a})$$

$$n_2(t) = \alpha_2 \sqrt{P_2} m_2(t) \tilde{n}_s(t) - \alpha_1 \sqrt{P_1} m_1(t) \tilde{n}_3(t) \quad (\text{B-20b})$$

$$n_3(t) = \alpha_1 \sqrt{P_1} m_1(t) \tilde{n}_s(t) + \alpha_2 \sqrt{P_2} m_2(t) \tilde{n}_c(t) \quad (\text{B-20c})$$

$$n_4(t) = \alpha_1 \alpha_2 \sqrt{P_1 P_2} m_1(t) m_2(t) \quad (\text{B-20d})$$

Then, if we denote by $S_i(0)$ the PSD at $f=0$ of $n_i(t)$, we conclude from (B-18) and (B-19) that

$$\sigma_z^2 = (\pi f_c) [S_1(0) + 4 \cos^2 \phi S_2(0) + 4 \sin^2 \phi S_3(0) + \sin^2 2\phi S_4(0)] \quad (\text{B-21})$$

However, by inspecting the noises $n_2(t)$ and $n_3(t)$ in (B-20a) and (B-20c) and realizing the existing symmetry (substitute n_c for n_s and disregard the sign change, as it does not affect the PSD), we immediately conclude that

$$S_2(f) = S_3(f) \quad (\text{B-22})$$

in which case, (B-21) simplifies to

$$\sigma_z^2 = (\pi f_c) [S_1(0) + 4 S_2(0) + \sin^2 2\phi S_4(0)] \quad (\text{B-23})$$

since $\cos^2 \phi + \sin^2 \phi = 1$. The individual forms in (B-23) are now evaluated.

Let $R_{\tilde{s}}(\tau)$ and $R_{\tilde{c}}(\tau)$ indicate the autocorrelation functions of the squared filtered noises $\tilde{n}_s^2(t)$ and $\tilde{n}_c^2(t)$, while $R_{\tilde{s}}(\tau)$ and $R_{\tilde{c}}(\tau)$ correspond to $\tilde{n}_s(t)$ and $\tilde{n}_c(t)$ (not squared). Because of the statistical symmetry between $n_s(t)$ and $n_c(t)$

$$R_{\tilde{s}}(\tau) = R_{\tilde{c}}(\tau); R_{\tilde{s}}(\tau) = R_{\tilde{c}}(\tau) \quad (\text{B-24})$$

But, from (B-20a),

$$S_1(0) = \int_{-\infty}^{\infty} \left(R_{\tilde{c}}^2(\tau) + R_{\tilde{s}}^2(\tau) \right) d\tau = 2 \int_{-\infty}^{\infty} R_{\tilde{s}}^2(\tau) d\tau \quad (\text{B-25})$$

where

$$\begin{aligned} R_{\tilde{s}}^2(\tau) &= \mathcal{E} \left\{ \left(\tilde{n}_s^2(t+\tau) - \mathcal{E} \{ \tilde{n}_s^2(t+\tau) \} \right) \left(\tilde{n}_s^2(t) - \mathcal{E} \{ \tilde{n}_s^2(t) \} \right) \right\} \\ &= \mathcal{E} \left\{ \tilde{n}_s^2(t+\tau) \tilde{n}_s^2(t) \right\} - \mathcal{E}^2 \left\{ \tilde{n}_s^2(t) \right\} \\ &= \mathcal{E} \left\{ \tilde{n}_s^2(t) \right\} + 2 \mathcal{E}^2 \left\{ \tilde{n}_s(t+\tau) \tilde{n}_s(t) \right\} - \mathcal{E}^2 \left\{ \tilde{n}_s^2(t) \right\} \\ &= 2 R_{\tilde{s}}^2(\tau) \end{aligned} \quad (\text{B-26})$$

In deriving (B-26), the familiar identity

$$\mathcal{E} \left\{ \prod_{i=1}^4 X_i \right\} = \mathcal{E} \{ X_1 X_2 \} \mathcal{E} \{ X_3 X_4 \} + \mathcal{E} \{ X_1 X_3 \} \mathcal{E} \{ X_2 X_4 \} + \mathcal{E} \{ X_1 X_4 \} \mathcal{E} \{ X_2 X_3 \}$$

for jointly Gaussian random variables has been used. Thus, from (B-25) and (B-26) and by using Parseval's theorem,

$$S_1(0) = 4 \int_{-\infty}^{\infty} R_{\tilde{s}}^2(\tau) d\tau = 4 \int_{-\infty}^{\infty} |S_{\tilde{n}_s}(f)|^2 df = 4 \int_{-\infty}^{\infty} \left(\frac{N_0}{2} \right)^2 |H_{\text{ARM}}(f)|^4 df$$

or

$$S_1(0) = N_0^2 \int_{-\infty}^{\infty} |H_{\text{ARM}}(f)|^4 df \quad (\text{B-27})$$

Proceeding in a similar manner, we get

$$\begin{aligned} S_2(0) &= \alpha_2 P_2 \int_{-\infty}^{\infty} R_{m_2}(\tau) R_{\tilde{s}}(\tau) d\tau + \alpha_1 P_1 \int_{-\infty}^{\infty} R_{m_1}(\tau) R_{\tilde{c}}(\tau) d\tau \\ &= \alpha_2 P_2 \left(\frac{N_0}{2} \right) \int_{-\infty}^{\infty} S_{m_2}(f) |H_{\text{ARM}}(f)|^2 df \\ &\quad + \alpha_1 P_1 \left(\frac{N_0}{2} \right) \int_{-\infty}^{\infty} S_{m_1}(f) |H_{\text{ARM}}(f)|^2 df \end{aligned}$$

or

$$S_2(0) = \left(\frac{N_0}{2} \right) \left[\alpha_2 P_2 + \alpha_1 P_1 \right] \quad (\text{B-28})$$

where the definition for α_j^2 in (B-6) has been used. Finally,

$$S_{4}(0) = \alpha_1^2 \alpha_2^2 P_1 P_2 \int_{-\infty}^{\infty} S_{m_1}(f) S_{m_2}(f) df \quad (\text{B-29})$$

To recapitulate our findings, let us define

$$C_1 \triangleq \alpha_1^2 = \int_{-\infty}^{\infty} S_{m_1}(f) |H_{ARM}(f)|^2 df \quad (\text{B-30a})$$

$$C_2 \triangleq \alpha_2^2 = \int_{-\infty}^{\infty} S_{m_2}(f) |H_{ARM}(f)|^2 df \quad (\text{B-30b})$$

$$C_3 \triangleq \int_{-\infty}^{\infty} |H_{ARM}(f)|^4 df \quad (\text{B-30c})$$

$$C_4 \triangleq \int_{-\infty}^{\infty} S_{m_1}(f) S_{m_2}(f) df \quad (\text{B-30d})$$

Then, from (B-15) and (B-30),

$$\mu_z = (C_2 P_2 - C_1 P_1) (\cos^2 \phi - \sin^2 \phi)$$

or

$$\mu_z = (C_2 P_2 - C_1 P_1) \cos 2\phi \quad (\text{B-31})$$

and, from (B-23) and (B-27) through (B-30),

$$\text{var}\{z\} = (\pi f_c)^2 N_0^2 \left[C_3 + 2C_1 \left(\frac{P_1}{N_0} \right) + 2C_2 \left(\frac{P_2}{N_0} \right) + \sin^2 2\phi C_1 C_2 C_4 \left(\frac{P_1}{N_0} \right) \left(\frac{P_2}{N_0} \right) \right] \quad (\text{B-32})$$

Note from (B-32) that the last term vanishes for $\phi=0$ (locked-on condition) or $\phi = \pi/2$ (flip condition).

The output signal-to-noise ratio, SNR_0 , is defined as

$$\text{SNR}_0 = \frac{\mu_z^2}{\text{var}(z)} \quad (\text{B-33})$$

From (B-31) through (B-33), we obtain

$$\text{SNR}_0 = \left(\frac{1}{\pi f_c} \right) \cos^2 2\phi \cdot \frac{\left[C_2 \left(\frac{P_2}{N_0} \right) - C_1 \left(\frac{P_1}{N_0} \right) \right]^2}{\left[C_3 + 2C_1^2 \left(\frac{P_1}{N_0} \right) + 2C_2^2 \left(\frac{P_2}{N_0} \right) + \sin^2 2\phi C_1 C_2 C_4 \left(\frac{P_1}{N_0} \right) \left(\frac{P_2}{N_0} \right) \right]}$$

which, for $\phi = 0$ (correct lock) or $\phi = \pi/2$ (flip), simplifies to

$$\text{SNR}_0 = \left(\frac{1}{\pi f_c} \right) \frac{\left[C_2 \left(\frac{P_2}{N_0} \right) - C_1 \left(\frac{P_1}{N_0} \right) \right]^2}{\left[C_3 + 2C_1^2 \left(\frac{P_1}{N_0} \right) + 2C_2^2 \left(\frac{P_2}{N_0} \right) \right]} \quad (\text{B-34})$$

It should be pointed out that μ_2 changes sign (see (B-31)) when ϕ goes from 0 to $\pi/2$ rad, provided that

$$\frac{P_2}{P_1} > \frac{C_1}{C_2}$$

This latter condition is satisfied in the UQPSK design since

$$\frac{P_2}{P_1} = 4 \quad \text{and} \quad \frac{C_1}{C_2} = 1$$

Therefore, the mean of the Gaussian distribution for $z(t)$ is positive in the correct lock condition and negative in the flip condition, as it should be (see threshold comparison in Figure B.1).

Let $(1 - P_e)$ indicate the probability that a sample of $z(t)$ at any $t = t_0$ will be positive, assuming the correct lock condition. In other words, $(1 - P_e)$ is the probability of correct indication conditioned on the correct lock. Due to the symmetry of expressions (B-31) and (B-32), $(1 - P_e)$ is also equal to the probability of a correct (negative) indication, given a flip. Thus, in both circumstances, P_e stands for the probability of an erroneous indication. Because of the Gaussian assumption,

$$P_e = Q \left[\sqrt{\text{SNR}_0} \right] \quad (\text{B-35})$$

where

$$Q(x) = \frac{1}{\sqrt{2\pi}} \int_x^{\infty} e^{-z^2/2} dz \quad (\text{B-36})$$

Now suppose that N samples are taken and each is T_s seconds apart. We assume that T_s is sufficiently large (few time constants of $H_0(f)$, i.e., 2 - 3 multiples of $1/15$ s) to render the successive samples statistically independent. Then the probability that all N samples indicate correctly is

$$\text{Pr}[\text{correct indication in } NT_s \text{ seconds}] = 1 - Q \left[\sqrt{\text{SNR}_0} \right]^N = 1 - NQ \left[\sqrt{\text{SNR}_0} \right] \quad (\text{B-37})$$

where it is assumed that $NP_e \ll 1$ (justified numerically below). Thus,

$$\text{Pr}[\text{false indication in } NT_s \text{ seconds}] = NQ \left[\sqrt{\text{SNR}_0} \right] \quad (\text{B-38})$$

For this latter probability to be considered appreciable, we set

$$NQ \left[\sqrt{\text{SNR}_0} \right] = 0.1 \quad (\text{B-39})$$

Therefore, the number of samples N (or, equivalently, the length of time NT_s) required to reach such a level of probability can be specified from (B-39) once SNR_0 is known for a particular system. Equation (B-24) can be rewritten in terms of the following parameters:

$$\frac{E_{b2}}{N_0} = \text{bit SNR in channel 2} = \frac{P_2 T_2}{N_0} = \frac{P_2}{N_0 R_2} \quad (\text{B-40a})$$

$$\rho \triangleq \frac{P_2}{P_1} = \text{power ratio} \quad (\text{B-40b})$$

$$g_c \triangleq \frac{f_c}{R_2} \quad (\text{B-40c})$$

$$g_{\text{ARM}} \triangleq \frac{f_{\text{ARM},C}}{R_2} \quad (\text{B-40d})$$

where we assume that the arm filters are identical, one-pole, with a 3-dB cut-off frequency of $f_{ARM,C}$ Hz. Then,

$$SNR_0 = \frac{\left(\frac{E_{b2}}{N_0}\right)^2 \left(C_2 - \frac{C_1}{\rho}\right)^2}{(\pi g_c) \left[2 \left(\frac{E_{b2}}{N_0}\right) \left(C_2 + \frac{C_1}{\rho}\right) + (\pi/2) g_{ARM} \right]} \quad (B-41)$$

For the particular system at hand, $f_c = 15$ Hz, $f_{ARM,C} = 1.8$ MHz, $R_1 = 192$ kbits/s and $R_2 = 0.96$ Mbits/s so that $\rho = 4$, $C_1 = 1$, $C_2 = 0.75$ (from tables), $g_c = 15.625 \times 10^{-6}$ and $g_{ARM} = 1.88$.

Table B.1 provides the values of SNR_0 from (A-41), where the above numbers have been used. The parameter (E_{b2}/N_0) was ranged from 2 dB to 10 dB for both $\rho = 4$ and $\rho = 2$. It is clear that, in all cases, SNR_0 is extremely high, thus assuring correct operation of the lock detector for practically an indefinite interval (hundreds of years!).

In conclusion, this analysis has shown the lock detector herein to be a most reliable component in both the correct-lock and the phase-flip conditions.

Table B.1. Values of SNR_0 as a Function of E_{b2}/N_0 ,
For Two Values of the Power Ratio ρ

E_{b2}/N_0 (dB)	10	8	6	4	2
SNR_0 (dB) $\rho = 4$	44.2	41.9	39.3	36.6	33.6
SNR_0 (dB) $\rho = 2$	37.2	34.9	32.4	29.8	27.0

APPENDIX C

S-CURVE OF A MODIFIED FOUR-PHASE COSTAS LOOP
FOR A PARTICULAR QUADRATURE SIGNAL INPUT

By

Raimundo Sampaio

In this appendix, we derive the tracking characteristic (S-curve) for a modified four-phase Costas loop when the input signal is of the following form: the inphase component is biphas modulated and the quadrature component is sine-wave modulated. The presence of thermal noise is not considered in this analysis.

The received signal $s(t)$ is of the form

$$s(t) = \sqrt{2} A_1 m_1(t) \cos(\omega_0 t + \theta) + \sqrt{2} A_2 m_2(t) \sin(\omega_0 t + \theta) \quad (C-1)$$

where $m_1(t)$ is a (± 1) binary data modulation,

$$m_2(t) = \sin(\omega_s t + \zeta)$$

is a sinusoidal modulation with radian frequency ω_s and arbitrary phase parameter ζ , and ω_0 and θ are the radian frequency and phase of the inphase and quadrature components of $s(t)$.

According to Figure C.1 herein, the received signal is cross correlated simultaneously with the inphase and quadrature versions of the VCO output reference signal

$$r(t) = \sqrt{2} \cos(\omega_0 t + \hat{\theta})$$

where $\hat{\theta}(t)$ is the instantaneous loop estimate of the unknown phase θ .

Assuming that θ and $\hat{\theta}$ are slow-varying quantities and that the lowpass arm filters reject double-frequency components, their outputs $\epsilon_1(t)$ and $\epsilon_2(t)$ can be written as

$$\epsilon_1(t) = A_1 m_{1F}(t) \cos(\theta - \hat{\theta}) + A_2 m_{2F}(t) \sin(\theta - \hat{\theta}) \quad (C-2a)$$

and

$$\epsilon_2(t) = A_2 m_{2F}(t) \cos(\theta - \hat{\theta}) - A_1 m_{1F}(t) \sin(\theta - \hat{\theta}) \quad (C-2b)$$

where m_{1F} and m_{2F} are the filtered versions of $m_1(t)$ and $m_2(t)$, respectively. If we consider as negligible the data distortion introduced by arm filtering of $m_1(t)$, we have

$$m_{1F}(t) = \sqrt{\alpha_1} m_1(t) \quad ; \quad m_{2F}(t) = \sqrt{\alpha_2} \sin(\omega_s t + \theta_s)$$

where

$$\alpha_1 = \int_{-\infty}^{+\infty} |L(f)|^2 S_{m_1}(f) df \quad (\text{assume } |L(0)| = 1) \quad (C-3)$$

and

$$\alpha_2 = |L(f_s)|^2 \quad (C-4)$$

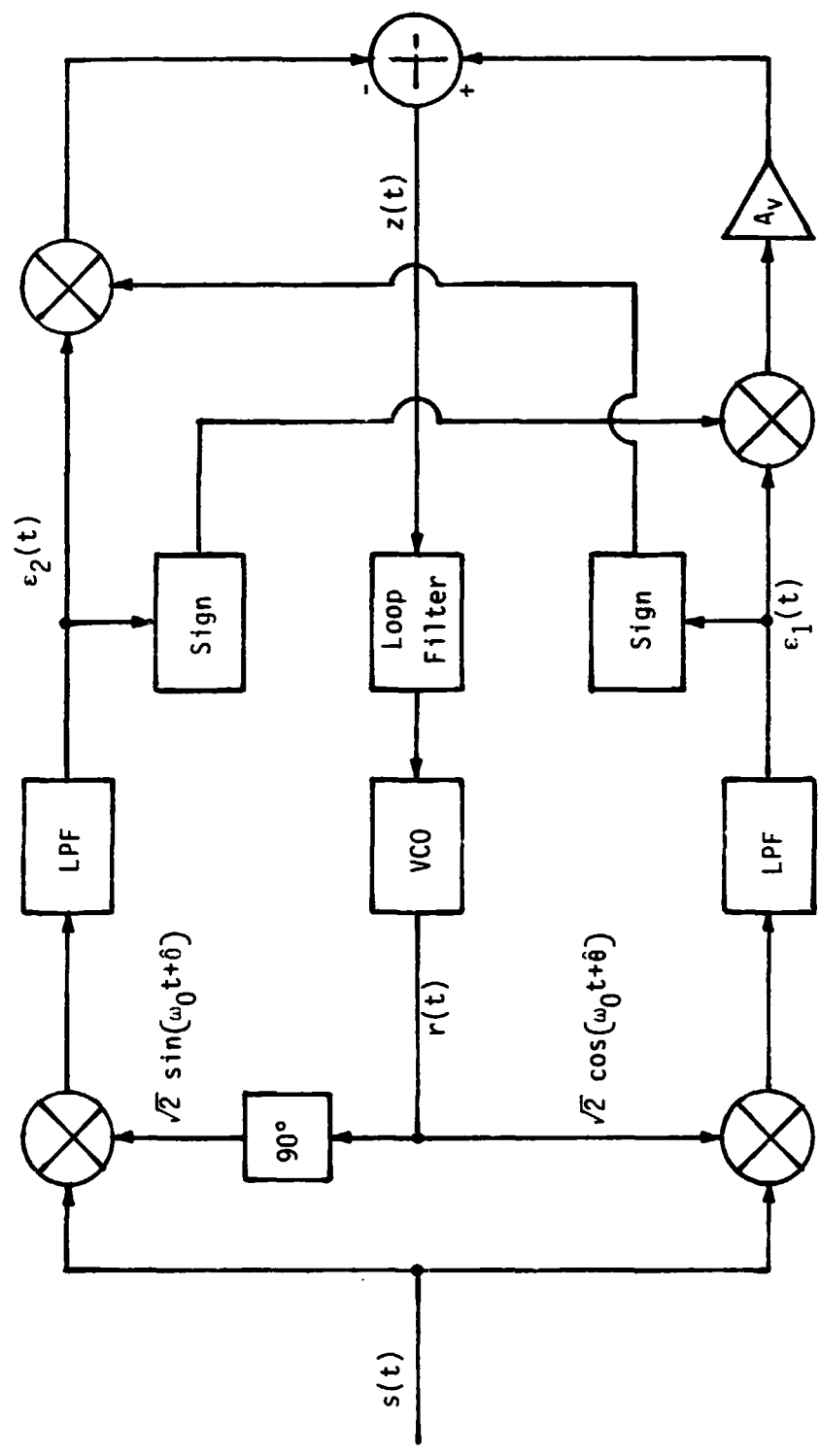


Figure C.1. Block Diagram of a Modified Four-Phase Costas Loop

are the power losses introduced by an arm filter with frequency characteristic $L(f)$.

If we let $\phi = \theta - \hat{\theta}$ represent the loop phase-tracking error, then (C-2) can be rewritten as

$$\epsilon_1(t) = A_1 \sqrt{\alpha_1} m_1(t) \left[\alpha_1 + \beta \frac{m_2(t)}{m_1(t)} \sin\phi \right] \quad (C-5a)$$

and

$$\epsilon_2(t) = A_1 \sqrt{\alpha_1} m_1(t) \left[\beta \frac{m_2(t)}{m_1(t)} \cos\phi - \sin\phi \right] \quad (C-5b)$$

where

$$\beta = \frac{A_2 \sqrt{\alpha_2}}{A_1 \sqrt{\alpha_1}} \quad (C-6)$$

With $\epsilon_1(t)$ and $\epsilon_2(t)$ as in (C-5a) and (C-5b), the control signal

$$z(t) = A_V \epsilon_1(t) \text{sign}[\epsilon_2(t)] - \epsilon_2(t) \text{sign}[\epsilon_1(t)]$$

assumes the form

$$z(t, \phi) = A_1^2 \alpha_1 \left\{ A_V \left(\cos\phi + \beta \frac{m_2(t)}{m_1(t)} \sin\phi \right) \text{sign} \left[\beta \frac{m_2(t)}{m_1(t)} \cos\phi - \sin\phi \right] - \left(\beta \frac{m_2(t)}{m_1(t)} \cos\phi - \sin\phi \right) \text{sign} \left[\cos\phi + \beta \frac{m_2(t)}{m_1(t)} \sin\phi \right] \right\} \quad (C-7)$$

The feedback signal $z(t, \phi)$ has random components and periodic oscillations.

The decomposition

$$z(t, \phi) = \overline{\langle z(t, x) \rangle} + \langle z(t, x) - \overline{\langle z(t, x) \rangle} \rangle \Big|_{x=\phi}$$

(where the overbar denotes statistical average and $\langle \rangle$ denotes time average) allows us to write $z(t, \phi)$ as a nonrandom, nontime-varying function of the tracking error ϕ (control voltage) plus a random component that acts as "modulation self noise." The S-curve of the system is therefore defined as the function $s(\cdot)$ given by

$$s(x) = \overline{\langle z(t, x) \rangle}$$

Averaging $z(t,x)$ with respect to the random (± 1) data signal $m_1(t)$, we obtain

$$\begin{aligned} \frac{\overline{z(t,x)}}{A_1^2 \alpha_1} &= \frac{A_V}{2} \cdot (\cos x + \beta m_2(t) \sin x) \text{sign} [\beta m_2(t) \cos x - \sin x] \\ &+ \frac{A_V}{2} \cdot (\cos x - \beta m_2(t) \sin x) \text{sign} [-\beta m_2(t) \cos x - \sin x] \\ &- \frac{1}{2} \cdot (\beta m_2(t) \cos x - \sin x) \text{sign} [\cos x + \beta m_2(t) \sin x] \\ &- \frac{1}{2} \cdot (-\beta m_2(t) \cos x - \sin x) \text{sign} [\cos x - \beta m_2(t) \sin x] \end{aligned} \quad (C-8)$$

The above function is periodic in t with the same period of $m_2(t)$. We also note that the particular value of the phase parameter θ_S of $m_2(t)$ is irrelevant for the computation of time average and can be taken as $\theta_S = 0$; that is,

$$m_2(t) = \sin(\omega_S t)$$

If we now define the periodic functions

$$f(t,x) = (\cos x + \beta \sin(\omega_S t) \sin x) \text{sign} [\beta \sin(\omega_S t) \cos x - \sin x] \quad (C-9a)$$

and

$$g(t,x) = (\beta \sin(\omega_S t) \cos x - \sin x) \text{sign} [\cos x + \beta \sin(\omega_S t) \sin x] \quad (C-9b)$$

then (C-8) can be expressed as

$$\frac{\overline{z(t,x)}}{A_1^2 \alpha_1} = \frac{A_V}{2} [f(t,x) + f(-t,x)] - \frac{1}{2} [g(t,x) + g(-t,x)] \quad (C-10)$$

The time average of (C-10) therefore reduces to

$$\frac{s(x)}{A_1^2 \alpha_1} = A_V \langle f(t,x) \rangle - \langle g(t,x) \rangle$$

or, by noting that $f(t,x + \pi/2) = -g(t,x)$, to

$$\frac{s(x)}{A_1^2 \alpha_1} = A_V G(x) + G(x + \pi/2) \quad (C-11)$$

where

$$G(x) \triangleq \langle f(t,x) \rangle = 1/T_S \int_0^{T_S} f(t,x) dt \quad (C-12)$$

with T_S being the period of the sinusoid $m_2(t)$.

Evaluation of G(x)

For a given x, f(t,x) can be written from (C-9a) as

$$f(t,x) = \begin{cases} K(t,x) = \cos x + \beta \sin\left(\frac{2\pi}{T_s} t\right) \sin x; t \in \left\{ t: \beta \sin\left(\frac{2\pi}{T_s} t\right) \cos x \geq \sin x \right\} \\ -K(t,x) \quad ; \quad \text{otherwise} \end{cases} \quad (C-13)$$

In evaluating G(x), it is convenient to consider the following cases:

$$(1) \quad 0 \leq x < \pi/2 ; G(x) \hat{=} G_1(x) \quad (\cos x > 0, \sin x \geq 0)$$

$$f(t,x) = \begin{cases} K(t,x) ; t \in I = \left\{ t: \sin\left(\frac{2\pi}{T_s} t\right) \geq \frac{\sin x}{\beta \cos x} \right\} \\ -K(t,x) ; \quad \text{otherwise} \end{cases}$$

Figure C.2 illustrates set I. Now,

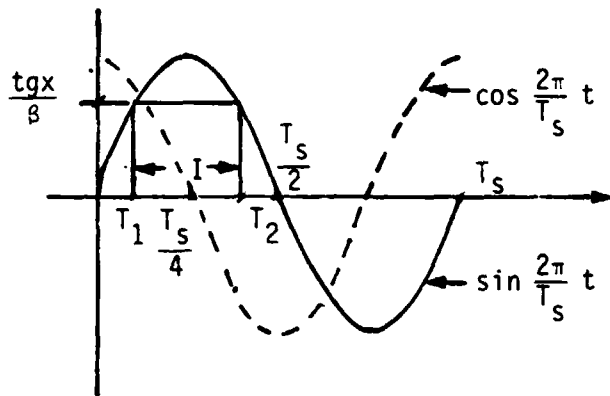
$$\begin{aligned} G_1(x) &= 1/T_s \int_0^{T_s} f(t,x) dt = 1/T_s \left[\int_0^{T_s} (-K(t,x)) dt - \int_I (-K(t,x)) dt + \int_I K(t,x) dt \right] \\ &= 1/T_s \left[2 \int_{T_1}^{T_2} K(t,x) dt - \int_0^{T_s} K(t,x) dt \right] \end{aligned} \quad (C-15)$$

Since

$$\int K(t,x) dt = t \cos x + \frac{T_s}{2\pi} \beta \cos\left(\frac{2\pi}{T_s} t\right) \sin x$$

then (C-15) reduces to

$$G_1(x) = \begin{cases} \frac{2(T_2 - T_1)}{T_s} \cos x - \frac{\beta}{\pi} \sin x \left[\cos\left(\frac{2\pi}{T_s} T_2\right) - \cos\left(\frac{2\pi}{T_s} T_1\right) \right] - \cos x; 0 \leq \frac{\sin x}{\beta \cos x} \leq 1 \\ -\cos x \quad ; \quad 1 \leq \frac{\sin x}{\beta \cos x} \end{cases} \quad (C-16)$$



$$\sin\left(\frac{2\pi}{T_s} T_1\right) = \sin\left(\frac{2\pi}{T_s} T_2\right) = \frac{\text{tg}x}{\beta}$$

(C-14)

$$\cos\left(\frac{2\pi}{T_s} T_2\right) = -\cos\left(\frac{2\pi}{T_s} T_1\right) = -\sqrt{1 - \left(\frac{\text{tg}x}{\beta}\right)^2}$$

Figure C.2. Interval I and the Relations Between T_1 , T_2 and $\frac{\text{tg}x}{\beta}$

The quantity between brackets in (C-16) is given by (see (C-14) in Figure C.2)

$$\cos\left(\frac{2\pi}{T_S} T_2\right) - \cos\left(\frac{2\pi}{T_S} T_1\right) = -2 \cos\left(\frac{2\pi}{T_S} T_1\right) = -2 \sqrt{1 - (\text{tg}x/\beta)^2} \quad (\text{C-17})$$

Now, since $(T_2+T_1)/2 = T_S/4$, then

$$\frac{T_2-T_1}{2} = T_2 - \frac{T_S}{4}$$

Therefore,

$$\cos\left(\frac{2\pi}{T_S} \left(\frac{T_2-T_1}{2}\right)\right) = \cos\left(\frac{2\pi}{T_S} T_2 - \frac{\pi}{2}\right) = \sin\left(\frac{2\pi}{T_S} T_2\right) = \frac{\text{tg}x}{\beta} = \frac{|\text{tg}(x)|}{\beta} \quad (\text{tg}x \geq 0)$$

which yields

$$\frac{T_2-T_1}{T_S} = \frac{1}{\pi} \cos^{-1} \frac{|\text{tg}(x)|}{\beta} \quad (\text{C-18})$$

Inserting (C-18) and (C-17) into (C-16) we obtain

$$G_1(x) = \begin{cases} -\cos(x) + \frac{2}{\pi} \left[\cos(x) \cos^{-1}\left(\frac{|\text{tg}(x)|}{\beta}\right) + \beta \sqrt{1 - \left(\frac{\text{tg}x}{\beta}\right)^2} \sin x \right] ; 0 \leq \frac{\text{tg}(x)}{\beta} \leq 1 \\ -\cos(x) ; \frac{\text{tg}(x)}{\beta} \geq 1 \end{cases} \quad (\text{C-19})$$

(2) $\pi/2 \leq x < \pi$; $G(x) \hat{=} G_2(x)$ ($\cos x \leq 0$, $\sin x > 0$)

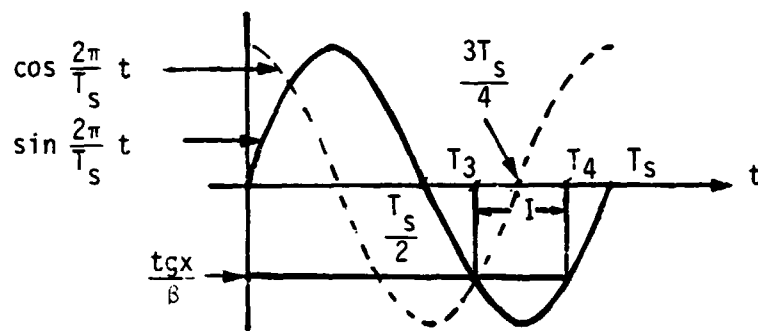
$$f(t,x) = \begin{cases} K(t,x) ; t \in I = \left\{ t : \sin\left(\frac{2\pi}{T_S} t\right) \leq \frac{\text{tg}(x)}{\beta} \right\} \\ -K(t,x) ; \text{otherwise} \end{cases}$$

The expression for $G_2(x)$ can be written in a form similar to (C-15) as*

$$G_2(x) = \frac{1}{T_S} \left[2 \int_{T_3}^{T_4} K(t,x) dt - \int_0^{T_S} K(t,x) dt \right]$$

*

Also refer to Figure C.3.



$$\sin\left(\frac{2\pi}{T_s} T_4\right) = \sin\left(\frac{2\pi}{T_s} T_s\right) = \frac{\text{tg}x}{\beta}$$

(C-20)

$$\cos\left(\frac{2\pi}{T_s} T_4\right) = -\cos\left(\frac{2\pi}{T_s} T_3\right) = \sqrt{1 - \left(\frac{\text{tg}x}{\beta}\right)^2}$$

Figure C.3. Interval I and the Relation Between T_3 , T_4 and $\frac{\text{tg}x}{\beta}$

yielding

$$G_2(x) = \begin{cases} \frac{2}{T_s}(T_4 - T_3)\cos x - \frac{\beta}{\pi} \sin x \left[\cos\left(\frac{2\pi}{T_s} T_4\right) - \cos\left(\frac{2\pi}{T_s} T_3\right) \right] - \cos x; & -1 \leq \frac{\text{tg}x}{\beta} \leq 0 \\ -\cos x; & \frac{\text{tg}x}{\beta} \leq -1 \end{cases} \quad (\text{C-21})$$

Using the fact that $(T_3 + T_4)/2 = 3T_s/4$ and working in a way similar to that for $G_1(x)$, we obtain

$$\cos\left(\frac{2\pi}{T_s}\left(\frac{T_4 - T_3}{2}\right)\right) = -\frac{\text{tg}x}{\beta} = \frac{|\text{tg}(x)|}{\beta} \quad (\text{tg}x \leq 0)$$

which yields

$$\frac{T_4 - T_3}{T_s} = \frac{1}{\pi} \cos^{-1}\left(\frac{|\text{tg}(x)|}{\beta}\right) \quad (\text{C-22})$$

Combining (C-20), (C-21) and (C-22) results in

$$G_2(x) = \begin{cases} -\cos x + \frac{2}{\pi} \left[\cos x \cos^{-1}\left(\frac{\text{tg}(x)}{\beta}\right) - \beta \sqrt{1 - \left(\frac{\text{tg}(x)}{\beta}\right)^2} \sin x \right]; & -1 \leq \frac{\text{tg}(x)}{\beta} \leq 0 \\ -\cos x; & \frac{\text{tg}(x)}{\beta} \leq -1 \end{cases} \quad (\text{C-23})$$

By developments similar to those performed for $G_1(x)$ and $G_2(x)$, we find that

$$(3) \quad \pi \leq x < 3\pi/2 \quad ; \quad G(x) = G_3(x) = -G_1(x) \quad (\text{C-24})$$

and that

$$(4) \quad 3\pi/2 \leq x < 2\pi \quad ; \quad G(x) = G_4(x) = -G_2(x) \quad (\text{C-25})$$

By using signs of $\cos(x)$ and $\sin(x)$ in different quadrants, expressions (C-19) and (C-23)-(C-25) can be expressed in a unified form by

$$\begin{aligned}
 G(x) = & - \text{sign}[\sin(x)] \cos(x) \\
 & + c(x) \frac{2}{\pi} \left\{ \text{sign}[\sin(x)] \cos^{-1} \left(\frac{|\text{tg}(x)|}{\beta} \right) \cos(x) \right. \\
 & \left. + \text{sign}[\cos(x)] \beta \sqrt{1 - \left(\frac{\text{tg}(x)}{\beta} \right)^2} \sin(x) \right\} \quad (C-26a)
 \end{aligned}$$

where

$$c(x) = \begin{cases} 1 & ; \quad |\sin(x)| \leq \beta |\cos(x)| \\ 0 & ; \quad \text{otherwise} \end{cases} \quad (C-26b)$$

The loop's S-curve, given by (C-11), is therefore

$$s(x) = A_1^2 \alpha_1 \left[A_V G(x) + G \left(x + \frac{\tau}{2} \right) \right] \quad (C-27a)$$

with $G(x)$ given by (C-26), β defined through

$$\beta = \frac{A_2}{A_1} \sqrt{\frac{\alpha_2}{\alpha_1}} \quad (C-27b)$$

and where α_1 and $\alpha_2(f_s)$ are given by (see (C-3) and (C-4))

$$\alpha_1 = \int_{-\infty}^{+\infty} |L(f)|^2 S_{m_1}(f) df$$

and

$$\alpha_2 = |L(f_s)|^2, \quad (f_s = \text{sinusoid frequency in Hz})$$

Note that the ratio A_2/A_1 in (C-27b) denotes the ratio of the amplitude of the sinusoidal modulation in channel 2 to that of the data modulation in channel 1 at the input of the tracking device.

Slope of the S-Curve at the Origin (x=0)

Let $s'(0)$ denote the derivative of $s(x)$ at $x=0$; then, from (C-27a), we have

$$\frac{s'(0)}{A_1^2 \alpha_1} = A_V G'(0) + G'\left(\frac{\pi}{2}\right) \quad (C-28)$$

The quantities $G'(0)$ and $G'(\pi/2)$ can be shown to be given by

$$G'(0) = (2/\pi)(1/\beta)(\beta^2 - 1)$$

and

$$G'(\pi/2) = 1 ,$$

which, when inserted into (C-28), yield

$$\frac{s'(0)}{A_1^2 \alpha_1} = \frac{2 A_V}{\pi \beta} (\beta^2 - 1) + 1 \quad (C-29)$$

Figure C.4 illustrates the dependence of $s'(0)$ on the parameter β . Note that $s'(0)$ becomes negative if β is less than a threshold value β^* . In this range, the loop will no longer have a stable point at $\phi=0^\circ$. By equating (C-29) to zero and solving for β , we find that

$$\beta^* = \frac{1}{2} \left[\sqrt{\left(\frac{\pi}{2A_V}\right)^2 + 4} - \frac{\pi}{2A_V} \right] \quad (C-30)$$

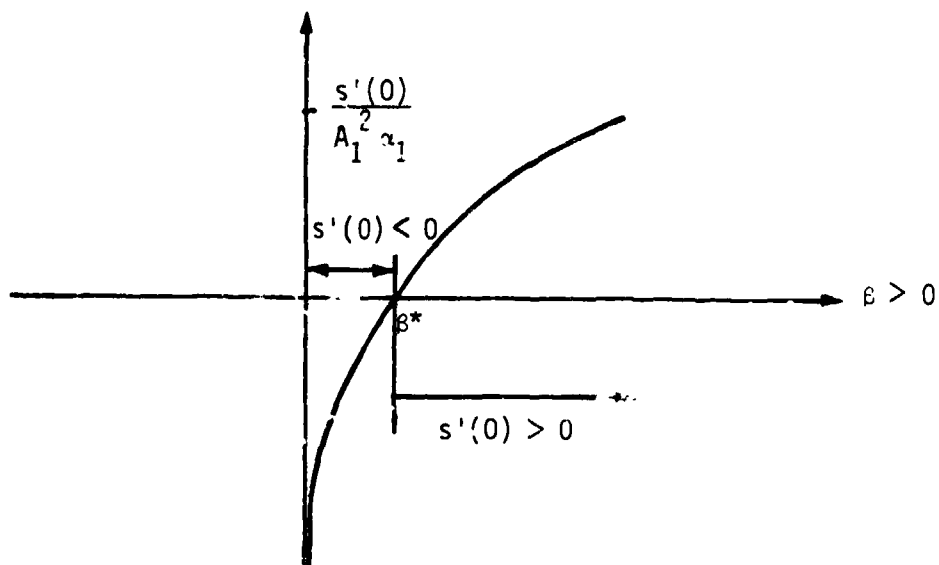


Figure C.4. Dependence of $s'(0)$ on the Ratio $\beta = \frac{A_2}{A_1} \sqrt{\frac{\alpha_2}{\alpha_1}}$

APPENDIX D

IMPULSE RESPONSE OF AN Nth-ORDER BUTTERWORTH FILTER

By

Raimundo Sampaio

Consider the squared-magnitude system function of an Nth-order analog Butterworth filter (BF) given by

$$|H(j\omega)|^2 = \frac{1}{1 + (j\omega/j\omega_c)^{2N}} \quad (D-1)$$

In (D-1), ω_c is the cut-off radian frequency. It follows from (D-1) that, in the Laplace domain,

$$H(s)H(-s) = \frac{1}{1 + (s/j\omega_c)^{2N}} \quad (D-2)$$

The poles of $H(s)H(-s)$ are

$$s_p = (-1)^{1/2N} (j\omega_c) \quad (D-3)$$

i.e., they are equally spaced in angle on a circle of radius ω_c in the s plane. For a causal and stable design, $H(s)$ is chosen to correspond to the poles in the left-half s plane, as shown in Figure D.1. Note that the poles have been assigned in complex conjugate pairs (b_j, b_j^*) , $j=1, \dots, (N-1)/2$ for N =odd and $j=1, \dots, N/2$ for n = even. Furthermore, for N =odd, there is an additional negative pole $b_0 = -\omega_c$.

It follows from the above that $H(s)$ can be expressed as

$$H(s) = \begin{cases} K \frac{1}{(s-b_0)} \prod_{i=1}^{(N-1)/2} \frac{1}{(s-b_i)} \prod_{i=1}^{(N-1)/2} \frac{1}{(s-b_i^*)} & N \text{ odd} \\ K \prod_{i=1}^{N/2} \frac{1}{(s-b_i)} \prod_{i=1}^{N/2} \frac{1}{(s-b_i^*)} & N \text{ even} \end{cases} \quad (D-4)$$

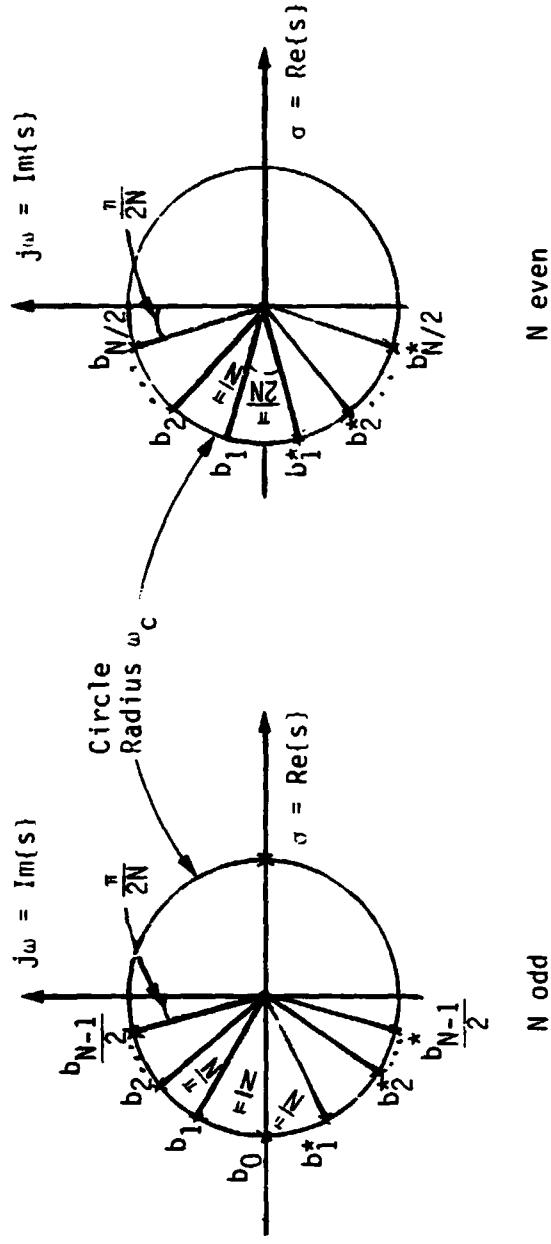
where, if we require the normalization $H(0)=1$, we must have

$$K = (\omega_c)^N \quad (D-5)$$

Now let $H_u(s)$ be the transfer function corresponding to $\omega_c=1$, with poles $\{a_i\}$ on the unit circle. Since

$$b_i = \omega_c a_i \quad (D-6)$$

it is easy to verify that the transfer function $H(s)$ associated with a general ω_c is related to $H_u(s)$ by



* Complex conjugate

Figure D.1. Causal and Stable Butterworth Filter Designs in the Complex s Plane (Pole identification is shown for N odd or even)

$$H(s) = H_U(s/\omega_c) \quad (D-7)$$

In the time domain, let $h_U(t), h(t)$ be the impulse responses corresponding to $H_U(s)$ and $H(s)$, respectively. In other words,

$$H_U(s) = \int_0^{\infty} h_U(t) e^{-st} dt \quad (D-8a)$$

and

$$H(s) = \int_0^{\infty} h(t) e^{-st} dt \quad (D-8b)$$

Combining (D-7) and (D-8a), we conclude that

$$H(s) = H_U\left(\frac{s}{\omega_c}\right) = \int_0^{\infty} h_U(t) e^{-(s/\omega_c)t} dt = \int_0^{\infty} \omega_c h_U(\omega_c t') e^{-st'} dt' \quad (D-9)$$

which, by mere comparison with (D-8b), results in

$$h(t) = \omega_c h_U(\omega_c t) \quad (D-10)$$

Therefore, the normalized and unnormalized impulse responses are related by an amplitude and time scaling by ω_c .

With the above in mind, let us now proceed to calculate $h_U(t)$; conversion to $h(t)$ is then immediate.

From (D-4), setting $\omega_c=1$; hence, $K=1$, we get*

$$H_U(s) = \begin{cases} \frac{1}{(s-a_0)} \prod_{i=1}^{(N-1)/2} \frac{1}{(s-a_i)(s-a_i^*)} = \frac{1}{(s-a_0)} \prod_{i=1}^{(N-1)/2} \frac{1}{(s-a_i)} \prod_{i=1}^{(N-1)/2} \frac{1}{(s-a_i^*)}; N=\text{odd} \\ \prod_{i=1}^{N/2} \frac{1}{(s-a_i)(s-a_i^*)} = \prod_{i=1}^{N/2} \frac{1}{(s-a_i)} \prod_{i=1}^{N/2} \frac{1}{(s-a_i^*)}; N=\text{even} \end{cases} \quad (D-11)$$

*

Recall that the poles of $H_U(s)$ are called a_i , as per (D-6).

Performing a partial-fraction expansion yields

$$H_U(s) = \begin{cases} \frac{A_0}{(s-a_0)} + \sum_{i=1}^{\frac{(N-1)}{2}} \frac{B_i}{(s-a_i)} + \frac{C_i}{(s-a_i^*)} & N=\text{odd} \\ \sum_{i=1}^{N/2} \frac{B_i}{(s-a_i)} + \frac{C_i}{(s-a_i^*)} & N=\text{even} \end{cases} \quad (D-12)$$

where the coefficients A_0 , B_i and C_i are found by standard formulae, as shown below. Assuming for a minute that $N=\text{odd}$, we have

$$\begin{aligned} A_0 &= H_U(s)(s-a_0) \Big|_{s=a_0} \\ B_i &= H_U(s)(s-a_i) \Big|_{s=a_i} \quad i=1,2,\dots,(N-1)/2 \\ C_i &= H_U(s)(s-a_i^*) \Big|_{s=a_i^*} \end{aligned} \quad (D-13)$$

Thus, using (D-13) into (D-11) yields

$$\begin{aligned} B_i &= \frac{1}{(a_i-a_0)} \prod_{\substack{k=1 \\ k \neq i}}^{\frac{(N-1)}{2}} \frac{1}{(a_i-a_k)} \prod_{k=1}^{\frac{(N-1)}{2}} \frac{1}{(a_i-a_k^*)} \\ C_i &= \frac{1}{(a_i^*-a_0)} \prod_{k=1}^{\frac{(N-1)}{2}} \frac{1}{(a_i^*-a_k)} \prod_{\substack{k=1 \\ k \neq i}}^{\frac{(N-1)}{2}} \frac{1}{(a_i^*-a_k^*)} \end{aligned} \quad \left. \begin{array}{l} \\ \\ \end{array} \right| \begin{array}{l} N=\text{odd} \\ (D-14) \end{array}$$

Since a_0 is real (it corresponds to a real pole), we conclude from (D-14) that

$$C_i = B_i^* ; i=1,2,\dots,(N-1)/2 \quad (D-15)$$

so that only the B_i 's of (D-14) need to be evaluated. Furthermore,

$$A_0 = \frac{\frac{(N-1)}{2}}{\prod_{i=1}^{\frac{(N-1)}{2}} \frac{1}{(a_0-a_i)(a_0-a_i^*)}} = \frac{\frac{(N-1)}{2}}{\prod_{i=1}^{\frac{(N-1)}{2}} |a_0-a_i|^2} \quad (D-16)$$

It follows from (D-12) and (D-15) that $H_U(s)$ is given by

$$H_U(s) = \frac{A_0}{s-a_0} + \sum_{i=1}^{\frac{(N-1)}{2}} \frac{B_i}{(s-a_i)} + \frac{B_i^*}{(s-a_i^*)} \quad (D-17)$$

Let

$$\sigma_i = \operatorname{Re}\{a_i\} \quad (\text{D-18a})$$

and

$$\omega_i = \operatorname{Im}\{a_i\} \quad (\text{D-18b})$$

so that

$$a_i = \sigma_i + j\omega_i \quad (\text{D-18c})$$

The inverse Laplace transform of (D-17) is then

$$h_u(t) = A_0 e^{a_0 t} + \sum_{i=1}^{\frac{(N-1)}{2}} B_i e^{a_i t} + B_i^* e^{a_i^* t} = A_0 e^{a_0 t} + 2 \sum_{i=1}^{\frac{(N-1)}{2}} \operatorname{Re}\{B_i e^{a_i t}\}$$

or

$$h_u(t) = A_0 e^{a_0 t} + 2 \sum_{i=1}^{\frac{(N-1)}{2}} e^{\sigma_i t} \operatorname{Re}\{B_i e^{j\omega_i t}\} \quad (\text{D-19})$$

which is a real function, as expected. In (D-19), A_0 and B_i are given in (D-16) and (D-14).

In an entirely similar way, when N =even,

$$h_u(t) = 2 \sum_{i=1}^{N/2} e^{\sigma_i t} \operatorname{Re}\{B_i e^{j\omega_i t}\} \quad (\text{D-20})$$

with

$$B_i = \prod_{\substack{k=1 \\ k \neq i}}^{N/2} \frac{1}{(a_i - a_k)} \prod_{k=1}^{N/2} \frac{1}{(a_i - a_k^*)} \quad (\text{D-21})$$

The poles a_i can also be expressed in trigonometric form as

N =odd

$$a_i = \underbrace{-\cos\left(\frac{i\pi}{N}\right)}_{\sigma_i} + j \underbrace{\sin\left(\frac{i\pi}{N}\right)}_{\omega_i}; \quad i=0, 1, \dots, (N-1)/2 \quad (\text{D-22})$$

N =even

$$a_i = \underbrace{-\cos\left(\frac{(2i-1)\pi}{2N}\right)}_{\sigma_i} + j \underbrace{\sin\left(\frac{(2i-1)\pi}{2N}\right)}_{\omega_i}; \quad i=1, \dots, N/2$$

APPENDIX E

SIMULATION OF THE MRD MODIFIED FOUR-PHASE COSTAS LOOP

By

Jack K. Holmes

The analog version of the modified four-phase Costas loop is illustrated in Figure E.1. Let the received signal be described by

$$r(t) = \sqrt{2P_1} m_1(t) \cos(\omega_{sc}t + \theta) + \sqrt{2P_2} m_2(t) \sin(\omega_{sc}t + \theta)$$

then the detected signals will be

$$e_1(t) = \sqrt{P_1} m_1(t) \cos(\theta - \hat{\theta}) + \sqrt{P_2} m_2(t) \sin(\theta - \hat{\theta}) \quad (1)$$

and

$$e_2(t) = -\sqrt{P_1} m_1(t) \sin(\theta - \hat{\theta}) + \sqrt{P_2} m_2(t) \cos(\theta - \hat{\theta}) \quad (2)$$

In order to utilize the results on a digital computer, we digitize the above equations to yield

$$e_1(k) = \sqrt{A} m_1(k) \cos(\theta(k) - \hat{\theta}(k)) + 2\sqrt{A} m_2(k) \sin(\theta(k) - \hat{\theta}(k)) \quad (3)$$

and

$$e_2(k) = -\sqrt{A} m_1(k) \sin(\theta(k) - \hat{\theta}(k)) + 2\sqrt{A} m_2(k) \cos(\theta(k) - \hat{\theta}(k)) \quad (4)$$

where we have let $P_2 = 4P_1$ because of the 4:1 power ratio, and $A = P_1$.

Out of the 1.8-MHz lowpass filters, we can write

$$\varepsilon_1(k) = \sum_{n=0}^k e_1(n) h_L(k-n) \quad (5)$$

and

$$\varepsilon_2(k) = \sum_{n=0}^k e_2(n) h_L(k-n) \quad (6)$$

where

$$h_L(n) = e^{-2\pi n f_0 T_s} \quad (7)$$

with T_s representing the symbol duration and f_0 being the 3-dB cutoff of the arm lowpass filters.

Now let the output of the limiters be denoted $L_1^{(k)}$ and $L_2^{(k)}$. Then

$$L_1(k) = \text{sgn}(\varepsilon_1(k)) \quad (8)$$

and

$$L_2(k) = \text{sgn}(\varepsilon_2(k)) \quad (9)$$

The analog version of the modified four-phase Costas loop is illustrated in Figure E.1. Let the received signal be described by

$$r(t) = \sqrt{2P_1} m_1(t) \cos(\omega_{sc}t + \theta) + \sqrt{2P_2} m_2(t) \sin(\omega_{sc}t + \theta)$$

then the detected signals will be

$$e_1(t) = \sqrt{P_1} m_1(t) \cos(\theta - \hat{\theta}) + \sqrt{P_2} m_2(t) \sin(\theta - \hat{\theta}) \quad (1)$$

and

$$e_2(t) = -\sqrt{P_1} m_1(t) \sin(\theta - \hat{\theta}) + \sqrt{P_2} m_2(t) \cos(\theta - \hat{\theta}) \quad (2)$$

In order to utilize the results on a digital computer, we digitize the above equations to yield

$$e_1(k) = \sqrt{A} m_1(k) \cos(\theta(k) - \hat{\theta}(k)) + 2\sqrt{A} m_2(k) \sin(\theta(k) - \hat{\theta}(k)) \quad (3)$$

and

$$e_2(k) = -\sqrt{A} m_1(k) \sin(\theta(k) - \hat{\theta}(k)) + 2\sqrt{A} m_2(k) \cos(\theta(k) - \hat{\theta}(k)) \quad (4)$$

where we have let $P_2 = 4P_1$ because of the 4:1 power ratio, and $A = P_1$.

Out of the 1.8-MHz lowpass filters, we can write

$$e_1(k) = \sum_{n=0}^k e_1(n) h_L(k-n) \quad (5)$$

and

$$e_2(k) = \sum_{n=0}^k e_2(n) h_L(k-n) \quad (6)$$

where

$$h_L(n) = e^{-2\pi n f_0 T_s} \quad (7)$$

with T_s representing the symbol duration and f_0 being the 3-dB cutoff of the arm lowpass filters.

Now let the output of the limiters be denoted $L_1^{(k)}$ and $L_2^{(k)}$. Then

$$L_1(k) = \text{sgn}(e_1(k)) \quad (8)$$

and

$$L_2(k) = \text{sgn}(e_2(k)) \quad (9)$$

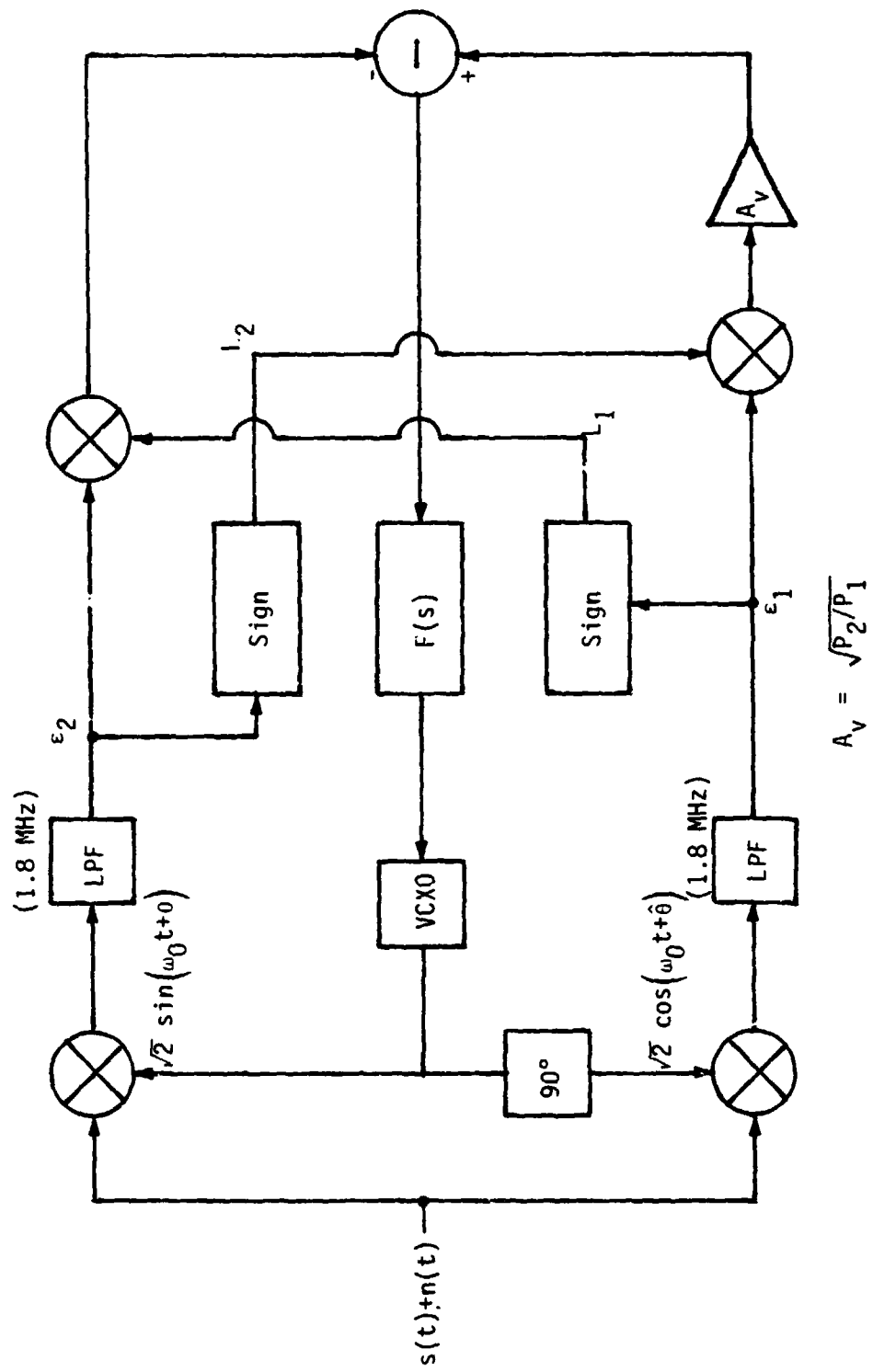


Figure E.1. Modified Four-Phase Costas Loop

The output of the second multipliers is given by

$$z_1(k) = \varepsilon_1(k) L_2(k) \quad (10)$$

and

$$z_2(k) = \varepsilon_2(k) L_1(k) \quad (11)$$

Out of the difference, we have

$$z(k) = A_V z_1(k) - z_2(k) \quad (12)$$

where $A_V = 2$ for our case. Now the output-phase estimate is given by

$$\hat{\theta}(k+1) = \hat{\theta}(k) + K_L T_S z(k) \quad (13)$$

for the first-order loop which is utilized in this simulation. Now,

$$K_L = \frac{2^n B_L(T_S f_0)}{(A_V^2 \sqrt{\gamma_2'} + \sqrt{\gamma_1'})} \quad (14)$$

relates the closed-loop one-sided noise bandwidth, B_L , to the recursion gain K_L . The γ parameters are the filtering loss of the respective data bit streams, i.e.,

$$\gamma_1' = \int_{-\infty}^{\infty} \frac{\mathcal{S}_{m_1}(f)}{\left[1 + \left(\frac{f}{f_0}\right)^2\right]} df \leq 1 \quad (15)$$

and

$$\gamma_2' = \int_{-\infty}^{\infty} \frac{\mathcal{S}_{m_2}(f)}{\left[1 + \left(\frac{f}{f_0}\right)^2\right]} df \leq 1 \quad (16)$$

Before the loop, the test filter (prelimiter) and limiter, plus a bandpass filter, are located and modeled in the simulation. The resulting baseband-equivalent model is illustrated in Figure E.2. The recorder signal model composed of a noise burst plus two sweeping tones were coded in the program.

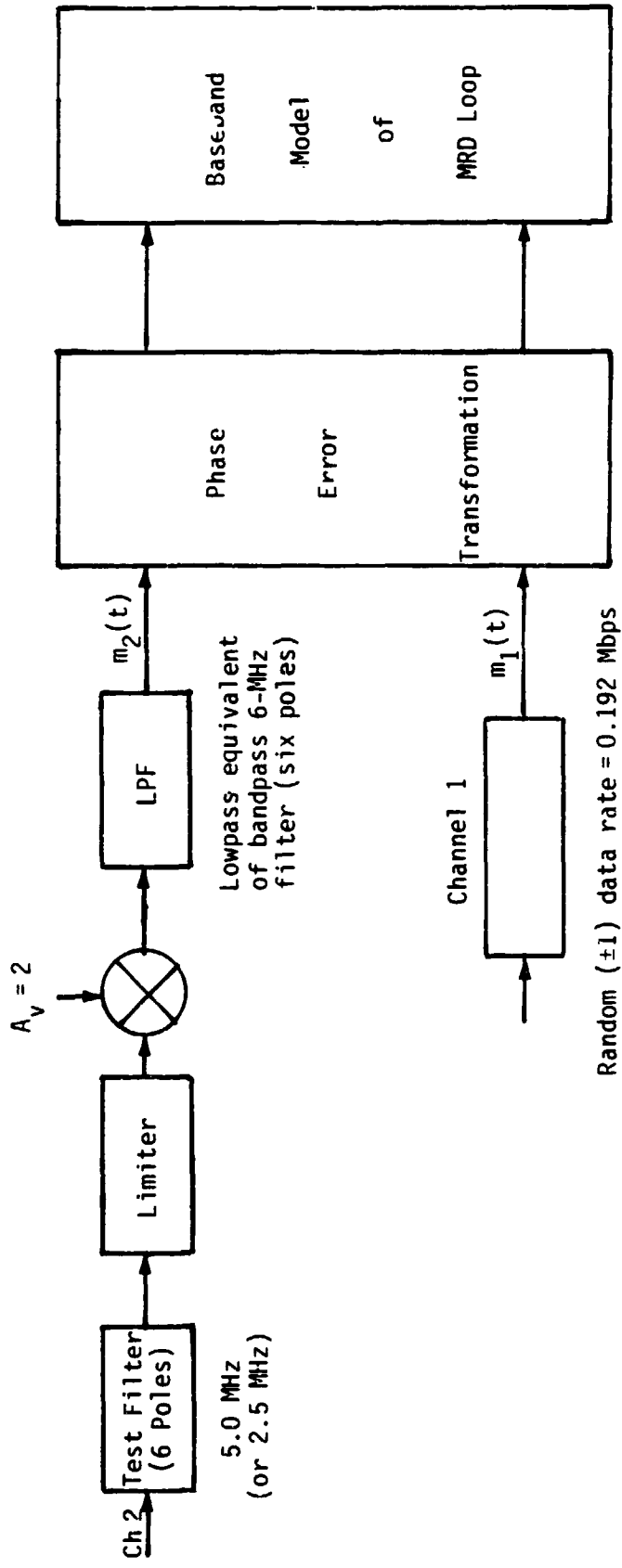


Figure E.2. Baseband Equivalent MRD Loop Model Simulation

ADDENDUM 3
RF COVERAGE ANALYSIS

TECHNICAL MEMORANDUM, AXIOMATIX

TO: JSC/EE8/J. Ratliff November 10, 1983
FROM: Axiomatix/J. Porter
SUBJECT: STS-9 Ascent RF Coverage; Comm Support Formulation

The enclosure provides the recommended STS-9 ascent-phase STDN support plan and the corresponding predicted Orbiter S-band PM automatic antenna switching up to and including TDRS ascent support, as derived from analysis of the STS-9 Cycle 1 reference trajectory. This information has been provided informally to FS4 GC's (Ground Controllers) per request and is currently baselined for STS-9.

The use of MIL and PDL embodied in items (1) through (7) on the enclosure is the standard scenario utilized for past missions and is unchanged for STS-9 (but the Orbiter automatic antenna switching called out is different from the past as a result of the 57° inc.). The ground-station and TDRS scenario from item (8) through item (11) is all new and is the result of two new considerations for the STS-9 mission: (1) the first TDRS support of ascent, and (2) the first 57° inc. mission, all previous missions being $\sim 28\frac{1}{2}^{\circ}$, or approximately due east.

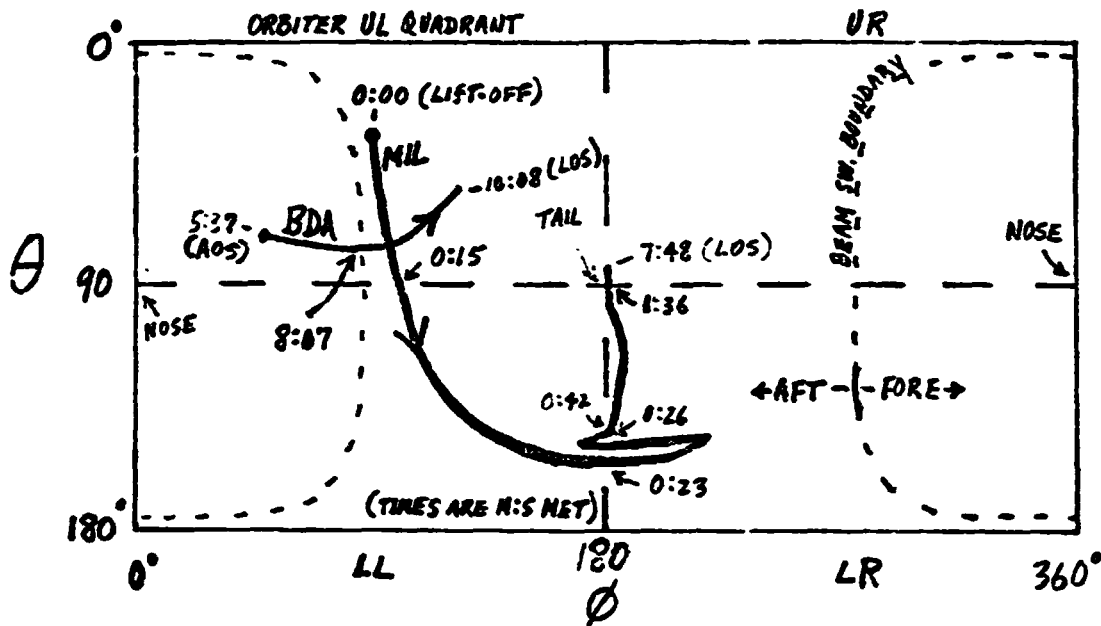
Because of the 57° inc, unlike previous missions BDA will be a low-EL ($<5^{\circ}$) and hence marginal pass. This led to the recommendation of the new MIL/BDA H/O time in item (8) of $6\frac{1}{2}$ min versus the previous $5\frac{1}{2}$ min. BDA 0° -EL horizon break will occur later for STS-9 (about 5:40 M:S MET) while MIL is still above 5° EL until 6:30 and also offers a significantly stronger link than BDA.

The recommended BDA/TDRS H/O of 9 to $9\frac{1}{2}$ min in item (10) was predicated on BDA showing line-of-sight terrain masking just after $9\frac{1}{2}$ min. Based on this recommendation, $9\frac{1}{2}$ min is currently baselined.

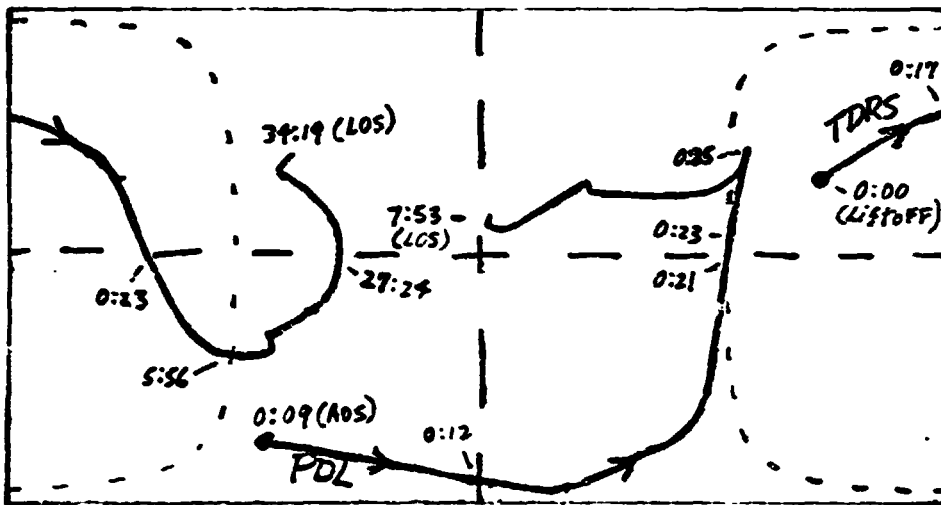

James A. Porter

Enclosure

cc:
JSC, EE8/W. Teasdale
B. Batson
JSC, EE/R. Sawyer
J. Johnson
Axiomatix, G. Huth



MIL
&
BDA



PDL
&
TDRS

AOS = Acq. of Sight
LOS = Loss of Sight

Shuttle Line-of-Sight Look Angles to MIL, PDL, BDA, and TDRS
During STS-9 Nominal Ascent (Ref. Traj: Cycle 1)

TECHNICAL MEMORANDUM, AXIOMATIX

TO: EE8/J. Ratliff January 28, 1984
FROM: Axiomatix/J. Porter
SUBJECT: Shuttle STS-8 Mission DTO 702 Report

STS-8 was the first Shuttle mission operation of communications via a TDRS satellite for both S-band and K-band comm. DTO 702 was an STS-8 comm flight test to exercise different operational configurations of the Orbiter's S-band comm system towards establishing flight readiness of TDRS-mode operation. K-band had separate DTO's, 710, 712, and 724.

DTO 702 required exercising S-band comm thru TDRS using HDR and LDR, with and without spreading, with and without encryption, Hi-Freq and Lo-Freq operation, acquisition without doppler compensation, plus a test part to verify that antenna and beam switching occurs at the projected boundaries.

The DTO assessment report is enclosed. DTO 702 is considered successful and completed. Assessment was based on the EE8 standard postmission data product CCO01F, with data printouts extracted per EE8 direction by Lockheed-EMSCO; and postmission reports distributed by the different mission operation groups; plus discussions with mission personnel. The report is co-authored by D. O'Herron/Lockheed-EMSCO, being a cooperative effort, and thus will also be provided under Lockheed-EMSCO cover.


James A. Porter

Enclosure

cc:
JSC, EE8/W. Teasdale
S. Novosad
B. Batson
EE/R. Sawyer
J. Johnson
EE3/J. Seyl, W. Seibert
EE4/M. Luse
Axiomatix, G. Huth
Lockheed-EMSCO, D. O'Herren

REPORT ON STS-8 DTO 702

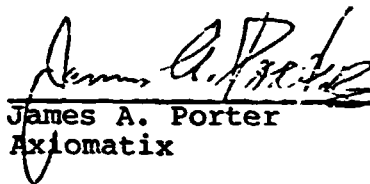
January 26, 1984

Prepared for James E. Ratliff, Manager NASA/JSC Task 530,
RF Coverage Analysis, EE8/Systems Analysis Office, Tracking
and Communications Division, Johnson Space Center, National
Aeronautics and Space Administration.

by

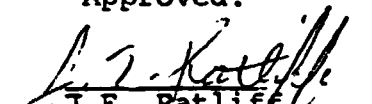


Dave O'Herren
Lockheed Engineering and
Management Services Company



James A. Porter
Axiomatix

Approved:



J.E. Ratliff
Manager, Task 530

Report on STS-8 DTO 702

STS-8 was the first Shuttle mission operation of communications via a TDRS satellite for both S-band and K-band comm. DTO 702 was an STS-8 comm flight test to exercise different operational configurations of the Orbiter's S-band comm system, towards establishing flight readiness for TDRSS-mode operations. K-band comm had separate DTO's, 710, 712, and 724, and these are being addressed in other reports.

Specifically, DTO 702 requires exercising S-band comm thru TDRSS using HDR and LDR, with and without spreading, with and without encryption, Hi-Freq and Lo-Freq operation, acquisition without doppler compensation, plus a test part for assessing antenna and beam switching. Table I identifies the comm system configuration elements addressed by each of the parts of 702. The criteria for success for each test part is simply proper end-to-end operation of the S-band link when exercising the configuration elements of that test part. More specifically, success is promptly establishing and continuing data lock. For purposes of the DTO, timely lock plus 3-min sustained operation is defined as adequate demonstration of success.

For this report, postflight data was available only from the Orbiter, and hence the assessment is based largely on forward (FWD) link performance; return (RTN) link observations from mission operation reports are included in the assessment when and where applicable.

Assessment

All tests required by DTO 702 were performed. Each designated configuration element was exercised. Since the purpose of the DTO was to simply establish that each Table I configuration is operational, timely lock plus a nominal 3-min sustained operation is defined as successful demonstration. To minimize the operational inconvenience of frequent configuration changes, the mission plan allowed that each configuration might be exercised the entire TDRS pass time, roughly an hour, of the orbit scheduled for that configuration. The scheduled orbits are listed in Table II. With these orbits as a guide, the mission time periods shown in Table II were selected for ordering post-mission data for analysis and assessment.

Data tabulations for these periods were prepared and first reviewed to ascertain if the proper configurations were employed and for what portions of these periods. The configurations selected by mission personnel for DTO 702 purposes are listed with corresponding DTO parts in Table II. These are total configurations and thus include selection elements which are incidental to the DTO, as can be seen by comparison with Table I. For example, per Table I, 702-1 requires a period of

Orbiter operation with the low set of operating frequencies, 2041.9-MHz receive/2217.5-MHz transmit, as opposed to 2106.4-MHz receive/2287.5-MHz transmit. Per Table II, the planned or designated configuration for 702-1 correctly includes Lo-Freq selection, whereas the other configuration elements are optional with 702-1.

The processed data shows that designated configurations were in some cases employed throughout the Table II periods, some roughly half, and some others much less. Since these configurations per se were not required, attention was directed to any configurations meeting Table I requirements. The data was then reviewed for segments meeting this criteria and also of at least 3-min duration, per the assessment guideline.

Such segments were found in the data set for the periods in Table II in all cases except 702-2 and of course 702-9 since, as noted in Table II, the source-data tape for the 702-9 period was faulty and a re-order failed to clear the problem. The 702-2 data shows HDR with spreading (SPD) beginning at the very end of the data period and providing only a few seconds of data lock. However, mission reports indicate this was successfully demonstrated shortly thereafter in a 5-min interval early in the next orbit, orbit 77 (247:00:27 - 00:32).

The assessment of the individual parts of 702 is as follows:

- 702-1. Successful. Extensively demonstrated throughout an entire TDRS pass, ~50 min.
- 702-2. Not adequately demonstrated by the data but mission reports indicate successful demonstration not in orbit 76 but shortly thereafter early in 77, in a 5-min segment 247:00:27 - 00:32. A supplemental data request is considered unmerited. Rated: (qualified) Successful.
- 702-3. Successful. Much like 702-1 above.
(702-4 replaced by 702-10 and 11 as explained in Table I)
- 702-5. Successful. Data indicates approximately 6 min of good operation during orbit 25. Non-related procedural problems and shortened TDRS support reported.
- 702-6. Successful. Acquisition without doppler compensation was demonstrated during normal mission operation. There is one exception, high positive doppler such as at the beginning of a TDRS pass where the doppler is +50 khz or more. With doppler comp inhibited at AOS on orbit 88, the Orbiter transponder did not lock to the FWD link, confirming a previous ground test result.
- 702-7. Successful. Data shows an interval approximately of 20 min of successful 702-7 operation during orbit 54.

- 702-8. Orbit 37 data shows only a short 702-8 test interval. Non-related procedural problems were reported for much of this orbit but the data appears to indicate a minimal period of successful 702-8 operation. Mission reports also state successfully demonstrated. Rated: Successful.
- 702-9. Not assessable by our data, source-data tape faulty, problem not cleared by re-order. Reported successfully demonstrated in mission reports. Rated: (qualified) Successful.
- 702-10, 11. Successful. Assessment of roll plane and pitch plane antenna and beam switching, comm mode configuration optional. Data shows switching occurs at each antenna and beam switching boundary. Some residual minor discrepancies as to precise boundaries remain after allowing for 2° hysteresis, and also allowing for relatively fast $1^{\circ}/2$ -sec rate-of-change versus a 2-sec staleness factor. Discrepancies typically less than 5° , with one on the order of 10° .

Conclusion

DTO 702 is considered successful and completed. Adequate tests are conducted for all ten DTO parts.

TABLE I. - Parts of STS-8 DTC 702 (S-band)

702-1	Lo-Freq Operation
702-2	HDR; SPD
702-3	HDR
702-4	(Deleted*)
702-5	LDR
702-6	Acq. without Doppler comp
702-7	Encrypted; D/L LDR, U/L LDR, SPD
702-8	Encrypted; D/L HDR, U/L HDR, SPD
702-9	Encrypted; D/L LDR, U/L LDR
702-10, 11	Antenna and beam switching assessment (roll and pitch planes, respectively)

* Part 702-4, originally the part requiring antenna and beam switching assessment, was deleted and replaced by 702-10 and 11 to parallel 702-1 and 2, a K-band DTO which fortuitously already provides roll and pitch plane rotations.

TABLE II.- STS-8 DTO 702 Postmission Data Set

<u>DTO Part*</u>	<u>STS-8 Designated Configuration For DTO Part</u>	<u>Reported Orb't No.</u>	<u>Period of Postmission Data Obtained (GMT)</u>
702-1	LDR/Coding/SPD/Lo-Freq	Orb. 9	242:19:05 - 20:01 (56 min)
702-2	HDR/Coding/SPD/Hi-Freq	Orb. 76	246:22:06 - 23:00, plus 23:43 - 23:59 (70 min)
702-3	HDR/Coding/Hi-Freq	Orb. 13	243:01:31 - 02:25 (54 min)
702-5	LDR/Coding/Hi-Freq	Orb. 25	243:19:40 - 20:30 (50 min)
702-6	LDR/Coding/SPD/Hi-Freq, No Doppler Comp	Orb. 88	247:17:04 - 17:57 (53 min)
702-7	LDR/Coding/SPD/ENCRP/Hi-Freq	Orb. 54	245:14:30 - 15:25 (55 min)
702-8	HDR/Coding/SPD/ENCRP/Hi-Freq	Orb. 37	244:12:50 - 13:50 (60 min)
702-9	LDR/Coding/ENCRP/Hi-Freq	Orb. 69	(Not available; bad data tape)
702-10	LDR/Coding/SPD/Hi-Freq	Orb. 49	245:06:38 - 07:30 (52 min)
702-11	LDR/Coding/SPD/Hi-Freq	Orb. 65	246:06:20 - 07:31 (71 min)

* 702-4 deleted (achieved in 702-10, 11)

TECHNICAL MEMORANDUM, AXIOMATIX

March 26, 1984

TO: EE8/J. E. Ratliff
FROM: Axiomatix/J. A Porter
SUBJECT: Shuttle STS-8 Mission DTO 710 Report

STS-8 was the first Shuttle mission operation of communications via a TDRS satellite for both S-band and K-band comm. DTO 710 was an STS-8 comm flight test to exercise different operational configurations of the Orbiter's K-band comm system towards establishing flight readiness of K-band operations. S-band had an analogous separate DTO (702) which was previously reported.

The intent of DTO 710 was that K-band comm be exercised and verified in each of the various combinations of FWD and RTN modes, with and without spreading, and with and without encryption. Additionally, that K-band acq be demonstrated in both the automatic and the manual modes, that K-band failover to S-band be demonstrated and finally, a demonstration of maintaining tracking and comm during an OMS burn.

The DTO assessment report is enclosed. DTO 710 is considered successful overall. One item is assigned TBD, as data products are being further analyzed for completeness. Assessment was based on the EE8 standard post-mission data product CCO01F as extracted and reported on by LEMSCO/D. O'Herren per EE8 direction, and various mission reports and data from direct mission support personnel or organizations. The report is co-authored with D. O'Herren and hence will also be forwarded under Lockheed-EMSCO cover.


James A. Porter

Enclosure

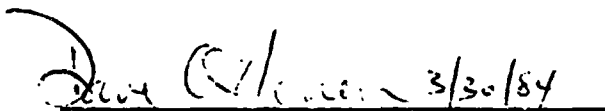
cc:
JSC, EE8/W. Teasdale
S. Novosad
EE/R. Sawyer
J. Johnson
EE3/J. Seyl
W. Seibert
EE4/M. Luse
Axiomatix, G. Huth
Lockheed-EMSCO, D. O'Herren

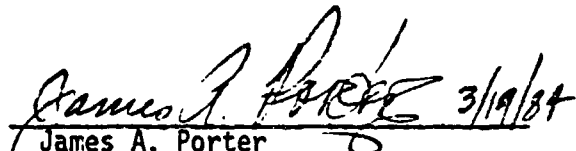
REPORT ON STS-8 DTO 710

March 14, 1984

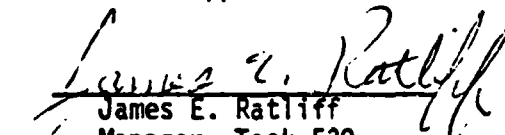
Prepared for James E. Ratliff, Manager NASA/JSC Task 530, RF Coverage Analysis, EE8/Systems Analysis Office, Tracking and Communications Division, Johnson Space Center, National Aeronautics and Space Administration.

by


Dave O'Herren 3/30/84
Dave O'Herren
Lockheed Engineering and
Management Services Company


James A. Porter 3/19/84
James A. Porter
Axiomatix
AXIO-3/84-HR1

Approved:


James E. Ratliff
Manager, Task 530

Report on STS-8 DTO 710

3/14/84

STS-8 was the first Shuttle mission operation of communications via a TDPS satellite for both S-band and K-band comm. DTO 710 was an STS-8 comm flight test to exercise different operational configurations of the Orbiter's K-band comm system, towards establishing flight readiness for K-band comm via TDRSS. S-band comm had an analogous separate DTO (702) which was previously reported.

The intent of DTO 710 was that K-band comm be exercised for each of the various combinations of FWD and RTN modes, with and without spreading, and with and without encryption. Additionally, that K-band acquisition be demonstrated both in the automatic mode and the manual mode, that K failover to S-band be demonstrated and finally, a demonstration of maintaining antenna tracking and the comm link during an OMS burn. Table I identifies the comm system configuration elements addressed by each of the parts of 710. The criteria for success for each test part is simply proper end-to-end operation of the K-band link when exercising the configuration elements of that test part. More specifically, success is promptly establishing and continuing data lock. For purposes of the DTO, timely lock plus 3-min sustained operation is defined as adequate demonstration of success.

For this report, postflight data was available only from the Orbiter, and hence the assessment is based largely on forward (FWD) link performance; return (RTN) link observations from mission operation reports are included in the assessment when and where applicable.

Assessment.

All tests required by DTO 710 were performed. Each designated configuration element was exercised. Since the purpose of the DTO was to simply establish that each Table I configuration item is operational, timely lock plus a nominal 3-min sustained operation is defined as successful demonstration. For each item in Table I, mission personnel defined a system configuration to include that item, and a mission period (orbit) in which that configuration would be exercised. The complete flight-designated configurations corresponding to the Table I items are listed in Table II. The orbit during which each configuration was exercised, as reported by mission personnel, is included. With these orbits as a guide, the mission time periods shown in Table II were selected for ordering postmission data for analysis and assessment. Data tabulations for these periods were prepared and first reviewed to ascertain if proper configurations were employed and for what portions of these periods. Segments of proper configuration were then addressed for an assessment of DTO test

results. Such segments were found in the data set for the periods in Table II in all cases except 710-1, -3, and -7. For the latter two, data either was not available and/or was faulty. For 710-1, the data for the orbit identified (21) shows the Orbiter uplink data source as being S-band rather than K-band during all of the data period except for 3 min., and for these 3-min. shows the K-band FWD mode to be mode 1 (216 KB) instead of the designated mode 2 (72 KB). This is at odds with mission support personnel reports that 72 KB was utilized and that 710-1 was successfully demonstrated in orbit 21. Whether the data is erroneous, or a processing error incurred, or the wrong orbit reported, etc., is being looked into. In the interim, DTO part 710-1 is rated as "Successful (qualified)" since it was directly reported accomplished by the mission comm officer (INCO).

Table III provides an assessment of DTO 710 by parts.

TABLE I. - Parts of STS-8 DTO 710 (K-hand)

710-1.	K U/L 72KB SPS
710-2	K U/L 72KB UNSPD
710-3	K D/L PM Mode; K U/L 216KB Mode UNSPD
710-4	K failover to S
710-5	(1) K D/L PM ENCRP; (2) K D/L FM ENCRP
710-6	K acq. while in D/L PM ENCRP
710-7	K U/L 72KB ENCRP/UNSPD
710-8	(1) K manual acq; (2) K track thru OMS burn

TABLE II.- STS-8 DTO 710 Postmission Data Set

<u>DTO Part</u>	<u>STS-8 Designated K-band Configuration For DTO Part</u>	<u>Reported Orbit No.</u>	<u>Period of Postmiss. Data Examined (GMT)</u>
710-1	FWD Mode 2 (72KB)/RTN Mode 2 (FM). SPD On, ENCRP OFF/ENCRP OFF	orb. 21	243:12:45 - 13:40
710-2	FWD Mode 2 (72KB)/RTN Mode 2 (FM). SPD OFF, ENCRP OFF/ENCRP OFF	orb. 82	247:07:22 - 08:22
710-3	FWD Mode 1 (216KB)/RTN Mode 1 (PM). SPD OFF, ENCRP OFF/ENCRP OFF	orb. 87	247:15:30 - 16:21*
710-4	FWD Mode 1 (216KB)/RTN Mode 2 (FM). SPD ON, ENCRP OFF/ENCRP OFF	Various	Various
710-5	FWD Mode 1 (216KB)/RTN Modes 1 & 2. SPD ON, ENCRP ON/ENCRP ON	orb. 54	245:14:30 - 15:23
710-6	FWD Mode 1 (216KB)/RTN Mode 1 (PM). SPD ON, ENCRP ON/ENCRP ON	orb. 37	244:12:50 - 13:55
710-7	FWD Mode 2 (72KB)/RTN Mode 2 (FM). SPD OFF, ENCRP ON/ENCRP ON	orb. 69	246:12:32 - 13:30*
710-8	FWD Mode 1 (216KB)/RTN Mode 2 (FM). SPD ON, ENCRP OFF/ENCRP OFF	orb. 48	245:05:03 - 06:18

*Data could not be obtained or was faulty.

ORIGINAL PAGE NO
OF POOR QUALITY

Report on STS-9 DTO 711
3/19/84

All parts of DTO 711 were previously verified in STS-8 DTO 710 except for exercising and verifying K-band RTN link PM mode channel 3 HDR in the highest HDR, 48 MB. This report addresses this latter.

The 48-MB HDR was exercised numerous times in STS-9, per mission reports. On many occasions performance was reported as very satisfactory. Occasions when it was not can generally be traced to circumstances such as K-band link outages due to antenna blockage or obscuration and/or outages unrelated to 48-MB performance. For purposes of this DTO, a sample period of sustained proper data flow is sufficient verification of the 48-MB capability; hence, timely lock plus 3-min sustained operation with good data is defined as adequate demonstration of success.

Assessment

Discussions with mission personnel identified several periods of 48-MB operation which were free of any blockage, etc outages not germane to whether or not the 48-MB channel operates properly. One of these periods, a 13-min interval from 336:21:42 to 336:21:55 D:R:M GMT, was one for which EE8 standard postmission data products were also available. This period was selected for DTO 711 assessment. RTN link performance, such as signal strength and data lock, is not an available postmission data product. Hence, the assessment of RTN link 48-MB performance must be evaluated by a combination of Orbiter onboard configuration status data and RTN link performance reports from mission personnel.

Orbiter data confirms that the Orbiter K-band system was configured, as required, for RTN Mode 1 (PM) with Channel 3 HDR at 48-MB throughout the period selected. Mission support personnel report 100% data quality for the received 48-MB data also throughout the period. DTO 711 is therefore rated successful and completed.

JP

jp

PHASES AND STAGES OF A DTO*

- I. COMPREHENSIVE REVIEW OF SYSTEM TO IDENTIFY CANDIDATE FTR'S (FLT TEST REQ'S)
- II. PRELIMINARY FORMULATION OF FLIGHT TESTS
- III. ATTAINING FTR STATUS
- IV. ATTAINING DTO STATUS
- V. MISSION INCORPORATION
----- (FLIGHT ACHIEVED) -----
- VI. POSTMISSION ANALYSIS AND ASSESSMENT
- VII. DTO FORMAL REPORT

* A FEW DTO'S, SPONTANEOUSLY BORN IN ANSWER TO A MISSION MANIFESTED NEED, BEGAN ESSENTIALLY AT STEP IV, BYPASSING THE EXTENSIVE TIME AND EFFORTS INVOLVED IN STEPS I, II, III.

(C&T DTO'S)

PART I.: COMPREHENSIVE C&T SYSTEM REVIEW TO IDENTIFY CANDIDATE FTR'S

- OVERVIEW OF SYSTEM COMPONENTS, CONFIGURATIONS, MODES
- DELINEATION OF REQUIREMENTS, CONSTRAINTS, LIMITS, OPERATING ENVIRONMENTS
- ASSESS VEHICLE-INTEGRATED OPERATION; VARIABLE-MISSION CONSIDERATIONS
- ASSESS EACH C&T RF SYSTEM'S ROLL IN ITS OWN RF LINK, AS A TRANSMITTER AND AS A RECEIVER, IN COMBINATION WITH THE SYSTEM(S) AT THE OTHER END OF THE LINK; COMBINED-OPERATION PROCEDURES, CHARACTERISTICS, CONSTRAINTS, LIMITS
- ASSESS WHAT EACH RF SYSTEM MUST PROVIDE TO AND OBTAIN FROM OTHER ONBOARD NON-C&T SYSTEMS, PLUS FROM OTHER ONBOARD RF SYSTEMS

PART II.: PRELIMINARY FORMULATION OF FLIGHT TESTS

- TO EXERCISE COMPONENTS AND CONFIGURATIONS; IN GSTDN-MODE, TDRSS-MODE, SGLS-MODE, ETC.
- USING THE VARIOUS ANTENNAS AND THEIR LOOK-ANGLE REGIONS OF OPERATION
- IN REAL FLIGHT, OVER A RANGE OF OPERATING ENVIRONMENTS, DISTANCES, ETC.

PART III.: ATTAINING FTR STATUS

- PROGRAM REVIEWS, TECHNICAL REVIEWS. CANDIDATE-FTR STATUS .
- RE-REVIEWS, COMPROMISES, RE-FORMULATIONS. SCRUBS, FINAL REVIEWS. FTR STATUS.

PART IV.: ATTAINING DTO STATUS

- REVIEW OF MISSION MANIFESTS FOR MISSION ASSIGNMENT, MISSION SELECTION .
- DTO INCORPORATION INTO MISSION AND PROGRAM DOCUMENTATION AND CONTROL. DTO STATUS .

PART V.: MISSION INCORPORATION

- PLANNING SESSIONS WITH ASSIGNED MISSION PERSONNEL TO FORMULATE TEST SCENARIO AND SPECIFIC PROCEDURES, AND INCORPORATE INTO MISSION TIMELINE
- FORMULATION OF SPECIFIC MEASUREMENTS REQUIRED; CORRELATION WITH LIST OF AVAILABLE MEASUREMENTS AND AVAILABLE FORMS AND FORMATS
- COORDINATION WITH POSTMISSION-DATA WORLD, WHO PROVIDES WHAT, WHEN, WHERE, AND HOW
- RE-ITERATIONS REQUIRED BY MISSION RE-SCHEDULING OR RE-FORMULATIONS

PART VI.: POSTMISSION ANALYSIS AND ASSESSMENT

- PRE-MISSION FORMULATION AND SUBMITTAL OF PRELIMINARY DATA REQUEST LISTING PLANNED TEST PERIODS AND DATA PRODUCTS REQUIRED
- POST-MISSION IDENTIFICATION OF ACTUAL TEST PERIODS AND RE-SUBMITTAL OF DATA REQUEST
- DELAYS DUE TO HIGHER-PRIORITY ORDERS, FACILITY/MANPOWER CONSTRAINTS, ETC.
- RECEIPT OF RAW DATA PRODUCTS; PRE-SCREENING AND RE-ORDERS FOR FAULTY DATA OR SHORTAGES
- DATA PROCESSING AND WORKAROUNDS OF UNAVAILABLE DATA
- DATA REDUCTION AND ANALYSIS; INCORPORATION OF OTHER SOURCE INFORMATION

PART VII.: DTO FORMAL REPORT

- FINDINGS AND ASSESSMENT. REPORT DRAFT FORMULATION AND REVIEW.
- PREPARATION AND SUBMITTAL OF DTO FORMAL REPORT

HOW TO ANALYZE THE STS-11 DELAYED-ACQ. PROBLEM

PREREQUISITES

1. Need management to instruct mission operation personnel to identify the passes where they experienced the delayed S-band acq. Identify by GMT start time of TDRS horizon break.
2. Need management to instruct postmission-data personnel to provide postmission data. Must be expedited with priority; otherwise can run into months. Re-orders due to bad data, etc. must be specifically spelled out in the expediting instructions or these likewise result in long delays.

METHOD

With the log from (1), and the full support per (2), could proceed as follows. First, order the Orbiter Roll/Pitch look angles to TDRS, from TDRS AOS horizon break to +15 min, and see if the bad passes show a pattern such as occurring when the line-of-sight is in the tail region, or in the nose region, or the upper left quadrant, etc. Second, obtain data and see if any coincidence between bad passes and system configuration. Third, obtain data that would show if any comm system parameters had off-nominal values at these times. This also requires ordering some good passes for reference.

This part could be completed in a few weeks if (1) and (2) were implemented with full expeditious support (i.e., a 1-day turnover, same for all re-orders).

If this investigation of the Orbiter side failed to provide any explanation, a second part would be to seek analogous status data for the TDRS to see if the problem can be explained on that end. (Efforts in past missions to obtain TDRS RIN link performance data have been without success; management assistance would be essential.)

JP

ADDENDUM 4

A TOROIDAL ANTENNA PATTERN FOR CENTAUR ISPM



Axiomatix

9841 Airport Boulevard • Suite 912 • Los Angeles, California 90045 • Phone (213) 641-8600

September 12, 1984

TO: Heinz Wimmer
FROM: Richard S. Iwasaki
SUBJECT: A Toroidal Antenna Pattern for the Centaur ISPM
CONTRACT: NAS 9-16893

The present General Dynamics Centaur antenna design is essentially omnidirectional and therefore is not suitable for the Solar Polar mission which requires a moderate gain toroidal pattern along the Centaur vehicle axis. A modified biconical array is proposed as a candidate configuration for achieving this toroidal pattern since it is readily adapted to the existing Centaur deployable antenna concept.

The biconical radiating element provides an inherent toroidal antenna pattern. Circular polarization is readily achieved by using orthogonal dipole elements spatially separated to provide the quadrature phase relationship. In this particular case, the circular symmetry of the biconical element is utilized to minimize the axial ratio considerations at the pattern extremes fore-and-aft of the Centaur vehicle since the biconical array axis will be perpendicular to the Centaur vehicle axis. The gain of the biconical array can be increased to the desired value by simply increasing the number of biconical elements in the array, as illustrated in Figure 1.

A simplified biconical dipole design has been developed based on the standing-waves of the radiating dipole element. The basic concept is to appropriately bend the dipole element to accommodate circular polarization. The dipole length is adjusted to permit three standing half wavelengths, sketched in Figure 2b. If the radiating current direction is superimposed on the shaped biconical radiating element, as shown in Figure 2c it is apparent that circular polarization is obtained. Use of an appropriate dielectric such as a ceramic can decrease the dimensions of the biconical element to optimize the antenna pattern.

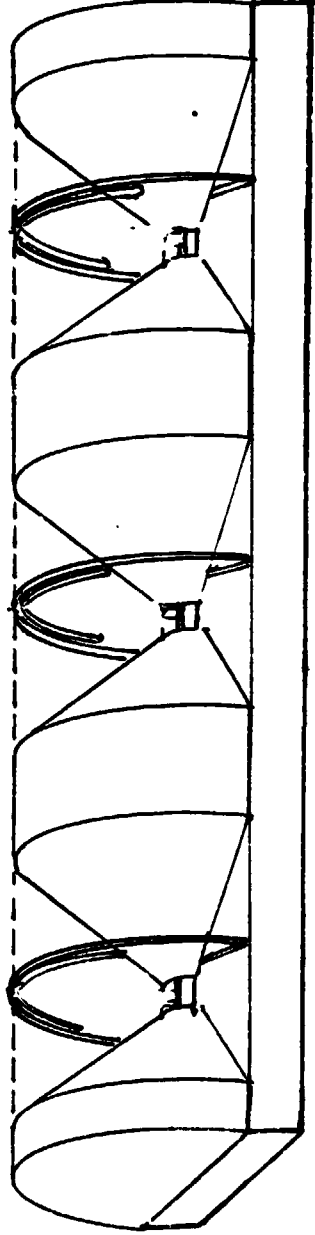


Figure 1. Modified Biconical Array

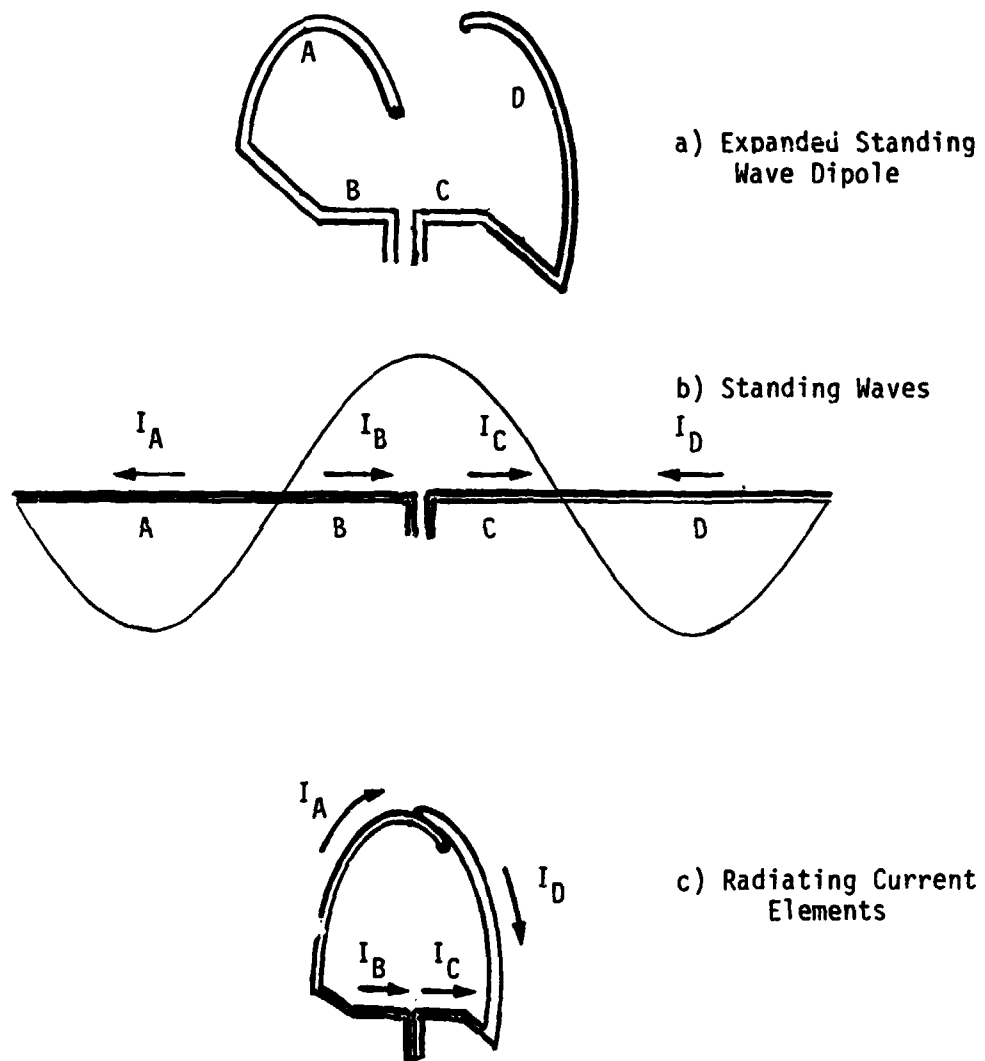


Figure 2. Radiating Currents on a Standing Wave Dipole

ADDENDUM 5

**BER DEGRADATION DUE TO CENTAUR TRANSMITTED
BIT TIMING JITTER NOISE THROUGH THE SHUTTLE
PAYLOAD COMMUNICATION SYSTEM**

**BER DEGRADATION DUE TO TRANSMITTED
BIT TIMING JITTER NOISE**

NAS 9-16893

Prepared for

**NASA Lyndon B. Johnson Space Center
Houston, Texas 77058**

Prepared by

Dr. Jack Holmes

**Axiomatix
9841 Airport Blvd., Suite 912
Los Angeles, California 90045**

**Axiomatix Report No. R8409-1
September 28, 1984**

TABLE OF CONTENTS

	<u>Page</u>
LIST OF FIGURES	ii
SUMMARY	1
1.0 CENTAUR TRANSMISSION TO THE SHUTTLE	2
2.0 CENTAUR DCU MODEL	2
3.0 SOURCE OF BIT ERROR RATE DEGRADATION	7
4.0 BIT ERROR RATE PROBABILITY FORMULATION	11
5.0 NUMERICAL EVALUATION OF σ_{ϕ}^2	13
6.0 EVALUATION OF THE BER DEGRADATION	13
CONCLUSIONS	14
REFERENCES	15

LIST OF FIGURES

	<u>Page</u>
1 Functional Flow Diagram - Centaur Transmission to Orbiter	3
2 Shuttle Payload Communications Receiver	4
3 NASA PSP Configuration	5
4 Single Sided Bit Timing Phase Noise Spectral Density (From LinCom Report TR-0394-8214-200)	6
5 NRZ Asymmetry in a Three Bit Pattern	8
6 NRZ Example of Duration Jitter	10

SUMMARY

It was determined that the Bit Error Rate (BER) degradation, due to just the DCU bit timing jitter, is approximately 0.04dB. It is concluded that this is a negligible amount of degradation.

1.0 CENTAUR TRANSMISSION TO THE SHUTTLE

The basic concern in this report is the bit error rate caused by the transmitted bit timing jitter, including continuous or discrete spectral components. The source of the bit timing jitter originates in the Digital Computer Unit (DCU), which modulates the Centaur subcarrier and in turn, phase modulates the carrier, see Figure 1. After S-Band transmission to the Shuttle Orbiter, the Payload Interrogator (PI) demodulates the carrier, and the data bits in the PSP bit synchronizer. Frame synchronizing is also done in the PSP. Figure 1 illustrates the system in block diagram form. Figure 2 shows the PI and Figure 3 illustrates the PSP.

2.0 CENTAUR DCU MODEL

The transmitted signal is described by

$$s(t) = \sqrt{2}A \sin(\omega_0 t + \theta d(t) \sin[\omega_{SC} t + \theta_0]) \quad (1)$$

where $d(t)$ is the data modulation on the subcarrier. Then the detected signal out of the subcarrier demodulator is given by

$$y(t) = 2A \cos[\phi(t)] \cos[\phi_{SC}(t)] J_1(\theta) d(t) \quad (2)$$

where A is the r.m.s. carrier amplitude, $\phi(t)$ is the RF phase error, $\phi_{SC}(t)$ is the subcarrier phase error, θ is the subcarrier phase modulation index, and $d(t)$ is the data bit stream. The data process $d(t)$ has timing jitter imbedded in the transition times.

For the general case that the timing jitter has both a continuous spectral density, plus discrete line spectral components, the bit timing error expressed in radians² is given by

$$\sigma_\phi^2 = 2 \int_0^\infty |1-H(f)|^2 S_{\phi_C}(f) df + 2 \sum_{k=1}^N |1-H(f_k)|^2 \lambda(f_k) \quad (3)$$

where the first term is due to the continuous timing bit jitter, and the second term is due to the discrete line components in the bit jitter process with weighting $\lambda(f_k)$.

Conversion to timing (5) jitter in seconds² is given by

$$\sigma_\epsilon^2 = \left(\frac{T}{2\pi}\right)^2 \sigma_\phi^2, \text{ seconds}^2 \quad (4)$$

where T is the bit duration in seconds. In equation (3) $S_{\phi_C}(f)$ is the single sideband timing bit jitter expressed in the rad²/Hz. Consequently, doubling the integral, weighted by the bit synchronizer loop error response [1], yields the variance of the bit timing error jitter. LinCom Corporation [2] has done the measurements for the curve of 16kBPS Manchester data and it is shown in Figure 4. We see that there are no discrete line components in the resulting spectral density.

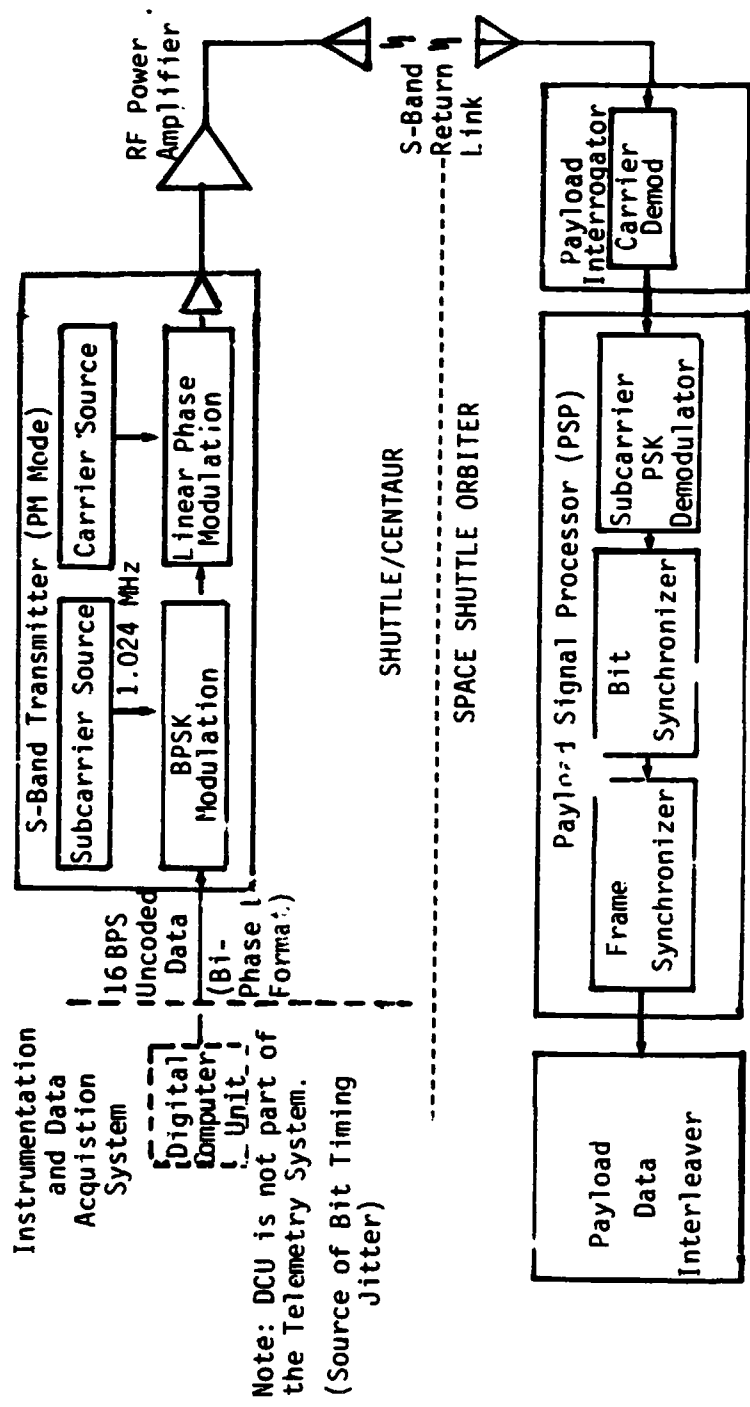


Figure 1. Functional Flow Diagram - Centaur Transmission to Orbiter

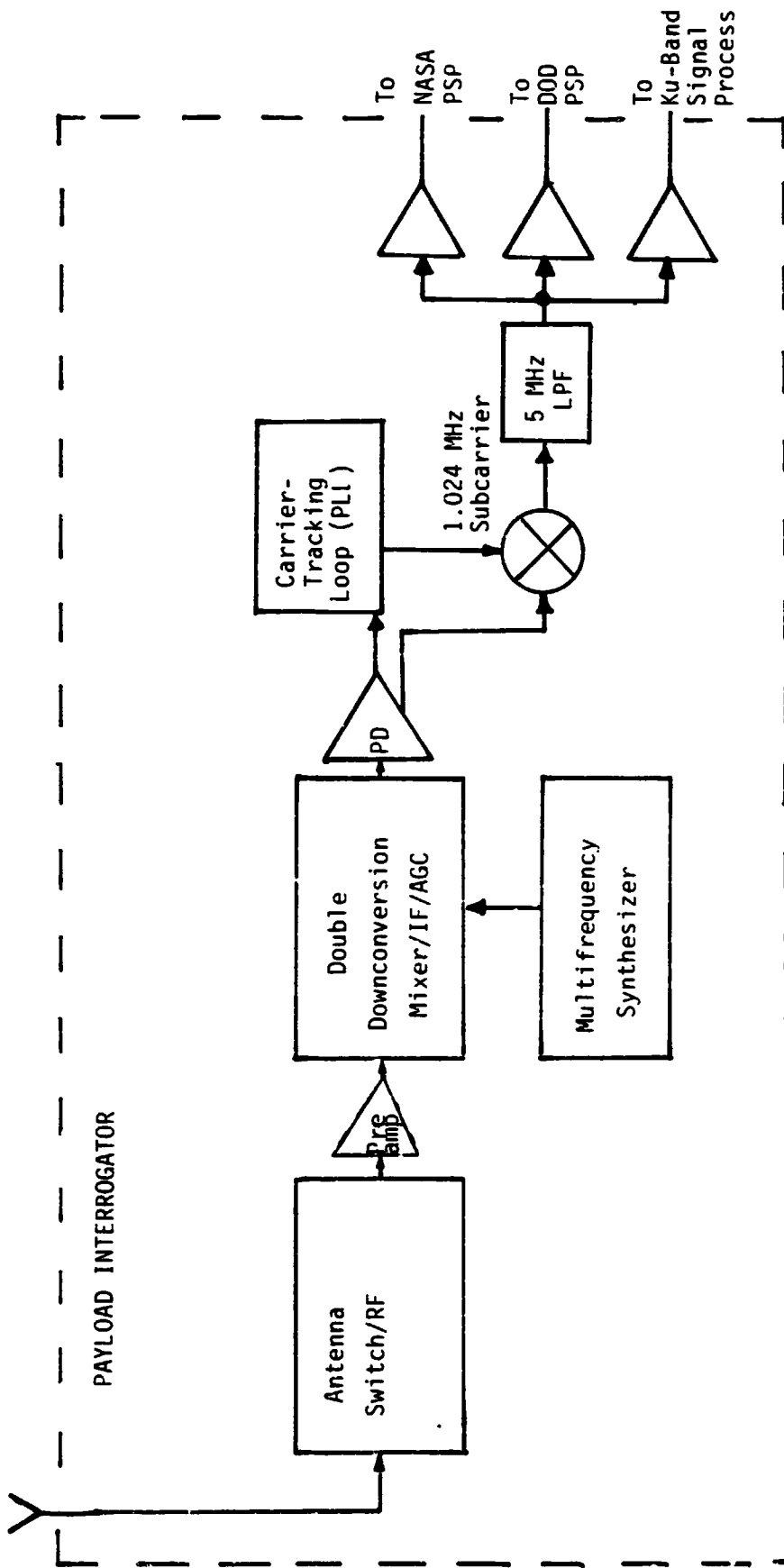


Figure 2. Shuttle Payload Communications Receiver

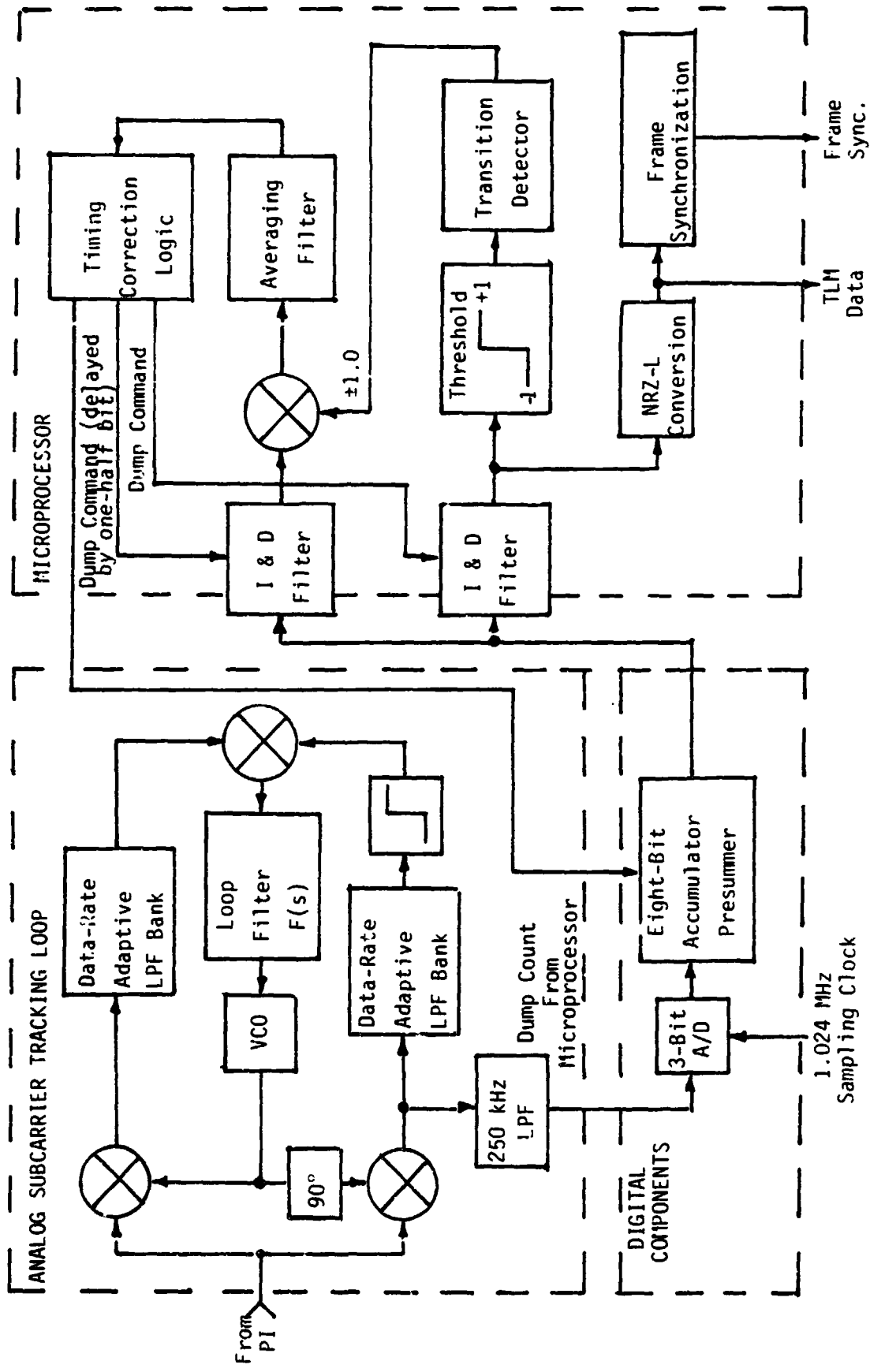


Figure 3. NASA PSP Configuration

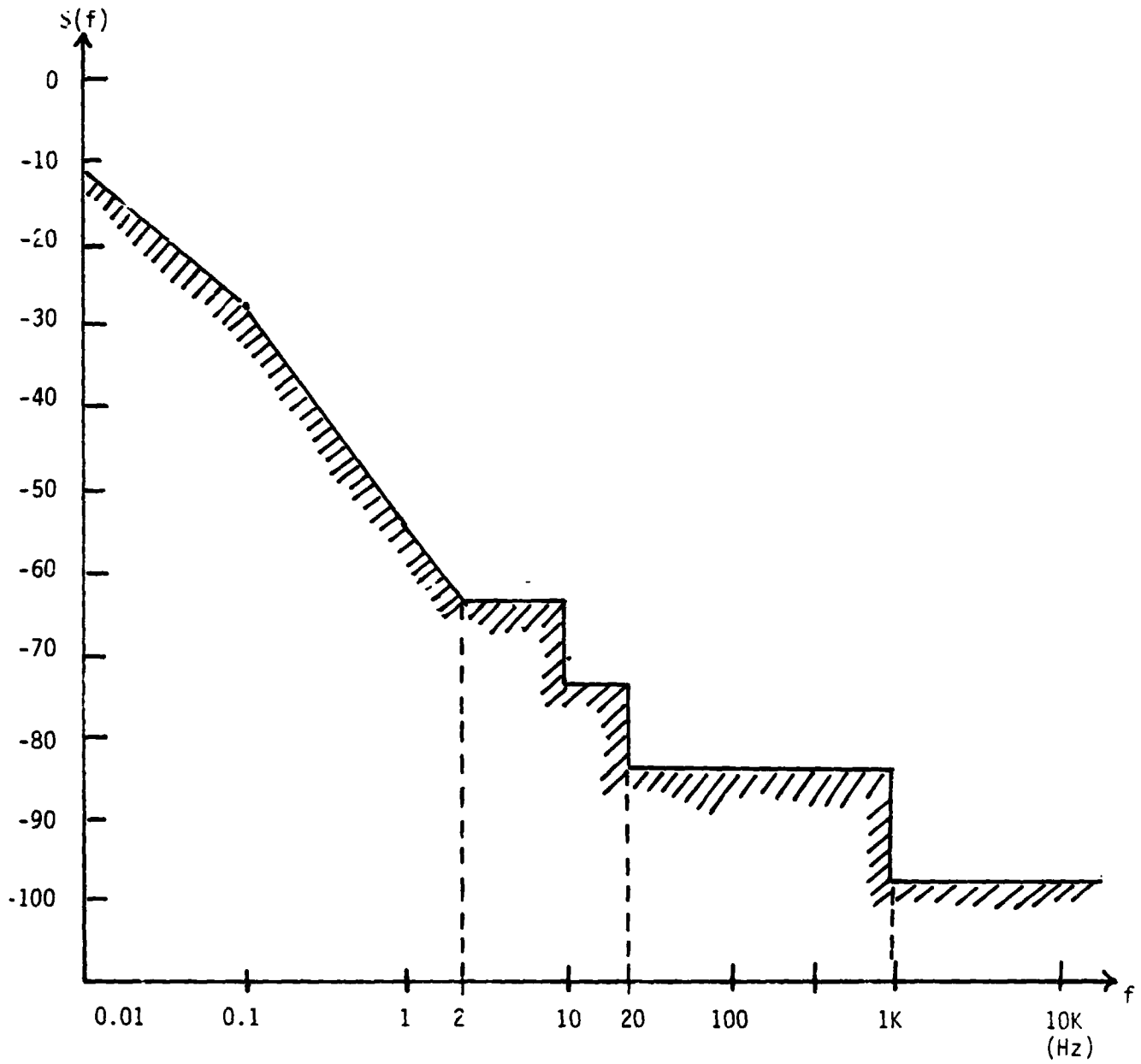


Figure 4. Single Sided Bit Timing Phase Noise Spectral Density
(From LinCom Report TR-0394- 214-200)

$$\sqrt{2} \int_{0.01}^{10\text{KHz}} \mathcal{P}_s(f) df = 2.7^\circ$$

The second term of equation (3) is the contribution of the discrete line spectral components. Now let us determine how to compute the value of $\lambda(f_k)$. For clarity, assume that two spurs are phase modulated on a carrier. We model this signal as

$$x(t) = \sqrt{2A} \sin(\omega_0 t + \beta_1 \sin \omega_1 t + \beta_2 \sin \omega_2 t) \quad (5)$$

or

$$x(t) = \sqrt{2A} \sin(\omega_0 t \cos(\beta_1 \sin \omega_1 t + \beta_2 \sin \omega_2 t)) + \sqrt{2A} \cos(\omega_0 t \sin(\beta_1 \sin \omega_1 t + \beta_2 \sin \omega_2 t)) \quad (6)$$

Assuming that $J_0(\beta_i) \approx 1$ ($|\beta_i| \ll 1$) allows us to obtain

$$x(t) \approx \sqrt{2A} \sin \omega_0 t + \sqrt{2A} J_1(\beta_1) [\sin(\omega_0 + \omega_1)t - \sin(\omega_0 - \omega_1)t] + \sqrt{2A} J_1(\beta_2) [\sin(\omega_0 + \omega_2)t - \sin(\omega_0 - \omega_2)t] \quad (7)$$

Hence, it can be deduced in the Nth phase modulation spur case that we have

$$x(t) \approx \sqrt{2A} \sin \omega_0 t + \sqrt{2A} \sum_{i=1}^N J_1(\beta_i) [\sin(\omega_0 + \omega_i)t - \sin(\omega_0 - \omega_i)t] \quad (8)$$

Since

$$J_n(\beta) \approx \frac{\beta^n}{2^n n!}, \quad |\beta| \ll 1 \quad (9)$$

We have

$$x(t) \approx \sqrt{2A} \sin \omega_0 t + \sqrt{2A} \sum_{i=1}^N \frac{\beta_i}{2} [\sin(\omega_0 + \omega_i)t - \sin(\omega_0 - \omega_i)t] \quad (10)$$

Hence the line (spur) components above ω_0 have (rms) dBc values of

$$\text{dBc}_i = \frac{\beta_i^2}{4} \text{ rad}^2 \text{ (SSB)} \quad (11)$$

and

$$\beta_i = 2.10 \text{ dBc}_i / 20 \quad (12)$$

The line components below ω_0 , also, have the same dBc values. Hence, the total mean squared timing jitter expressed in rad^2 (using single sided notation) is given by

$$\sigma_\phi^2 = 2 \int_0^\infty |1 - H(f)|^2 \mathcal{P}_\phi(f) df + \sum_{k=1}^N |1 - H(f_k)|^2 (\beta_k^2 / 2) \quad (13)$$

3.0

SOURCE OF BIT ERROR RATE DEGRADATION

In this section we will discuss various sources of possible bit error rate degradation. First consider asymmetry with NRZ symbols, which are illustrated in Figure 5.

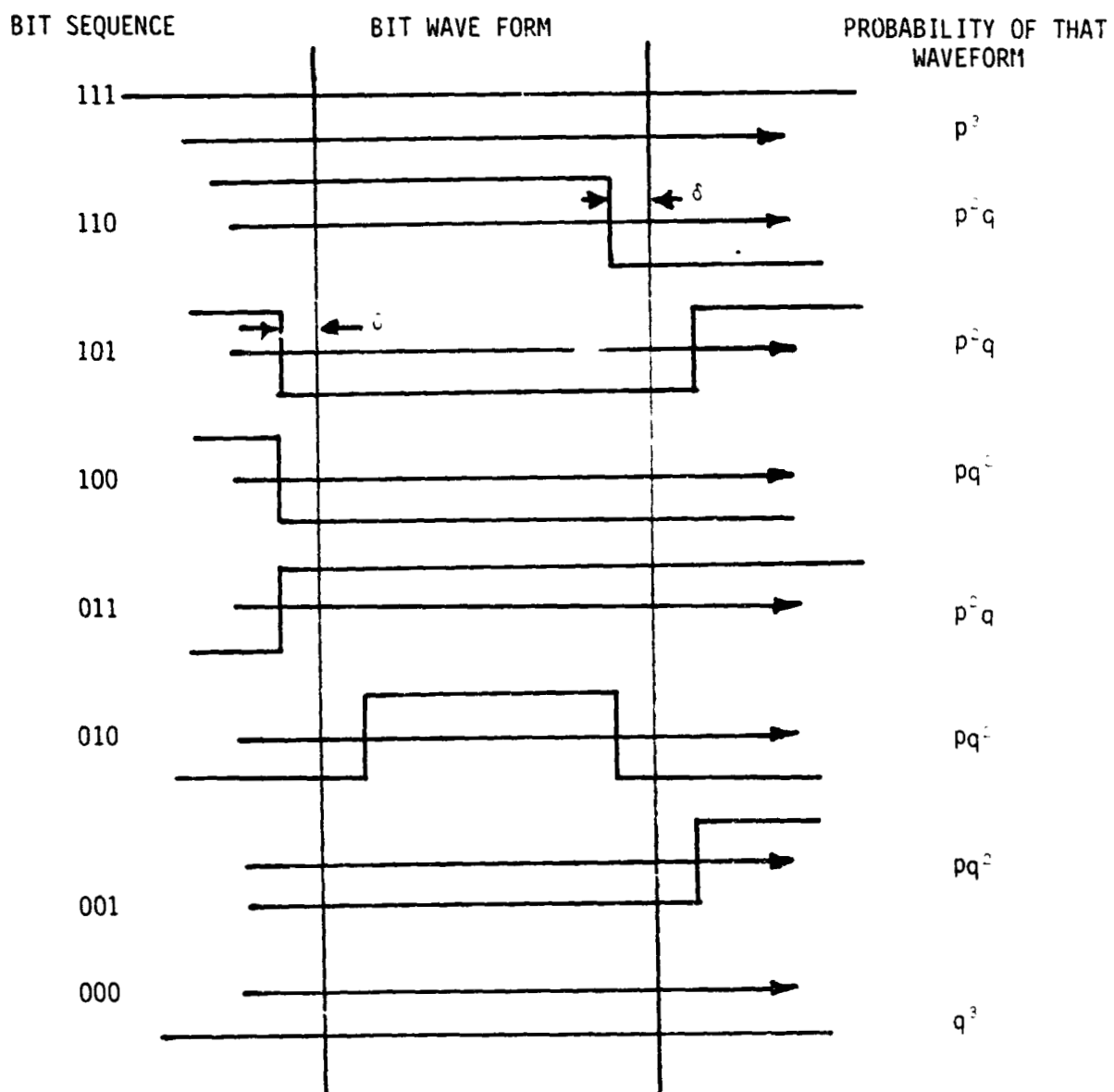


Figure 5. NRZ Asymmetry in a Three Bit Pattern

As can be seen in the figure, "zero" bits are wider than "one" bits so that in six cases out of the eight cases there is no degradation; one case (110) has a relative energy loss of $(1 - 2\delta/T)$, and the last case (010) a relative energy loss of $(1 - 4\delta/T)$, with $\delta < T/4$. Hence, we see that the asymmetry will degrade two of the 3 bit sequences, and hence the overall Bit Error Rate will be degraded. Further details can be found in reference [3]. Since, to the first order, asymmetry degradation is not affected by bit jitter, we will neglect it in what follows.

Next we consider bit duration jitter and see how it is related to the bit tracking jitter. Let the transmitted time epochs have a nominal bit duration of T seconds, then transmit time epochs are given by

$$T(t_j) = T_0 + jT + \epsilon_j \quad (14)$$

where

$$\epsilon_j = (T_0 + jT) \quad (15)$$

and

$$t_j = T_0 + jT \quad (16)$$

with ϵ_j being the transmitted bit jitter process. As we noted above, the time base jitter is assumed to be the linear sum of a random component, plus sinusoidal terms representing the spurs.

It follows that the duration of the j th bit has a duration $D(t)$ given by

$$D(t_j) = T(t_{j+1}) - T(t_j) = T + (\epsilon_{j+1} - \epsilon_j) \quad (17)$$

Hence, the duration is nominally T seconds but is perturbed according to $(\epsilon_{j+1} - \epsilon_j)$, which is a random sequence. In other words, the duration of the bit integration time (bit synchronizer estimate of the bit duration) is a random sequence varying around the mean value of T seconds, with $1/T = R$ the bit rate.

Hence, we see that the effect of duration jitter is to expand and contract the bit integration time. Consider Figure 6, which illustrates (a) a zero timing error at both edges, and (b) consecutive timing errors ϵ_1 and ϵ_2 .

Note first that if $|\epsilon_1| > |\epsilon_2|$, then duration jitter has no effect. Secondly, if the timing error process has most of the bit jitter noise spectral density located below the data rate, then $\epsilon_1 \approx \epsilon_2$ and again bit duration does not contribute to BER. We conclude that bit duration jitter has a much smaller component of BER degradation than bit jitter itself.

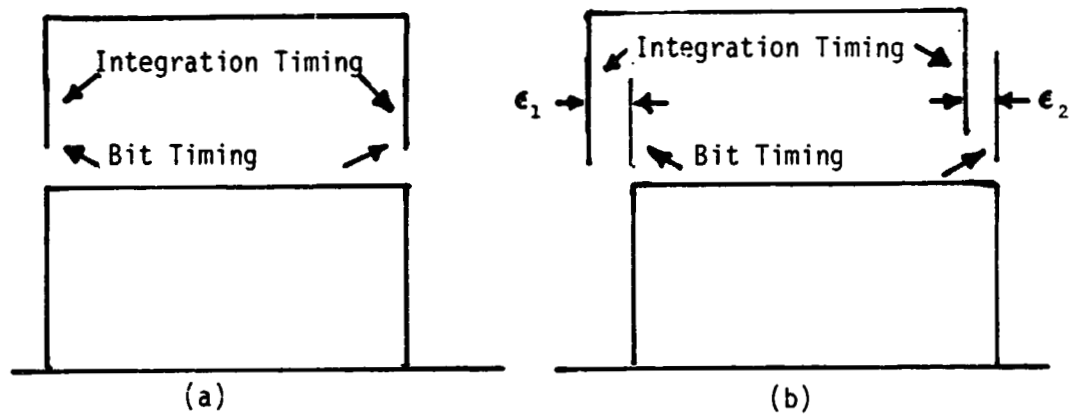


Figure 6. NRz Example of Duration Jitter

- (a) No Error
- (b) Errors ϵ_1 and ϵ_2

The above discussion is for NRZ, but the same argument applies to Bi- ϕ -L data too, that is, bit duration is small compared to the bit timing error.

4.0 BIT ERROR RATE PROBABILITY FORMULATION

To estimate the bit error rate, we consider the bit timing jitter which can be broken up into (a) a component slow compared to the data rate and (b) a component fast compared to the data rate. For convenience, we use the frequency $f=R_b$ (the data rate) as the dividing point between region (a) and (b). Then we model the bit timing error $\epsilon(t)$ as the sum of two statistically independent processes in the form

$$\epsilon(t) = \epsilon_L(t) + \epsilon_H(t) \quad (18)$$

with $\epsilon_L(t)$ the below R_b timing error component and $\epsilon_H(t)$ is above R_b timing error component. We, then, assume that $\epsilon_L(t)$ is constant over the duration of one bit time and $\epsilon_H(t)$ varies very fast over one bit time. Let the respective variances be given by σ_L^2 and σ_H^2 . Now the bit error rate, given that a transition occurs, is given by

$$PE(\epsilon | Tr) = Q[\sqrt{2R^1} (1 - \frac{2|\epsilon|}{T})] \quad (19)$$

where
$$Q(x) = \int_x^\infty \frac{1}{\sqrt{2\pi}} e^{-t^2/2} dt \quad (20)$$

$$R^1 = E[1 - \frac{2|\epsilon|}{T}] \quad (21)$$

or
$$R^1 = \frac{1}{\sqrt{2\pi}\sigma_H} \int_{-\infty}^{\infty} [1 - \frac{2|\epsilon_H|}{T}] e^{-\epsilon_H^2/2\sigma_H^2} d\epsilon_H \quad (22)$$

Also, the bit error rate, given that no transition occurs, is given by

$$PE(\epsilon | \bar{Tr}) = Q[\sqrt{2R''} (1 - \frac{4|\epsilon|}{T})] \quad |\epsilon| \leq \frac{T}{4} \quad (23)$$

where
$$R'' = E[1 - \frac{4|\epsilon|}{T}] \quad (24)$$

or
$$R'' = \frac{1}{\sqrt{2\pi}\sigma_H} \int_{-\infty}^{\infty} [1 - \frac{4|\epsilon_H|}{T}] e^{-\epsilon_H^2/2\sigma_H^2} d\epsilon_H \quad (25)$$

and, therefore, the resulting probability of error, for equally likely data, is given by

$$PE = \frac{1}{4\pi\sigma_L} \int_{-\infty}^{\infty} \frac{e^{-\epsilon_L^2/2\sigma^2}}{e^{-t^2/2}} dt d\epsilon_L + \frac{1}{4\pi\sigma_L} \int_{-\infty}^{\infty} \frac{e^{-\epsilon_L^2/2\sigma^2}}{\sqrt{2R^2(1-\frac{2|\epsilon_L|}{T})}} e^{-t^2/2} dt d\epsilon_L \quad (26)$$

where $N_L \ni f_{N_L} \leq R_b$

$$\sigma_L^2 = 2 \int_0^{R_b} |1-H(f)|^2 \mathcal{P}_C(f) df + \sum_{k=1}^{N_L} |1-H(f_k)|^2 \frac{B_k^2}{2} \quad (27)$$

$$\sigma_H^2 = 2 \int_{R_b}^{f_u} |1-H(f)|^2 \mathcal{P}_C(f) df + \sum_{k=N_L}^{N_U} |1-H(f_k)|^2 \frac{B_k^2}{2} \quad (28)$$

where $f_{N_L} \leq R_b$ (29)

$$f_{N_L} + 1 \geq R_b \quad (30)$$

and also,

$$f_{N_U} \approx BW_i \quad (31)$$

with BW_i being the bandwidth into the bit synchronizer.

5.0 NUMERICAL EVALUATION OF σ_{ϕ}^2

We need to evaluate the value of

$$\sigma_{\phi}^2 = 2 \int_0^{f_u} \mathcal{S}_{\phi}(f) |1-H(f)|^2 df, \text{ rad}^2 \quad (32)$$

with f_u being the upper limit of the timing jitter noise, as determined by the bandwidth into the bit synchronizer (250 kHz). R. Helgeson, has indicated to the author that the bit synchronizer loop bandwidth is between 2 and 10 Hz. Assuming a damping factor of 0.707, we have that

$$|1-H(f)|^2 = \frac{f^4}{f^4 + f_n^4} \quad (33)$$

and $f_n = 0.3B_L = 0.6$ to 3 Hz. To obtain worst case, we let $f_n = 0.6$ Hz. Then (32) becomes

$$\sigma_{\phi}^2 = 2 \int_0^{f_u} \mathcal{S}_{\phi}(f) \frac{f^4}{f^4 + 0.1296} df \quad (34)$$

where f_u is the upper frequency limit and is 250 kHz, as is clear from the low-pass filter feeding the 3 bit A/D converter in Figure 3.

Evaluating the integral yields the bit jitter

$$\sigma_{\phi} = 0.64^{\circ} \quad (35)$$

or

$$\frac{\epsilon_L}{T} = 0.00178, \text{ fractions of a bit} \quad (36)$$

Note that we have included all the bit timing jitter (phase noise) as being below the data rate; whereas, a major portion exists above the data rate. However, this approach bounds the performance, since any other apportionment yields lower PE.

6.0 EVALUATION OF THE BER DEGRADATION

Using the worst case assumption for the phase (assumes that all the non zero density exists below R_b) yields a worst case estimate for the BER degradation. Using the value of 0.00178, we find using equation (26) or equivalently Figure 12.21 of Holmes [1], that 0.4 dB degradation occurs at $\frac{\epsilon_L}{T} = 0.015$.

Using linear extrapolation, again, a pessimistic assumption yields an estimated degradation of 0.04dB!

We have not included thermal noise, nor the fact that the loop is actually a discrete loop in our BER degradation estimate. It was understood that, the intent of the analysis was to ascertain the degradation based on bit timing jitter only, and not thermal effects or imperfections in the loop.

CONCLUSION

It was determined that the bit error rate (BER) degradation, due to DCU bit timing jitter, is approximately 0.04 dB. It is concluded that this is a negligible amount of degradation. Neither thermal noise, nor the discrete nature of the loop has been included in this analysis. It is felt that a full bore simulation would be needed to estimate the effects of the discrete loop. However, it is doubtful whether the discrete nature of the loop would add more than 0.1 dB. It was concluded that, due to the very involved nature of the loop, it would not be reasonable to construct a simulation.

REFERENCES

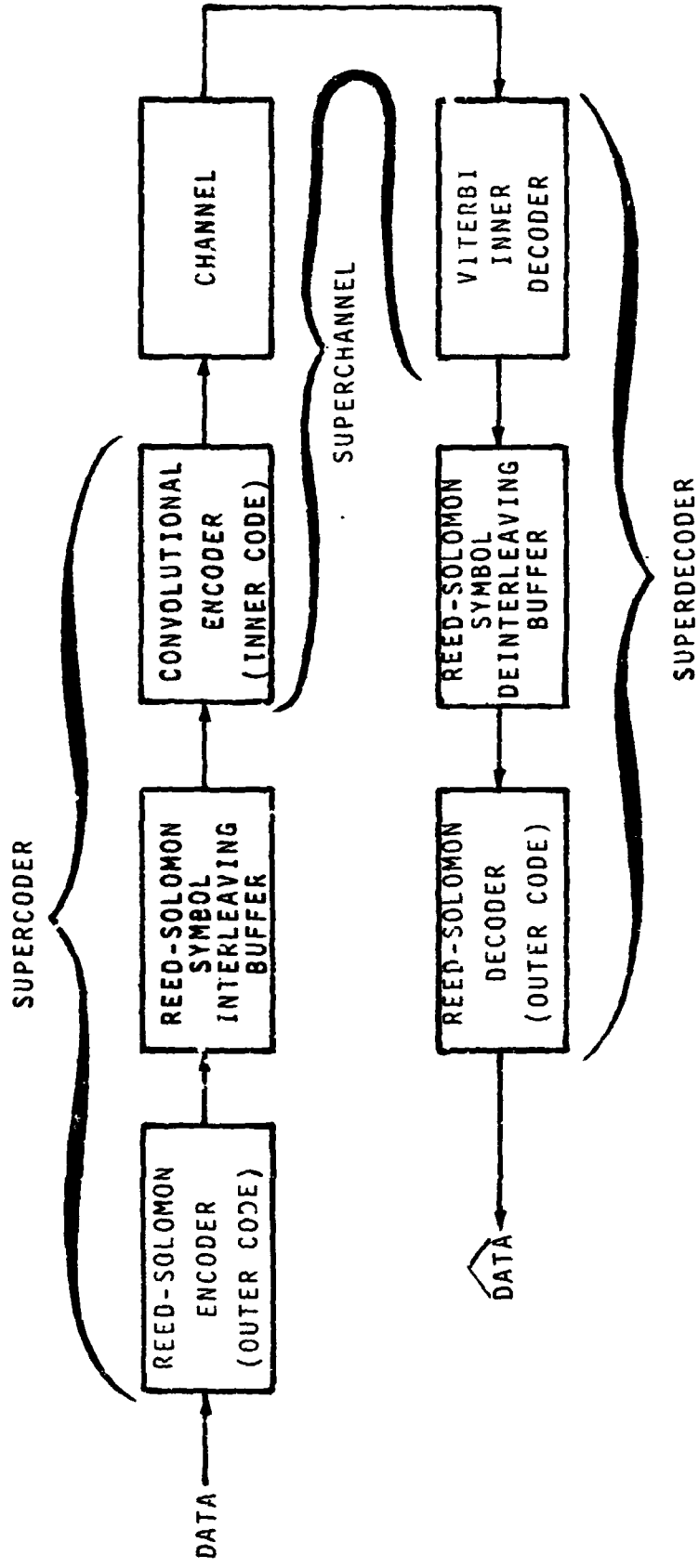
15

1. J.K. Holmes, "Coherent Spread Spectrum Communication," Chapter 12, 1984.
2. H.J. Choi, C.M. Chie, W.C. Lindsey, T. McKenzie, "Centaur Data Bit Jitter Test Results," Prepared for NASA Goodard Space Flight Center, March 20, 1984, Report No. TR-0384-8214-200, LinCom Corporation.
3. M.K. Simon, K. Tu and B.H. Batson, "Effects of Data Asymmetry on Shuttle Ku-Band Communications Link Performance," IEEE Transactions on Communications, Part I, November, 1978.

ADDENDUM 6

**PERFORMANCE ANALYSES OF USING CONCATENATED-CODING
FOR CENTAUR SIGNALING THROUGH TDRSS**

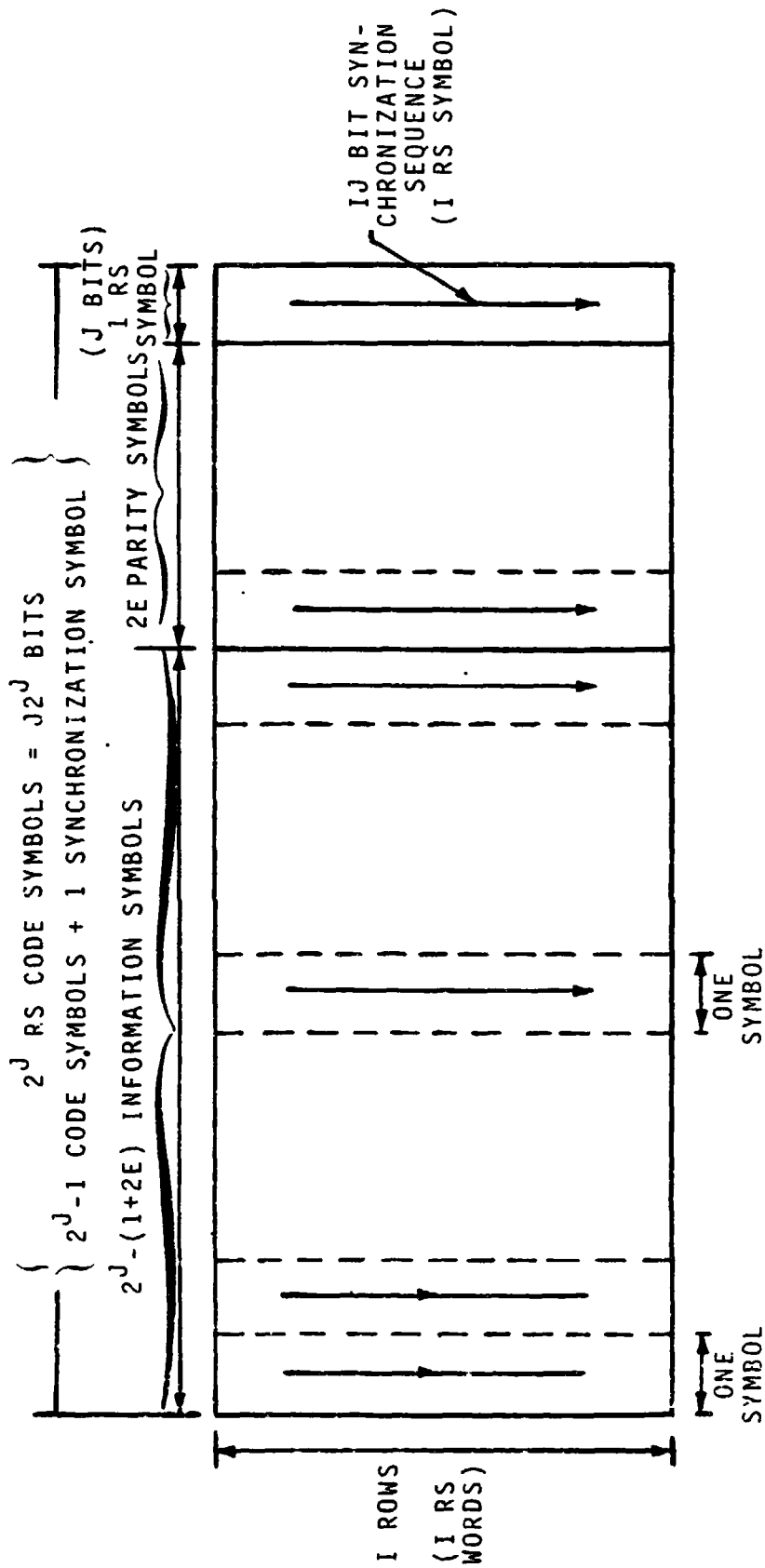
CONCATENATED CODING SCHEME WITH REED-SOLOMON
OUTER CODE AND CONVOLUTIONAL INNER CODE



INNER AND OUTER CODING PARAMETERS

- INNER CODE PARAMETERS
 - CONVOLUTIONALLY ENCODED
 - VITERBI DECODING
 - $R = 1/n$ (1/2)
 - CONSTRAINT LENGTH = K (7)
- OUTER CODE PARAMETERS
 - REED-SOLOMON (n, k) CODE
 - J = NUMBER OF BITS PER RS SYMBOL
 - $n = 2^J - 1$ NUMBER OF SYMBOLS PER RS CODEWORD (255)
 - E = NUMBER OF ERRORS THAT CAN BE CORRECTED (16)
 - $k = n - 2E$ NUMBER OF RS SYMBOLS (OUT OF n) REPRESENTING INFORMATION (223)

PERIODIC BLOCK INTERLEAVER STRUCTURE



NOTES

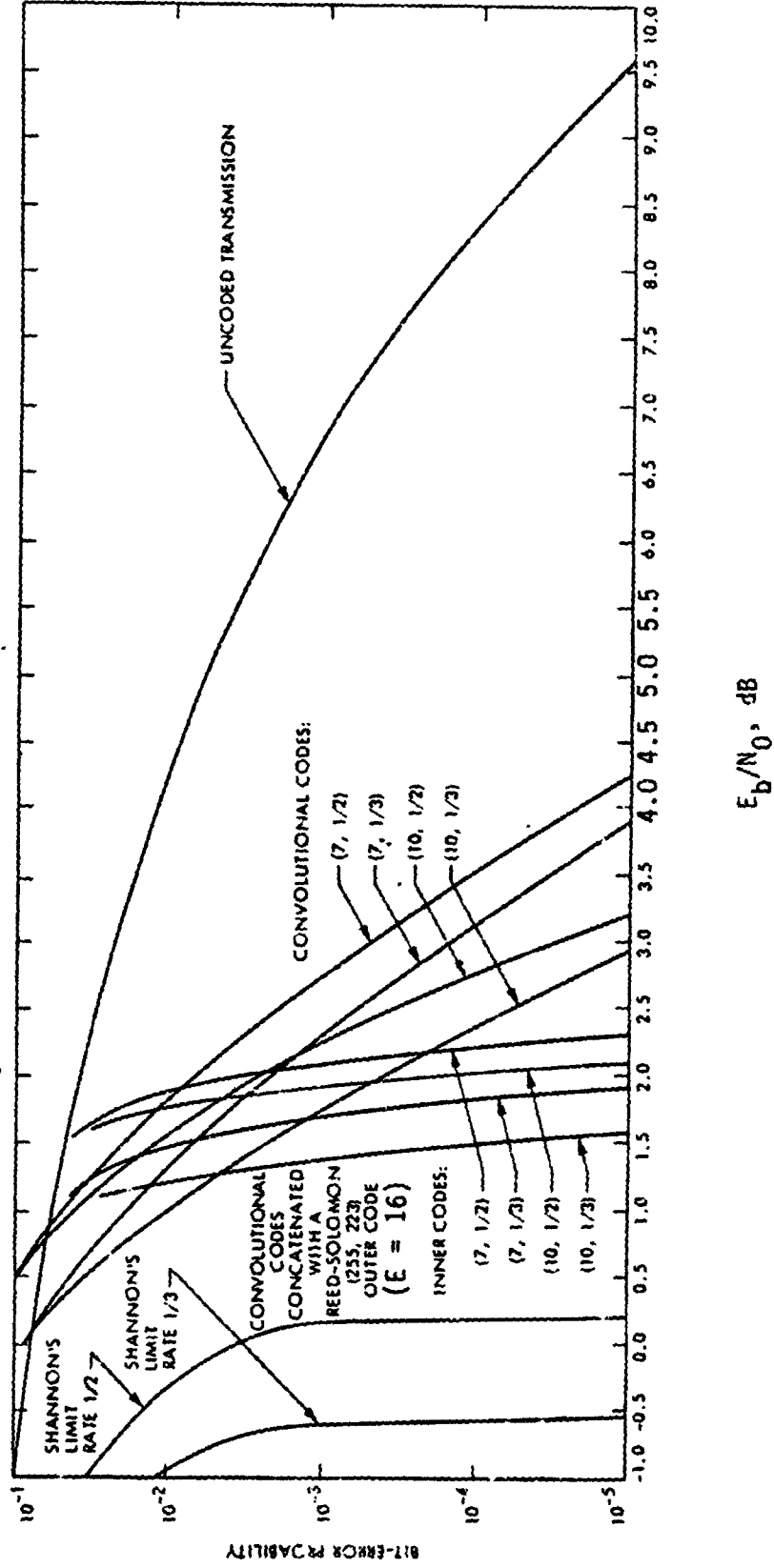
(DELAY = I WORDS = $I \cdot 2^J$ RS SYMBOLS = $I \cdot 2^J$ BITS)

($I \geq 16$ TYPICALLY FOR $K = 7$)

(J BITS PER RS CODE SYMBOL)

CODES	$PE_b = 10^{-3}$	$PE = 10^{-5}$	$PE = 10^{-7}$
(a) CONVOL-VITERBI K = 7, R = 1/2	4.0	5.35	6.0
(b) CONVCL-VITERBI K = 7, R = 1/3	4.6	5.75	6.4
(c) CONCAT RS: CONVOL E = 16 (255,223), (7, 1/2)	4.7	7.3	8.85
(d) CONCAT RS: CONVOL E = 16 (255,223), (7, 1/3)	5.1	7.7	9.2
• COMPARISON			
$\Delta((a)-(c))$	0.7	1.95	2.85
$\Delta((a)-(d))$	1.1	2.35	3.2

A COMPARISON OF SEVERAL CODING SCHEMES (SIMULATION)



CONSEQUENCES OF ADDING REED-SOLOMON
ENCODING AND DECODING



- REQUIRES RS ENCODER/DECODER
- REQUIRES RS INTERLEAVER/DEINTERLEAVER (BUFFER)
- INCREASED DECODING DELAY
- REQUIRES SYNCHRONIZATION SYMBOLS FOR RS SYMBOL SYNCHRONIZATION
- POSSIBLE INCREASED NODE SYNCHRONIZATION ERRORS (CATASTROPHIC)
- SOME LOSS OF CODING GAIN MAY OCCUR IF RS DECODING IS DONE
AT THE CENTAUR OPERATIONS CENTER

TECHNICAL MEMORANDUM NO. M8404-1

TO: S. Novasad

DATE: April 6, 1984

FROM: U. Cheng

FILE: NAS9-16893

SUBJECT: Bit-Error Rate of the Concatenated-Coding System
With Multiple Encryptors

1.0 SUMMARY

The bit-error rate (BER) performance of a single-channel concatenated-coding system with multiple encryptors is discussed in this memorandum. The general block diagram of this system is shown in Figure 1. The BER's of this system at the output of the RS decoder and each decryptor are shown in Figure 2. At $BER = 10^{-3}$, decryptor #1 causes a degradation of 0.14 dB, decryptor #2 causes an additional degradation of 0.023 dB and decryptor #3 causes an additional degradation of 0.01 dB. It is also worth noting that, due to the steepness of the curves, a small amount of degradation in SNR still implies a large difference in BER. All results presented in this memo are for the ideal concatenated-coding system. The effect of antenna dropout is not included.

2.0 INTRODUCTION

The BER performance of a single-channel concatenated-coding system with multiple encryptors is discussed in this memorandum. The general block diagram of this system is depicted in Figure 1.

The decryptor output-error model described in [1] can be summarized as follows:

- Each decryptor input error bit will result in an output error burst of a fixed length of 100 bits and a fixed bit-error density of 0.5
- If two input error bits are separated by less than 100 correct bits, the corresponding two output 100-bit error bursts abut or overlap to form an extended-length error burst with the bit-error density remaining 0.5.

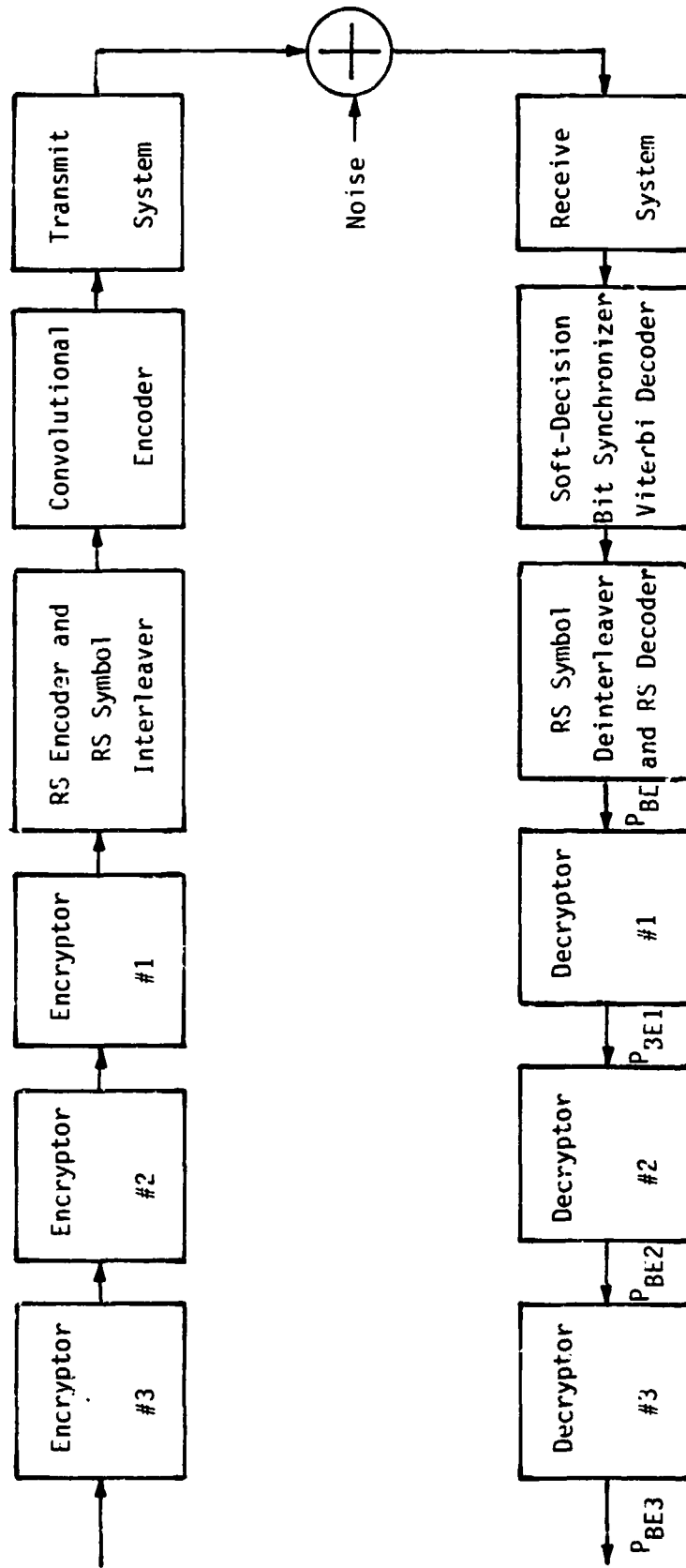
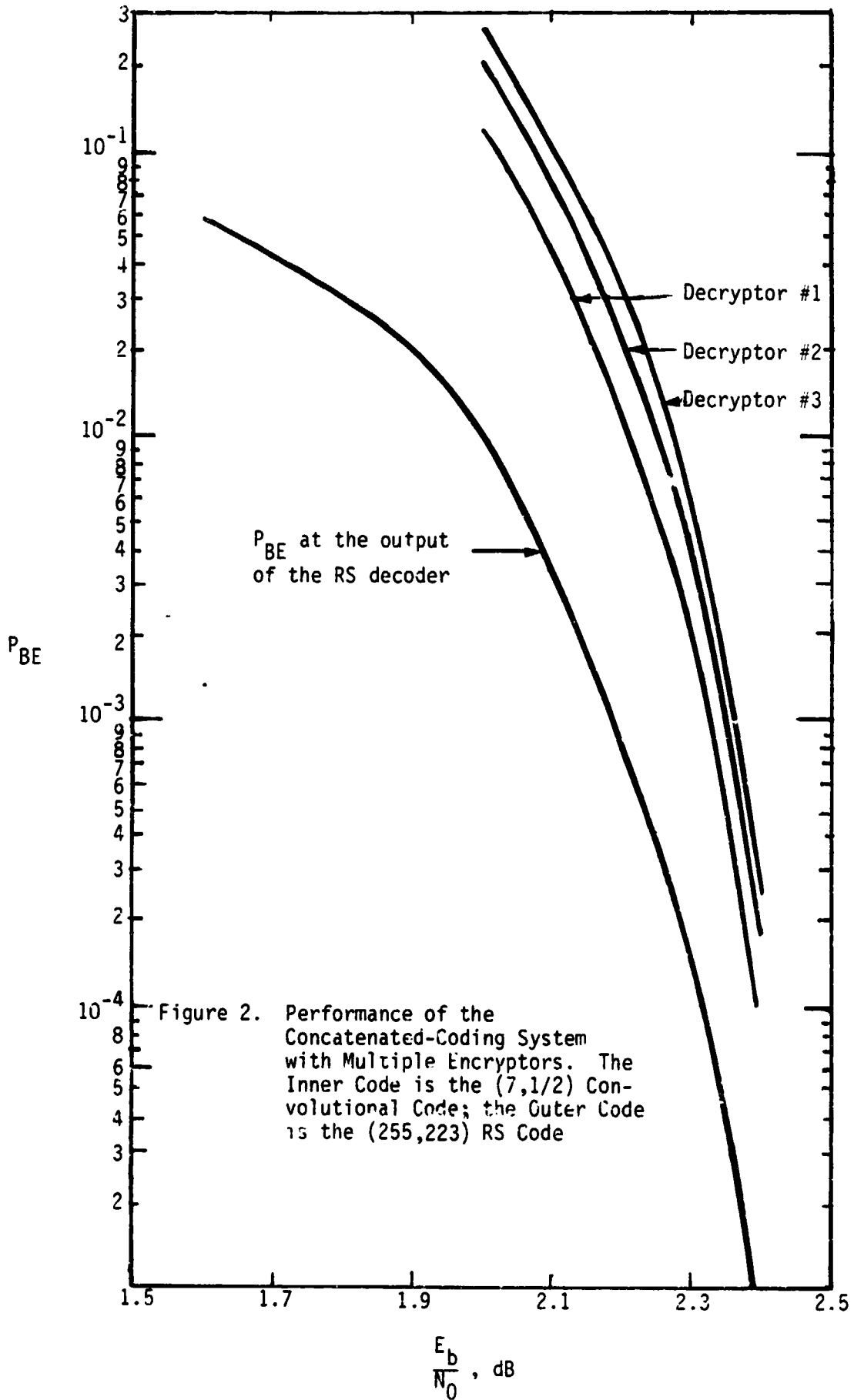


Figure 1. The Concatenated-Coding System with Multiple Encryptors



Let us call a string of correct bits of length N which is sandwiched by two error bits as a wait of length N . Based on the above model, it is clear that a wait of length $N \geq 100$ in the input of the decryptor will result in a wait of length $N-99$ in the output of the decryptor. If all three decryptors shown in Figure 1 are identical, we have the result shown below.

Lemma

Let

N_j = the length of a wait in the output of decryptor #j,
 $1 \leq j \leq 3$

and

N_0 = the length of a wait in the output of the RS decoder.

A wait of length N_0 in the output of the RS decoder will then result in a wait of length N_j in the output of decryptor #j such that

$$N_j = \begin{cases} 0 & \text{if } N_0 \leq 99j \\ N_0 - 99j & \text{if } N_0 \geq 99j + 1 \end{cases} \quad (1)$$

The above result can be understood by a simple example. A wait of length 300 in the output of the RS decoder will result in a wait of length 201 in the output of decryptor #1. This wait of length 201 will then result in a wait of length 102 in the output of decryptor #2. Finally, a wait of length 3 will result in the output of decryptor #3.

3.0 DECRYPTOR OUTPUT BER

Since the output of the RS decoder has very complicated error statistics, some assumptions must be made. We assume that the eight-bit RS symbols in the output of the RS decoder are mutually independent. Let P_{SE} denote the RS symbol-error probability and P_{BE} denote the bit-error probability. It is well known that

$$P_{BE} = \frac{2^{l-1}}{2^l - 1} P_{SE}$$

where we assume that each RS symbol contains ℓ bits. If the eight-bit RS symbol is considered, one has

$$P_{BE} = 0.502 P_{SE}$$

Letting L_S = the length of a run of incorrect RS symbols and N_S = the length of a run of correct RS symbols, clearly

$$\text{Prob}\{N_S = n\} = (1 - P_{SE})^{n-1} P_{SE} \quad (3)$$

and

$$\text{Prob}\{L_S = \ell\} = P_{SE} (1 - P_{SE})^{\ell-1} \quad (4)$$

Therefore,

$$\bar{L}_S = E\{L_S\} = \frac{1}{1 - P_{SE}} \quad (5)$$

and

$$\bar{N}_S = E\{N_S\} = \frac{1}{P_{SE}} \quad (6)$$

Now, a wait of length N_S RS symbols in the output of the RS decoder will result in a wait of length N_j bits in the output of decryptor #j such that

$$N_j = \begin{cases} 0 & , & \text{if } N_S \leq C_{Sj} - 1 \\ 8N_S - 99j & , & \text{if } N_S \geq C_{Sj} \end{cases} \quad (7)$$

where

$$C_{Sj} = \begin{cases} 13 & \text{if } j=1 \\ 25 & \text{if } j=2 \\ 38 & \text{if } j=3 \end{cases}$$

It is easy to see that

$$\text{Prob}\{N_S \geq C_{Sj}\} = (1 - P_{SE})^{C_{Sj}-1}$$

and

$$E\{N_S | N_S \geq C_{Sj}\} = \frac{\sum_{n=C_{Sj}}^{\infty} n(1 - P_{SE})^{n-1} P_{SE}}{(1 - P_{SE})^{C_{Sj}-1}} = \frac{1 + (C_{Sj} - 1)P_{SE}}{P_{SE}}$$

Therefore, the BER in the output of decryptor #j can be expressed as

$$P_{BEj} = \frac{1}{2} \left(1 - \frac{\text{Prob}\{N_S \geq C_{Sj}\} E\{N_j\}}{8(\bar{L}_S + \bar{N}_S)} \right) = \frac{1}{2} \left(1 - (1 - P_{SE})^{C_{Sj}-1} \left(1 + (C_{Sj} - 1) \left(1 - \frac{99j}{8} \right) P_{SE} \right) \right)$$

Hence, one ends up with

$$P_{BE1} = \frac{1}{2} \left(1 - (1 - P_{SE})^{13} \left(1 - \frac{3}{8} P_{SE} \right) \right) \quad (8)$$

$$P_{BE2} = \frac{1}{2} \left(1 - (1 - P_{SE})^{25} \left(1 - \frac{6}{8} P_{SE} \right) \right) \quad (9)$$

$$P_{BE3} = \frac{1}{2} \left(1 - (1 - P_{SE})^{38} \left(1 - \frac{1}{8} P_{SE} \right) \right) \quad (10)$$

Given P_{BE} at the output of the RS decoder, P_{BE1} , P_{BE2} and P_{BE3} can be computed by (2), (8), (9) and (10). These results are plotted in Figure 2. At $BER = 10^{-3}$, decryptor #1 causes a degradation of 0.14 dB, decryptor #2 causes an additional degradation of 0.023 dB, and decryptor #3 causes an additional degradation of 0.01 dB. It is also worth noting that, due to the steepness of the curves, a small amount of degradation in SNR still implies a large difference in BER.

Reference

1. E. E. Dodd, "Encoded Multiple-Encrypted Data Transmission Bit Error Rate," Lockheed Services Technical Report, December 1983.

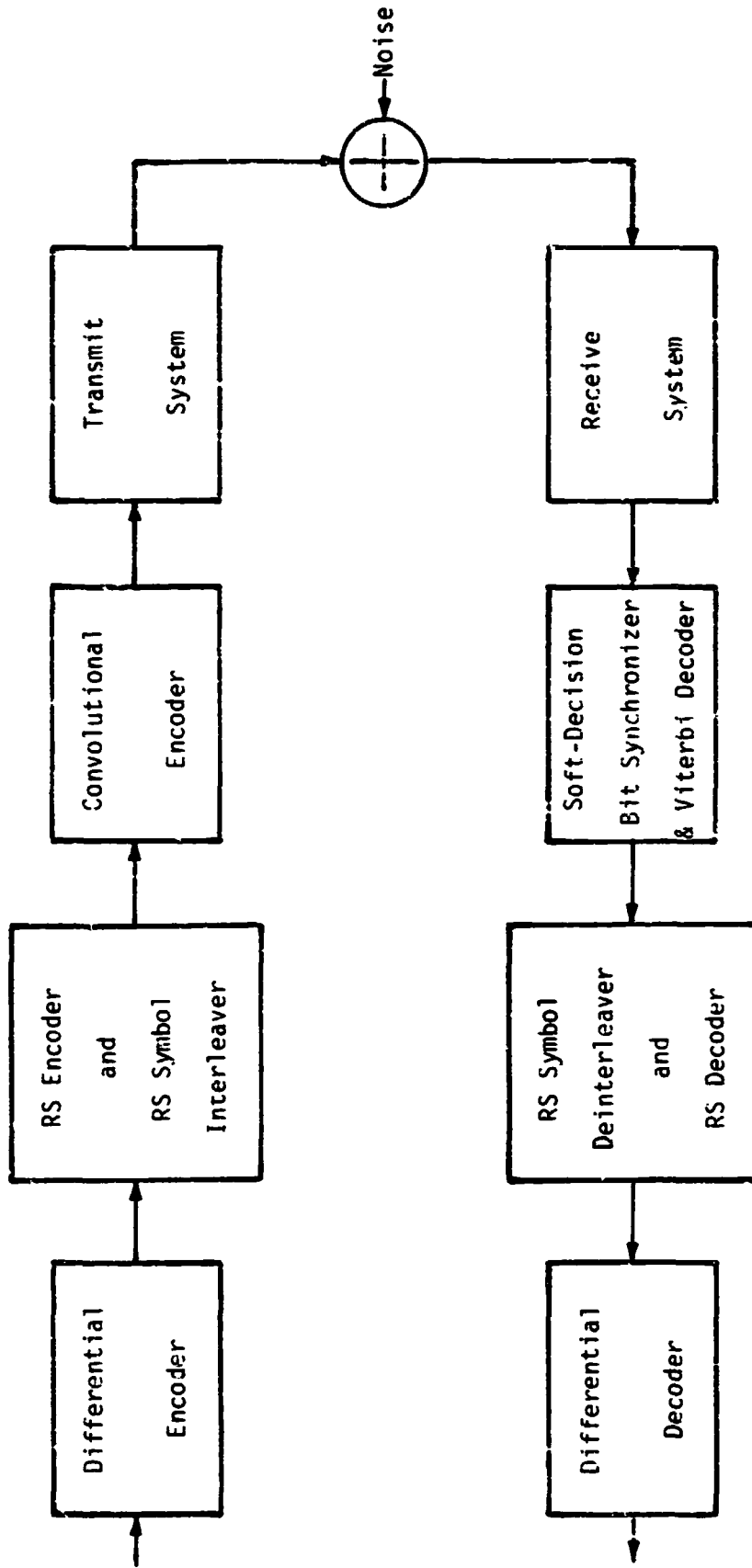


Figure 1. The Concatenated-Coding System with Differential Encoding; The First Method

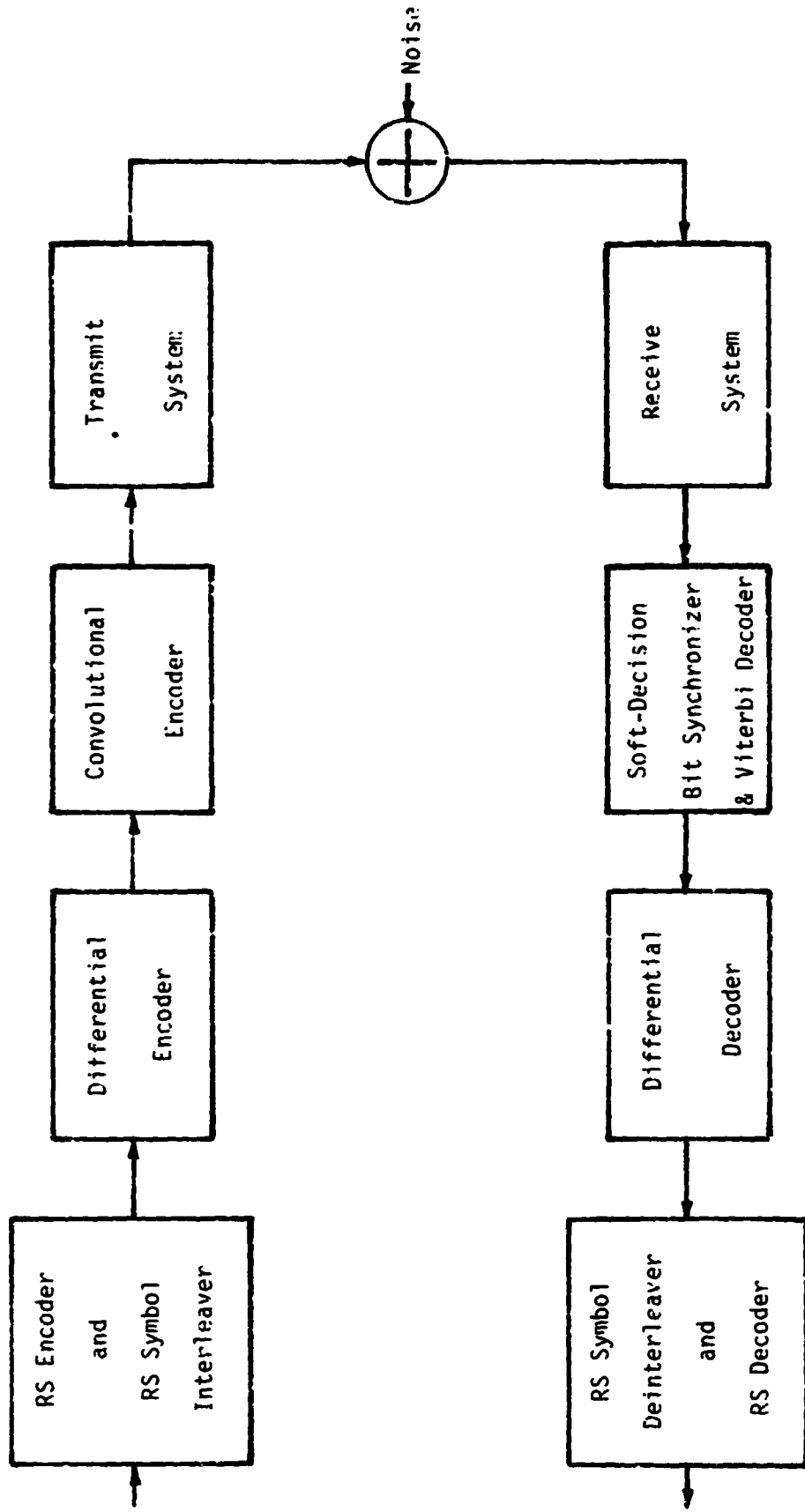


Figure 2. The Concatenated-Coding System with Differential Encoding; The Second Method

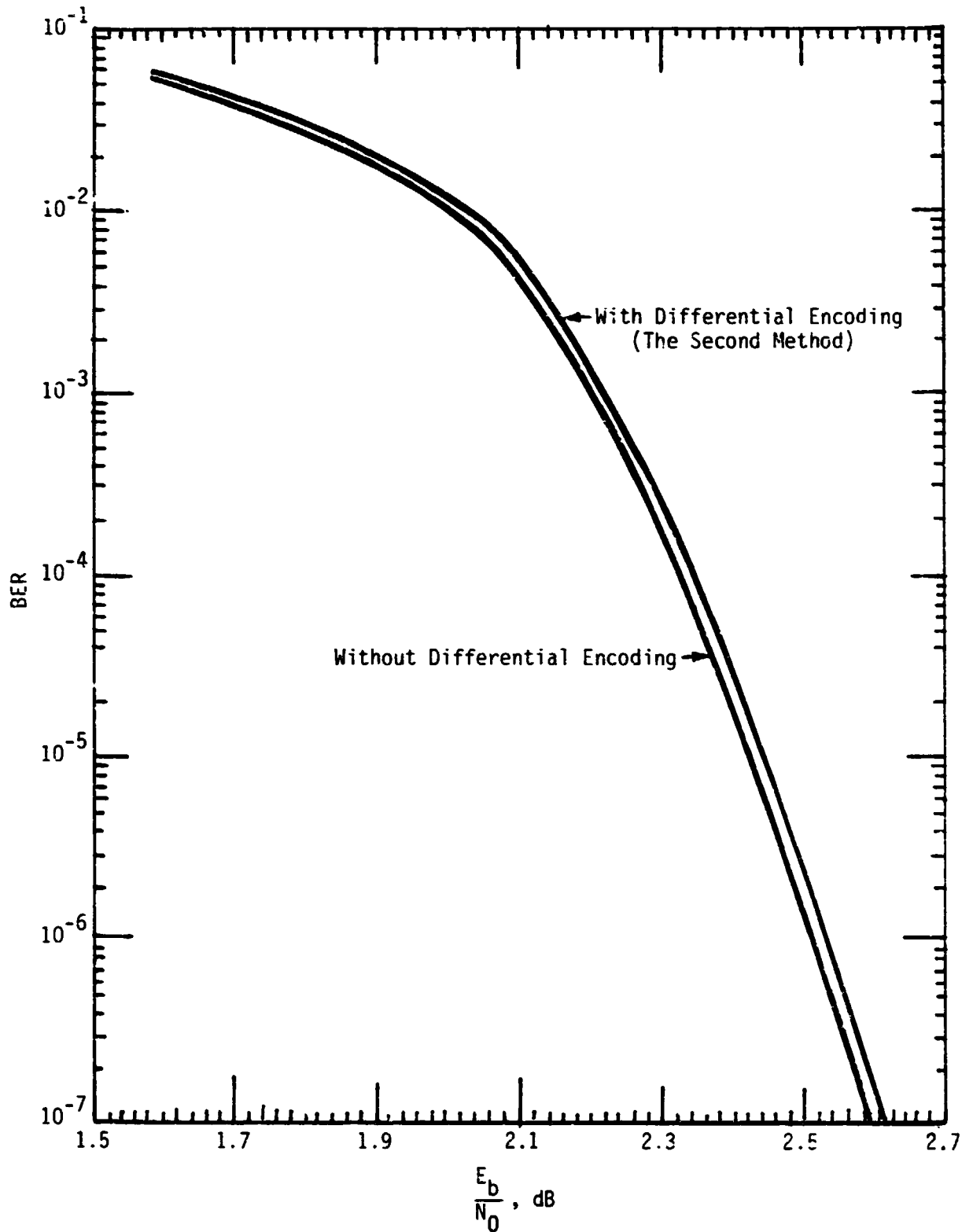


Figure 3. The BER of the Concatenated-Coding System With and Without Differential Encoding; The (7,1/2) Convolutional and the (255,223) RS Codes Are Used

Let us consider the second method in the following. We first note that the Viterbi decoder will generate error bursts at its output. The differential decoder will then process the data with these error bursts. After passing the differential decoder, the number of error bursts will not be changed and the length of each error burst will be increased by one. Assume that there are M error bursts in a string of N output bits at the output of the Viterbi decoder. Let B_1, B_2, \dots, B_M denote the length of these M error bursts. For the case without differential encoding, the number of ℓ -bit RS symbols which can be in error is upper bounded by [2]

$$\sum_{i=1}^M \frac{B_i + \ell - 1}{\ell} \quad (1)$$

Therefore, the RS symbol error probability at the input of the RS decoder is

$$P_{\text{CSE}} = \frac{\sum_{i=1}^M \frac{B_i + \ell - 1}{\ell}}{\frac{N}{\ell}} = \frac{(\ell-1)M}{N} + \frac{\sum_{i=1}^M B_i}{N} \quad (2)$$

For the case with differential encoding, the number of ℓ -bit RS symbols which can be in error is upper bounded by

$$\sum_{i=1}^M \frac{(B_i+1) + \ell - 1}{\ell} \quad (3)$$

Therefore, the RS symbol error probability at the input of the RS decoder is, in this case, given by

$$P_{\text{CSE}} = \frac{\ell M}{N} + \frac{\sum_{i=1}^M B_i}{N} \quad (4)$$

Let P_{BE1} = bit-error probability in the output of the Viterbi decoder, θ = bit-error rate in the error bursts at the output of the Viterbi decoder, and P_{Burst} = average number of error bursts in the output of the Viterbi decoder. Then one has

$$P_{CSE} = \begin{cases} \ell P_{Burst} + \frac{P_{BE1}}{\theta} & , \text{ if differential encoding is used} \\ (\ell-1)P_{Burst} + \frac{P_{BE1}}{\theta} & , \text{ if differential encoding is not used} \end{cases} \quad (5)$$

The simulation results on P_{Burst} , P_{BE1} , and θ for (7,1/2), (7,1/3), (10,1/2) and (10,1/3) convolutional codes are available in [2]. The bit-error probability following the RS decoder can be computed by the following equation:

$$P_{BE} \leq \frac{2^{\ell-1}}{2^{\ell} - 1} \sum_{i=e+1}^{\ell} \binom{\ell}{i} \frac{2^{i+e}}{2^{\ell} - 1} P_{CSE} (1 - P_{CSE})^{2^{\ell} - i - 1} \quad (6)$$

where P_{CSE} is the RS symbol error probability at the input of the RS decoder, each RS symbol contains ℓ bits and $2e+1$ is the designed minimum distance of the RS code.

In Figure 3, we show the BER of the concatenated-coding system with and without differential encoding. It shows that the use of differential encoding will cause a degradation of 0.02 dB in a wide range of BER (10^{-3} - 10^{-7}).

References

1. E. R. Berlekamp, "Bit-Serial Reed-Solomon Encoders," IEEE Transactions on Information Theory, Vol. IT-28, No. 6, November 1982, pp. 869 - 874.
2. R.L. Miller, L. J. Deutsch and S. A. Butman, "On The Error Statistics of Viterbi Decoding and the Performance of Concatenated Codes," NASA/JPL Publication No. 81-9, September 1, 1981.

ADDENDUM 7

**INVESTIGATION OF POTENTIAL INTERFACE
BETWEEN THE SHUTTLE AND THE SPACE STATION**

SPACE STATION RETURN-LINK
MULTIPLE-ACCESS COMMUNICATION STUDY

Interim Report

Prepared by

James Dadds
Richard Iwasaki
Peter Nilsen
Don Roberts
Sergei Udalov

Axiomatix
9841 Airport Blvd., Suite 912
Los Angeles, California 90045

Axiomatix Report No. R8310-3
October 14, 1983

TABLE OF CONTENTS

	<u>Page</u>
LIST OF FIGURES	ii
LIST OF TABLES	iii
1.0 INTRODUCTION	1
2.0 EXECUTIVE SUMMARY	2
3.0 BASELINE COMMUNICATION REQUIREMENTS	4
4.0 MULTIPLE-ACCESS LINK-DESIGN TRADE-OFFS	7
4.1 Frequency-Division Multiple-Access	7
4.1.1 Introduction	7
4.1.2 Discussion	7
4.2 Frequency-Hop FDMA for Antijam Performance	19
4.2.1 Introduction	19
4.2.2 Discussion	19
4.3 Time-Division Multiple-Access Return Links	27
4.3.1 Introduction	27
4.3.2 Baseline TDMA System Example	27
4.4 TDMA and Antijam Modulation	34
5.0 MULTIPLE-ACCESS ANTENNA-DESIGN CONSIDERATIONS	48
APPENDIX A - VIDEO DATA-COMPRESSSION TECHNIQUES STUDY	

LIST OF FIGURES

	<u>Page</u>
4.1 The FDMA Concept as Applied to the Communication Satellite Repeater	8
4.2 Typical MOTV of EMU FDMA User Return-Link Communication System . .	9
4.3 FDMA Channel Modulation with Ranging Option	10
4.4 Functional Block Diagram of the User FDMA Transmitter/Receiver with a PN Ranging Provision	11
4.5 FDMA Channel Allocation Allowing Maximum Simultaneous Return-Link Services	13
4.6 Comparison of Power Spectral Densities for Various Digital Modulation Formats	14
4.7 FDMA Channel Allocation That Meets User Return-Link Requirements Utilizing the Minimum RF Bandwidth	15
4.8 Space Station FDMA Receiver	16
4.9 Potential AGC Scheme to Accommodate 110-dB Dynamic-Range Requirement	18
4.10 Worst-Case P_b versus E_b/N_j ; FH-QPSK (Tone Jamming)	20
4.11 Basic Phase Estimator for m-FSK Carriers	22
4.12 Functional Block Diagram of the User FH-FDMA Transmitter/Receiver	25
4.13 Space Station FH-FDMA Receiver	26
4.14 TDMA Channelization with M-ary MFSK Modulation	28
4.15 TDMA Receiver	29
4.16 P_T (min) versus Range: Return-Link TDMA (15.84 Mbps)	31
4.17 P_T (min) versus Range: Return-Link TDMA (5.6 Mbps)	32
4.18 P_T (min) versus Range: Return-Link TDMA (484 kbps)	33
4.19 P_T (min) versus Range: TDMA 15.84-Mbps Burst Rate	35
4.20 P_T (min) versus Range: TDMA 5.6-Mbps Burst Rate	36
4.21 P_T (min) versus Range: TDMA 464-kbps Burst Rate	37
4.22 Baseline TDMA/FH System	40
4.23 The 4-ary MFSK with J/S Jamming Tones.	41
4.24 Time/Frequency Utilization with Interleaved TDMA/FM, Multiple Symbols per Hop.	43
4.25 m-Diversity Frequency Hopping.	47
5.1 Gains and Beamwidths of Commercially Available Parabolic-Dish Antennas	51
5.2 CCD Video-Camera Candidate for Visual-Acquisition Aid	53
5.3 Hemispheric Array of Parabolic Dishes	54
5.4 RF Switching Network Using Ferrite-Latching Circulators	56
5.5 Five-Horn Cross Feed with Dielectric Polarizers and Orthomode Transducer for Transmit/Receive	57

LIST OF TABLES

	<u>Page</u>
3.1 Baseline User Group, MA Return Link	5
3.2 Expanded User Group, MA Return Link	5
4.1 Hard-Decision Coded-FH Performance	23
4.2 Hard-Decision Coded-FH/PN Performance	23
4.3 Summary of AJ Performance for SS FH-FDMA System	24
4.4 Energy Per Bit and Bandwidth (Unhopped) Required as a Function of Signal Alphabet with Noncoherent Demodulation, $P_B \leq 10^{-5}$	39
4.5 Energy Per Bit Required, $P_B \leq 10^{-2}$	39
4.6 Maximum J/S with $E_c/N_j = 20$ dB, $R = 15.84$ Mbps	44
4.7 Maximum J/S with $E_c/N_j = 10.4$ dB, $R = 15.34$ Mbps	46
5.1 Idealized Planar-Phased-Array Parameters for Various Gain Levels	49
5.2 Parabolic-Dish Dimensions for Higher Gains	52
5.3 Parabolic-Dish Spherical Coverage Using Idealized Gain Values	52

1.0 INTRODUCTION

This report discusses several key issues relating to Space Station (SS) communications. The type of communications discussed are between the SS and a group of 18 users consisting of a combination of free fliers, unmanned orbital-transfer vehicles (OTV's), manned orbital-transfer vehicles (MOTV's), teleoperator maneuvering systems (TV's), and extravehicular mobility units (EMU's). The return-link communications from the aggregate of the users is referred to as the user multiple-access (MA) return link. Because the MA return links must simultaneously support TV links, voice links and telemetry links from a multitude of users, the network comprising these links poses a more difficult design than the forward link (SS to user). Thus, this report concentrates on trade-offs and performance issues for the return MA links.

Since the highest data rate which the MA return link must handle is for digital TV, it is appropriate to include a discussion of digital TV herein. Thus, a comprehensive survey and analysis of digital TV techniques and implementations comprise a vital part of this report. Motivated by a desire to provide AJ protection to the TV links, several digital TV systems capable of bit rates on the order of 2 Mbps are discussed.

The SS MA return-link antenna-design requirements are particularly challenging due to the MA return-link requirement to simultaneously communicate with up to 18 users (to a range of 2000 km). Consequently, Section 5 of this report discusses several antenna approaches that can be considered in meeting these requirements. Also included in Section 5 is the performance of solid-state, low-noise amplifiers (LNA's) and high-power amplifiers (HPA's) as a function of frequency. The performance obtainable from these devices will have a strong influence on the choice of MA link frequency. At present, it is felt that, because of the military-satellite work at 44 GHz and the NASA work at 30 GHz, a good choice of high-performance devices will be available at these frequencies.

2.0 EXECUTIVE SUMMARY

Axiomatix has examined alternative modes of return-link (user to Space Station) multiple-access (MA) communications. Basic requirements of the Space Station (SS) return-link system consist of the following:

(1) service 18 users simultaneously, seven with television (TV) and four with voice

(2) user vehicle range can vary from 100 m to 2600 km.

./ data rates can vary from 2.048 Mbps (compressed) to 64 kbps slow scan. If required, 22 Mbps TV service can be provided by reconfiguring the receiver to a single TV channel and expanding the bandwidth slightly. Telemetry channels run at 64 kbps, which includes user synchronization, and voice (delta modulation) channels run at 16 kbps.

Two methods of MA channelization in the presence of jamming are examined: frequency-division MA (FDMA) and time-division MA (TDMA). A third, code-division MA (CDMA), is not considered practical with this number of users in a jammed environment. Principal trade-offs between FDMA and TDMA are complexity versus timing requirements. FDMA has the following advantages relative to TDMA:

(1) lower burst rate and lower user EIRP

(2) greater MA network capacity in the antijam (AJ) mode.

TDMA has the following advantages relative to FDMA:

(1) less complex receiver hardware

(2) less complex antenna: single-beam versus multiple simultaneous beams

(3) does not require user power control for simultaneous near/far operations.

The SS is assumed to be the master node in either system.

The performance of phase-shift and frequency-shift-keying (FSK) modulation is examined. Quadrature-phase-shift-keying (QPSK) modulation is practical for the longer symbol times used in FDMA. Methods of coherent and noncoherent demodulation are discussed, including a new technique for acquiring rapid phase reference. Multiple-frequency-shift-keying (MFSK) is examined; it is shown that 4-ary MFSK is superior to higher order modulations for conserving the data bandwidth.

For systems-comparison purposes, it is assumed that error-correcting coding is employed, with a channel bit-error rate (BER), P_c , less than 10^{-2} , and a decoder BER, P_B , less than 10^{-5} .

The FDMA system with QPSK and coherent demodulation has the performance edge over TDMA; however, the complexity of the FDMA system, particularly the antenna requirements for 18 simultaneous high-gain beams, may be the deciding factor. At this point, a clear-cut choice of multiple-access technique (i.e., TDMA or FDMA) cannot be made. Further analyses and hardware trade-offs are required.

3.0 BASELINE COMMUNICATION REQUIREMENTS

The communication systems described in subsequent sections address the multiple-access (MA) return-link requirements, which are a subset of the Space Station (SS) communication requirements described in "Space Station Program Description Document, System Requirements and Characteristics, Book 3," published in November 1982. Users in the MA network, derived from Table 2.7-2 of the requirements document, includes six free fliers (FF's), two orbital-transfer vehicles (OTV's), two manned orbital-transfer vehicles (MOTV's), two teleoperation-maneuvering systems (TMS's) and six extravehicular-mobility units (EMU's), for a total of 18 network members. Users range is from 100 m to 2000 km. Each user is given one 64-kbps telemetry channel. In addition, any seven of the 18 users can be given a 2-Mbps TV channel upon request. The manned units require voice on the return link. Any two of the six EMU's and two OTV's can be given a voice channel.

The above requirements are considered a baseline for the MA system. Enhancements will increase the capacity of the system and additional requirements for MA at extreme ranges can reduce system accessibility. The ensemble of users is outlined in Tables 3.1 and 3.2. Table 3.1 shows a baseline group of 18 users, with TV limited to a 2-MHz bandwidth. Table 3.2 depicts an expanded group of users, with one user having a 22-MHz TV channel. The MA user community consists of unmanned OTV's, FF's and TMS's, and manned OTV's and EMU's. The difference in communication requirements between the unmanned and manned units is the voice requirement for the manned units. The exact capacity of the expanded system in mode 2 is dependent on the specific overhead requirements of the various MA schemes considered.

We also discuss the acquisition requirements of the MA schemes considered. Acquisition is a cooperative procedure between the SS and a user requesting access to the network. In particular, accurate time synchronization is needed to accommodate MA waveforms with minimum multiuser interference. The requirement for time synchronization implies that relative ranges be established between the user and the SS, with either a navigation or an acquisition protocol. More detailed discussions of acquisition are covered in later sections describing specific MA schemes, but an underlying assumption is that the SS is the master node.

Table 3.1. Baseline User Group, MA Return Link

Number of Simultaneous Users	Data Type
7 plus 18 plus 4	2 Mbps TV or digital data 64 kbps telemetry, including synchronization bits 16 kbps digital voice

Table 3.2. Expanded User Group, MA Return Link

Mode	Number of Simultaneous Users	Data Type
1	1 plus 18 plus 4	22 Mbps TV 64 kbps telemetry 16 kbps voice
OR		
2	Any combination of 2 Mbps TV, 64 kbps telemetry and 16 kbps voice requiring less than 25 Mbps total capacity	

In addition to range knowledge requirements for time synchronization, MA schemes employing simultaneous reception of energy from multiple users (non-TDMA systems) may require transmit-power control by each user, based on range, in order to ensure that the SS receiver is needed to prevent close-in users from suppressing low-range users. All system designs considered incorporate AJ modulation.

4.0 MULTIPLE-ACCESS LINK-DESIGN TRADE-OFFS

4.1 Frequency-Division Multiple Access

4.1.1 Introduction

This section discusses the use of frequency-division multiple access (FDMA) for meeting the return-link requirements of the users given in Table 3.1. Although the discussion given here addresses a clear mode, i.e., a non-antijam communication network, it will be shown in section 4.2 that the FDMA concepts outlined here can be extended to provide antijam (AJ) protection.

One of the most common uses of FDMA is seen in communication-satellite repeaters, wherein a major communication resource--the satellite repeater--is shared by a large number of users who access the repeater by employing different carrier frequencies. This concept is illustrated in Figure 4.1. Each of the several transponders can be viewed as a separate resource that can be shared by utilizing FDMA. A typical 36-MHz repeater can have an FDMA scheme wherein approximately 1600 users, each having a bandwidth of about 20 kHz, can access the transponder simultaneously. In this discussion, this concept will be extended to the Space Station (SS).

4.1.2 Discussion

The FDMA user return links must be capable of supporting television, voice, and telemetry. For each user, these services could be FDM'd together before transmission. However, since each service would already be digitally encoded, TDMA makes much more sense when combining. This concept is shown in Figure 4.2, which illustrates a typical FDMA user employing all three services, such as MOTV or EMU. Prior to error-correction encoding, the required data rate (referring to Appendix A) would be 2 Mbps for TV, plus 16 kbps for voice, plus 64 kbps for telemetry, or 2.08 Mbps. When rate-1/2 error-correction encoding is used, the symbol rate is 4.16 Msps. QPSK or SQPSK modulation could be used, so that the required RF channel bandwidth would be on the order of $1.5 \times 2.08 \approx 3$ MHz. However, it is desirable to include a ranging capability. This capability is readily provided by means of a PN range code and can be conveniently added via quadrature phase modulation of the carrier, as shown in Figure 4.3. The PN range code could also be added by exclusive OR'ing with the symbol stream that is split in two, which is also shown in Figure 4.3. A top-level functional block diagram of a user transmitter/receiver with ranging provisions is shown in Figure 4.4.

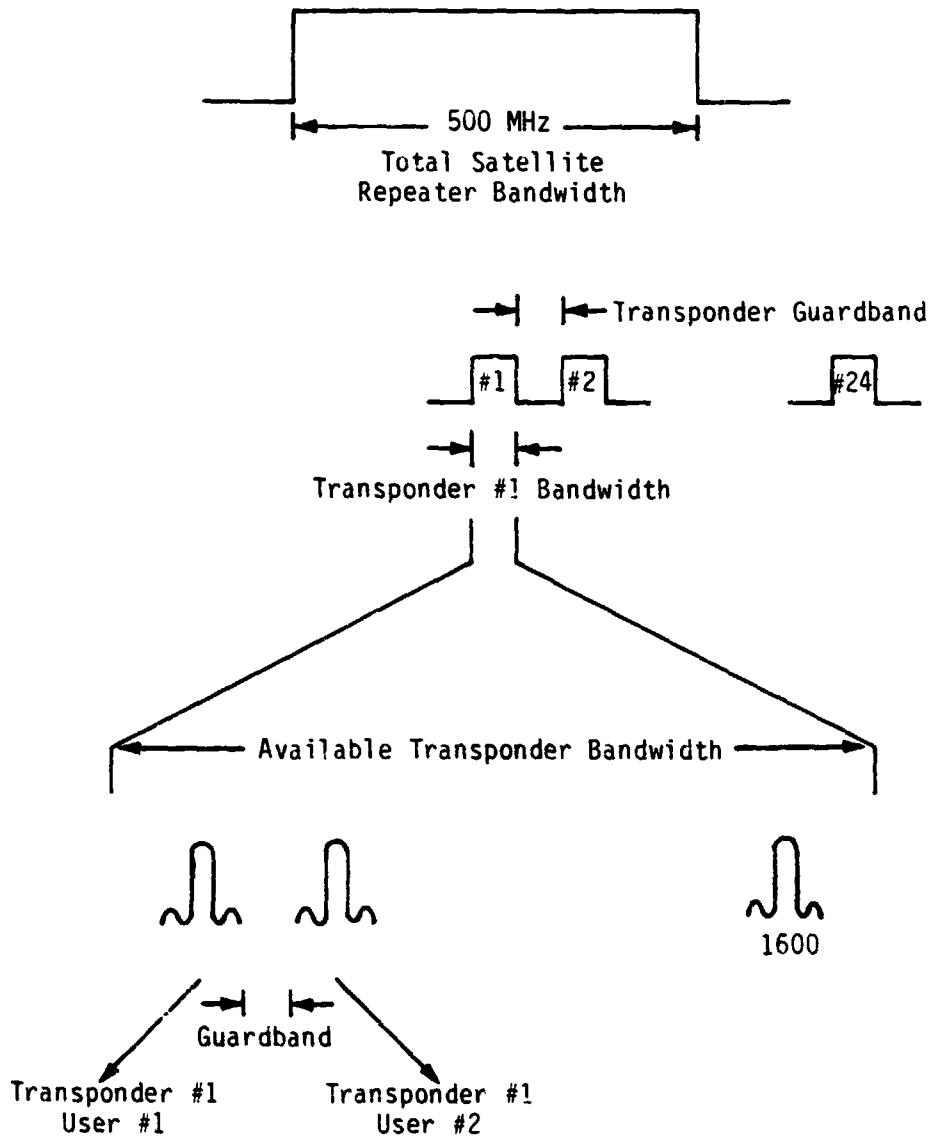


Figure 4.1. The FDMA Concept as Applied to the Communication Satellite Repeater

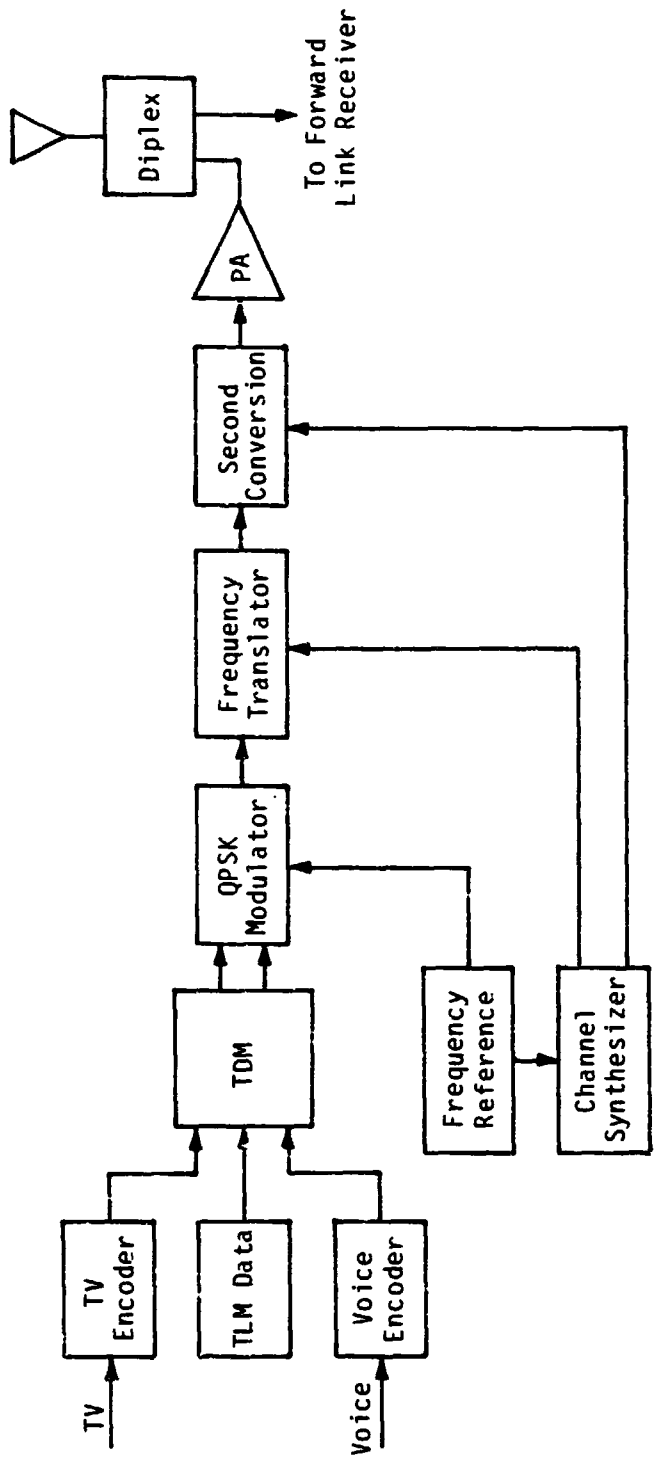
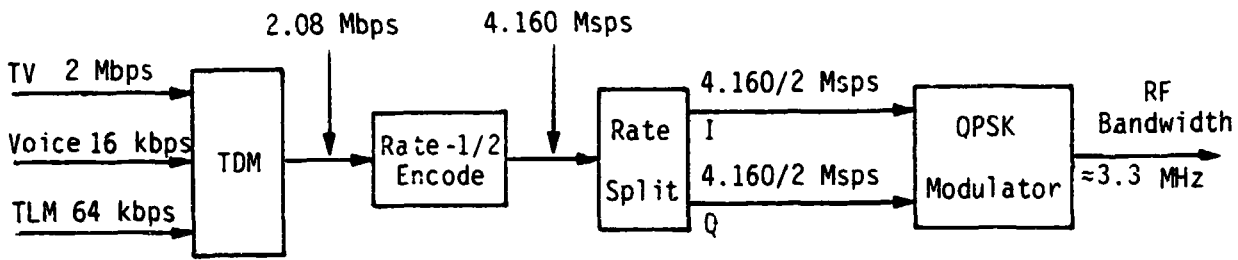
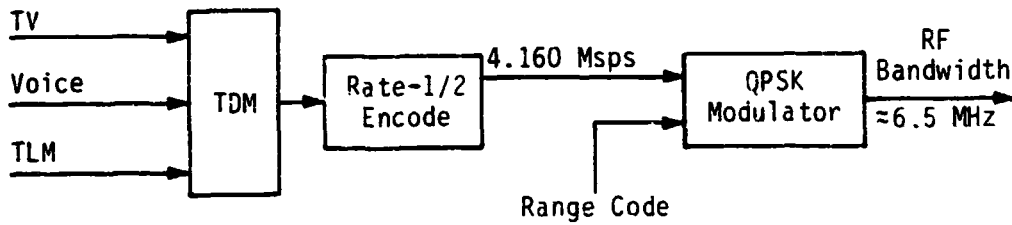


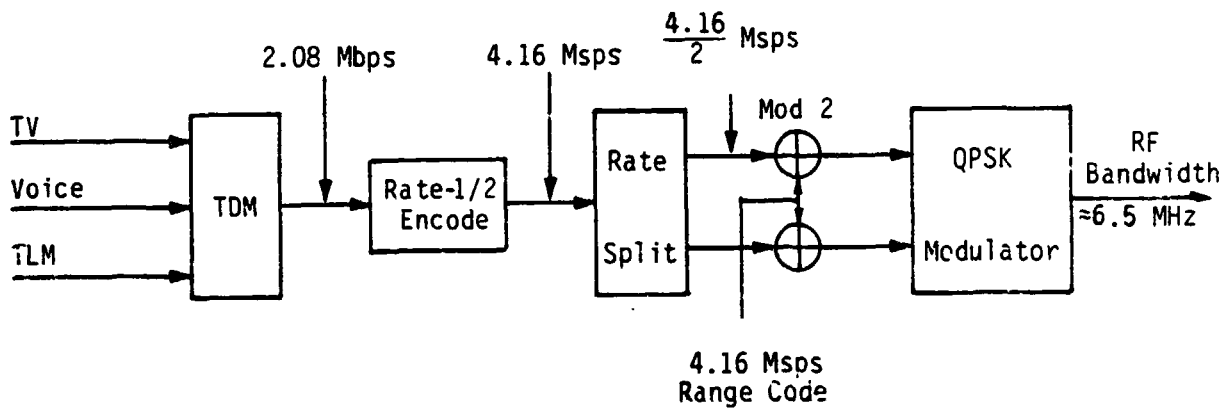
Figure 4.2. Typical MOTV of EMU FDMA User Return-Link-Communication System



(a) Channel Modulation, No Ranging



(b) Channel Modulation with Ranging, Option 1



(c) Channel Modulation with Ranging, Option 2

Figure 4.3. FDMA Channel Modulation with Ranging Option

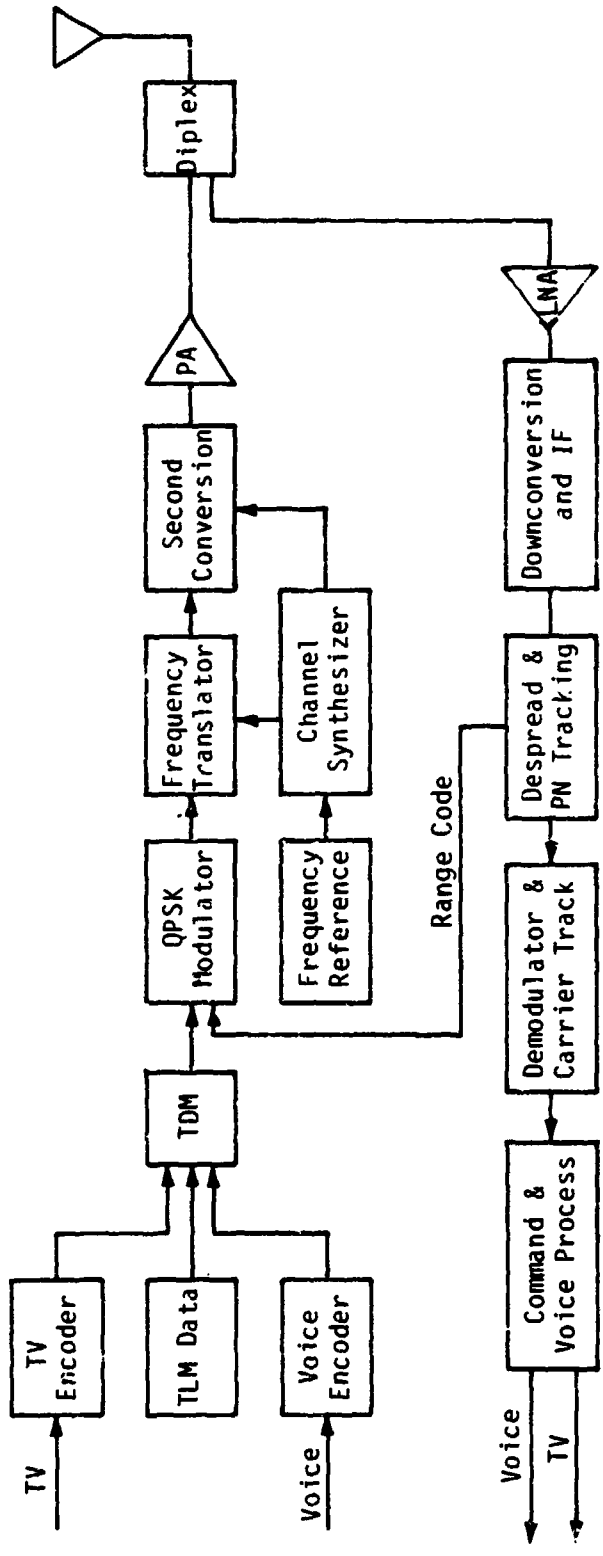


Figure 4.4. Functional Block Diagram of the User FDMA Transmitter/Receiver with a PN Ranging Provision

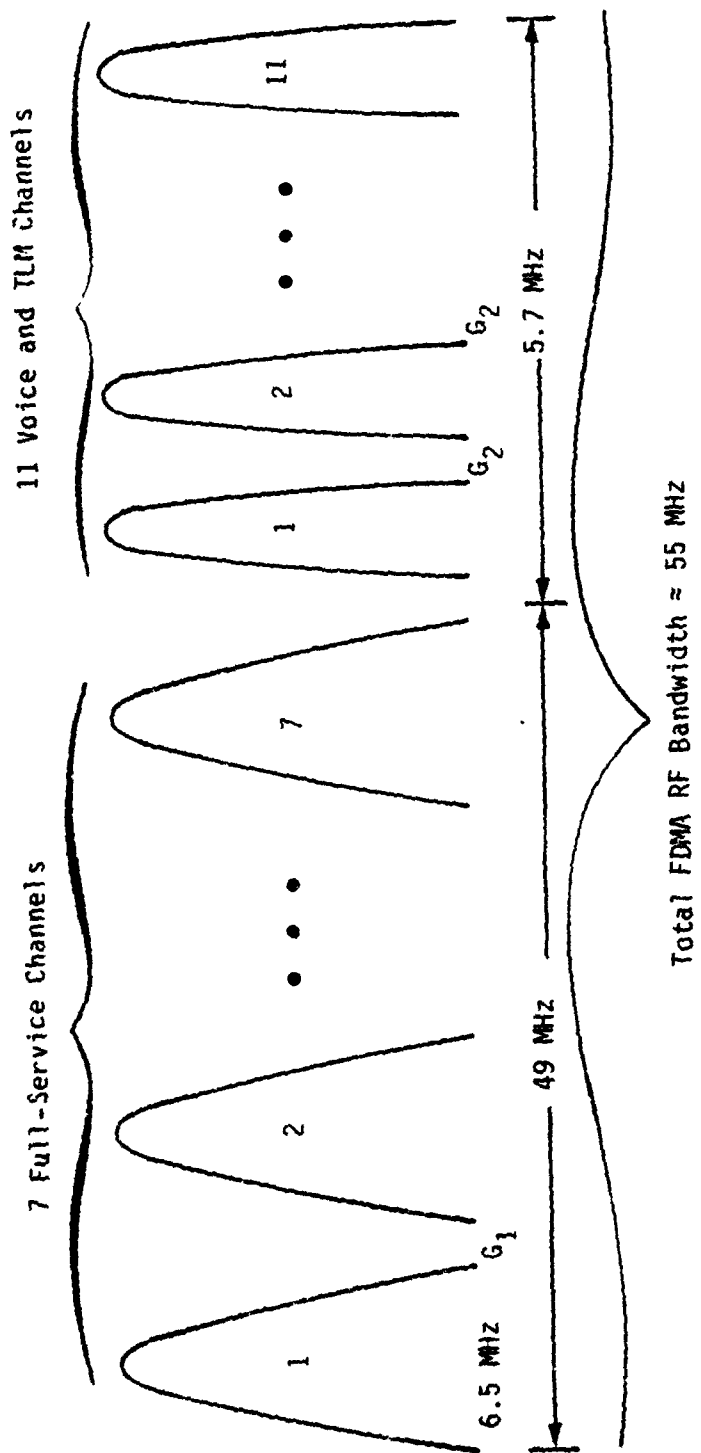
A candidate FDMA channel allocation is depicted in Figure 4.5. This allocation allows all seven TV users to transmit a return-video signal simultaneously. Each of the remaining 11 users are allocated a 160-kbps channel which will simultaneously provide both voice and telemetry services. This FDMA allocation plan requires approximately 55 MHz of RF bandwidth, assuming a frequency guard band of 0.5 MHz between the full-service (TV, voice and telemetry) channels and 40 kHz between the voice and telemetry channels. The choice of frequency guard bandwidth is dependent on user transmitter-oscillator stability and adjacent channel interference from modulation spectral spillover. The modulation spectral spillover is dependent on the specific modulation format, the linearity of the user transmitter, and/or the SS receiver. Since the user transmitter power amplifier would probably be operated in a saturated mode, a modulation that minimizes spectral spillover with a hard limiter will be chosen. Some of the modulation candidates are staggered quadriphase-shift-keying (SQPSK) or tamed frequency modulation (TFM). A plot of the relative modulation rolloff of these and several other spectrally efficient modulations is shown in Figure 4.6. An additional driver on guard bandwidth is intermodulation products. The exact choice of guard bandwidth must be investigated further.

Another possible FDMA channel allocation is shown in Figure 4.7. While it does not provide the full flexibility of the previously discussed allocation, this allocation does meet the minimum requirements for simultaneous user MA return-link service. Furthermore, it requires only 22 MHz of RF bandwidth compared to 55 MHz for the former allocation. The best choice of FDMA allocation requires further investigation but, for the purpose of this report, the former allocation (i.e., 55 MHz RF bandwidth) is chosen as the FDMA baseline.

Figure 4.8 shows the conceptual top-level block diagram of the SS return-link FDMA receiver. The common resource shared among MA users is the receiver front end, including the first two downconverters and IF's. Beyond that, a DMOD and a TDM DMUX are required for each user channel, which leads to as many as 18 DMOD's and 18 DMUX's for the SS MA return-link service for FDMA.

This proliferation of receiver equipment is the result of any FDMA scheme wherein the stringent timing requirements and high burst rates of TDMA are traded off for an FDMA receiver entailing a much greater amount of hardware.

As indicated in the block diagram of Figure 4.8, AGC is provided at the front end of the receiver. However, the approximately 110-dB dynamic range required to accommodate the distance range of the MA user return links poses a



G_1 = Guardband for Full-Service Channels (~0.5 MHz)
 G_2 = Guardband for Voice and TLM Channels (~40 kHz)

Figure 4.5. FDMA Channel Allocation Allowing Maximum Simultaneous Return-Link Services

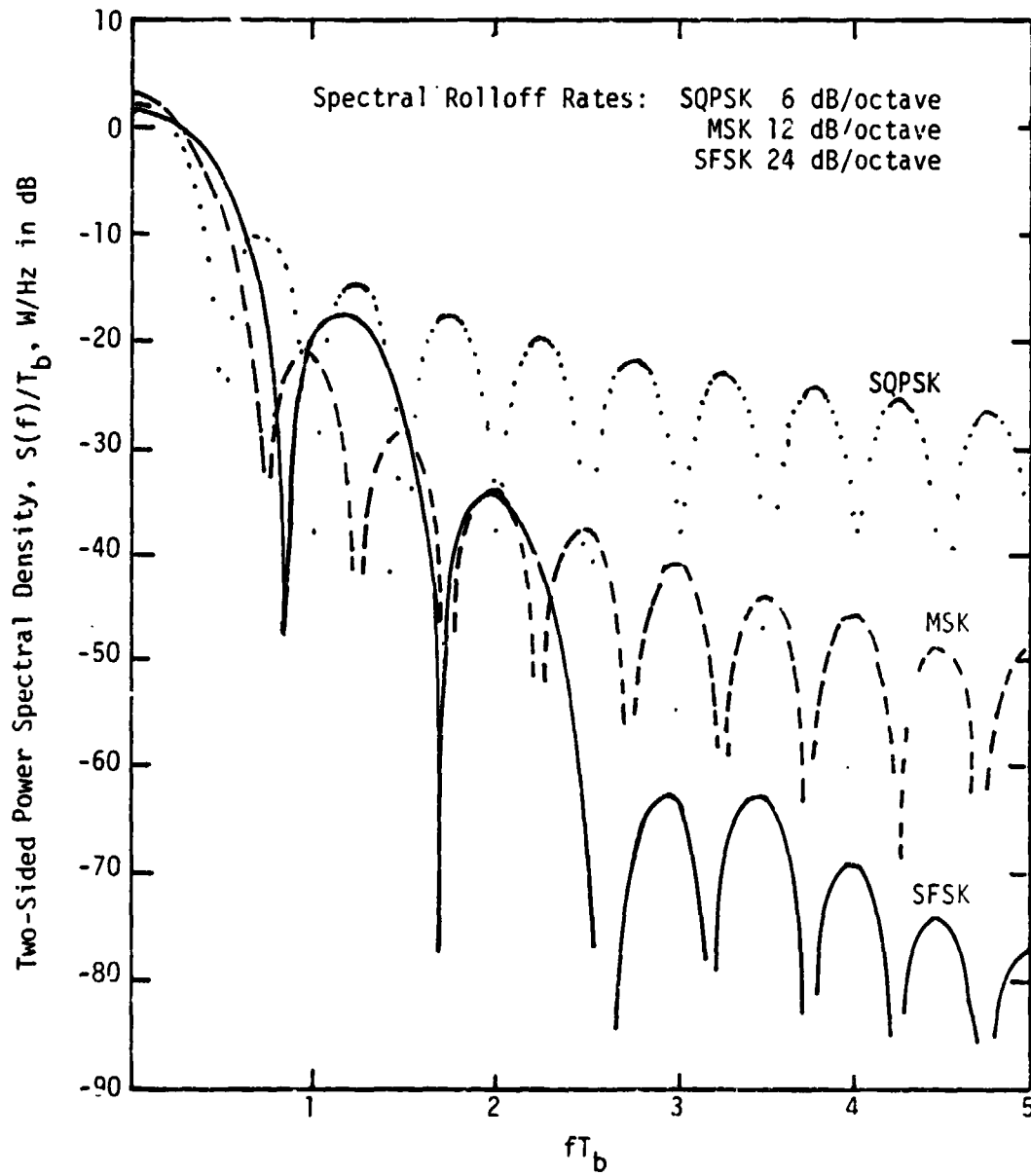
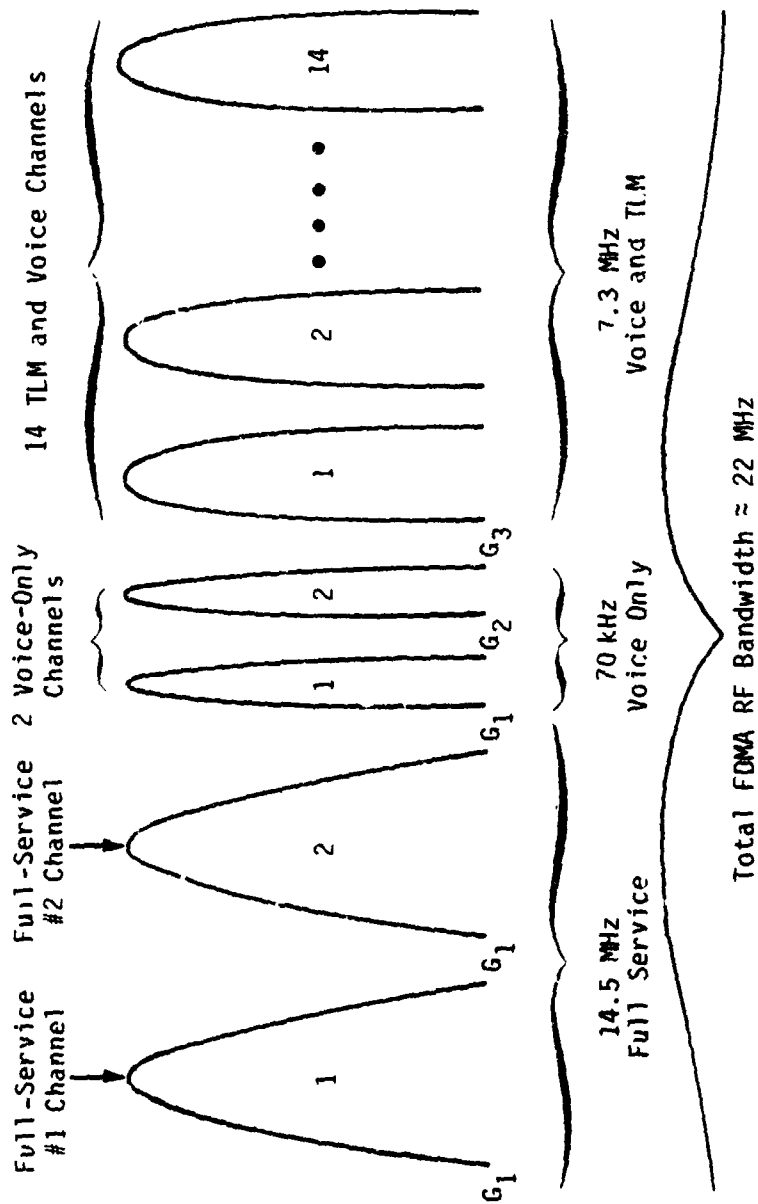


Figure 4.6. Comparison of Power Spectral Densities for Various Digital Modulation Formats



G_1 = Full-Service Guardband (0.5 MHz)

G_2 = Voice-Service Guardband (3 kHz)

G_3 = Voice and TLM Guardband (40 kHz)

Figure 1.7. FDMA Channel Allocation That Meets User Return-Link Requirements Utilizing the Minimum RF Bandwidth

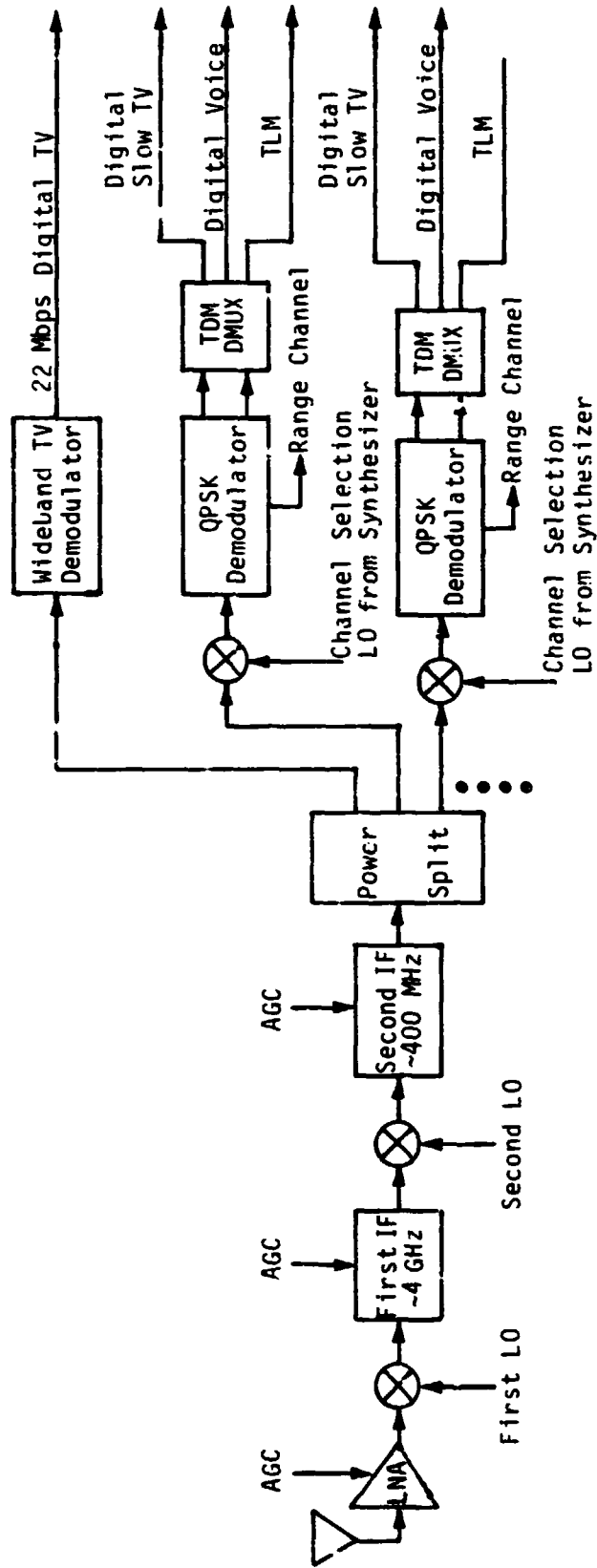


Figure 4.8. Space Station FDMA Receiver

a difficult problem for the AGC design as well as maintaining the required linear-amplitude range. Two approaches can be considered in solving this problem. The first approach is to group the users' frequency allocations into two 55-dB-amplitude groups. As an example, the first group would be the "close-in" group and the distance range of this group would correspond to a signal-power range of 55 dB. Likewise, the second, or "far-away," group would also correspond to a 55-dB signal-power range. The total RF band could then be divided into two, with one half of the band dedicated to each user group. Then, the IF amplifier and AGC control scheme shown in Figure 4.9 could be used to provide AGC independently as well as 55 dB of dynamic range to each group.

The second approach in accommodating the 110-dB signal-power range is to use active power control on the return link. This would effectively narrow the signal-power range to something much more tractable, say, on the order of 50 to 60 dB, or even less if required. Users of the more distant ranges (up to 2000 km) would utilize their full EIRP, whereas users at the closer ranges would lower their EIRP. The user could determine its appropriate EIRP setting by either forward-link command or sensing the AGC level of the user forward-link receiver.

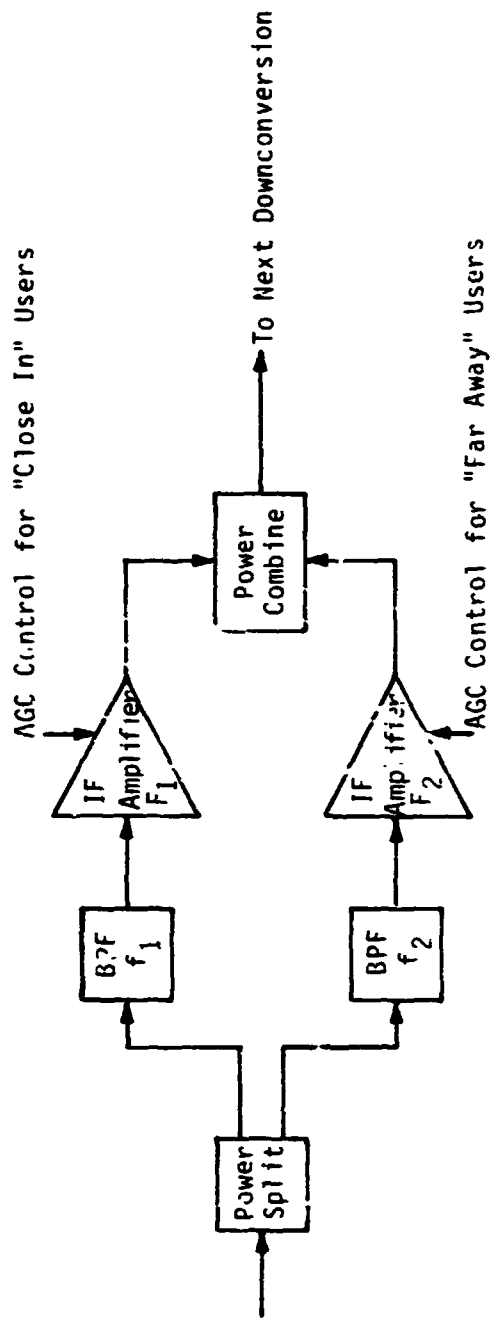


Figure 4.9. Potential AGC Scheme to Accommodate 110-dB Dynamic-Range Requirement

4.2 Frequency-Hop FDMA For Antijam Performance

4.2.1 Introduction

The concepts of FDMA that were discussed in section 4.1 can be extended to provide antijam (AJ) protection in which AJ can be added by frequency hopping the carrier frequencies. This section discusses the approaches and performance of FH FDMA for the space station (SS) multiple-access (MA) links.

4.2.2 Discussion

AJ protection can be obtained by either direct-sequence (DS) spreading or frequency hopping (FH) the data. In the DS case, the 2.16-Mbps data rate necessitates an inordinately high and impractical PN chip rate, e.g., in order to obtain 30 dB of processing gain, a PN code rate of 2×10^9 chips per second would be required. This high a rate is unworkable for many reasons.

If frequency hopping is utilized, the full-service user (2.160 Mbps) would be spread over approximately 2 GHz so as to obtain 30 dB of processing gain. The amount of AJ protection is determined from the relationship:

$$J/S_{dB} = PG_{dB} - E_b/N_J_{dB}$$

where E_b/N_J is the energy-per-bit-to-noise-density ratio necessary to meet the performance requirements; usually, a final BER of 10^{-5} . The E_b/N_J also depends on the choice of data modulation and type of jammer. In keeping with the concept of extending the FDMA concepts to AJ, we shall first consider QPSK data modulation. The E_b/N_J required for QPSK can be determined from the curve given in Figure 4.10. We shall consider the performance requirement to be BER = 10^{-2} (uncoded which, assuming a rate-1/2 convolutional code with Viterbi decoding, is equivalent to BER = 10^{-5} coded). Then, from Figure 4.10, E_b/N_J is approximately 11 dB, an amount to which we must add 3 dB in order to account for the rate-1/2 coding. Thus, the E_b/N_J required for FH-QPSK against a tone jammer is approximately 14 dB. This means that, for the 2-GHz hopping bandwidth, i.e., $PG = 30$ dB, the J/S is only 16 dB. By increasing the hopping bandwidth to 4 GHz and using soft-decision decoding, the J/S is approximately 20 dB.

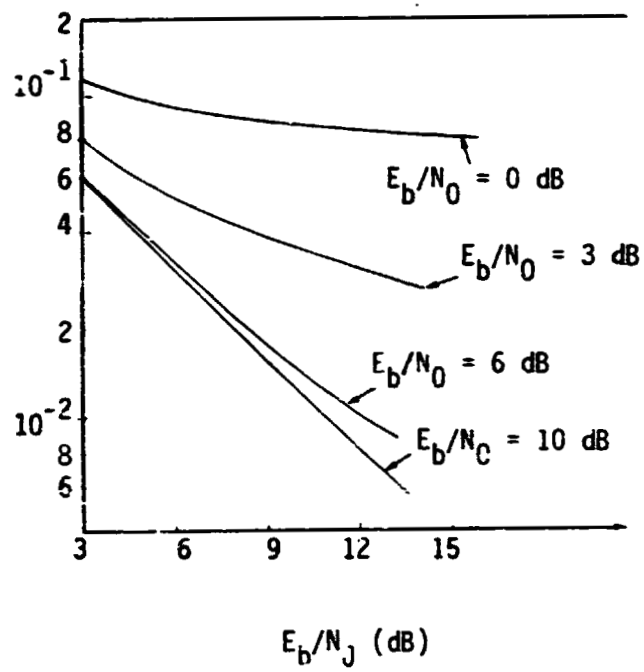


Figure 4.10. Worst-Case P_b versus E_b/N_J ; FH-QPSK (Tone Jamming)

Use of QPSK modulation requires that a coherent carrier reference be obtained. This can be accomplished by either closed-loop techniques, such as a Costas carrier-tracking loop, or open-loop phase-estimation techniques. The open-loop phase-estimation technique is preferred since it requires far less time than a Costas loop to generate a coherent phase reference. This is particularly true since the frequency hopper would be noncoherent; thus, requiring that a new phase acquisition be accomplished at the start of each hop. If we postulate a hopping rate of $f_h = 4 \times 10^3$ hops/second, there are approximately $2 \times 10^6 / 4 \times 10^3 = 500$ bits per hop. By using an open-loop phase-estimation technique, as described by Viterbi and Viterbi [2], it should be possible to lose no more than 25 of these bits to the phase-acquisition process at the start of each hop, i.e., approximately 0.2 dB loss. A block diagram of the Viterbi phase-estimation process is shown in Figure 4.11. Since this concept is relatively new, it should be investigated further for its applicability to SS MA communication.

An alternate data modulation to coherent QPSK that may be suitable to SS AJ communications is M-ary FSK. This modulation offers the advantage of not requiring a coherent reference. If straight FH MFSK is used, the AJ performance will be approximately 6 dB worse than in the QPSK case. This result is based on the 19.8 dB E_b/N_0 required for 8-ary FSK, as shown in Table 4.1 [3]. However, if a hybrid FH scheme is used in which DS PN is added, the AJ performance is found to be almost the same as that for QPSK. This is based on the E_b/N_0 required of 13.6 dB, as shown in Table 4.2 [3]. The disadvantage of this FH/PN hybrid AJ modulation is the increased system complexity. The best choice of data modulation and AJ modulation requires further investigation but, at this point, FH-QPSK is recommended as the baseline for the SS FDMA AJ network.

The J/S of 20 dB that was derived in the preceding paragraphs may not meet the requirements of a specified jamming threat. If this is the case, two options are open. These are: (1) reduce the data rate, or (2) utilize a null-steering antenna. It is important to note that the 20-dB J/S is for the full-service user, i.e., TV plus voice plus telemetry. Thus, a user requiring voice and telemetry only, i.e., 160 kbps, represents a data-rate reduction factor of 12.5, or a J/S increase of approximately 11 dB to J/S = 31 dB. Likewise, a user requiring only slow-scan TV transmission and utilizing a 64-kbps slow-scan TV system with 160 kbps of voice and telemetry would have a J/S of approximately 30 dB. These J/S ratios are summarized in Table 4.3. Therefore, it is necessary to further investigate the user-community data requirements in a jamming scenario as well as the jamming threat to specify the SS AJ communication system.

ORIGINAL PAGE IS
OF POOR QUALITY

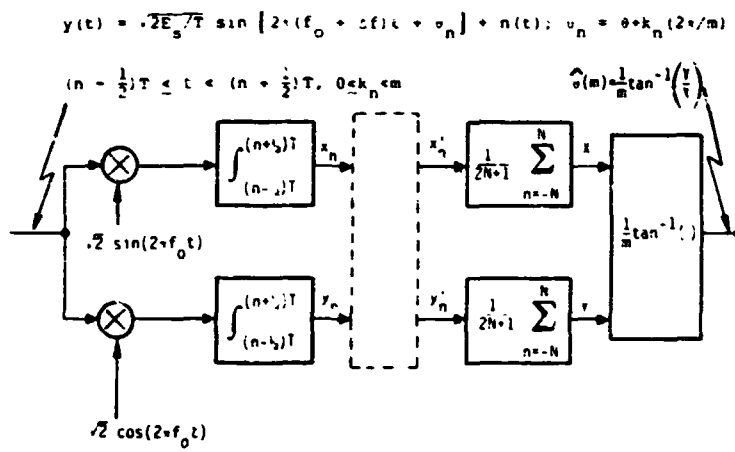


Figure 4.11. Basic Phase Estimator for m-PSK Carriers

Table 4.1. Hard-Decision Coded-FH Performance

Error-Correcting-Code Technique	Required $(E_b/N_0)_{\text{eff}}$ Worst-Case Jamming			
	FH/DPSK (dB)	FH/DQPSK (dB)	FH/MFSK (dB)	FFH/MFSK (dB)
No Coding:				
$P_b = 10^{-3}$	27.0	24.1	31.2	12.2
$P_b = 10^{-5}$	47.0	44.1	51.2	16.5
R = 1/2 Convolutional Viterbi Decoding:				
$P_b = 10^{-3}$	13.8	10.9	18.0	10.1
$P_b = 10^{-5}$	17.7	14.8	21.9	11.1

Table 4.2. Hard-Decision Coded-FH/PN Performance

Error-Correcting-Code Technique	Required $(E_b/N_0)_{\text{eff}}$ Worst-Case Jamming			
	FH-PN/DPSK (dB)	FH-PN/DQPSK (dB)	FH-PN/MFSK (dB)	FFH-PN/MFSK (dB)
No Coding:				
$P_b = 10^{-3}$	22.6	23.3	22.9	11.2
$P_b = 10^{-5}$	42.6	43.3	42.9	12.1
R = 1/2 Convolutional Viterbi Decoding:				
$P_b = 10^{-3}$	9.5	10.0	9.7	9.7
$P_b = 10^{-5}$	13.4	14.0	13.6	11.1

Table 4.3. Summary of AJ Performance for SS FH-FDMA System

User Service	Data Rate	J/S (dB)
Full (TV, TLM, Voice)	2.08 Mbps	20
Partial, No TV (TLM, Voice)	80 kbps	34
Partial, Slow-Scan TV (SCTV, TLM, Voice)	144 kbps (64 kbps for SCTV)	32

A block diagram of the FH-FDMA user transmitter/receiver and Space Station FH-FDMA receiver is illustrated in Figures 4.12 and 4.13, respectively. The most significant aspect of this frequency-hop scheme is that all users hop synchronously (adjusted for individual range to SS) so that the Space Station requires only one dehopper and synthesizer, as shown in Figure 4.13. However, this requires each user to adjust its hop clock phase so that its frequency hopping is in exact synchronization with the SS dehopper frequency at the SS. This is accomplished via the user tracking the forward link and exchanging its time-of-arrival information with the SS via a synchronization channel. This approach is commonly used in military AJ communication systems. Provisions for the synchronization channel are depicted in Figure 4.12.

The link calculation for the FH-FDMA return link at 30 GHz results in the following system parameters:

User transmitter power	10 W
User transmitter antenna gain	0 dB
SS receive antenna gain	50 dB
Effective receiver noise temperature	825°K
Maximum range	2000 km
BER (coder output)	10^{-5}

These parameters support a full-service return link (TV + voice + TLM) with a jammer-to-signal ratio of approximately 20 dB. The 50 dB of antenna gain may represent the most difficult aspect of the FH-FDMA concept. This is certainly true if an electronically steered phase array is used which must create 18 simultaneous independent beams. On the other hand, if multiple parabolic-reflector antennas are used, 60 dB does not represent a significant problem.

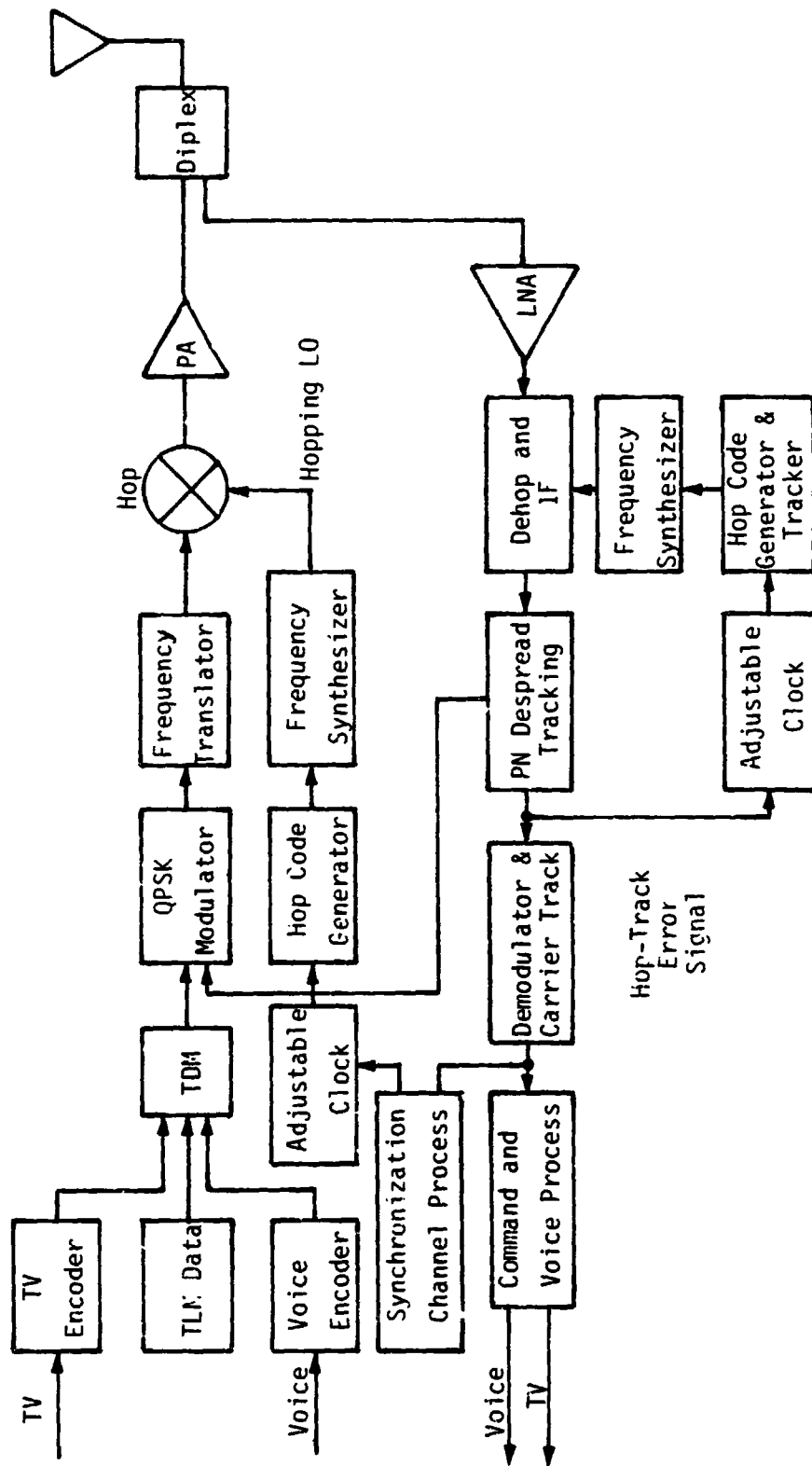


Figure 4.12. Functional Block Diagram of the User FH-FDMA Transmitter/Receiver

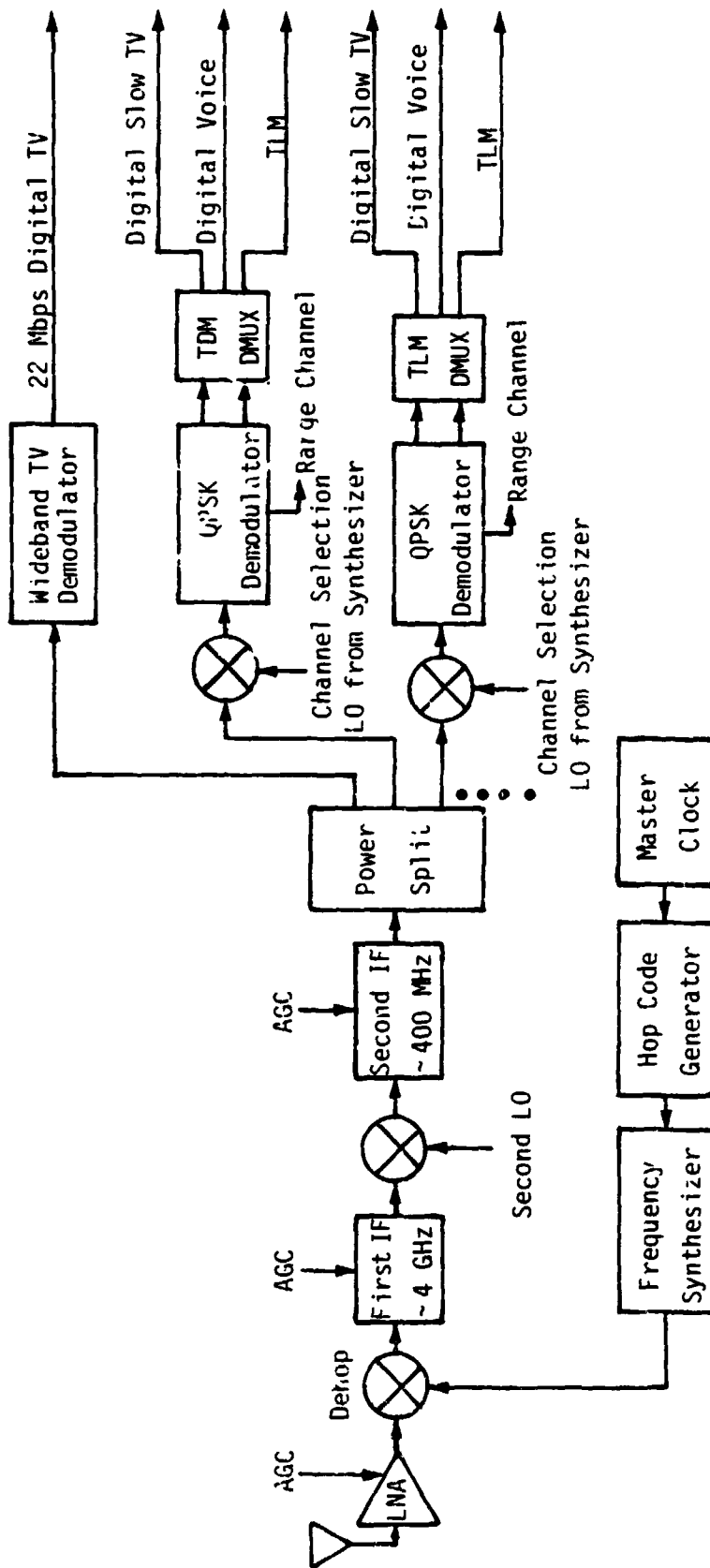


Figure 4.13. Space Station FH-FDMA Receiver

4.3 Time-Division Multiple-Access Return Links

4.3.1 Introduction

The basic time-division multiple-access (TDMA) scheme assigns specific time slots to each user, with high-data-rate users accorded proportionally more slots than low-data-rate users. User slots can be assigned prior to a mission, which simplifies the MA assignment strategy, or assigned on demand, which results in a more flexible system. A typical TDMA channelization is shown in Figure 4.14.

A common requirement for all TDMA schemes is the need for a guard time to separate users and prevent overlays. Guard time is overhead, and reduces the effective data rate of the system; however, the duration of the guard band can be minimized if accurate relative timing is maintained between the SS and the users. Another common consideration is the high burst rate of TDMA systems. Since the time allotted to a given user is a fraction of the total time available, the burst rate is correspondingly higher. From the examples, we can see that the narrow symbol times, coupled with anticipated relative velocities, will require the SS to time track each user and broadcast updated timing and range information to each user.

4.3.2 Baseline TDMA System Example

A TDMA system based on the requirements shown in the Table 3.1 user group will consist of a single receiver, as shown in Figure 4.15, wherein time samples of received data are routed to their respective destinations. A current history of each user's parameters, e.g., time offset, range, range rate and bearing, is maintained in order to rapidly acquire the user during the next dwell time.

A total of 18 users can be accommodated, with each user given one telemetry channel (64 kbps) and one guard time. In addition, seven users are given a TV channel (2.048 Mbps) and four users are given a voice channel (16 kbps). For system-definition purposes, we assume that a guard time is equal to a least-common multiple of the channel time which, in this case, is one voice channel time, which we can call a time unit. One user frame consists of a guard time (one time unit), a telemetry time (four time units), a possible voice time (one time unit) and a possible TV time (128 time units). The total system time requirement is derived as shown below.

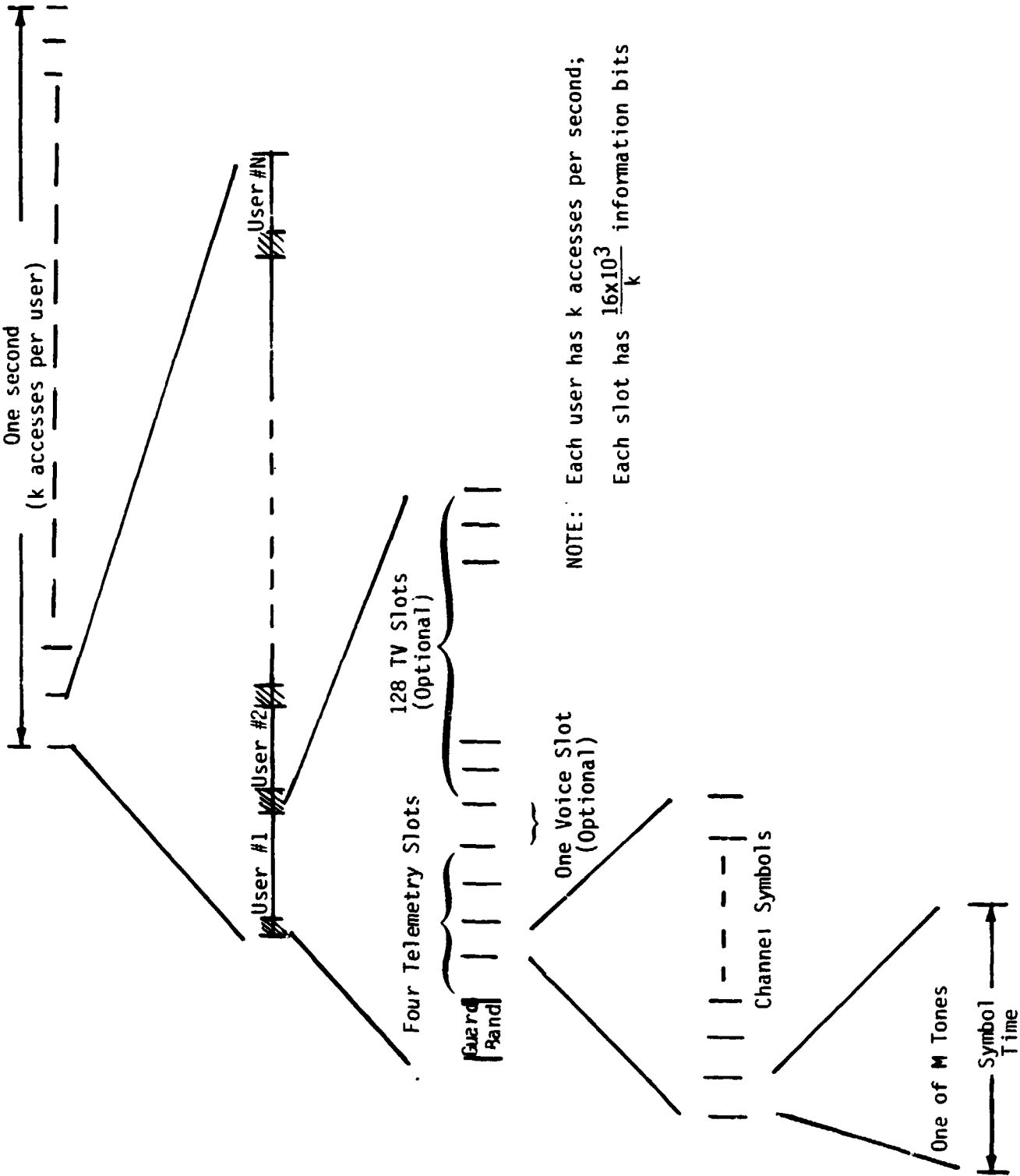


Figure 4.14. TDMA Channelization with M-ary MFSK Modulation

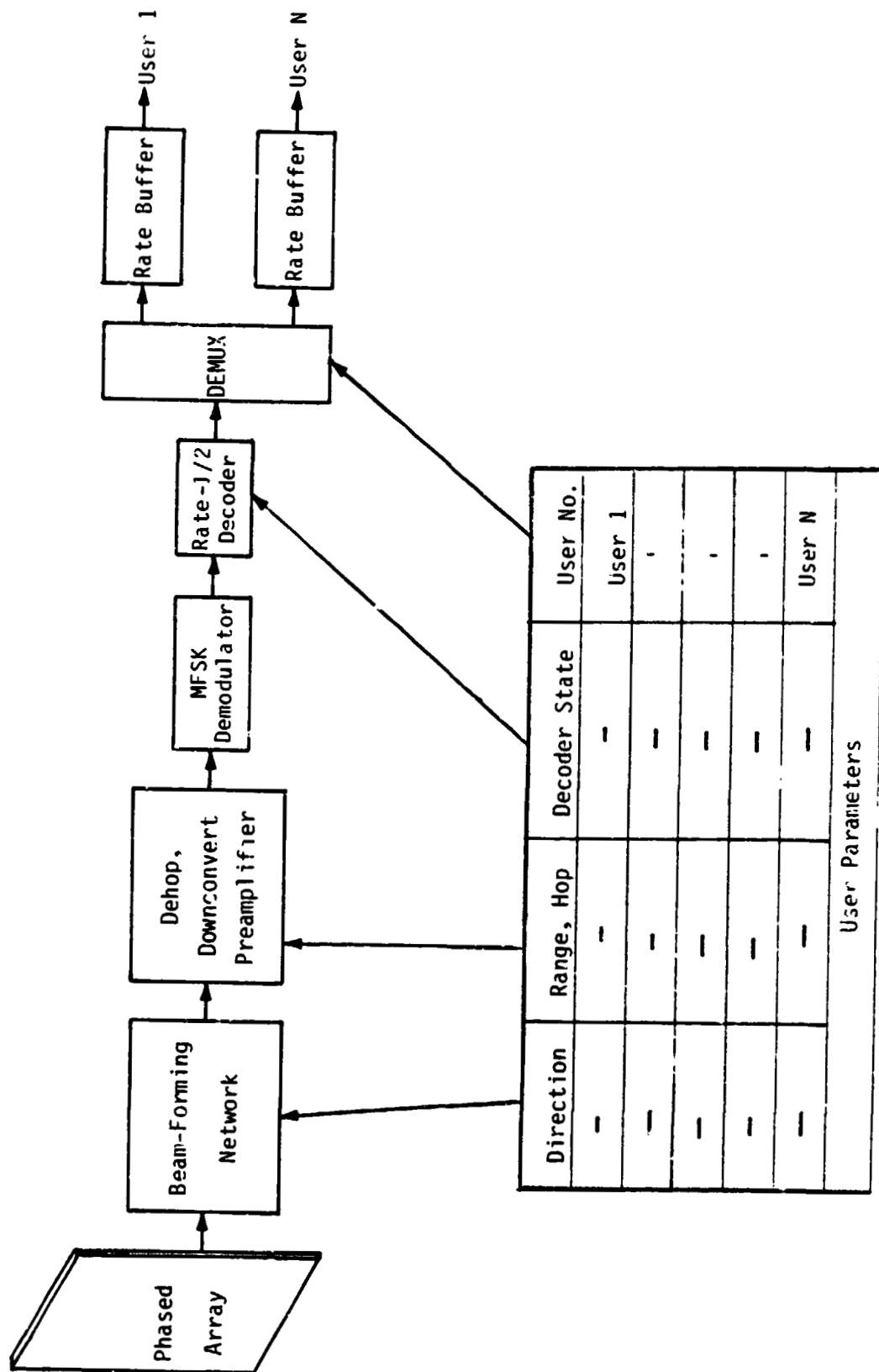


Figure 4.15. TDMA Receiver

18 guard times	18 x 1	=	18 time units
18 telemetry channels	18 x 4	=	72 time units
7 TV channels	7 x 128	=	896 time units
4 voice channels	4 x 1	=	<u>4</u> time units
			990 time units

A single time unit, e.g., one voice channel, can accommodate one 32-kbps channel, which gives a system burst rate of 990×16 kbps, or 15.840 Mbps. Thus, a single bit time is 57.7 ns and, with rate-1/2 coding, symbol time is 28.8 ns, assuming binary modulation. In order to achieve low-symbol error rates, timing uncertainty should be a small fraction of a symbol time, but range uncertainty must still be resolved to within several meters. Clearly, it is impossible to range track a user this accurately over the extremes of range and range rate considered. Thus, data-tracking loops will be required. It is assumed that a portion of the telemetry channel for each user will be devoted to carrier, data, code and frame acquisition/synchronization.

Figure 4.16 presents the results of a sample link-budget calculation in the presence of noise, with required transmitter power given as a function of range; this is a K_a -band link with a transmitter-plus-receiver antenna gain of 40 dB and a burst rate of 15.84 Mbps. We see that a peak user power of -5.6 dBW is required at 100 m, but a peak power of 30 dBW is required at 2000 km! No margins are included in this calculation, but a reasonable margin implies that a peak power in excess of 1 kW would be needed. The average power of a single user, with only telemetry, would be $4/999 \times 1$ kW = 4.0 W. A realistic upper limit of 10 dBW user peak power implies an antenna gain of 60 dB. The link budget calculation is based on the following:

$$P_T = 10 \log \text{Rate} + 9.5 - 228.6 + T_{dB} - (G_R + G_T) + 92.5 + 20 \log f_{\text{GHz}} + 20 \log R_{\text{km}}$$

with $T_{dB} = 29.2$ at 30 GHz and 31.2 at 44 GHz. No margin or implementation loss is included.

Figure 4.17 gives the required power with reduced service; 18 telemetry channels, two TV channels and four voice channels. At the extreme range, an antenna gain of 56 dB is required with a 10-dBW transmitter. If the SS receiver is reconfigured to provide dedicated service to one user with telemetry, slow-scan TV (384 kbps) and voice at 2000 km, an antenna gain of 45 dB would be required. The performance of this configuration is given in Figure 4.18.

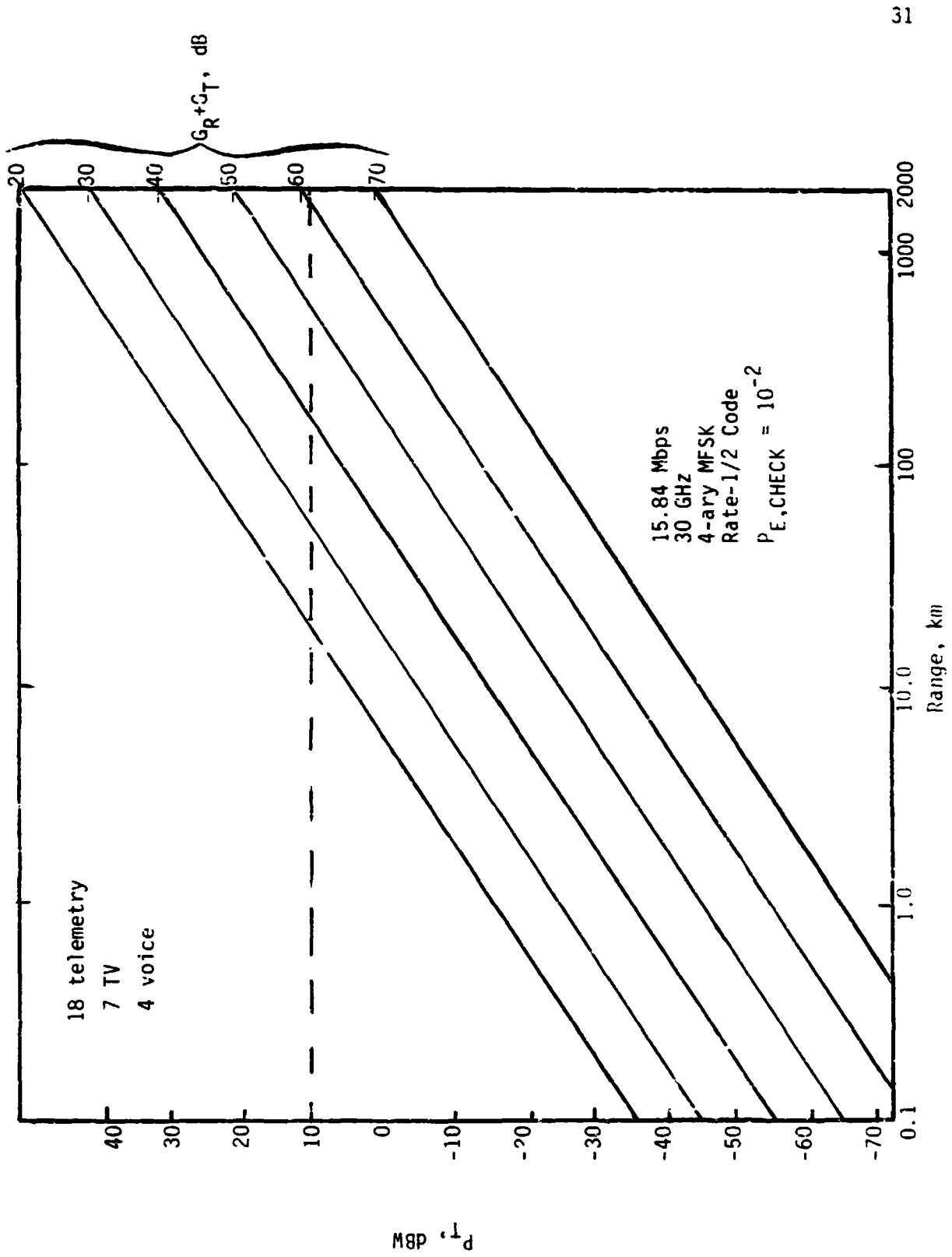


Figure 4.16. P_T (min) versus Range: Return-Link TDMA

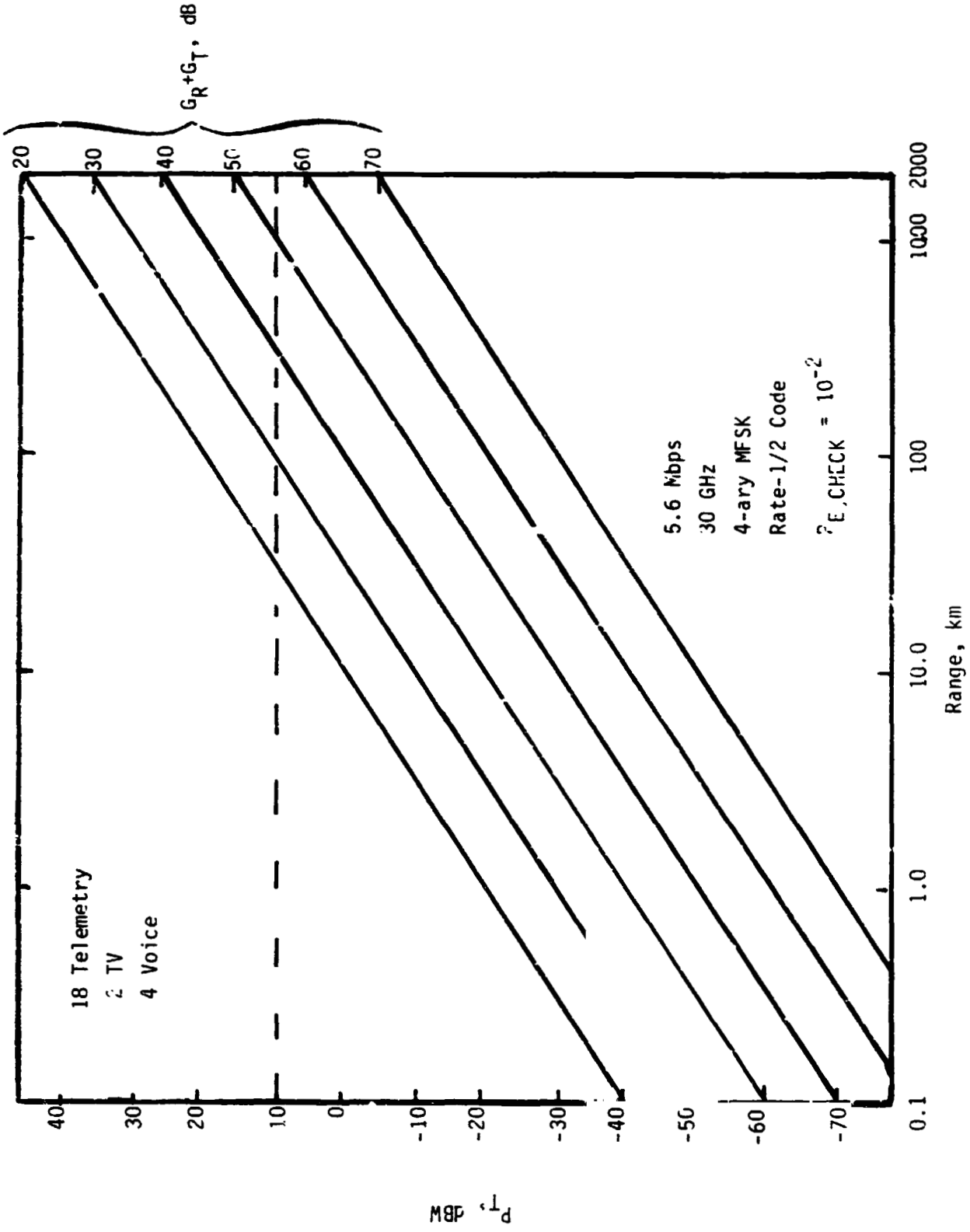


Figure 4.17. P_T (min) versus Range: Return-Link TDMA

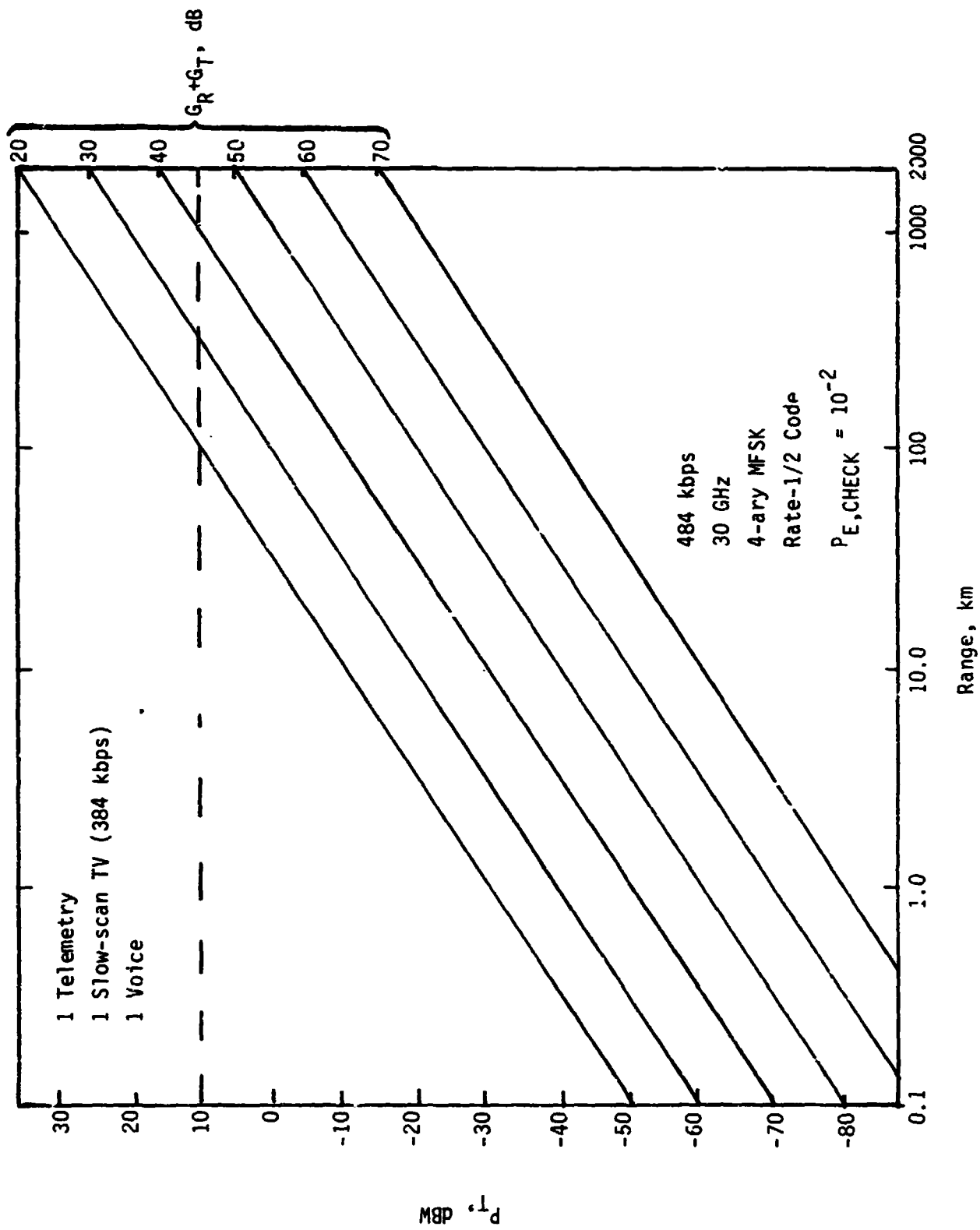


Figure 4.18. P_T (min) Versus Range: Return-Link TDMA

Figures 4.19, 4.20 and 4.21 represent the same user configuration as Figures 4.16, 4.17 and 4.18, but with a 44-GHz RF link. The antenna technology required to support these links is discussed in Section 5.

The preceding results show that we cannot expect full-user service-ability at extreme ranges unless the user has high EIRP available.* The same methodology is used to show the performance with the expanded user group of Table 3.2. Figure 4.19 represents the expanded user group with a 30-GHz link.

4.4 TDMA and Antijam Modulation

The previous section discussed TDMA in general, without regard to modulation and synchronization. In this section, we discuss modulation techniques to provide jam resistance. Additional protection against a jammer can be provided by antenna-null steering, which is discussed in a separate section.

There are two candidate AJ-modulation schemes to be considered with TDMA: direct-sequence (DS) spreading and frequency hopping (FH). Direct spreading is not considered a viable alternative for SS TDMA; a chip time, which is a small fraction of a symbol time, implies sub-nanosecond chip times at the data rates envisioned for the SS NA return link.

FH AJ can employ either frequency-shift-keying (FSK) or phase-shift-keying (PSK). Generally, PSK requires as much as 3 dB less energy per bit to achieve a given bit-error rate (BER), but requires a derived phase reference that is more complex than FSK demodulation. Additionally, with the bandwidth available, a higher order alphabet can be employed (more bits per symbol) and timing constraints can be relaxed due to longer symbol times. To compare TDMA with FDMA, we will examine a system with 4-ary MFSK modulation, i.e., two bits per symbol. Assuming that all channels have rate-1/2 convolutional codes, the net result is two code-check bits per symbol, or one information bit per symbol. symbol error rate is given as:

$$P_{E,S} = \frac{3}{2} e^{-\frac{E_s/N_0}{2}} - e^{-\frac{2E_s/N_0}{3}} + \frac{1}{4} e^{-\frac{3E_s/N_0}{4}}$$

for a noncoherent 4-ary receiver. In this case, with rate-1/2 coding, $E_s/N_0 = E_b/N_0$. The check BER is given as:

$$P_{E,C} = \frac{2^2-1}{2^2-1} P_{E,S} = \frac{2}{3} P_{E,S}$$

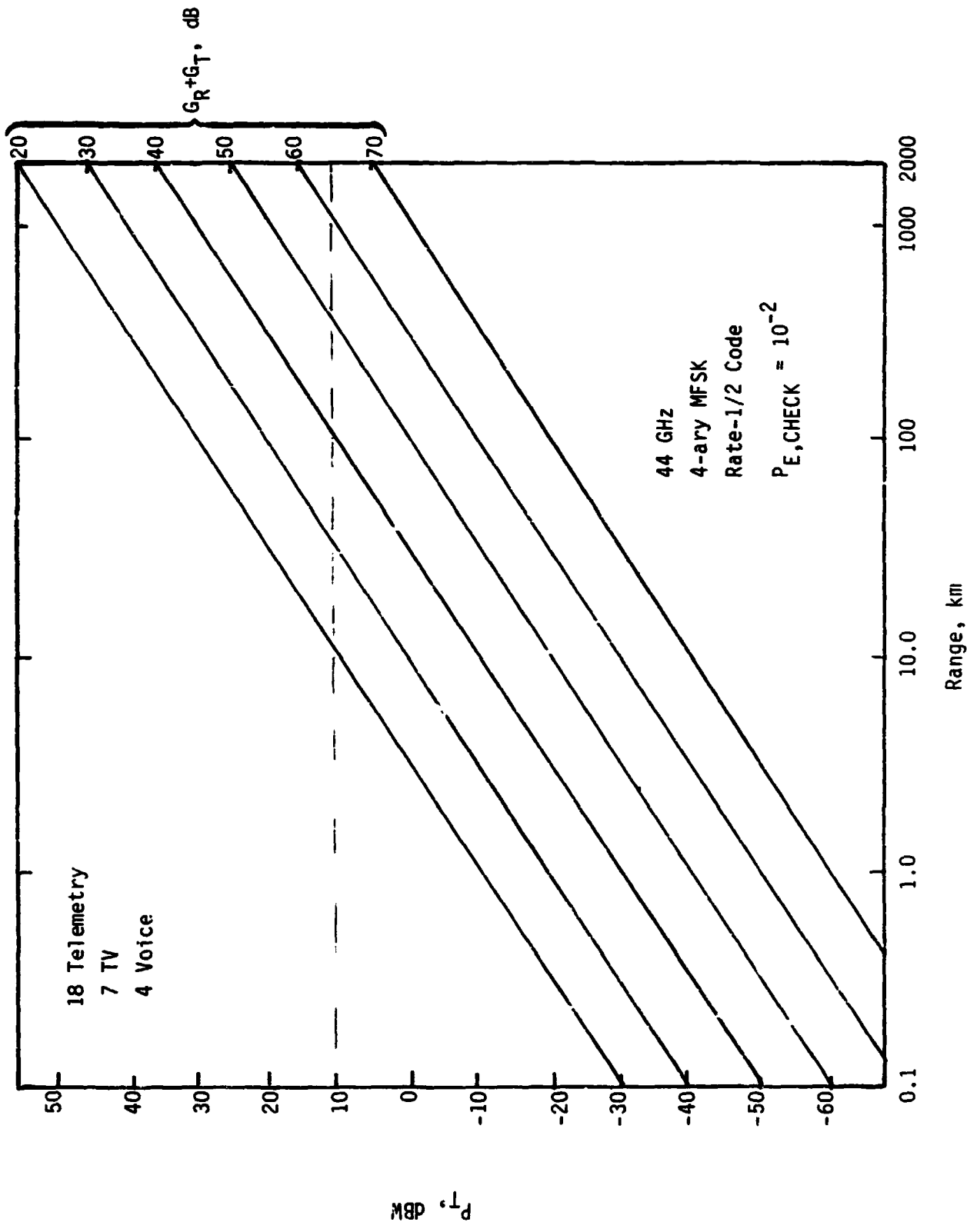


Figure 4.19. P_T (min) versus Range: TDMA 15.84-Mbps Burst Rate

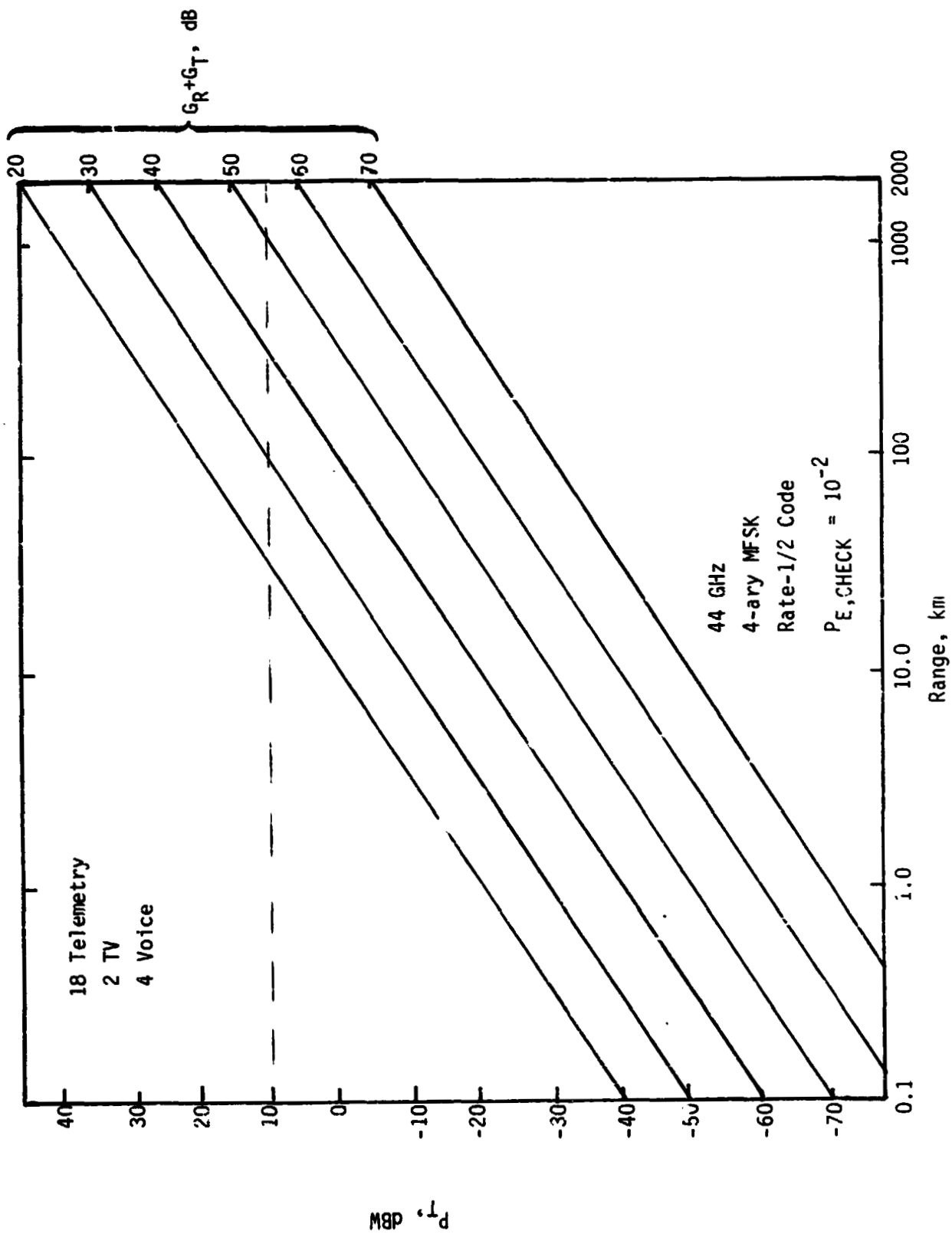


Figure 4.20. P_T (min) versus Range: TDMA 5.6-Mbps Burst Rate

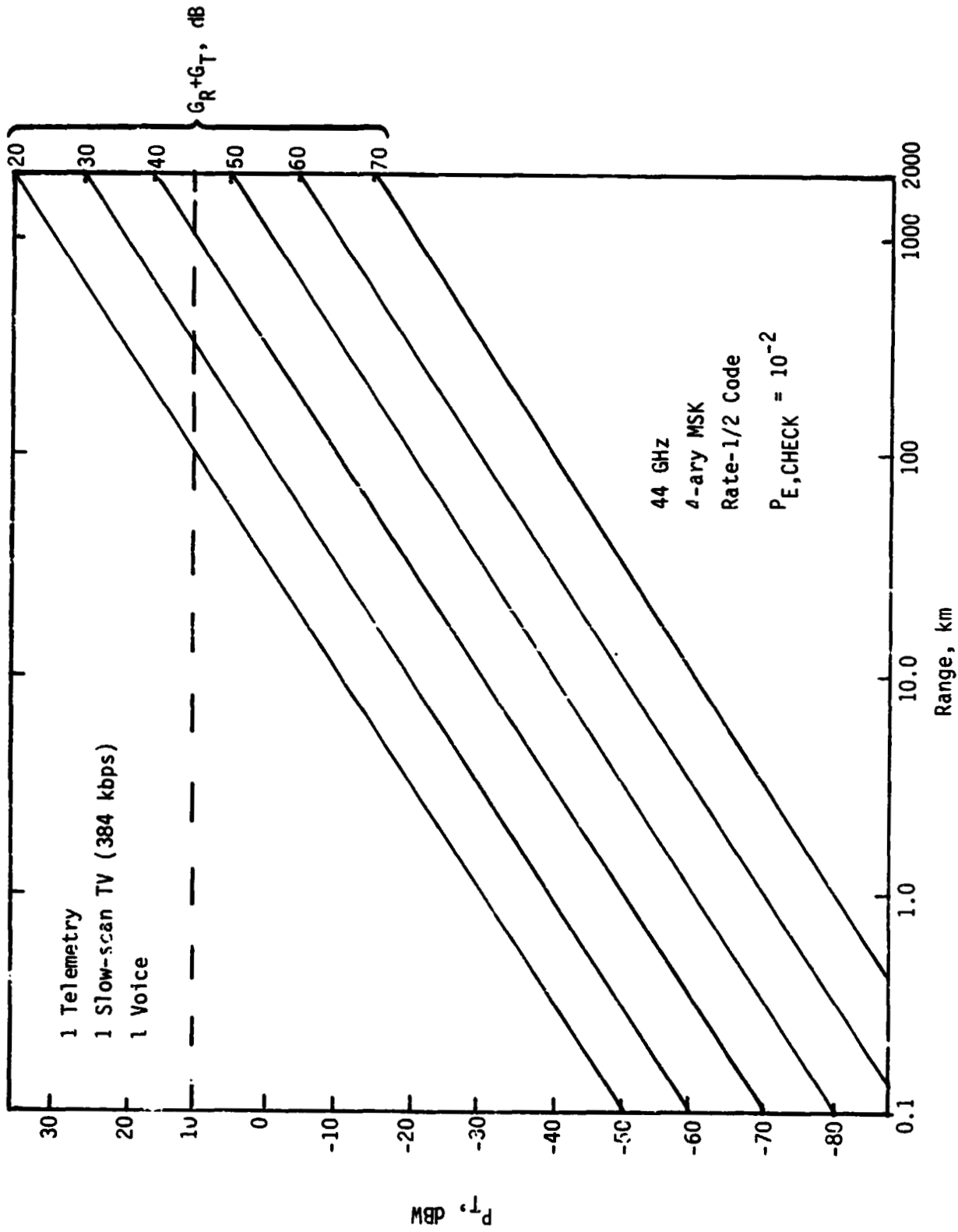


Figure 4.21. P_T (min) versus Range: FDMA 484-kbps Burst Rate

If we desire a check BER of 10^{-5} or better, then $P_{E,S} \leq 1.5 \times 10^{-5}$ and $E_s/N_0 > 13.6$ dB. For purposes of comparison, a coherent receiver would require $E_s/N_0 > 12.9$ dB since $P_{E,S} < 3Q(\sqrt{E_s/N_0})$ for 4-ary coherent demodulation. $Q(x)$ is the Q function defined as

$$Q(x) = \frac{1}{\sqrt{2\pi}} \int_x^{\infty} e^{-y^2/2} dy < \frac{1}{\sqrt{2\pi} x} e^{-x^2/2}$$

Binary FSK would require E_c/N_0 of 13.3 dB, or an E_b/N_0 of 16.4 dB since

$$P_{E,C} = \frac{1}{2} e^{-\frac{E_c/N_0}{2}}$$

and two check bits are required for one information bit. The results are summarized in Table 4.4 for various alphabet sizes, and we see that the choice of a 4-ary alphabet minimizes the signal bandwidth required as well as providing for a somewhat simpler demodulator. However, if a large enough hop bandwidth is available, larger alphabet sizes will be practical due to the improved error rate performance. In the presence of a tone jammer, however, we shall see that a 4-ary alphabet provides the best performance. Table 4.5 summarizes the performance for a check BER of 10^{-2} , which will give a decoded BER less than 10^{-5} .

The performance estimates given so far represent the system performance in thermal noise only. In order to communicate against a jamming threat, we propose to introduce several levels of AJ modulation. The AJ modulation is progressive; against a low-threat jammer, pure FH is employed. The adaptive nature of the TDMA system can be exploited to provide increased resistance to a more serious jammer at the expense of reduced data rate. First, we will discuss the basic system performance with wideband FH. As discussed earlier, other forms of spectrum spreading are impractical at these burst rates. In fact, at the rate of 17.344 MHz, the system must dwell on one hop for several symbols, which requires that symbols be interleaved over several decoder constraint lengths in order to prevent a jammer hit from causing errors in contiguous check bits. Figure 4.22 illustrates the block diagram of a baseline TDMA receiver which corresponds to the baseline user's group of Table 3.1. Figure 4.23 depicts a simplified example of the time/frequency occupancy of the signal tones. After interleaving, symbols S_1 , S_4 and S_7 are sent during hop 1, with

Table 4.4. Energy per Bit and Bandwidth (Unhopped) Required as a Function of Signal Alphabet with Noncoherent Demodulation, $P_B \leq 10^{-5}$

$M = 2^n$	$P_{E,S} = \frac{2^n - 1}{2^{n-1}} \times 10^{-5}$	$\frac{E_s^*}{N_0}$	$\frac{E_b}{N_0} = \frac{2}{n} \frac{E_s}{N_0}$	$T_s = \frac{n}{2} T_{17.344 \text{ Mbps}}$	$BW = \frac{M}{T_s}$
2	10^{-5}	13.34 dB	16.35 dB	31.6 ns	63.4 MHz
4	$3/2 \times 10^{-5}$	13.62 dB	13.62 dB	63.1 ns	63.4 MHz
8	$7/4 \times 10^{-5}$	13.86 dB	12.10 dB	94.7 ns	84.5 MHz
16	$15/8 \times 10^{-5}$	14.10 dB	11.09 dB	126.3 ns	127.0 MHz

* NOTE:
$$P_{E,S} = \sum_{j=1}^{M-1} \frac{(-1)^{j+1}}{j+1} \binom{M-1}{j} e^{-\left(\frac{j E_s/N_0}{j+1}\right)}$$

Table 4.5. Energy Per Bit Required, $P_B \leq 10^{-2}$

$M = 2^n$	$P_{E,S}$	E_s/N_0 , dB	E_b/N_0 , dB
2	10^{-2}	8.9	11.9
4	$3/2 \times 10^{-2}$	9.5	9.5
8	$7/4 \times 10^{-2}$	10.0	8.2
16	$15/8 \times 10^{-2}$	10.5	7.5

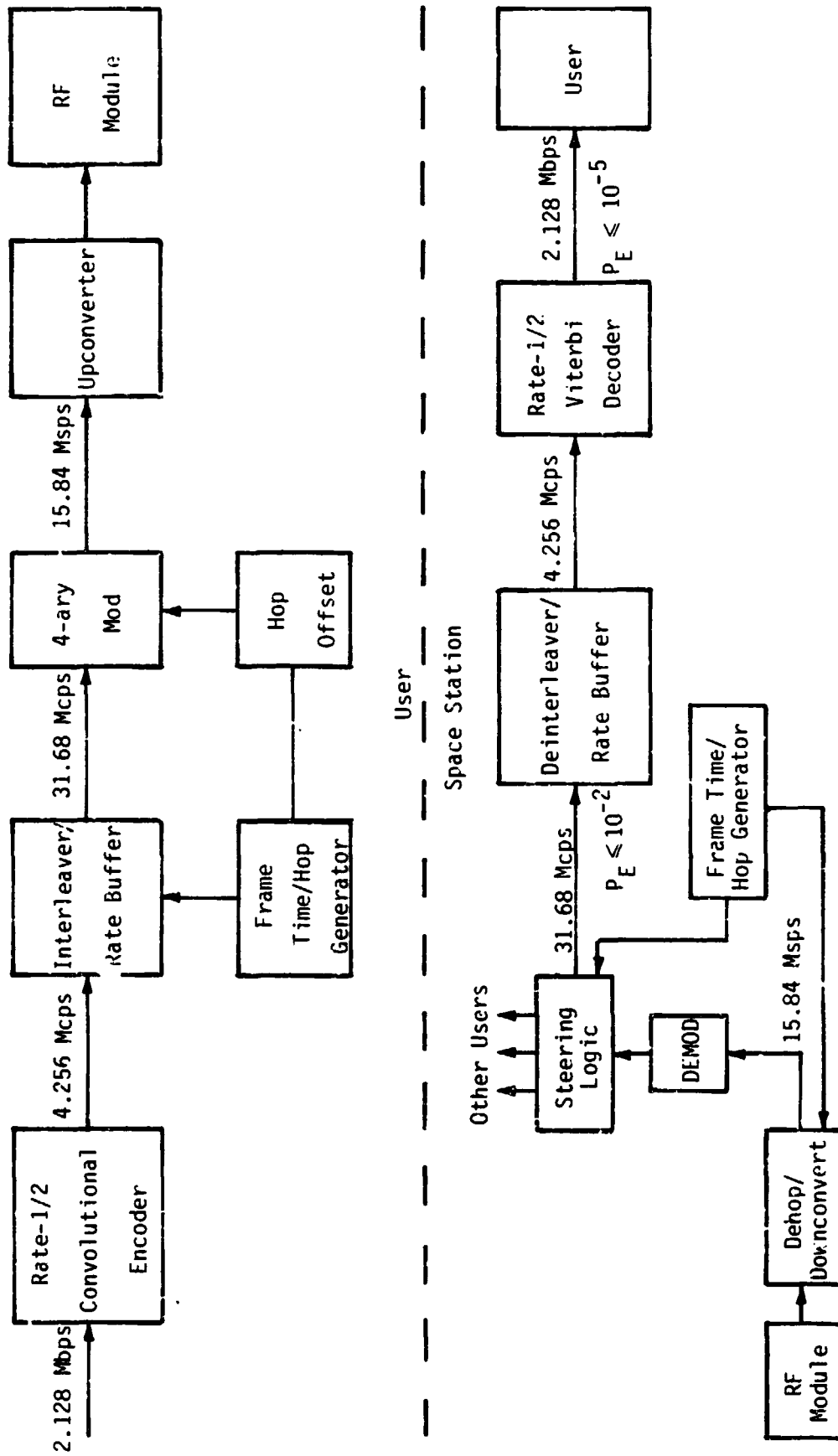


Figure 4.22. Baseline TDMA/FH System

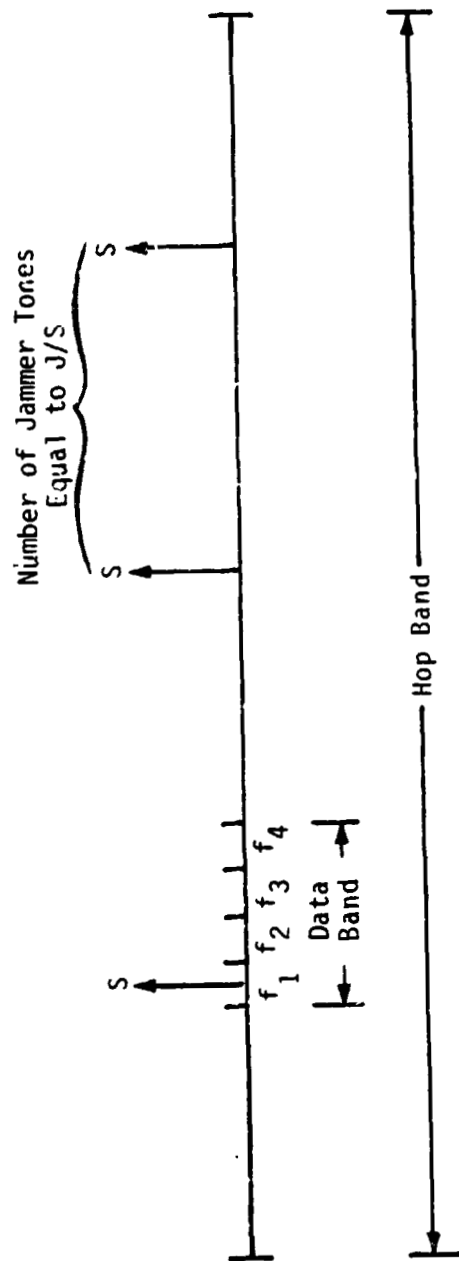


Figure 4.23. The 4-ary MFSK with J/S Jamming Tones

symbol S_1 (shaded) at frequency f_1 , symbol S_4 at f_2 , etc. We can consider f_0 the hop frequency, $f_1 = f_0 + 1/T_s$, $f_2 = f_1 + 2/T_s$, and $f_3 = f_2 + 3/T_s$, with T_s representing the symbol duration. In the example presented in Figure 4.22,

$$T_s = \frac{1}{15.84 \times 10^6} = 63.13 \text{ ns.}$$

In the baseline receiver, the signal is dehopped, downconverted and demodulated. During a user's time slot, the demodulated check bits are rate buffered down to 4.256 Mcps and deinterleaved. The minimum E_b/N_0 specified in the performance curves of the prior section gives a check BER of 10^{-2} at this point. This is reduced to 10^{-5} error rate or better by the Viterbi decoder.

The worst-case (WC) jammer for MFSK is a partial-band tone jammer, as depicted in Figure 4.24. The jammer's tones have just enough power ($S+\epsilon$) to exceed the communicator's signal S . Thus, if a jamming tone hits a data band, it has a probability of $(M-1)/M$ of causing an error. One time out of $M = 2^k$, it will reinforce the desired tone. If the jammer has power J , then he can transmit J/S tones, each with power S . In a hop band W , there are

$$\frac{W}{\frac{W_s}{M}} = \frac{W T_s}{M}$$

possible data bands for the communicator; thus, the probability of symbol error due to jamming is $(M-1)/M$ times the probability that one jammer tone hits one data band, or

$$P_E = \left(\frac{M-1}{M}\right) \left(\frac{J}{S}\right) \left(\frac{M}{W T_s}\right)$$

From a previous section, we know that

$$P_B = \frac{2^{k-1}}{2^k - 1} \times P_E = \frac{1}{2} \frac{M P_E}{M-1}$$

Therefore,

ORIGINAL QUALITY
OF POOR QUALITY

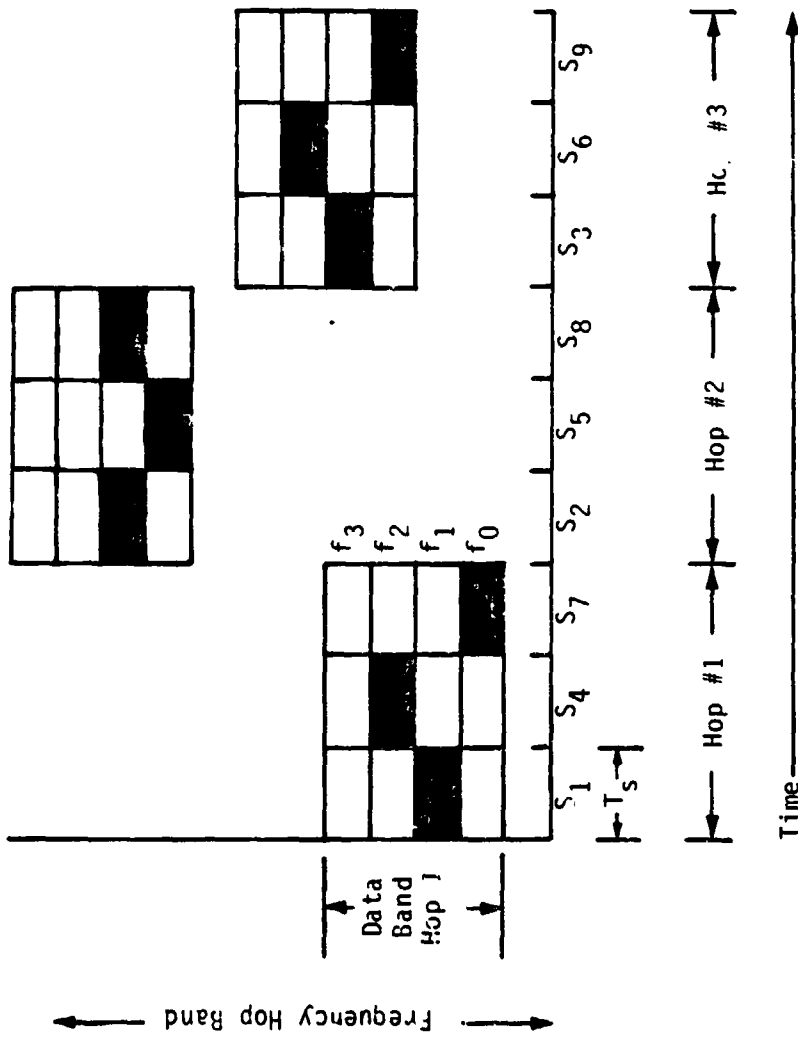


Figure 4.24. Time/Frequency Utilization with Interleaved TDMA/FM, Multiple Symbols per Hop

$$P_E = \frac{1}{2} \frac{J}{S} \frac{M}{WT_s}$$

With $E_c ST_c/k$ and $N_j = J/W$,

$$P_c = \frac{2^{k-1}}{k} \frac{1}{E_c/N_j}$$

For a given energy-to-jammer power ratio, the minimum probability of error is given with $k = 1$ or 2 . Higher order alphabets have reduced AJ performance by this measure. With $k = 2$,

$$P_c = \frac{1}{E_c/N_j}$$

and we need 20 dB of E_c/N_j to achieve a 10^{-2} BER into the decoder. In Table 4.6, we give the maximum AJ protection afforded (J/S) with this scheme, assuming that the bandwidth W is 10% of the RF bandwidth. We derive this from the relation

$$\frac{E_c}{N_j} = \frac{W T_c S}{J} \quad \text{or} \quad \frac{J}{S} = \frac{W}{R} - \frac{E_c}{N_j} \quad \text{in dB.}$$

Table 4.6. Maximum J/S with $E_c/N_j = 20$ dB, $R = 15.84$ Mbps

Carrier Frequency	W, GHz	J/S, dB
30	3.0	2.8
44	4.4	4.4
60	6.0	5.8

For purposes of estimating system performance in a jammed environment, we make the simplifying assumption that jammer power is the dominant factor in symbol-decision errors. Note from Table 4.6 that, even at 60 GHz, a maximum J/S of 5.8 dB is available at a data rate of 15.84 MHz and bandwidth of 6 MHz while maintaining a check BER of 10^{-2} . The frequency-hopped TDMA system performance can be improved by employing frequency diversity, e.g., multiple hops per symbol at the expense of increased system complexity and reduced throughput.

An example of m -diversity AJ modulation is given in Figure 4.25. Symbols S_1 through S_N are transmitted on hops 1 through m . The receiver has storage for N symbol decisions, and is capable of determining whether or not a given symbol has been jammed. It is assumed that the jammer is asynchronous with the communicator and portions of a hop can be toned jammed. The receiver makes symbol-by-symbol decisions on hop 1, erasing symbols that are ambiguous due to jamming. This process continues until all m hops have been examined by the receiver. Thus, the probability of symbol error is equal to the probability that all m hops have been jammed. In the example of Figure 4.25, symbols S_1 and S_2 of hop 1 would be ignored, while S_{N-1} and S_N would be stored in memory. The probability of a check bit error can be shown to be:

$$P_b = \frac{1}{2} e^{-\left(\frac{k}{2^k} e^{-1}\right) \frac{E_c}{N_j}}$$

with $M = 2^k$ and the optimum diversity to be

$$m = e^{-1} \left(\frac{E_c}{N_j}\right) \frac{K}{2^k}$$

For $P_b \leq 10^{-2}$ and $M = 4$, $m = 4$ and $E_c/N_j = 10.4$ dB. The resultant AJ margin is given in Table 4.7.

Table 4.7. Maximum J/S with $E_c/N_j = 10.4$ dB, $R = 15.84$ Mbps

Carrier Frequency	M , GHz	J/S, dB
30	3.0	12.4
44	4.4	14.0
60	6.0	15.4

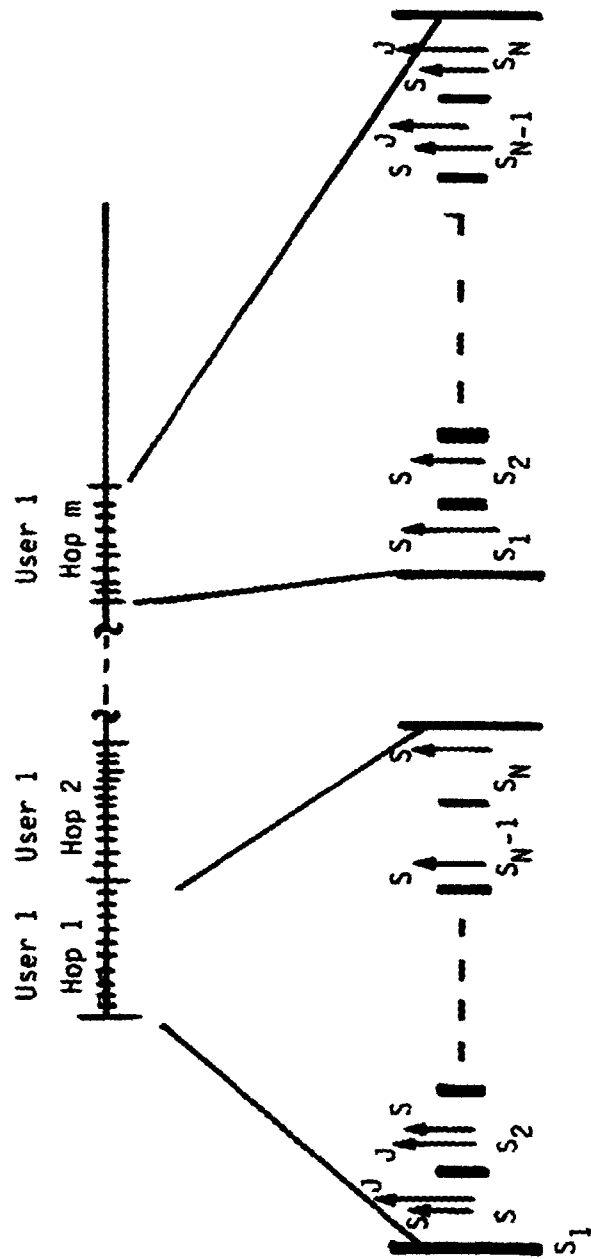


Figure 4.25. m-Diversity Frequency Hopping

5.0 MULTIPLE-ACCESS ANTENNA-DESIGN CONSIDERATIONS

The omnidirectional antenna-coverage requirement for the Space Station (SS) for 18 simultaneous users out to 2,000 km is a difficult problem. A number of possible antenna configurations have been studied in order to develop a viable system. The outcome of the preliminary investigation is that planar phased-array antennas are the best candidates to fulfill system requirements, but the implementation is difficult to perform. An alternate scheme which shows some promise has also been developed which may overcome some of the problems associated with phased arrays uses a combination of mechanically and electronically scanned parabolic dishes.

In order to simplify the antenna-coverage problem, two range regions are delineated. For near coverage out to 50 km, antenna gains of 20 dB are adequate while, for the extreme ranges out to 2,000 km, 40 dB of gain will be considered reasonable, at least initially, with 60 dB of gain desirable. The baseline frequency will be 30 GHz, with 44 GHz also being studied since many new generations of military satellites will be using this frequency band.

The electronic planar-phased array is capable of being scanned rapidly by phase shifters for TDMA applications and forming multiple beams for FDMA systems. Nulling for AJ performance is also possible with the new beam-forming/nulling processors which adjust amplitude and phase shifts at each radiating element in order to optimize multiple-beam pointing and jammer nulling.

When considering planar-phased arrays, some important features are that very large numbers of phase shifters are required, the array-feed network is lossy, the phased array is frequency sensitive for frequency-hopped (FH) systems, and multiple beams/nulling and beam-steering degrade the array performance. Table 5.1 shows an attempt to outline the basic requirements of an idealized array at various gain levels.

At close ranges where 20 dB of gain is required, the planar-phased array is only a square-inch wide, with 36 phase shifters for one beam (i.e., TDMA). However, if 16 simultaneous multiple beams (FDMA) are required, the gain-design criteria must be increased by 12 dB, so that a 36 in² array with nearly a thousand phase shifters (filled array) are necessary. The selection of TDMA and/or FDMA techniques is therefore extremely important in determining the required size of the antenna. This choice is even more apparent when the 40-dB gain array is designed, since a TDMA planar array is only one square foot in area with 3,000 phase shifters versus an FDMA planar array 9 ft² in area with 30,000 phase shifters.

Table 5.1. Idealized Planar-Phased-Array Parameters for Various Gain Levels

Gain	20 dB	25 dB	30 dB	35 dB	40 dB	50 dB	60 dB
$(n\lambda)^2 = \frac{G}{4} \lambda^2$ Dimension of Square Array (λ)	3	5	9	16	28	89	282
Number of Filled-Array Phase Shifters	36	100	324	1,024	3,100	31,700	318,000
$\theta_{3dB} = \sqrt{\frac{27,000}{G}}$	16.4°	9.2°	5.2°	2.9°	1.6°	0.5°	0.16°
θ States in 90°	6	10	18	32	56	180	562
Dimensions: 30 GHz 44 GHz	1.2 in 0.8 in	2 in 1.34 in	3.5 in 2.4 in	6.3 in 4.3 in	11 in/0.9 ft 7.5 in/0.6 ft	35 in/2.9 ft 24 in/2.0 ft	111 in/9.3 ft 75.5 in/6.3 ft

Due to the spherical-coverage requirement, five or six of these phased arrays will surround the SS. A multiple-gain capability may be developed where the aperture area is electronically adjusted but, if not, both a 20-dB array and a separate 40-dB array will have to be used, thus doubling the number of planar arrays. In addition, the receive and transmit functions may or may not be integrated into the same system. Practically speaking, since the transmitter uses a different frequency set in the same band and therefore requires another set of phase shifters, a separate transmit planar array is feasible because of the additional isolation obtainable. Thus, as many as 24 planar arrays may be needed to fulfill the spherical-coverage, near/far requirements.

The alternate antenna configuration considered is the parabolic dish, which has extremely high gains (up to 60 dB, i. desired). If mechanical beam steering is allowed, 18 separate dishes can accommodate 18 users simultaneously without TDMA and FDMA using individual transmitters/receivers. Orthogonal circular polarizations for transmit and receive provide additional isolation by using quarter-wavelength diagonal-dielectric slabs as polarizers in a square waveguide. Figure 5.1 shows the gains achievable with commercially available dishes and Table 5.2 outlines idealized parabolic dish diameters for various gain levels.

As an aside, an acquisition aid that might be considered is a sensitive CCD video camera which can visually locate a blinking stroboscopic light beacon on the user, as described in Figure 5.2. Monopulse autotracking is readily available once acquisition occurs. An obvious advantage of this concept is the inherent redundancy and the incremental growth capability.

The use of parabolic dishes at near ranges is not as practical, but a modification of the feed into an electronically scanned array offers a means of substantially reducing the number of phase shifters required. A five-horn cross feed, with the central horn fed directly and the surrounding horns with phase shifters, provides an electronic-scanning capability of ± 5 beamwidths, for a total of 100 beam positions. Table 5.3 outlines the number of parabolic dishes necessary to attain spherical coverage for a given gain. For example, 25 dB of gain implies a 3-dB beamwidth of 9.2° , and 10 beam positions gives 90° coverage. Theoretically, five paraboloids would provide spherical coverage. At 30 GHz, since the aperture diameter of 6λ is 6 cm or 2.5 inches, the total antenna set of five paraboloids is quite small. Even at 35 dB gain, 46 paraboloids, eight inches in diameter, scattered about the large SS, is not unreasonable since only 184 phase shifters are required. Figure 5.3 attempts to show the appearance of one-half of a 40-sided polygon parabolic dish array. Since it uses electronic

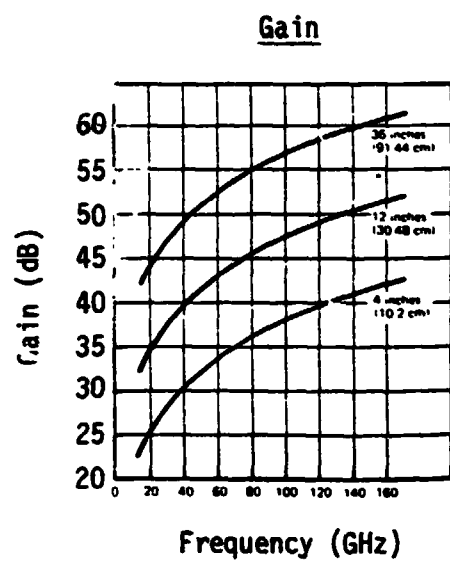
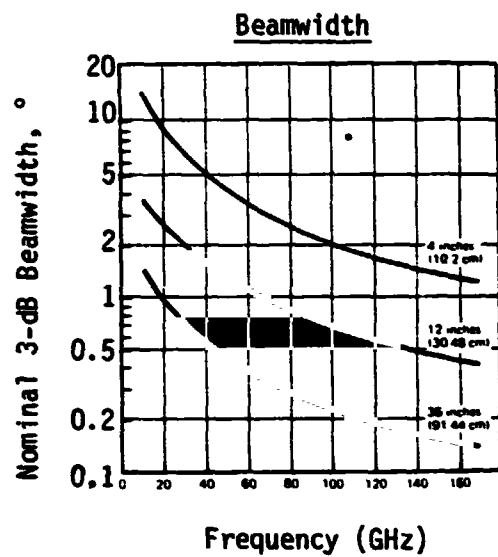


Figure 5.1. Gains and Beamwidths of Commercially Available Parabolic-Dish Antennas

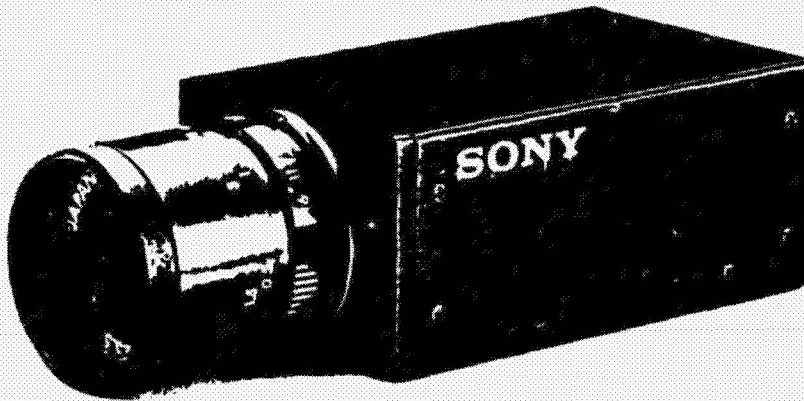
Table 5.2. Parabolic-Dish Dimensions for Higher Gains

Gain (dB)	θ_{3dB}	Aperture Diameter ($n\lambda$)	Aperture Diameter at 30 GHz	Aperture Diameter at 44 GHz
60	0.16°	318	10.5 ft	7.2 ft
55	0.29°	180	5.9 ft	4 ft
50	0.5°	100	3.3 ft	2.3 ft
45	0.9°	57	1.9 ft	1.3 ft

Table 5.3. Parabolic-Dish Spherical Coverage Using Idealized Gain Values

$\theta(^{\circ})$	Gain (dB)	Circumference (Paraboloid Diameter)	Radius (Paraboloid Diameter)	Surface Area (Paraboloids)	Aperture Diameter ($n\lambda$)
1.6	40	22	3.6	161	32
2.0	38	18	2.9	103	28
2.5	36	14.4	2.3	66	20
3.0	35	12	1.9	46	18
3.5	33	10.3	1.6	34	14
4.0	32	9	1.4	26	13
4.5	31	8	1.3	21	11
5.0	30	7.2	1.2	17	10
5.5	29.5	6.6	1.1	14	9.5
6.0	29	6.0	1.0	12	9
9.2	25	4.0	0.6	5	6
16.4	20	2.2	0.35	1.5	3.2

SONY Miniature CCD Video Camera Module



FEATURES

- CCD (Charge Coupled Device) solid state image sensor replaces tube type pickup and provides extended life and improved stability
- Miniaturized design is only 1 1/4" high by 1 1/4" wide by 2 1/4" deep and weighs just 4.1 ounces
- Ultra stable, extended life operation due to completely solid state componentry with virtually no maintenance
- Low lag and high image burn resistance
- Precise image geometry
- Shock and vibration resistance exceeds all tube cameras
- Instant shooting with a start-up time of 1/2 second due to elimination of electron gun/pick up tube
- Anti-magnetic properties of CCD allow camera to be used in areas with strong magnetic fields
- High sensitivity enables camera to shoot in 3 lux illumination
- Low power consumption of less than 2.3 Watts
- Special mini bayonet lens mount plus C lens mounting with an optional adaptor

SPECIFICATIONS (TENTATIVE)

Pick up device: Interline Transfer Type CCD

Optical system: Special mini bayonet/ "C" mount with adaptor

Scanning system: 525 lines, 60 fields/sec, 2:1 interlace

Video output: 1.0 Vp-p sync negative, 75 Ohms

Resolution: Horizontal: 280 lines
Vertical: 350 lines

Sensitivity: 400 lux, F4, typical (3200°K, S/N 46dB with Infrared cut filter)

Minimum illumination: 3 lux F1.4 (without infrared cut filter)

Signal-to-noise ratio: more than 46 dB

Power requirement: 12 V DC with power unit

Power consumption: 2.3 W

Weight: 4.1 oz., 115 grams (without lens & power unit)

Dimensions: 1 1/4" x 1 1/4" x 2 1/4" (HWD)
28.5mm x 43mm x 72.5mm (HWD)

Specifications subject to change without notice

Figure 5.2. CCD Video-Camera Candidate for Visual-Acquisition Aid

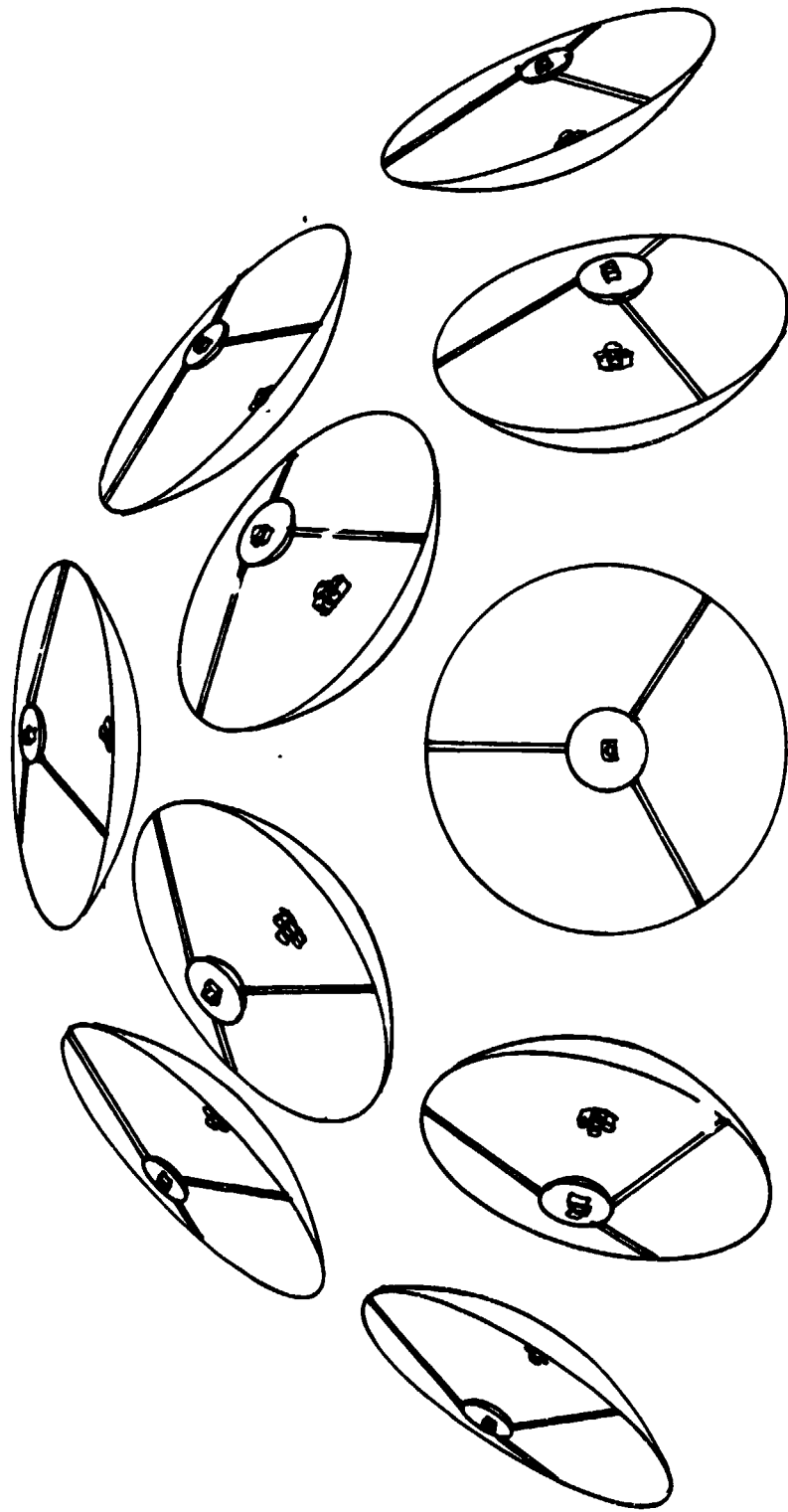


Figure 5.3. Hemispheric Array of Parabolic Dishes

scanning for the limited coverage of one paraboloid, a parabolic-dish array is suitable for TDMA techniques within the coverage area of one dish and multiple beams from individual parabolic dishes are attained by selective IF signal combining, so that FDMA is feasible.

The beam-selection process uses latching-reciprocal ferrite phase shifters and latching-ferrite SPDT switches. Figure 5.4 shows a possible switching network connecting 2^N paraboloids, where N is the number of switching levels. This complexity can be avoided if individual transmitters/receivers are provided at each paraboloid, so that switching is done at the IF level.

The five-horn feed configuration with phase shifters in the outer horns would allow electronic acquisition even for the high-gain, mechanically steered parabolic dish. If the monopulse-tracking magic tee is located after the phase shifters, the sum signal indicates acquisition, and the difference signal will allow autotracking, even off-axis, or indicate the correct phase adjustments needed to mechanically align the beam. Since latching-ferrite phase shifters with $1 \mu\text{s}$ switching times are used, TDMA within the 100-beam electronic-scan sector is possible if more than one user is in that sector.

Since the orthogonal modes of circular polarization for the transmitter require separate sets of phase shifters, the required phase shifts for the FH signal can be individually tailored to point at the user, independent of the receive FH signals. Figure 5.5 sketches the transmit/receive phase shifter configuration. Note that this approach doubles the number of phase shifters required but, since the parabolic-dish-array concept uses fewer phase shifters, the total number of phase shifters is not unreasonable.

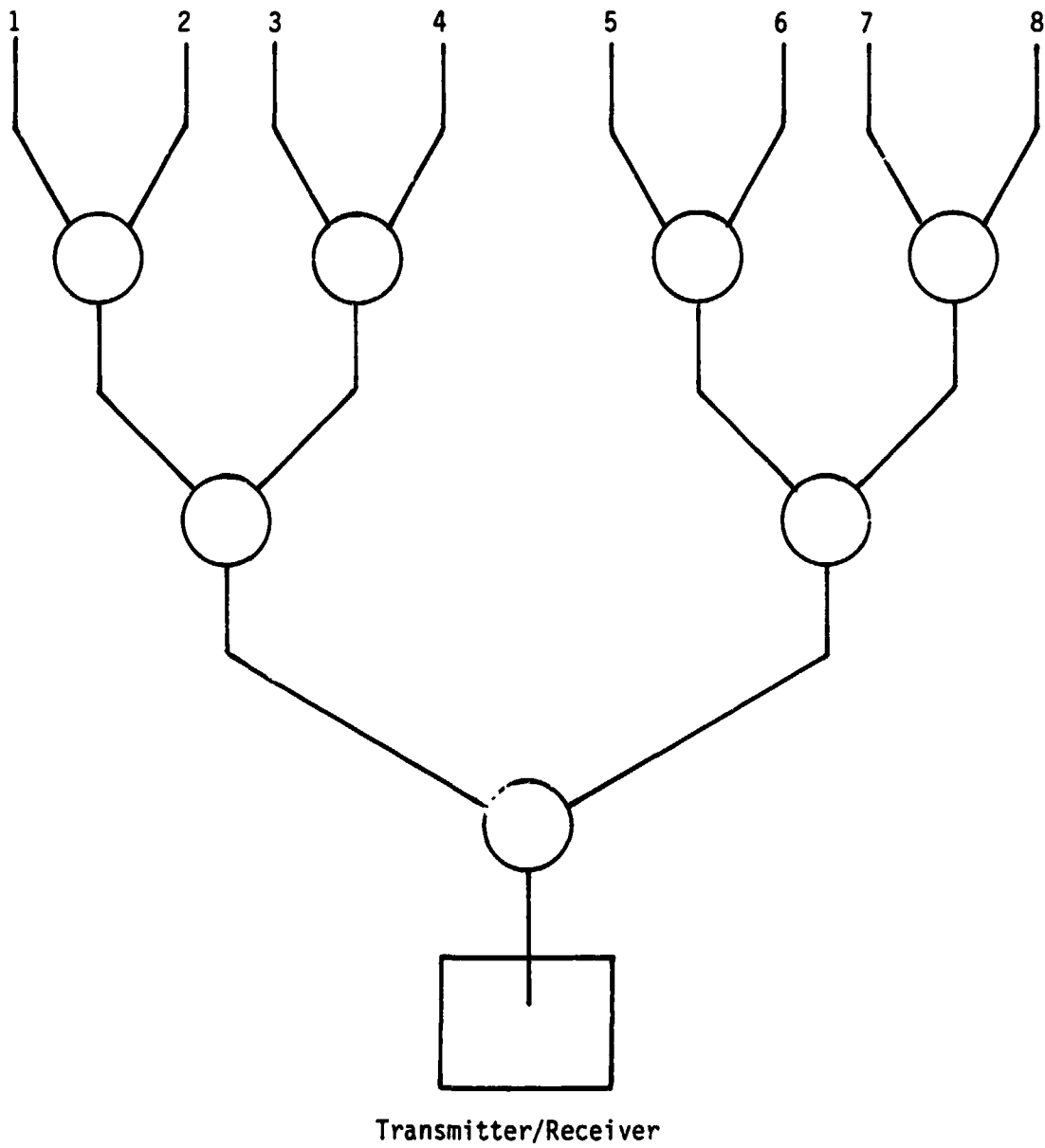


Figure 5.4. RF Switching Network Using Ferrite-Latching Circulators

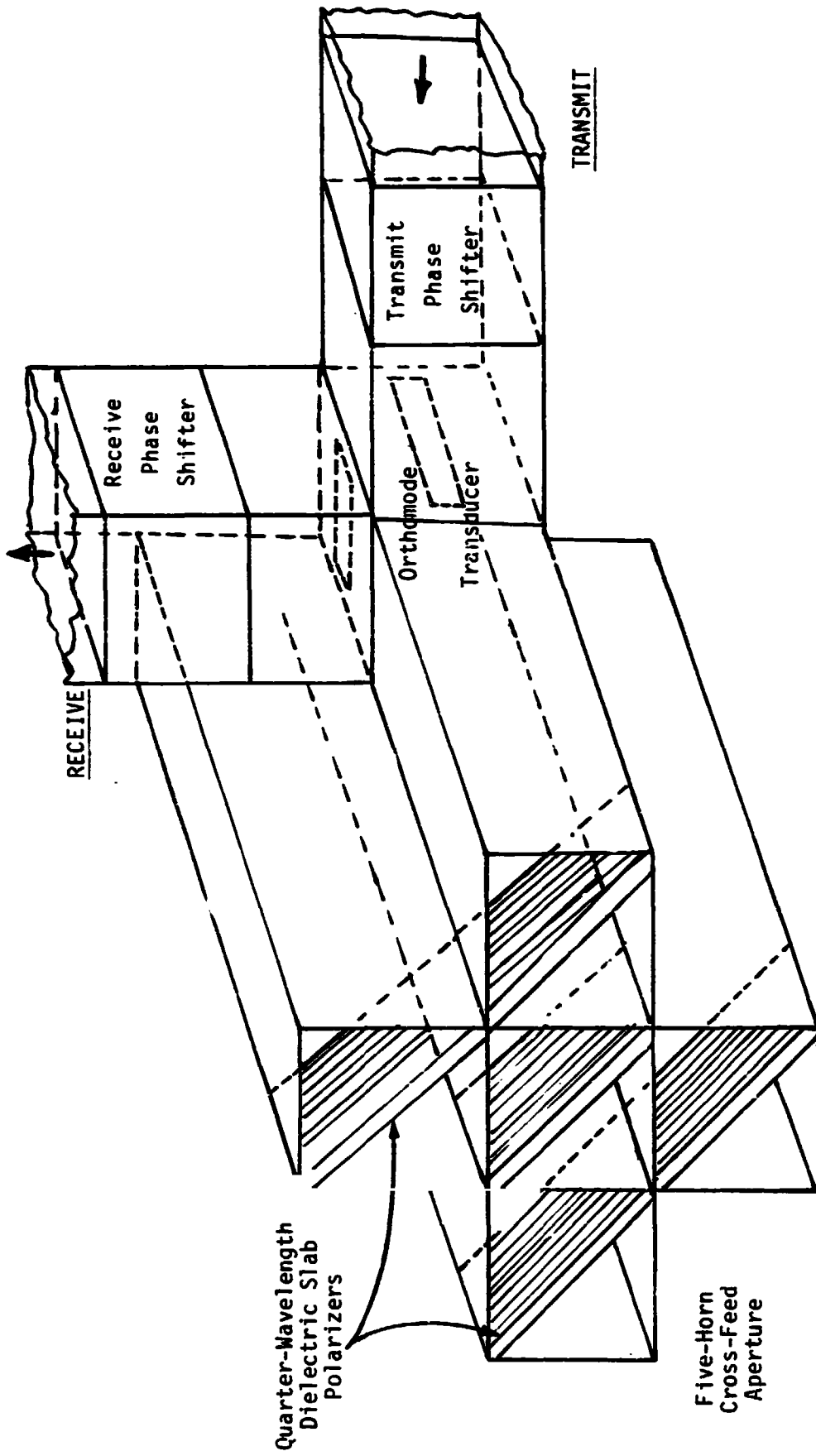


Figure 5.5. Five-Horn Cross Feed with Dielectric Polarizers and Orthomode Transducer for Transmit/Receive

When evaluating antenna configurations, component availability is an important consideration because the feasibility of an approach hinges on realistic design practices. Two frequency ranges studied for the SS communication links are as follows: The 30-GHz range is desirable due to NASA/DOD technology developments and 44 GHz is used for military satellites such as MILSTAR. The baseline frequency of 30 GHz is attractive due to the FET low-noise amplifiers (LNA's) and the higher power transmitters available. The 44-GHz region allows wider frequency-hopping (FH) bandwidths and therefore greater anti-jam (AJ) capability, but the device technology is not as well developed and thus is deemed a higher risk, although the SS program will not be fully implemented until the 1990's time frame.

Both antenna configurations discussed--planar-phased array and phased-array-fed parabolic dish--use many common components. Latching ferrite phase shifters having 1 μ s switching speeds are now commercially available at both 30 and 44 GHz. Similarly, low-noise-figure, double-balanced mixers are available off the shelf. The primary difference between the choice of these two frequencies is that low-noise FET preamplifiers with 3.5-dB noise figures at 30 GHz are being developed, which greatly enhances receiver sensitivity and therefore increases link margin. In addition, the available transmitter powers are inherently higher at 30 GHz, approximately double that at 44 GHz--an especially critical factor since the free fliers are transmitter-power limited.

The Cassegrain configuration parabolic dish with five horn feeds and orthomode transducers is a standard antenna system. The proposed high-gain, mechanically steered dish is closely related to existing ground station dishes. The major advantages of this system are: (1) extremely high gains are readily achievable and, (2) adding electronic beam-scanning requires only eight phase shifters per dish (a set of four each for the transmitter and receiver). Each dish has its own LNA and transmitter amplifier and, therefore, does not have to be shared. Microwave circuit losses are lower since no power-dividing, beam-switching networks are needed, which also greatly adds to system complexity. The independence of each dish provides redundancy and incremental growth capability, valuable features for space operation. Full-spherical antenna coverage is available with high gains. Since each parabolic dish in the set of fixed low-gain parabolas points in a different direction, the off-axis axial ratio and beam-spreading performance is greatly improved--a definite limitation of planar-phased arrays. Finally, if each dish has its own low-noise receiver and transmitter, the antenna gain and transmitter powers do not have to be shared, as in the case of planar-phased arrays with multiple beams, which sacrifices gain to produce multiple beams.

On the other hand, the planar-phased array is definitely a viable antenna-configuration candidate due to its flexibility. For TDMA operation, it can rapidly scan a spot beam. Conversely, multiple-beam forming and nulling capabilities are realizable for FDMA and AJ applications. However, there are some definite design constraints which must be considered when evaluating the antenna configurations. First, the multiple-beam forming and nulling capabilities are complex and require much larger apertures in order to compensate for sharing the achievable gains since the antenna pattern is simply being redistributed. For example, when two main beams are formed instead of one, there is at least a 3-dB loss in gain in each beam when the pattern is shared. Therefore, the phased-array aperture area must be correspondingly doubled in order to maintain a constant value of main-beam gain, also doubling the number of phase shifters required. Since each radiating element is spaced approximately a half-wavelength apart and large aperture areas are needed for high gain, very large numbers of phase shifters are required, even for thinned arrays. The power-dividing/combining networks for these large arrays are complex and quite lossy, thus degrading the receiver sensitivity and increasing the transmitter power requirements. Simultaneous receiver and transmitter operation demands a separate array for each function, especially since both forward and return links are independently frequency hopped. Another limitation is that the off-axis performance of a planar array is severely degraded, both in axial ratio and beam broadening, which reduces the gain. Under these conditions, it is not unreasonable to consider a larger number of smaller planar arrays distributed about the SS to overcome some of these limitations, as proposed for similar reasons for the parabolic dishes. The increased number of planar-phased arrays also increases the available transmit power since it does not have to be shared, at the expense of additional high-power amplifiers and low-noise receivers, but which provides redundancy.

In conclusion, the high-gain antenna requirement for spherical coverage about the SS can be satisfied by either large planar arrays or mechanically steered large parabolic dishes with approximately the same size apertures. If there are 12 simultaneous users for the far ranges (50-2000 km), then 12 mechanically steered parabolic dishes or six equivalent-sized planar-phased arrays faced in the appropriate directions are required. If one planar-phased array services one quadrant for the 12 users employing FDMA, the aperture size must increase by a factor of 16 in order to compensate for the gain loss due to redistributing the pattern for multiple beams with the same gain, so the TDMA approach is appealing for high-gain applications using the planar-phased arrays.

The low-gain spherical coverage can be handled readily by either the planar-phased array or multiple parabolic dishes. The lower gain permits the use of smaller apertures and, therefore, fewer phase shifters. The dimensions of the apertures are reasonable and acceptable. The problems of separate transmit and receive arrays as well as acquisition and tracking still exist for the planar-phased array, but they are not insurmountable. Again, the driving consideration is the type of multiple access used, either TDMA or FDMA or combinations thereof.

One aspect of the communication link which is not fully discussed is the antenna requirement of the free flier, which generally is omnidirectional in order to avoid pointing problems. If directional antennas with higher gain can be used, the SS gain problem can be correspondingly reduced.

It is obvious that no apparent solution to the SS antenna-gain-coverage requirement exists. Much of the technology being developed for geosynchronous satellites cannot be readily adapted to SS use since the antenna coverage is limited to earth coverage from a distance--a very small sector compared to the spherical coverage requirements of the SS. The SS antenna design is a challenging area worthy of extensive investigation in the future.

APPENDIX A

VIDEO DATA-COMPRESSSION TECHNIQUES STUDY

TABLE OF CONTENTS

	<u>Page</u>
LIST OF FIGURES	iii
LIST OF TABLES.	iv
1.0 INTRODUCTION.	1
2.0 VIDEO DATA-COMPRESSION TECHNOLOGY STATUS AND TRENDS	3
2.1 Factors Contributing to Digital Video Data Compression	3
2.1.1 Advantages of Digital Video Data Transmission	3
2.1.2 Current Digital Video Uses Which Provide a Data Base for SS Video Bandwidth-Compression Techniques	5
2.2 Video-Digitizing and Bandwidth-Compression Techniques Identification	5
2.2.1 Technique Identification.	5
2.2.2 Encoding-Scheme Evaluation Criteria	6
2.3 Video Bandwidth-Compression-Techniques Description	11
2.3.1 Motion-Compensation Technique	12
2.3.2 Hybrid Coding for Bandwidth Compression of Video Signals	17
2.3.2.1 General Considerations	17
2.3.2.2 Harris Corp. hybrid-coding system for RPV use	21
2.3.2.3 Other efforts in hybrid coding	26
2.3.3 Delta-Modulation Techniques for 15-t0-30-Mbps Digital TV Links.	28
2.3.3.1 Overview	28
2.3.3.2 Bistate adaptive delta modulation	28
2.3.3.3 Tri-state delta modulation for run-length encoding	33

	<u>Page</u>
2.4 VLSI Utilization Potential	43
2.4.1 Capabilities and Limitations of VLSI Applications to Bandwidth-Reduction Systems	43
2.4.2 Specific Systems to be Potentially Reduced Through VLSI	46
2.4.2.1 VTS 1.5E System made by Compression Labs, Inc.	46
2.4.2.2 NETES-X1TV Codec, made by Nippon Electric Co., Ltd.	47
3.0 RELATED VIDEO-TECHNOLOGY DEVELOPMENTS	48
3.1 CCD Cameras.	48
3.2 Digital TV Devices Applicability	48
4.0 SUMMARY AND CONCLUSIONS	50
REFERENCES.	51

LIST OF FIGURES

	<u>Page</u>
2.1 Comparison of Analog FM and Digital Transmission in Terms of RF Bandwidth and Transmitter [1]	4
2.2 Digitized Video Signal Lends Itself to a Relatively Simple Encryption/Decryption Method.	4
2.3 Television Source-Encoding Categorization	7
2.4 Alternative Methods of Digitized TV Signal Coding	8
2.5 Coding Bit Rate Versus Picture Quality for Typical Coding Methods [1]	9
2.6 Interframe-Coding Performance Features [1]	9
2.7 Relative Performance of Coding Techniques in Terms of Picture Quality Versus Transmission Rate [2].	10
2.8 Principle of Basic Interframe Coding.	13
2.9 Generic Configuration of an Interframe Encoder.	13
2.10 The Principle of Motion-Compensated Interframe Coding	13
2.11 Motion-Compensated Coder and Decoder Block Diagram.	15
2.12 Mean-Square Error Performance of Different Transforms for the Two-Dimensional Markov Image Source with Horizontal Correlation Factor of ρ_c and Vertical Correlation Factor of ρ_v [3].	18
2.13 Block Diagram of a Hybrid Transform/DPCM Encoder.	20
2.14 Functional Block Diagram of the Video-Bandwidth Compression and Reconstruction Units.	23
2.15 Hardware Systems Design of Compression and Reconstruction Units .	24
2.16 Conventional (Bistate) Delta Modulator Functional Block Diagram .	30
2.17 Field-Sequential Color System [10].	32
2.18 Tri-State Delta Modulator (TSDM) Functional Block Diagram	34
2.19 Tri-State Video Digitizer (and Reconstructor) Implementation. . .	37
2.20 Run-Length Encoder (Transmitter Side)	39
2.21 Run-Length Decoder (Receiver Side).	41
2.22 NTSC Color TV Component Digitization.	42
2.23 Speed-Power-Density Diagram [14].	45

LIST OF TABLES

	<u>Page</u>
2.3-1 Salient Characteristics of the Harris Corp. Hybrid-Coding System [4]	22
2.3-2 RPV Compression Hardware Evaluation [5]	27
2.3-3 Encoding Table for TSDM	40

EXECUTIVE SUMMARY

Video data-compression techniques applicable to space station (SS) communication requirements are considered from the standpoint of their realizability with existing hardware. Projections toward future implementations with respect to size reduction are made. Specifically, recent developments in the area of frame-to-frame (interframe) coding are examined in terms of commercially available existing equipment. Also, examples of existing hybrid-coding equipment developed for remotely piloted vehicles (RPV'S) are presented and discussed in terms of SS applicability. Furthermore, relatively simple encoding systems, such as delta modulation, are considered for utilization in links which do not permit complex-terminal encoding equipment.

The study addresses two general types of bandwidth-compression schemes. One scheme is characterized by the rather complex equipment yielding good-quality pictures at rates less than 3 Mbps. One such scheme is motion compensation combined with interframe encoding. Hybrid-transform coding with reducible frame rates is also described in this category. The second scheme considered is that of delta modulation with relatively simple intraframe encoding, such as run-length encoding. The channel rates for these types of systems are in the 15-to-30-Mbps range, with about 20 Mbps being a baseline number.

Also in this study, the applicability of VLSI techniques for potential size reduction of existing schemes is discussed, and projections based on our engineering judgment are made. Furthermore, recent developments in CCD technology are considered, particularly with respect to miniaturized components such as the CCD-based TV camera.

Our findings can thus be summarized as follows:

- Good-quality, moderate-motion TV color pictures can be transmitted at a rate of 2.048 Mbps using interframe encoding with motion compensation. The video processor for this transmission can be packaged to within 1 ft³ using VLSI.
- For channel rates much lower than 2.048 Mbps, low-frame rate, black-and-white pictures can be transmitted using hybrid coding. The processor volume for this type of transmission is about 25 in³ using LSI.
- For requirements where a lot of picture motion has to be accommodated, delta modulation can be used provided that a channel capacity of 15-30 Mbps is available. Depending on the requirements (i.e., color versus black and white, resolution, etc.), the processor volume may range from 25 in³ to 0.5 ft³.

1.0 INTRODUCTION

This report describes recent developments in video data-compression techniques from the standpoint of applicability to Space Station (SS) requirements. The particular slant of this report is the hardware aspect of the latest video data compression. Thus, the techniques themselves are described only in general terms and, wherever applicable, the hardware implementation aspects of such techniques are mentioned.

The methodology used to obtain the material for this report consisted of the following activities:

- (1) Survey of recent technical literature pertaining to video data compression
- (2) Study of vendor/manufacturer/supplier brochures
- (3) Direct vendor/representative contact (by telephone)
- (4) Our own interpretation and projection of the gathered information, i.e., analysis/synthesis method.

Due to the formative nature of the SS requirements, it is difficult to make a specific and final recommendation at this time with respect to the "optimum" technique for digital video compression. Requirements will have to be defined by various users and these requirements, in turn, will be mission dependent.

Consequently, the best we can do at this point is to describe what is available today in terms of the video data-compression techniques in order to identify the trends and make some reasonable prediction of what will be available in the near future.

In making such assessments and predictions, we chose to be guided by the following assumptions:

- (1) The video-compression techniques must be compatible with an all-digital communication channel
- (2) The baseline goal for the maximum data-transmission rate for reasonable quality TV picture transmission is 2.048 Mbps, with only special situations requiring up to 22 Mbps

(3) No video data-compression technique can be considered "superior" to any other technique in that the customer requirements dictate the trade-offs in selecting a particular data-compression method.

Thus, the contents of this report should be judged in terms of the aforementioned assumptions. Furthermore, it must be emphasized that, because of the rapidly evolving developments in TV video data-compression techniques, any opinion expressed at this time must be reexamined at some later date when: (1) the SS detailed requirements will come into better focus and, (2) the video data-compression techniques will undergo a considerable evaluation in their respective fields of application.

2.0 VIDEO DATA-COMPRESSSION TECHNOLOGY STATUS AND TRENDS

2.1 Factors Contributing to Digital Video Data Compression

2.1.1 Advantages of Digital Video Data Transmission

The advantages of video data transmission via digital, rather than analog, methods have been demonstrated in the past by both theory and practical implementations. However, it is only recently that the digital signal-processing technology has reached the point where operational use of the digital techniques is possible. In general, for an equivalent picture quality, digital technology offers a marked advantage over analog methods in that it has the following features: (1) lower RF power requirements, (2) lower RF bandwidth requirements, (3) data-encryption capability, (4) picture quality is solely determined by terminal equipment--not by the communication link, and (5) error-control techniques are applicable.

Figure 2.1 demonstrates the transmitter-power-requirements advantage of the digital-picture-transmission method as compared with the FM analog techniques. Although Figure 2.1 does not contain any reference to the absolute quality of analog and digital transmissions, it clearly demonstrates the power and RF bandwidth advantages of the digital-transmission techniques.

The relative ease with which a digital picture transmission can be encrypted is demonstrated in Figure 2.2. As shown there, encryption/decryption can be implemented, at least in principle, by means of EXCLUSIVE-OR digital-logic gates. In comparison, an equivalent process for analog video signal encryption would require a considerable amount of signal-processing equipment.

Since the quality of a digital transmission is determined by the processing capability of the terminal equipment--not by the transmission media--the digitized video signal becomes particularly attractive for digital RF links utilizing multiplexing for multiple access. This is particularly true for the case of time multiplexing, which is one of the candidates for the SS communication link design.

Furthermore, the error-control techniques to which the digital signal lends itself provide a means for improving the tolerance of the digital video-transmission systems to the system bit-error rate (BER). This feature is of great advantage of the space-borne links, where the RF transmitter power is at a premium and, thus, a significant savings in power, size and weight can be realized by using digital error-correction codes implemented with a relatively

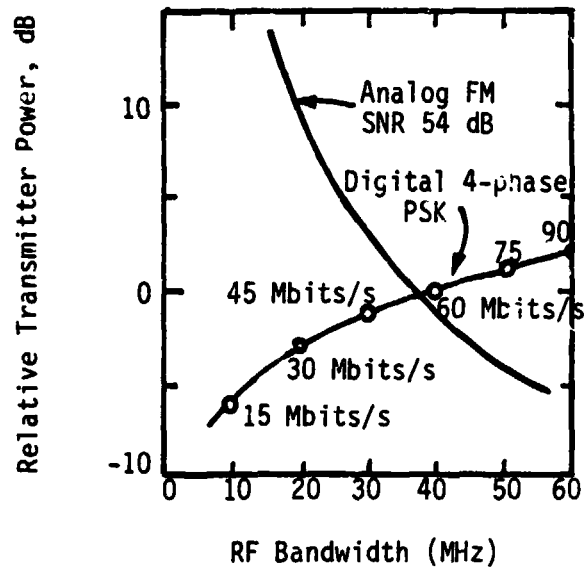


Figure 2.1. Comparison of Analog FM and Digital Transmission in Terms of RF Bandwidth and Transmitter [1]

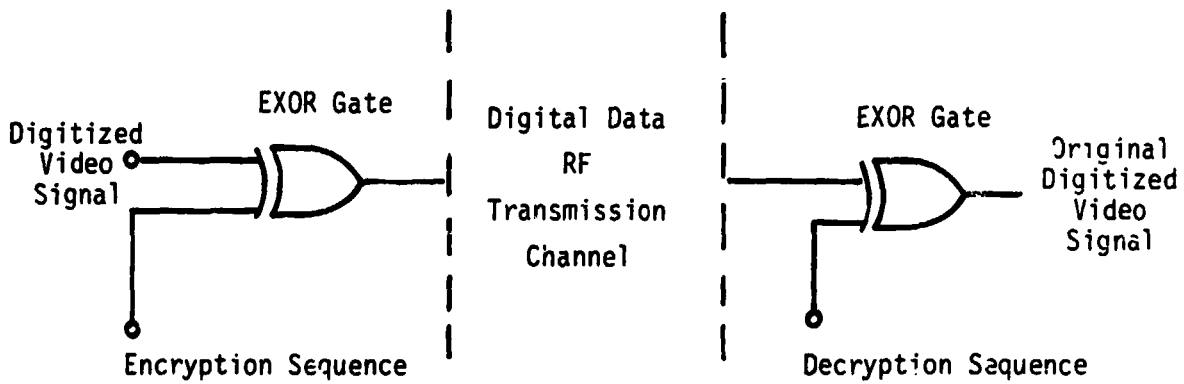


Figure 2.2. Digitized Video Signal Lends Itself to a Relatively Simple Encryption/Decryption Method

low-power technology such as CMOS. Utilization of the latter technology for encoding and decoding is particularly attractive for the relatively low video digital-data rates such as those baselined at 2.048 Mbps for SS operation.

• 2.1.2 Current Digital Video Uses Which Provide a Data Base for SS Video Bandwidth-Compression Techniques

As the result of the aforementioned advantages of digital video transmission, there recently emerged several areas of active development and utilization of such transmissions. Of particular interest for SS use are the existing techniques for bandwidth compression of the digital video signal. At least three areas can presently be identified, where efficient use of advanced techniques for bandwidth compression are successfully utilized. These techniques are used for transmission of video pictures, either still or time variant, consistent with the desired picture quality. The three areas are: (1) network high-quality digital TV, (2) video conferencing and, (3) remotely piloted vehicle (RPV) video transmission.

The first two techniques are driven by commercial, nonmilitary users. Thus, a considerable amount of competitive development activity has been exhibited in these areas in recent years. Not bound by military-component specifications, these two civilian application areas of digital video techniques have benefited greatly from the recent development of computer-oriented digital LSI technologies. On the other hand, the military-oriented RPV video-transmission technologies make use of custom developments that are tailored to specific video digitizing and processing techniques. Consequently, a considerable data base exists for SS digital video requirements from which applicable techniques can be synthesized.

2.2 Video-Digitizing and Bandwidth-Compression Techniques Identification

2.2.1 Technique Identification

Depending on the coding-bit rate, the existing video-digitizing and signal-processing techniques can be divided into three general categories, as follows: (1) conventional PCM, (2) intraframe coding, (3) interframe coding.

The conventional PCM does not fall into the bandwidth-compression techniques area. It is characterized by reasonably high quality and requires digital channel-bit rate in the 50-80 Mbps range. Typically, it consists of straightforward analog-to-digital (A/D) conversion of video information. The

levels of conversion may range from six to eight bits, and no attempt is made to perform any coding of the digitized-video information. Because of its reasonably high quality, the conventional PCM is often used as a quality reference for video-digitizing processes.

To achieve bandwidth compression, encoding techniques must be applied to the digitized video stream. Because the encoding is applied to the digitized signal per se and its purpose is bandwidth compression rather than the protection of the digitized data within the communication channel, it is referred to as "source encoding." Figure 2.3 shows the categorization of source-encoding techniques.

Source coding can be applied either within a single frame (intraframe coding) or over a series of several frames (interframe coding). For the case of intraframe coding, the signal processing can be applied either in one dimension, such as on a single-line basis, or over two dimensions, which include coding across a space extending over several lines within a single frame. Figure 2.4 provides a qualitative illustration of the intraframe and interframe coding. Motion compensation is one of the examples where efficient interframe-encoding algorithms are applied to achieve significant bandwidth compression.

2.2.2 Encoding-Scheme Evaluation Criteria

Unfortunately, no single scheme has yet been developed for evaluating picture quality versus bandwidth compression of various encoding schemes. This is because each case is not only applications oriented, but is also a function of picture content. Figure 2.5 shows a general relationship between the coding bit rate, coding technique, and picture quality. From Figure 2.5, it is evident that some sort of interframe coding, such as that used for teleconferencing, must be utilized for the SS to achieve channel rates below 10 Mbps, such as a baseline rate of 2.048 Mbps.

On the other hand, once one resorts to interframe coding, the picture quality becomes highly content dependent, as illustrated in Figure 2.6. From this figure, it is evident that, in order to accommodate picture-content variations such as those caused by motion, rather sophisticated interframe-coding algorithms have to be employed to preserve an acceptable degree of picture quality. Figure 2.7 demonstrates the importance of coding algorithms for interframe (i.e., frame-to-frame) signal processing for bandwidth compression. As indicated in this figure, neither simple frame-to-frame coding nor even complex interframe coding,

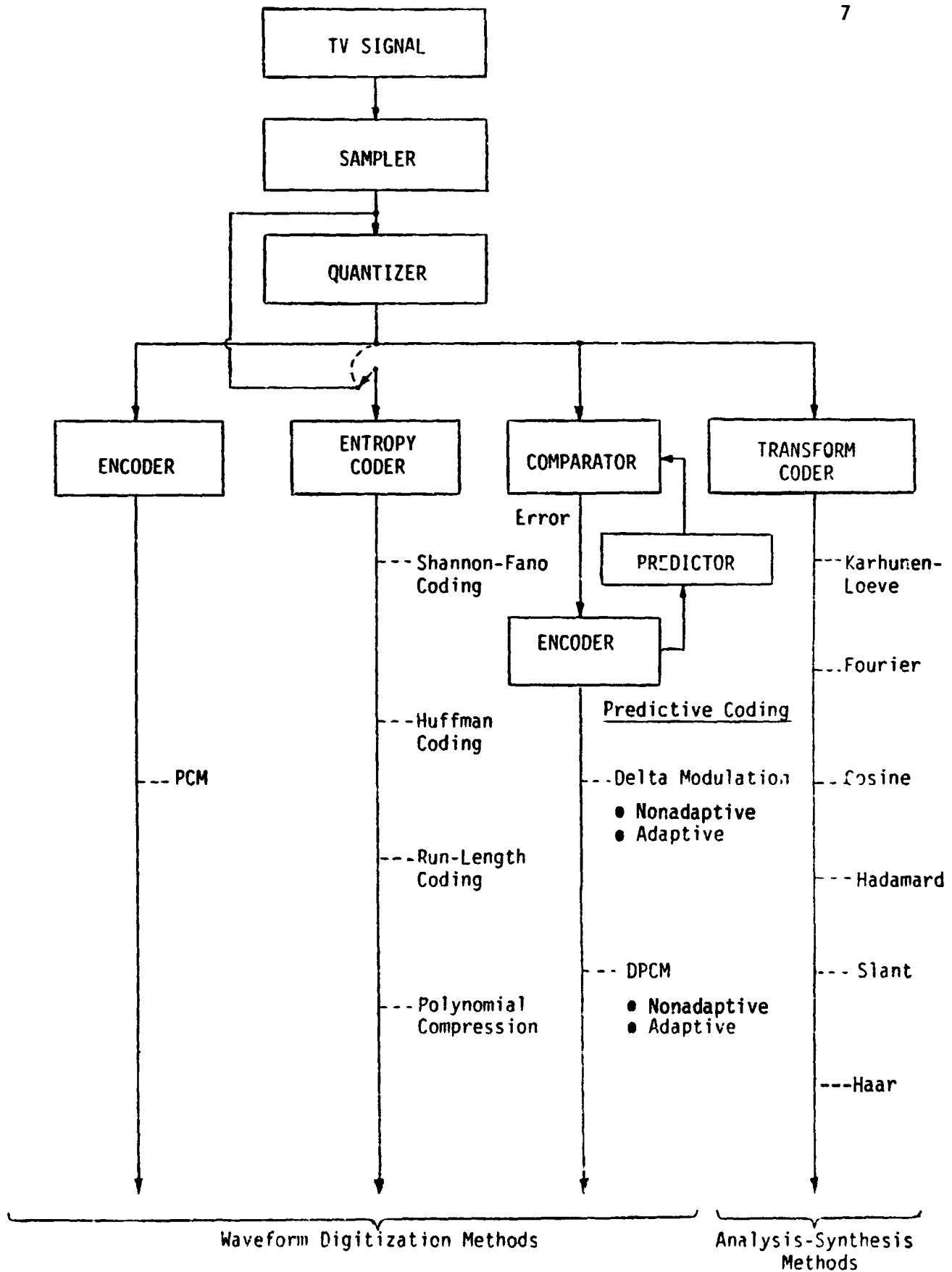
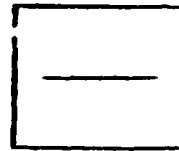


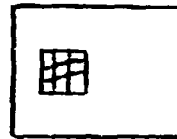
Figure 2.3. Television Source-Encoding Categorization

INTRAFRAME (Spatial)

One Dimensional



Two Dimensional



INTERFRAME (Temporal)

Three Dimensional

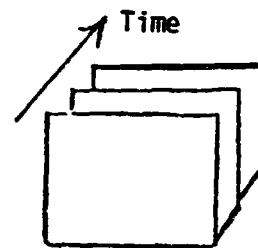


Figure 2.4. Alternative Methods of Digitized TV Signal Coding

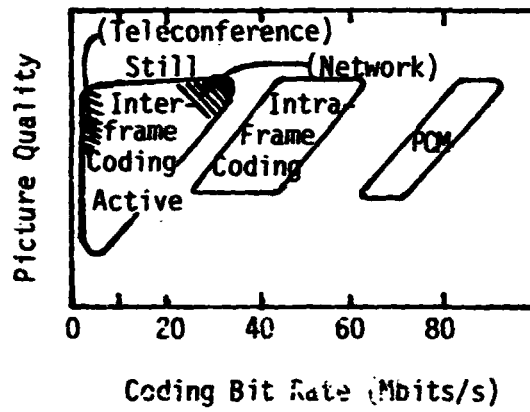


Figure 2.5. Coding Bit Rate Versus Picture Quality for Typical Coding Methods [1]

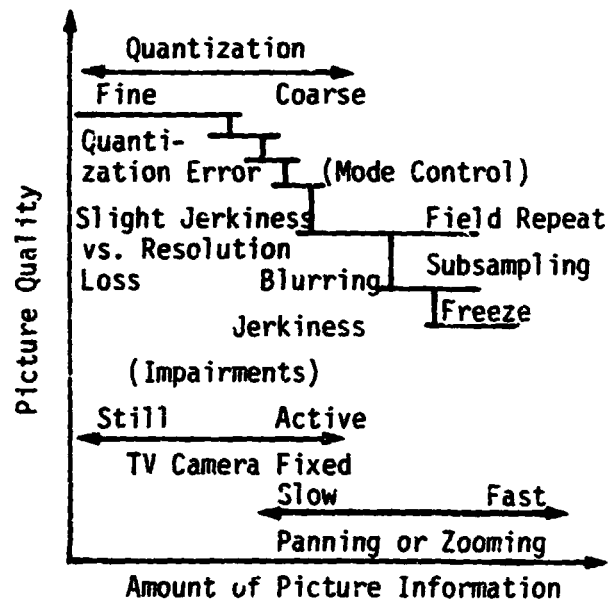


Figure 2.6. Interframe-Coding Performance Features [1]

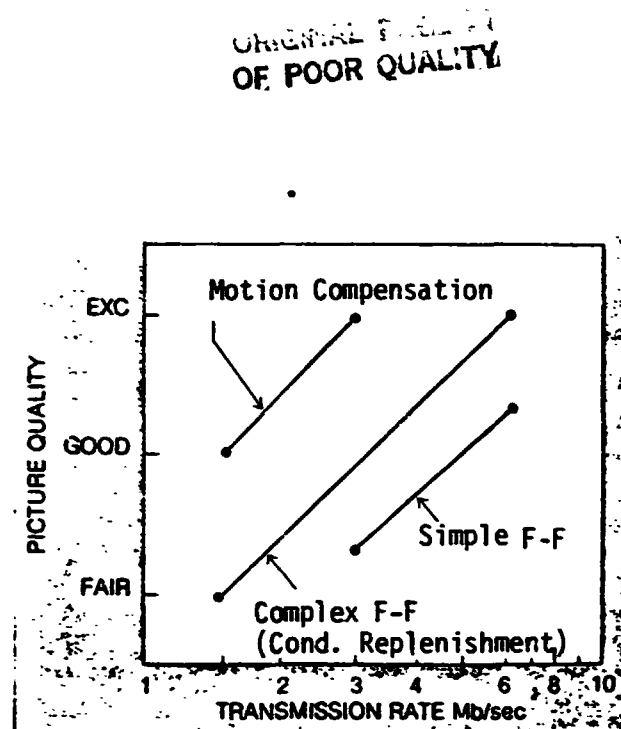


Figure 2.7. Relative Performance of Coding Techniques in Terms of Picture Quality versus Transmission Rate [2]

such as conditional replenishments, can provide good quality with transmission rates in the range of 1.5 to 3.0 Mbps. A special motion-compensation algorithm is required that achieves the most efficient utilization of interframe-comparison information. Such an algorithm is described in section 2.3.1.

Before concluding this rather general discussion of the relationship between the coding techniques for bandwidth compression and picture quality, the following criteria for judging picture quality [2] should be listed. These are: (1) edge sharpness, (2) edge accuracy, (3) flat-area busyness, (4) image continuity and, (4) distortion.

Edge sharpness defines the degree of edge blurring that is typical of bandwidth-limited TV pictures. Edge accuracy deals with the degree of waviness occasionally observed with some of the coding schemes. Flat-area busyness is a result of quantization noise-limited numbers of bits in a sample. This phenomenon is manifested as a grainy noise or false contouring in the flat areas. Image continuity manifests itself as breaks in the image resulting from frame-rate (interframe) processing techniques. Distortion defines the displacement of objects from their correct relative positions within the image.

For each given mission, the relative weight of these criteria can be only roughly assessed. Precise weighting will be impossible until there is more agreement between the users on the subjective criteria used for evaluation.

2.3 Video Bandwidth-Compression-Techniques Description

In this section, we consider some of the video bandwidth-compression techniques applicable to SS, TV and picture transmission at rates comparable to the baseline maximum channel rate of 2.048 Mbps. In this case, the emphasis is on those techniques whose feasibility has been demonstrated either in the field or in the laboratory. Not all of these techniques have been reduced to the size required for SS-type use but, at least in principle, such reduction appears feasible in the future, particularly in view of the continued progress in LSI and VLSI technology developments. In section 2.4, we make our first-cut predictions on the possible size reduction due to LSI/VLSI utilization.

2.3.1 Motion-Compensation Technique

Motion compensation is an algorithm which is added to interframe (i.e., frame-to-frame) encoding in order to improve picture quality at lower transmission rates (1.5 to 6 Mbps). Relative improvements due to this algorithm were shown in Figure 2.7. Prior to discussing the details of the motion-compensation principle, a brief description of interframe-coding principles is in order.

The interframe coding achieves the reduction in transmission bit rate by transmitting the difference signal between two successive frames. As shown in Figure 2.8, an object moving across the TV screen is positioned differently at each successive frame. The position difference, when digitized, represents a relatively small amount of information compared to that contained in the entire frame. Thus, if there is no movement, no new information needs to be transmitted. On the other hand, large displacements require a considerable amount of new information to be transmitted from frame to frame.

Figure 2.9 shows the generic configuration of an interframe coder. The analog video signal is first quantized by an A/D converter. The digital samples are then applied to the interframe coder which stores at least one entire frame in a digital format. When the subsequent frame is received and digitized, the encoder compares it to the previous frame. The difference information developed as a result of this comparison is then processed by a variable-length coder that removes the redundancy contained in the frame-difference signal. The buffer memory then performs smoothing of the difference signal. This smoothing ensures that the transmission rate is constant, independent of the movement of picture objects. In order to prevent buffer-memory overflow, a feedback-control is used to suppress excessive generation of information as a result of the frame-differencing process. Because the control of information rate is implemented by changing the quantization-step size, the signal-to-noise ratio (SNR) degrades as the amount of motion increases. Consequently, when the information rate exceeds the permissible transmission channel rate, the quality of the encoded picture starts to deteriorate. Conversely, if the picture quality is not allowed to deteriorate below a certain limit, the channel rate must increase, as indicated in Figure 2.7.

The motion-compensation algorithm provides picture-quality improvement for a given channel bit rate. Figure 2.10 illustrates the principle of motion compensation. As shown there, the picture element $S_n(i,j)$ is the sample to be transmitted, where the subscript n designates the frame number and i and j give the x and y coordinates of the element within the frame.

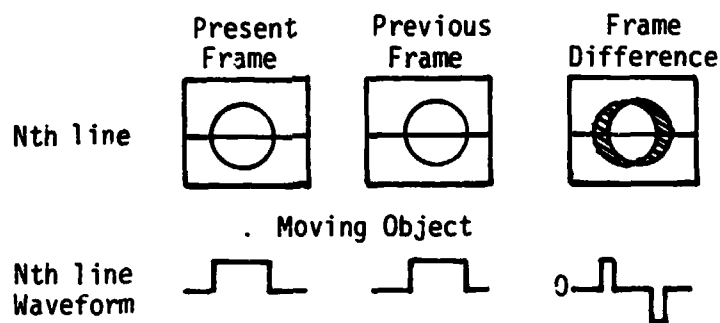


Figure 2.8. Principle of Basic Interframe Coding

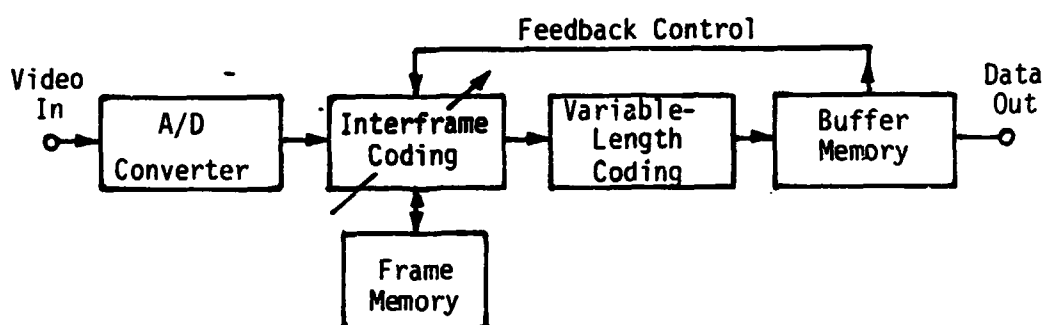


Figure 2.9. Generic Configuration of an Interframe Encoder

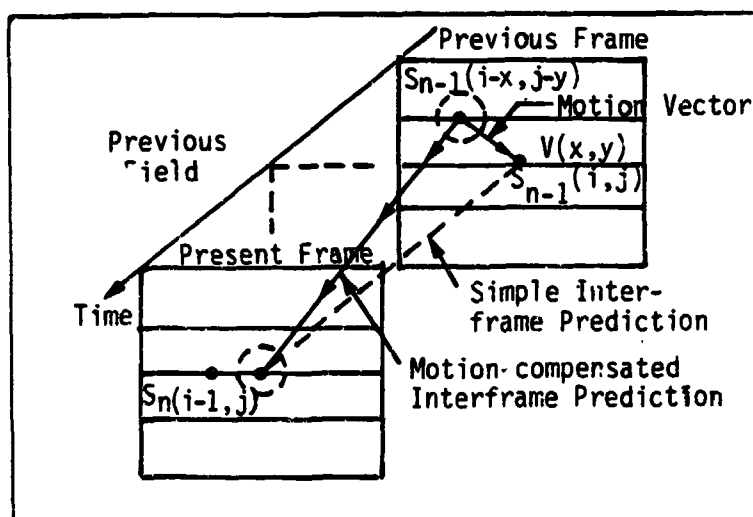


Figure 2.10. The Principle of Motion-Compensated Interframe Coding

If the object displacement in one time frame is given by the motion vector $V(x,y)$, one can then predict the position of the element $S_n(i,j)$ for the time of arrival of the n th frame using an estimate of this vector. Such a prediction thus minimizes the interframe difference between the element of the previous frame, i.e., $S_{n-1}(i-x,j-y)$ and the same element $S_n(i,j)$ of the current frame. Thus, it is the function of the motion-compensation interframe-coding algorithm to determine the estimate of the motion vector $V(x,y)$ from the picture.

Figure 2.11 shows a functional block diagram of the motion-compensated interframe coder and decoder such as Nippon Electric Company's (NEC) models no. NETEC-6/3 and NETEC-X1. The input video in Figure 2.11 is the NTSC color television signal. This signal is first digitized, then it is applied to a color signal processor (CSP-5) which converts the NTSC formatted signal into a time-division-multiplex (TDM) signal. The TDM signal is a baseband video signal with a time-compressed chrominance signal inserted into the horizontal-blanking interval. The TDM signal is then applied to the movement detector and an interframe coder.

In the NEC system, the picture field is subdivided into subblocks of seven picture elements (pel's) times seven lines. Calculation of the motion vector $V(x,y)$ is then performed for each subblock using high-speed parallel processors. Interframe coding is then performed on a frame-to-frame basis, with the variable delay controlled by the motion vector. As in sample interframe coding, special techniques are used to prevent buffer overflow in the coder. The techniques used are: (1) adaptive quantization, (2) field repeating and, (3) subsampling. These techniques correspond, respectively, to resolution control in the amplitude, time and space domains. Huffman codes and run-length codes are then used to compress video data corresponding to interframe differences and the motion vectors.

The decoding process is the inverse of coding. But, because the motion vector is transmitted as a separate signal, motion detection is not required at the decoder. The interframe decoder unit converts the predetection error signals to TDM signals. This is accomplished by adding the error signals to the motion-compensated prediction signals. Subsequently, the TDM signal is converted back to the NTSC format and the latter applied to the D/A converter. In all, the receiver (i.e., decoder) configuration is much simpler than the transmitter.

Figure 2.7 shows that good-to-excellent picture quality can be obtained at channel bit rates in the range from 1.5 Mbps to 3 Mbps, with the motion-compensation algorithm added to the simple and complex frame-to-frame

ORIGINALITY OF
OF POOR QUALITY

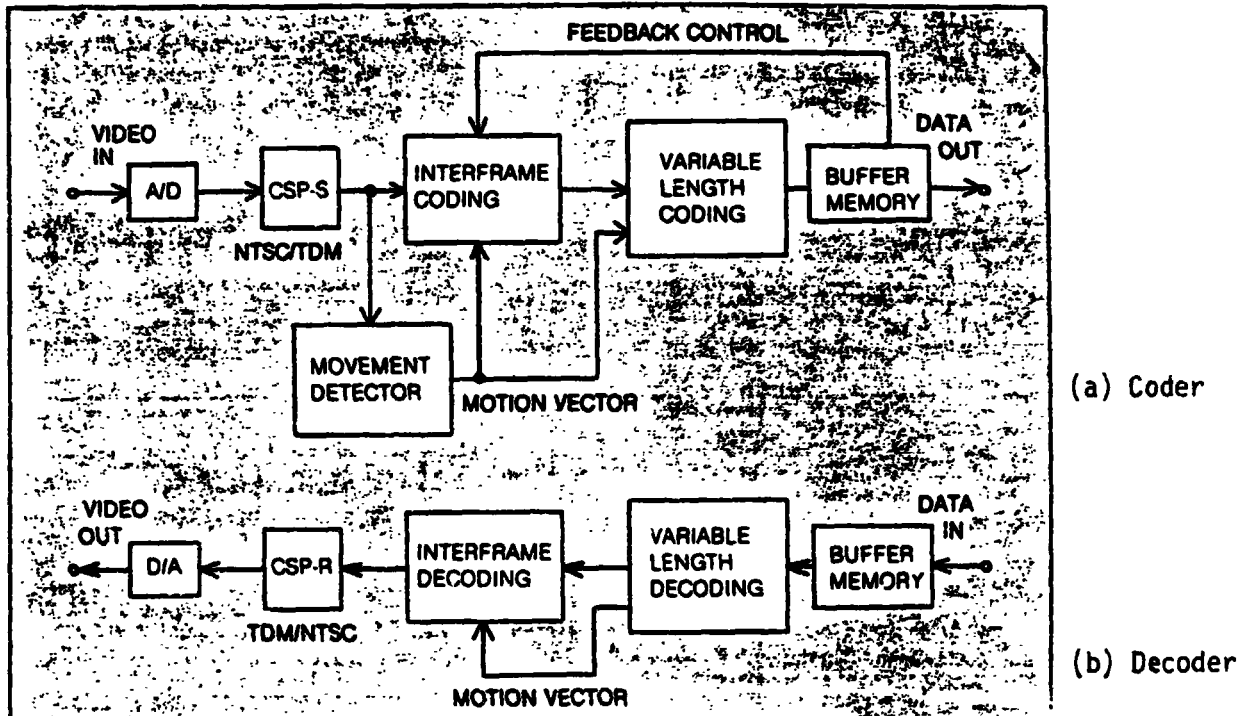


Figure 2.11. Motion-Compensated Coder and Decoder Block Diagram

encoding. Realization of this algorithm is provided in operational video-conferencing systems such as NEC's NETEC-6/3 and NETEC-X1 equipment as well as the VTS 1.5E system of Compression Labs, Inc. Specifications for these systems are provided in Appendix A.

2.3.2 Hybrid Coding for Bandwidth Compression of Video Signals

2.3.2.1 General considerations

Hybrid coding usually refers to an encoding process whereby the video information is first subjected to a transform process, then the transform is digitized according to some quantizing process, such as differential pulse-code modulation (DPCM).

With a "full-blown" transform coding, either the entire picture or a frame may be transformed using either of the techniques listed in Figure 2.3 (see analysis-synthesis methods), then the transform coefficients are transmitted by means of DPCM. Such "pure" transform coding, however, is rather complex to be implemented in real time because: (1) it requires excessive storage of data and, (2) a large number of operations per pel are required. On the other hand, hybrid coding offers a partial solution to this problem. Specifically, hybrid coding is characterized by: (a) use of relatively small blocks for obtaining transform coefficients and (b) implementing DPCM of the transform coefficients for these blocks by making use of the coefficients of the previously transmitted block, i.e., using the past coefficients as predictors.

The use of smaller blocks for encoding is justified since, as shown in Figure 2.12, little is gained in picture-error reduction as the number of pels per block is increased. With respect to selecting the method, or an "algorithm" for encoding the transform coefficients via DPCM, the following three types have been considered for the hybrid coding:

- (1) A one-dimensional block along the horizontal scan line with DPCM in the vertical direction
- (2) A small, two-dimensional block and DPCM using the coefficients of a horizontal previous block for predictions
- (3) A two-dimensional block with the DPCM implemented in the temporal direction.

It must be noted that methods (1) and (2) above are intraframe (or intrafield), whereas method (3) is interframe. It is also interesting to point out that considerable savings in data storage is realized with the third hybrid-coding scheme as compared to the "pure" transform-coding method which uses three-dimensional blocks.

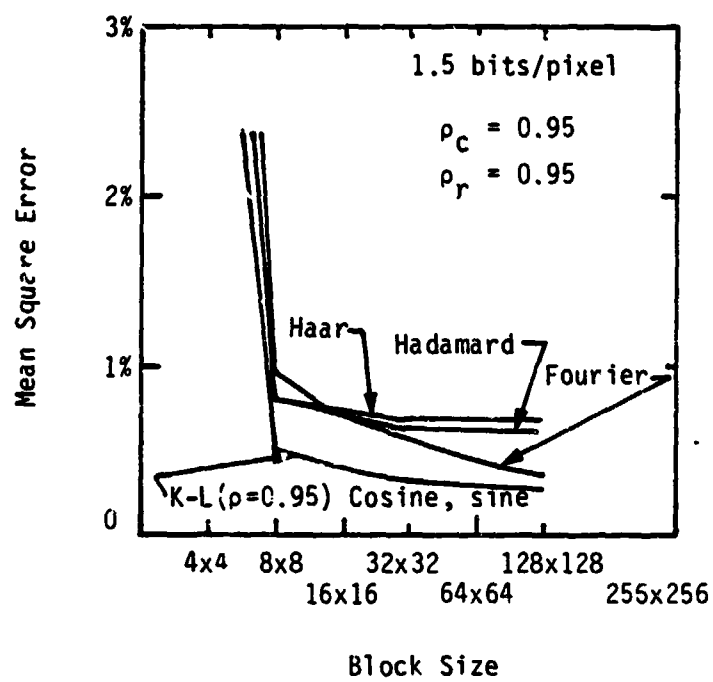


Figure 2.12. Mean-Square Error Performance of Different Transforms for the Two-Dimensional Markov Image Source with Horizontal Correlation Factor of ρ_c and Vertical Correlation Factor of ρ_r [3]

Figure 2.13 shows a generic block diagram of a hybrid-transform/DPCM encoder. As shown therein, the video is first transformed, then applied to DPCM encoders which, in turn, are followed by the code-assignment units. We show more than one DPCM encoder in order to indicate that, ideally, each transform coefficient should be encoded by its own DPCM unit that is specifically adapted to the particular coefficient. However, such implementation is not efficient from the standpoint of hardware realization. Thus, as described in following sections, in a practical system, an attempt is made to design a single DPCM encoder which can handle all the coefficients. Also, as indicated in Figure 2.13, certain transform coefficients are dropped so as to minimize the bits/pel ratio.

The code-assignment unit and a quantizer that precedes it (not shown in Figure 2.13) are very important subblocks of a hybrid coder. These units determine the manner in which the quantization levels are established for the purpose of digitizing and transmitting the transform coefficients for the various blocks.

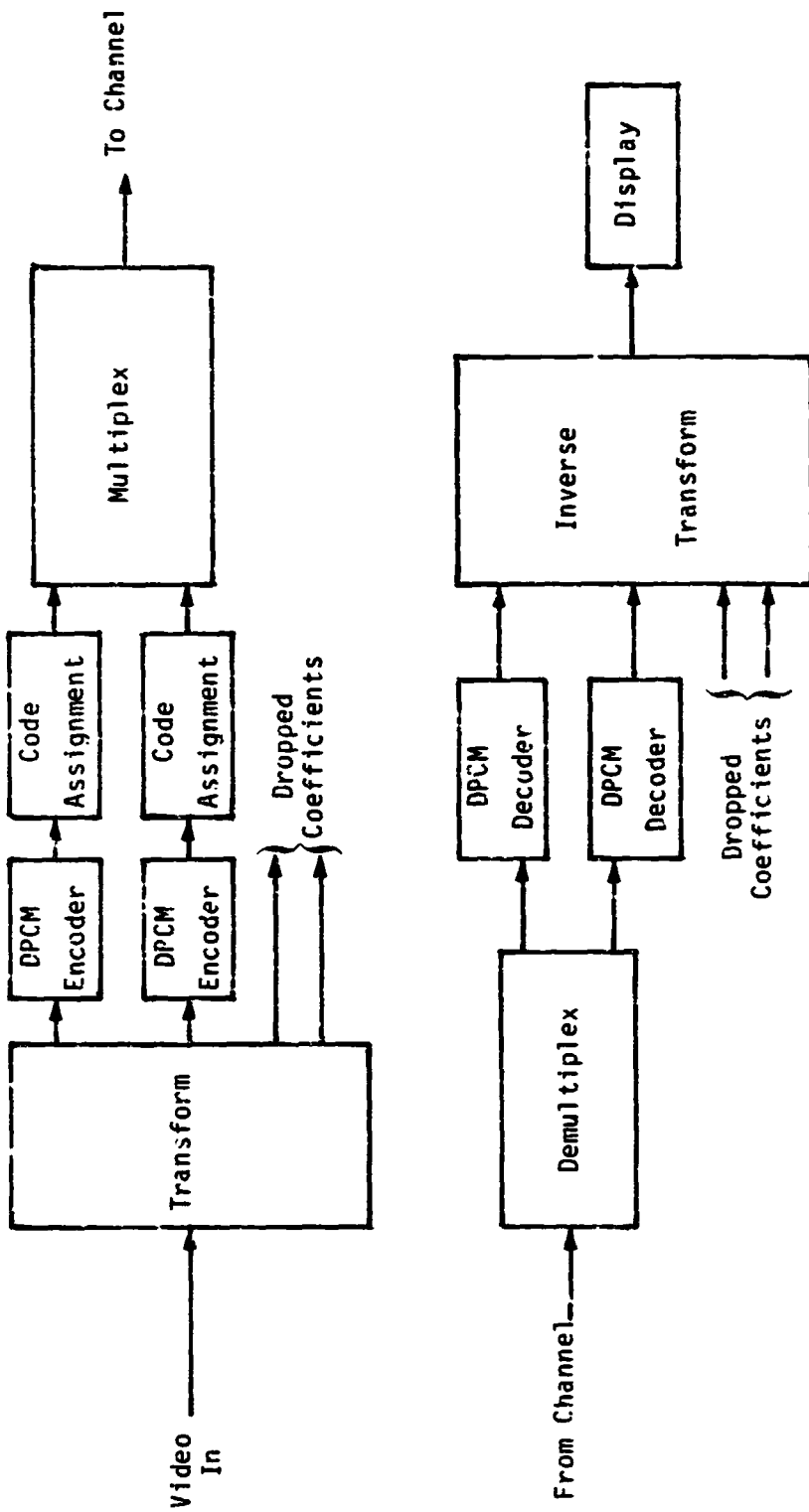


Figure 2.13. Block Diagram of a Hybrid Transform/DPCM Encoder

2.3.2.2 Harris Corp. hybrid coding system for RPV use

A system developed by Harris Corporation for RPV applications [4] is an example of the practical implementation of a hybrid-coding method. We have chosen to describe this system because it has been implemented with LSI components to dimensions suitable for space-borne applications in addition to having been tested in the laboratory. This system is not in the same class as the previously described motion-compensated, full-color, video-conferencing equipment in that it is black and white only and has a maximum frame rate of 7-1/2 frames per second. However, because of its already demonstrated size-reduction and variable-bandwidth-compression capabilities, it is of definite interest to potential applications in SS communications. Table 2.3-1 lists the salient characteristics of the Harris Corporation hybrid-coding system.

Figure 2.14 shows the functional block diagram of the video-bandwidth-compression system made by Harris. This system utilizes the discrete-cosine transform (DCT). As shown there, the image is first cosine transformed, then applied to the scaler, which then feeds the DPCM unit. The transform size is 16 elements along the scan line. From this ensemble, 16 transform coefficients are obtained. Harris claims [4] that their system implements an optimum-bit assignment with respect to the block-quantization process. This claim is based on their assumption that each transform coefficient at the output of the DCT is an independent Markov process with different correlation coefficients for each frequency term.

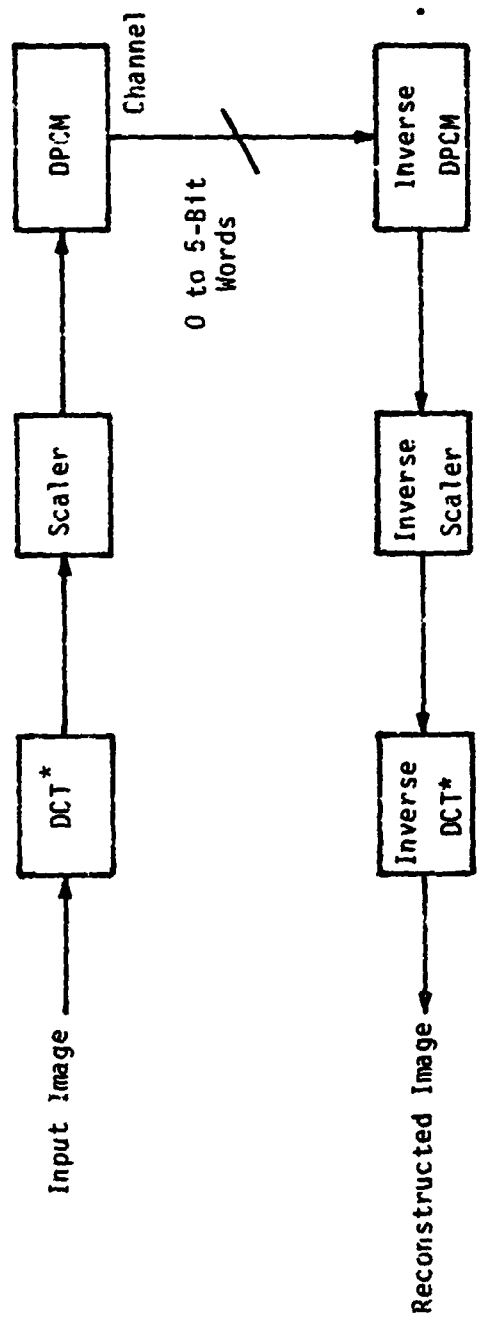
Figure 2.15 explains some details of the Harris system hardware implementation. One of the unique features of this implementation is the use of a table look-up technique instead of either a hardware or software multiplication which is required for the DCT process. Thus, the hardware complexity is simplified, and the high-speed-transform process is realized. Another feature of this system is the use of a scaler to equalize the values of the transform coefficients prior to the DPCM. Specifically, the scale factors are selected in such a manner that the scaled values of the non-DC component variances are as close as possible to the DC component's variance. Thus, although a limiter is shown in the block diagram after the scaler, proper design of the latter minimizes the possibility of coefficient clipping prior to DPCM. The use of the scaler prior to DPCM allows a single one-step predictor to be employed for all 15 coefficients. This, too, simplifies the complexity of the hardware implementation.

Table 2.3-1. Salient Characteristics of the Harris Corp. Hybrid-Coding System [4]

Parameter	Value/Description
Transform type	Cosine
Maximum resolution	Horizontal: 640 pixels Vertical: 420 lines
Frame rate	Maximum: 7-1/2 fps* Minimum: 15/128 fps**
Channel-rate requirement	Maximum: 4.608 Mbps (at 7-1/2 fps) Minimum: 72 kbps (at 15/128 fps)
Bits/pel range (selectable)	Two, one, and one-half
Dimensions (LSI implementation)	Two modules 4.5" x 4.5" x 0.5" each

* Frame refreshed every 0.133 seconds.

** New frame every 8.53 seconds.



*DCT = Discrete Cosine Transform

Figure 2.14. Functional Block Diagram of the Video-Bandwidth Compression and Reconstruction Units

The system operates in the following manner. The A/D converter digitizes the input video to eight bits. An entire frame is stored in the frame-grab memory at full resolution and at eight bits per pixel. Loading of the frame is done in real time. At the rate of 7-1/2 frames per second, there are four frame periods of the standard 30-fps rate. During the first frame period, the memory is loaded with data. The processing commences immediately, continues during the loading period, then extends for the duration of four frame periods. Thus, at the input rate of 30 fps, three of the four frames are not processed. The resulting average output data rate, D , in megabits per second (Mbps), is

$$D = F \times H \times V \times b \times T \times 10^{-6}$$

where:

F = transmitted frame rate in frames per second

H = number of pixels in the horizontal line

V = number of lines (vertical resolution)

b = bits per pixel

T = truncation area ratio

For example, if $F = 7\frac{1}{2}$ fps, $H = 640$ pixels, $V = 480$ lines, $b = 2$ bits per pixel, and $T = 1$, the required channel rate is 4.6080 Mbps. On the other hand, if $F = 15/128$ fps, $H = 640$, $V = 480$, $b = 2$, and $T = 1$, then D is 0.072 Mbps or 72 kbps. For comparison purposes, with uncompressed, eight-bit quantized PCM video, $F = 30$, $H = 640$, $V = 480$, $b = 8$ and $T = 1$, and the corresponding required channel rate is 73.728 Mbps. Thus, an approximate compression ratio of 1000:1 can be realized with this hybrid-coding system.

According to Harris Corporation, the entire DCT hybrid-compression system has been implemented in LSI and packaged onto two 4.5"x4.5"x0.5" modules. One module contains the bandwidth-compression circuitry and the second contains the frame memory.

2.3.2.3 Other efforts in hybrid coding

As mentioned earlier, the requirement for transmission of bandwidth-compressed video from RPV's resulted in the development of compact, low-power-consuming equipment. Several of these developments are listed in [5] and are presented in Table 2.3-2. Although the information in this table is somewhat out of date (1979), it is indicative of the trends in this area of development. Because of the military application of the RPV's and the potentially classified nature of the associated hardware, no effort was made on our part to obtain an update to Table 2.3-2.

Table 2.3-2. RPV Compression Hardware Evaluation [5]

	RCA	Northrop	Motorola	TRW	Lockheed
Dimensionality	1	2	2	2	1
Transform operator	Cosine; DPCM between lines	Haar	Hadamard	Adaptive	Constant-area quantization
Frame memory type	Sample	Full Grabber	Full Grabber	Full Grabber	Full Grabber
Relative MIPS required	Moderate	Low	Moderate	Low	Low
Quantizer complexity	Low	High	Low	High	Moderate
Frame-rate-reduction complexity	Low	Moderate	High	Moderate	Moderate
Effective compression range bits/pixel	0.75 - 2.0	0.75 - 2.0	75 - 2.0	1.0 - 2.0	1.2 - 2.0
Edge quality	Moderate	Good	Good	Moderate	Moderate
Distortion	Poor for fast-moving scenes	Good	Good	Good	Good
Flat-region noise	Good	Good	Good	Moderate	Moderate
Noise immunity	Good	Moderate	Good	Moderate	Moderate
Size of physical hardware	Small	Moderate	Moderate	Small	Small

2.3.3 Delta-Modulation Techniques for 15-to-30-Mbps Digital TV Links

2.3.3.1 Overview

Several video-digitizing techniques exist, or are in the development stage, which can provide transmission of either field-sequential or NTSC-format color signals. These techniques utilize adaptive delta-modulation systems that can yield reasonably good-quality pictures, with full-color capability, at channel rates in the 15-to-30 Mbps range.

The primary advantage of these techniques is that they can be implemented with relatively few components. Thus, they can be used where space and power limitations are of importance. The disadvantage of using these techniques is a relatively high-channel-data rate. In a power-constrained link, this limits the operating range of the system.

Over the past several years, three approaches for employing delta modulation for TV purposes have evolved. One is to use a single adaptive delta modulator for transmitting either black-and-white (B/W) or field-sequential color television. Another approach is to use the same delta modulation for the transmission of digitized composite NTSC color signals. A third approach is to first decode the composite NTSC signal into the Y (luminescence) component and the I&Q (chrominance) components, then transmit these components by means of separate delta modulators. With the latter approach, intraframe techniques such as run-length encoding can be used to reduce the overall channel bandwidth rate. Some of the technical aspects of these approaches are described herein.

2.3.3.2 Bistate adaptive delta modulation

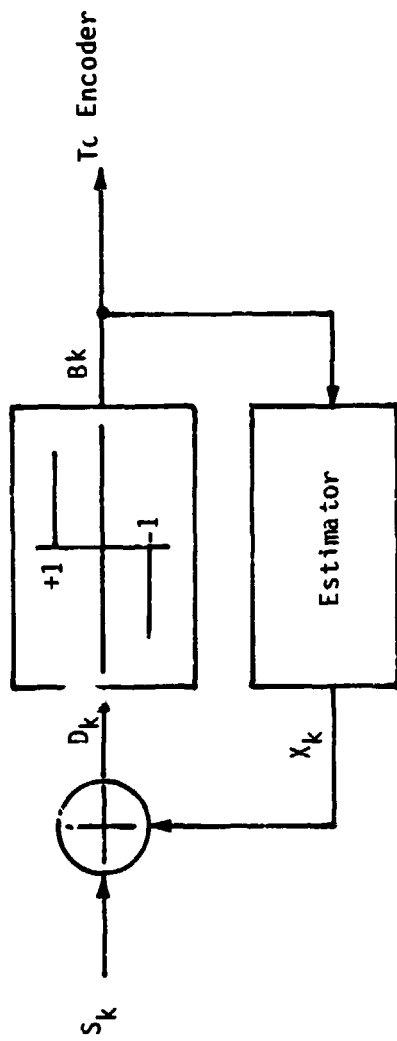
Successful applications of delta modulation to TV signal digitization has been reported in the literature [6,7] and experimental work continues with respect to different algorithms used for digitization and encoding. The commonly used delta-modulation encoder produces a sequential output that indicates whether the final output voltage should increase or decrease. It acts like a DPCM system with only one bit per sample. Hence, it is referred to as a "bistate" encoder. Acceptable performance with this encoding scheme is realized by an increased sampling rate as compared to a PCM coding scheme. Because the bistate delta modulator requires relatively low data rates compared to PCM, considerable effort has been spent trying to perfect a delta modulation system.

The goal of every design approach is to trade off fidelity of reproduction versus the allowable data transmission rate and the amount of hardware used. The best solution also depends on the qualities of the signal being sampled. Video information tends to be a series of amplitude steps from one luminance level of another. These level steps are connected by voltage changes with large dV/dt values. When handling a video signal, a delta modulator must handle very sharp rise and fall time signals, then settle rapidly to a new luminance value, with no overshoot, ringing or other added noise. The relative delay for different frequency components in the picture is also important.

Figure 2.16 is a block diagram of a bistate delta modulator which illustrates its operation. D_k is the difference between the input signal S_k and the output of the estimator X_k . This difference signal is passed through a hard limiter whose output is a bit B_k which causes the estimator to change its output. This bit is the signal which is transmitted over a communication link to the receiver. The receiver consists of only the estimator portion of the transmitter block diagram. The sampling rate of the delta modulator determines the amount of delay inherent in the digitizing process. The faster the sampling rate, the smaller the inherent delay.

The hard limiter shown in Figure 2.16 guarantees that the estimator will increase or decrease its output every time the sample clock cycles. This characteristic of indicating only changes results in the inherent "granularity" in the reproduction of a constant-luminance signal since the modulation scheme must always output a sample corresponding to an increase or decrease in voltage. The reconstructed signal will average to the correct level by varying up and down around the desired output level. Any attempt to smooth the delta modulation output will slow the response to step changes and, therefore, reduce picture "sharpness."

Conversely, if the bistate delta-modulation scheme is designed to provide good rise and fall times, the amplitude of the level jitter around the desired output will increase and more granularity will appear. Furthermore, the amount of overshoot and ringing after an abrupt edge will usually increase as the delta-modulation system is designed to reduce slew time. Various attempts to alleviate these conflicting requirements and reduce the overshoot and ringing have been proposed [8,9].



where:

S_k = signal to be transmitted (sampled and digital)

X_k = estimate of signal to be transmitted

D_k = quantized difference ($D_k = S_k - X_k$)

B_k = activity vector (signal rising or falling)

Figure 2.16. Conventional (Bistate) Delta Modulator Functional Block Diagram

Figure 2.17 shows how a bistate adaptive delta modulator (ADM) is used to provide field-sequential encoding of color signals. As illustrated in this figure, the ADM sequentially encodes the red, green and blue signals generated by the TV camera [10]. Thus, a typical sequence of color encoding and transmission would be: field 1--red, field 2--green, field 3--blue. The advantages of this scheme of color-picture transmission are twofold: (1) extreme simplicity of the camera* and, (2) the channel-bit rate is the same as that required for transmission of black-and-white pictures. Another sideline advantage of this scheme is that the edge busyness, which is typical of delta modulators and is a random process within each frame, tends to be masked when the three color fields are recombined in the scan converter prior to being displayed on the screen.

The disadvantage of this field-sequential system is that only one color is transmitted per field. Thus, the color components tend to separate at the edges of moving objects. This is because the color rate frame is only 10 frames per second, i.e., only one-third of the normal rate. The disadvantage associated with the color misregistration when using the ADM for transmitting field-sequential color video can be overcome if a camera providing an NTSC composite signal is used as a source of video. With this approach, the ADM samples and encodes the composite signal, which includes both luminance and color modulated subcarrier signals at 3.58 MHz. Although reasonably good color picture quality can be obtained with this scheme, some interaction between the ADM sampling rate and the color subcarrier signal is inevitable. Thus, efforts to optimize the ADM algorithm with respect to sampling the color subcarrier signal have been reported in recent literature [11].

* A simple color-wheel camera can be used for this application.

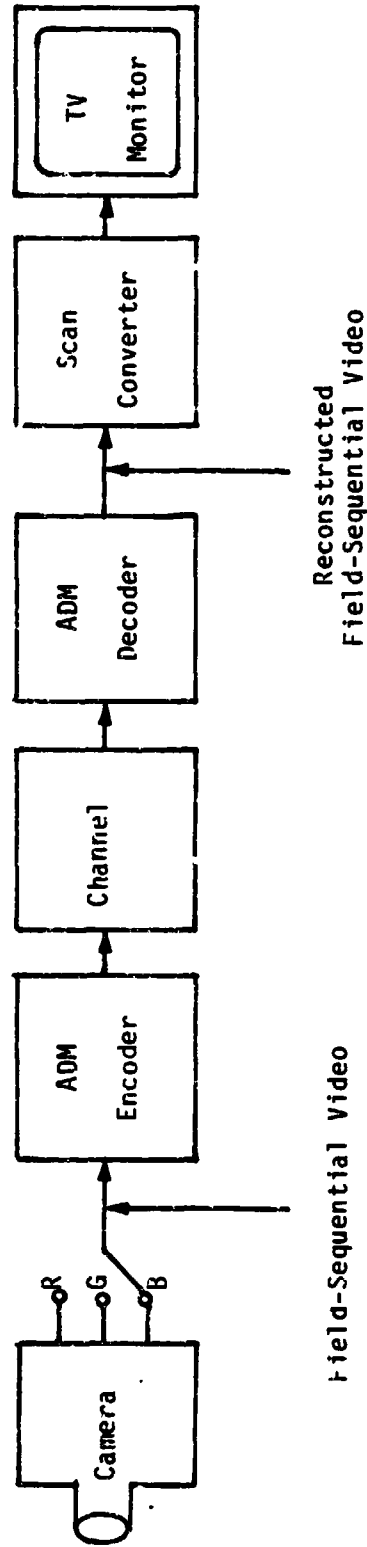


Figure 2.17. Field-Sequential Color System [10]

2.3.3.3 Tri-state delta modulation for run-length encoding

2.3.3.3.1 General principles

The effort to take advantage of video signal statistics has been applied to delta-modulation encoding. Specifically, an algorithm has been developed that allows the delta modulator to "sense" or "detect" those regions of the video picture where virtually no change in intensity is present. By providing a special code that indicates a "no-change" condition, only the number of samples of such a no-change condition has to be transmitted instead of the samples themselves. Thus, a potential channel data-rate reduction can be realized by using such a run-length (R/L) encoding technique.

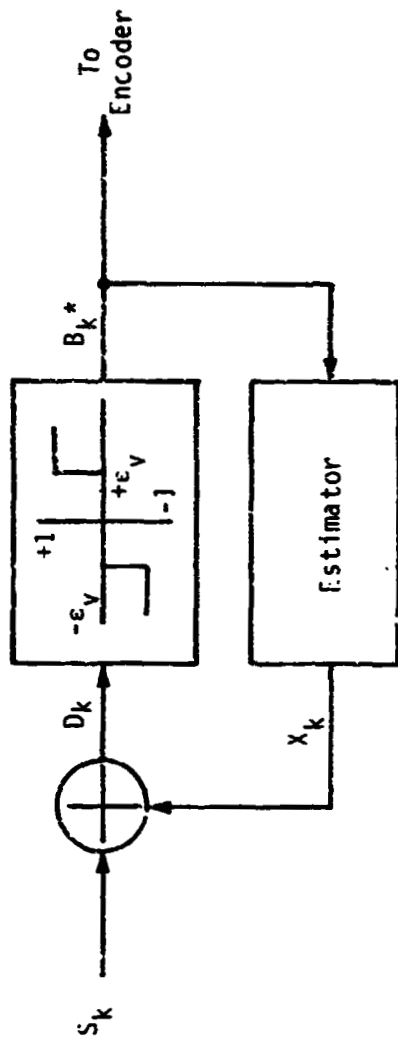
The tri-state delta modulator (TSDM) [12,13] has characteristics that make it especially suitable for R/L encoding of video information. By indicating the "no-change condition" with a special code, the TSDM breaks the connection between rise-time performance and steady-state level jitter inherent in a bistate delta modulator.

In comparison with the bistate delta modulation, the TSDM approach shown in Figure 2.18 quantizes D_k into three values instead of two. The third value indicates that D_k is between $-\epsilon_v$ and $+\epsilon_v$. This condition causes the output of the estimator to remain at its previous value. Just as in the case of bistate delta modulation, the receiver consists of only the estimator. This third state eliminates the granularity inherent in bistate delta modulation; it permits the TSDM to be optimized for transient performance without considering granularity problems. With the exception of the third state, operation of the TSDM is identical to the bistate delta modulator shown in Figure 2.17.

As indicated in Figure 2.18, the TSDM state is determined by comparing the estimate X_k with the input signal S_k to produce a voltage difference signal D_k . This voltage D_k is tested for sign and magnitude to produce B_k . The rule is:

$$B_k = \begin{cases} \text{Sgn} [D_k], & \text{whenever } |D_k| > \epsilon_v \\ 0 & , \text{ whenever } |D_k| \leq \epsilon_v \end{cases}$$

Since $D_k = S_k - X_k$, a positive voltage for D_k signifies that X_k must be made more positive in order to match S_k ; therefore, $B_k = +1$ must cause X_k to become more positive. The equation used to calculate X_{k+1} from X_k is simply



* With TSDM, the B_k vector can also represent a "signal-steady" condition.

Figure 2.18. Tri-State Delta Modulator (TSDM) Functional Block Diagram

$$X_{k+1} = X_k + B_k |\Delta_{k+1}|$$

where B_k may be +1, 0 or -1, and $|\Delta_{k+1}|$ is given by

$$|\Delta_{k+1}| = \begin{cases} 1.5 \Delta_k & \text{if } B_k = B_{k-1} \neq 0 \text{ and } |\Delta_k| > 2\Delta_0 \\ 3\Delta_0 & \text{if } B_k = B_{k-1} \neq 0 \text{ and } |\Delta_k| \leq 2\Delta_0 \\ 0.5 \Delta_k & \text{if } B_k \neq B_{k-1}, B_k \neq 0, B_{k-1} \neq 0 \\ 0 & \text{if } B_k = 0 \\ 3\Delta_0 & \text{if } B_{k-1} = 0, B_k \neq 0 \end{cases}$$

When $|D_k| \leq \epsilon_v$, the feedback signal X_k is close enough in value to the input signal S_k so that the system should maintain its state. It does this by making $X_{k+1} = X_k$ and setting $\Delta_{k+1} = 0$ whenever $B_k = 0$. That process is unique to tri-state delta modulation.

The adaptive characteristic of the system is realized by the $|\Delta_{k+1}| = 1.5 \Delta_k$ term. When B_k has the same sign m times in sequence, the value of Δ_k is multiplied by $(1.5)^{m-1}$, so the slope of the feedback signal increases without limit until $X_k \geq S_k$. In this case, the B_k vector changes sign, and the value of $|\Delta_{k+1}| = 0.5 \Delta_k$ reduces the slope as the X_k signal changes direction. This provides for the eventual settling of X_k to a value near S_k by reducing the value of Δ_k by a factor of 2 every time X_k crosses S_k . If S_k remains constant long enough, X_k will eventually settle to within $\pm \epsilon_v$ of it if ϵ_v is at least as large as one-half the resolution of the DAC that produces X_k . Once this happens, B_k will be equal to 0 and the systems will stay at rest until S_k changes again.

When B_k changes from $B_{k-1} = 0$ to either $B_k = +1$ or $B_k = -1$, the system must inject a starting value for $|\Delta_{k+1}|$ since $|\Delta_k|$ was 0. That is handled by the $2\Delta_0$ term which is simply a constant value selected to provide a large enough initial slope to the S_k feedback signal when it must adjust to a step input in S_k , so that the slew time is minimized.

2.3.3.3.2 TSDM digitizer/reconstructor implementation*

Figure 2.19 is a block diagram of a tri-state video digitizer with the receiver input and output indicated by dotted lines. Because the receiver is only a portion of the transmitter, it will not be discussed separately. As shown in this diagram, the analog video signal S_k is compared with the reconstructed analog estimate of the previous sample X_k . The analog difference D_k is applied to the A/D converter. The hysteresis bias, or "dead zone," $\pm\epsilon$, is also applied to the analog bias input of the A/D converter. The analog error is then sampled by the A/D unit and transformed into B_k values according to the previously described algorithm.

The hardware block diagram illustrated in Figure 2.19 implements the required tri-state algorithm. To provide the fastest sampling rate possible, the various alternative computations are performed in parallel and the appropriate result is selected by a 4-to-1 MUX. There are two 4-to-1 multiplexers: one for the next value of x and one for the next value of Δx . The decision concerning which input to select is made by the output of the A/D converter B_k and the comparator which operates on both $2\Delta_0$ and the output of the Δx register. The implementation shown in Figure 2.19 provides the maximum amount of time for the DAC, analog subtractor and three-state A/D converter to settle by performing all possible calculations while they are settling, then selecting the actual output needed. The x register input, for example, may be any one of the following numbers: x , $x + 3\Delta_0$, $x - 3\Delta_0$, $x + 1.5 \Delta x$, $x - 1.5 \Delta x$, $x + 0.5 \Delta x$, and $x - 0.5 \Delta x$.

Depending on the present vector B_k and the preceding vector B_{k-1} , the logic and decision unit (LDU) sends the appropriate commands to the 4-to-1 multiplexers. It also sends the appropriate add/subtract commands to the x register arithmetic logic units (ALU's) A, B and C. To ensure that the delta modulator does not "hang up" with a dead zone, the output of the Δx register is always compared with the $2\Delta_0$ value. If the value of the Δx register is less than $2\Delta_0$, the comparator controls the 4-to-1 multiplexers to select $3\Delta_0$ as the next increment. The value of $3\Delta_0$ is also selected when the LDU indicates that a transition from a no-change state (i.e., constant intensity) to a change stage, i.e., an increase or decrease in intensity has occurred on the latest sample.

* This implementation was carried out under a NASA contract by Axiomatix Corporation of Los Angeles, California.

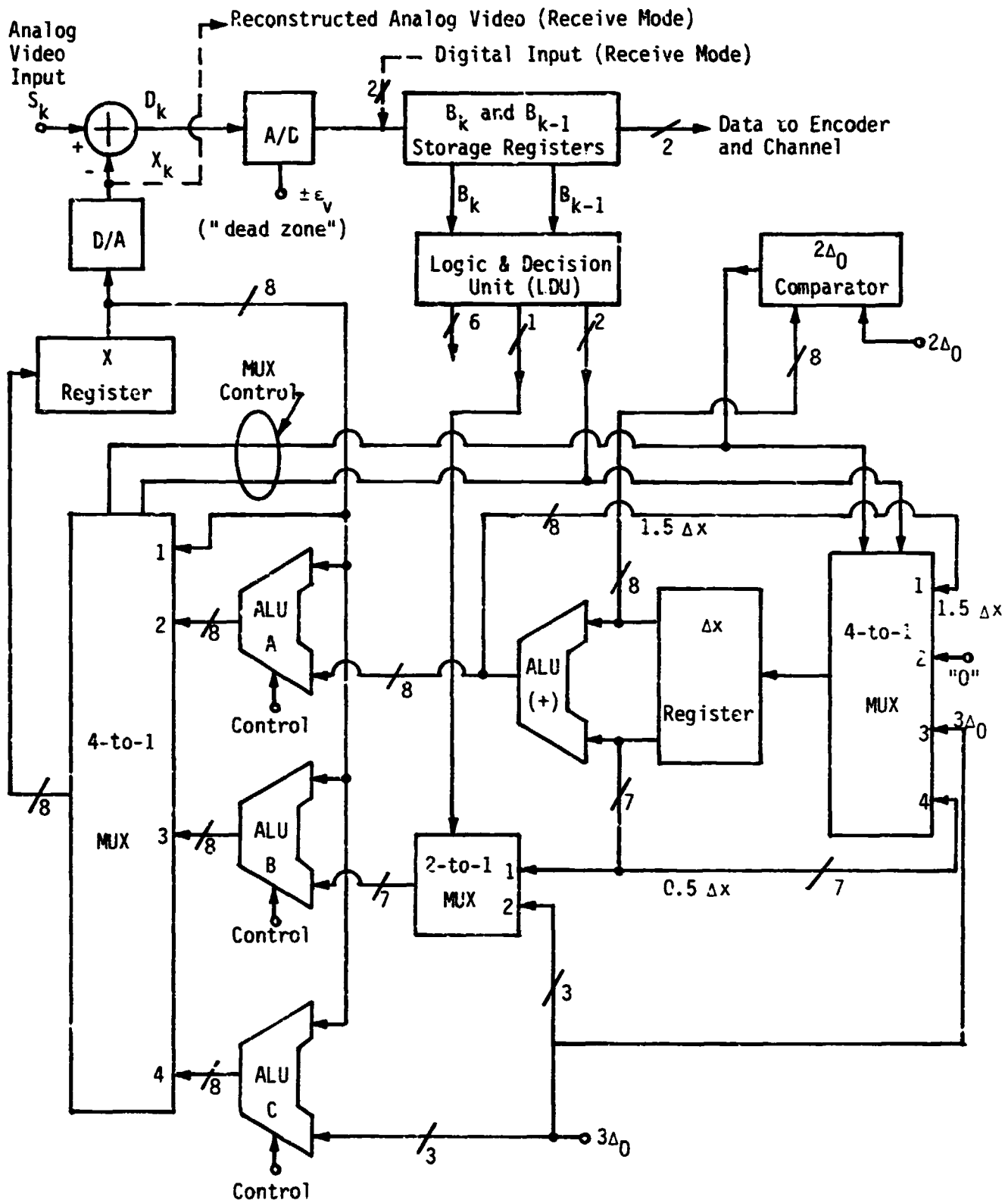


Figure 2.19. Tri-State Video Digitizer (and Reconstructor) Implementation

For the receive mode, the logic implementation is the same as that shown in Figure 2.19, but without the analog subtractor or A/D converter. As indicated by the dotted lines, the received data stream is applied directly to the B_k and B_{k-1} storage registers and the reconstructed analog video is taken from the output of the D/A converter.

2.3.3.3.3 Run-length encoder/decoder implementation

The block diagram of the TDSM R/L encoder is depicted in Figure 2.20. The high-speed encoding circuitry accepts the B_k values at the sample clock rate and outputs a sequence from that sample, as shown in Table 2.3-3. The sample clock rate is fixed. Since the encoding process produces a variable number of bits out, depending on the sample inputs, the data output rate of the encoder varies.

The rotating buffer provides the necessary elastic storage between the varying input data rate and the fixed output rate. The output of the FIFO, under normal circumstances, is clocked by the transmission channel clock that is supplied to the TDSM from an external source. If the picture being transmitted happens to encode very efficiently so that insufficient data is entering the FIFO to replace the data being clocked out, the R/L encoder circuitry is apprised of this by the "potential underflow" line shown in Figure 2.20. When a potential underflow problem exists, the R/L encoder circuitry waits until a new horizontal synchronization pulse occurs. At this time, the R/L encoder generates a codeword indicating the end of valid data. The rotating buffer has another output that indicates potential overflow. This output feeds back to the encoding circuitry, which changes its operating mode when the possibility of overflow occurs.

Figure 2.21 is a block diagram of the receiver R/L decoder. It is essentially the encoder turned around. The FIFO provides data to the decoding circuitry upon demand, so the output of the decoder can be a constant sample rate despite the variable-length decoding process. The elastic storage in the receiver rotating buffer forms the other half of the elastic storage in the transmitter. The total information stored in the two memories should vary, roughly together, depending on how the picture data is modified by the encoding algorithm. The sample rate into the encoder is constant, as is the output at the decoding end of the link. The link between the encoder and decoder also has a fixed rate which is somewhat greater than the sample rate in order to obtain the improved picture quality of tri-state delta modulation. The actual link data rate and the type of picture being scanned determine how often the system degrades to bistate delta modulation.

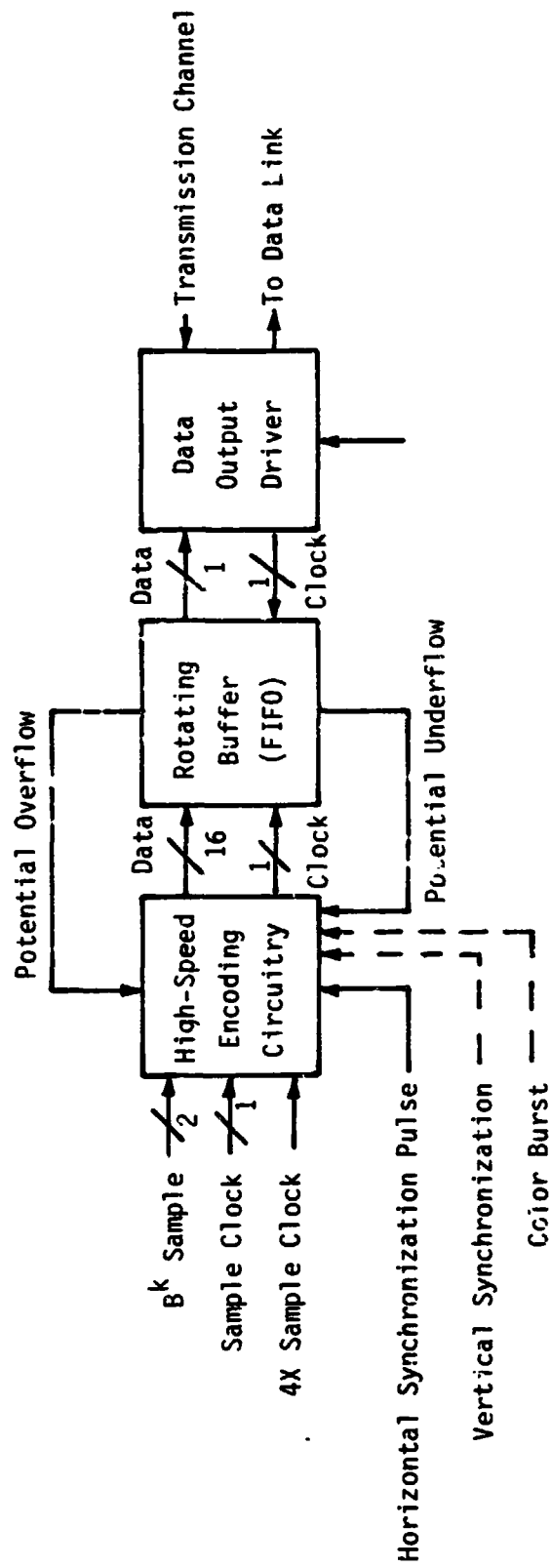


Figure 2.20. Run-Length Encoder (Transmitter Side)

Table 2.3-3. Encoding Table for TSDM

B_k Vector	Transmitted Sequence
+1	10
-1	11
0	01110
Two 0's in a row	01101
Three 0's in a row	01100
Four 0's in a row	01011
Five 0's in a row	01010
Six 0's in a row	01001
Seven 0's in a row	01000
Eight 0's in a row	00

2.3.3.3.4 Extension of TSDM to NTSC color TV

In the previous discussion, TSDM was considered as a technique for digitizing a single video signal that is presumed to be the NTSC luminance component used for black-and-white TV transmission. Because field-sequential color transmission utilizes a sequence of such components, as provided at the output of a rotating color-wheel filter, the approach described is applicable without modification for systems such as those in use today by the Space Shuttle. For standard NTSC color TV transmission, however, the TSDM technique is applied to each of the three color components, Y, I and Q, where Y is the luminance component and I and Q are the chrominance components.

Figure 2.22 shows the method of handling those components, each with its own R/L encoder. For maximum data comparison, each component should have its own R/L encoder before multiplexing. Otherwise, since the color and luminance components do not correlate well, there is little data-rate reduction for the chrominance component when multiplexed with the luminance information. The current breadboard for the NTSC color TSDM system requires a volume of about 5 ft³ each for the transmitter and receiver. With LSI packaging, this system may be reduced to a volume of about 0.5 ft³.

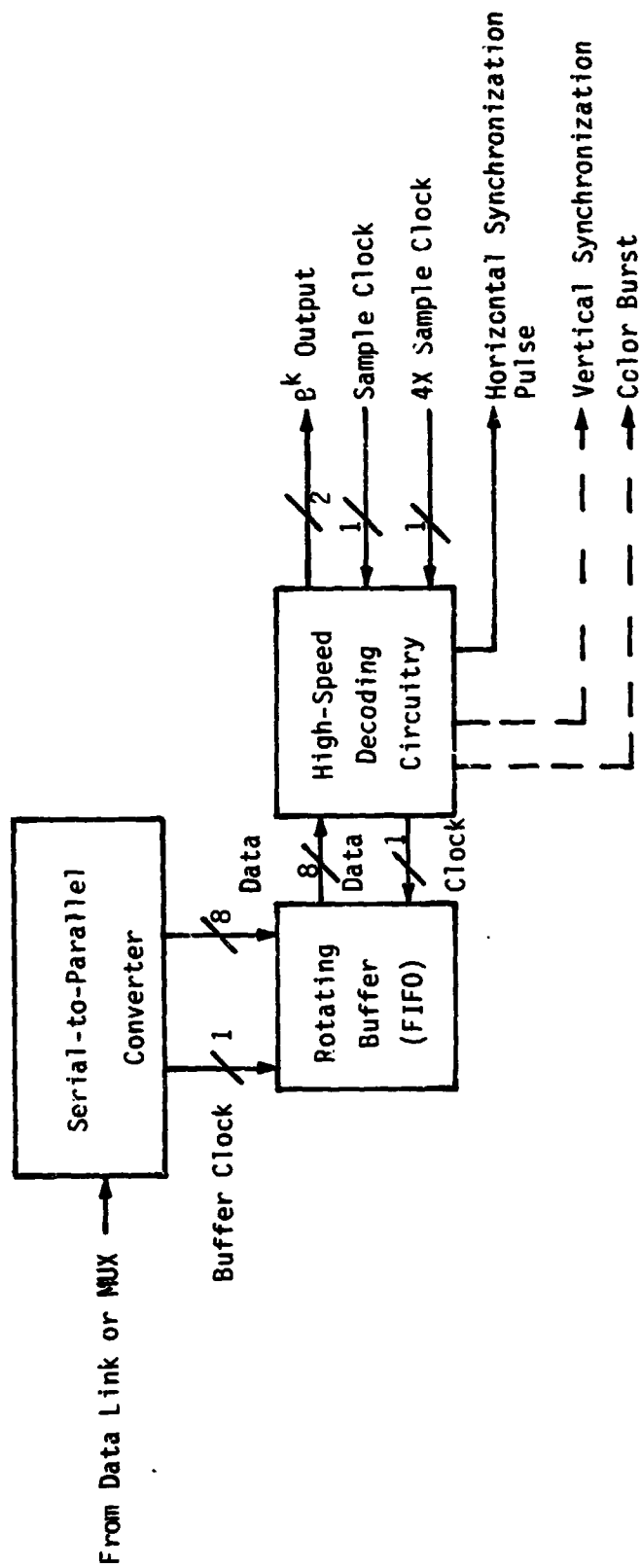
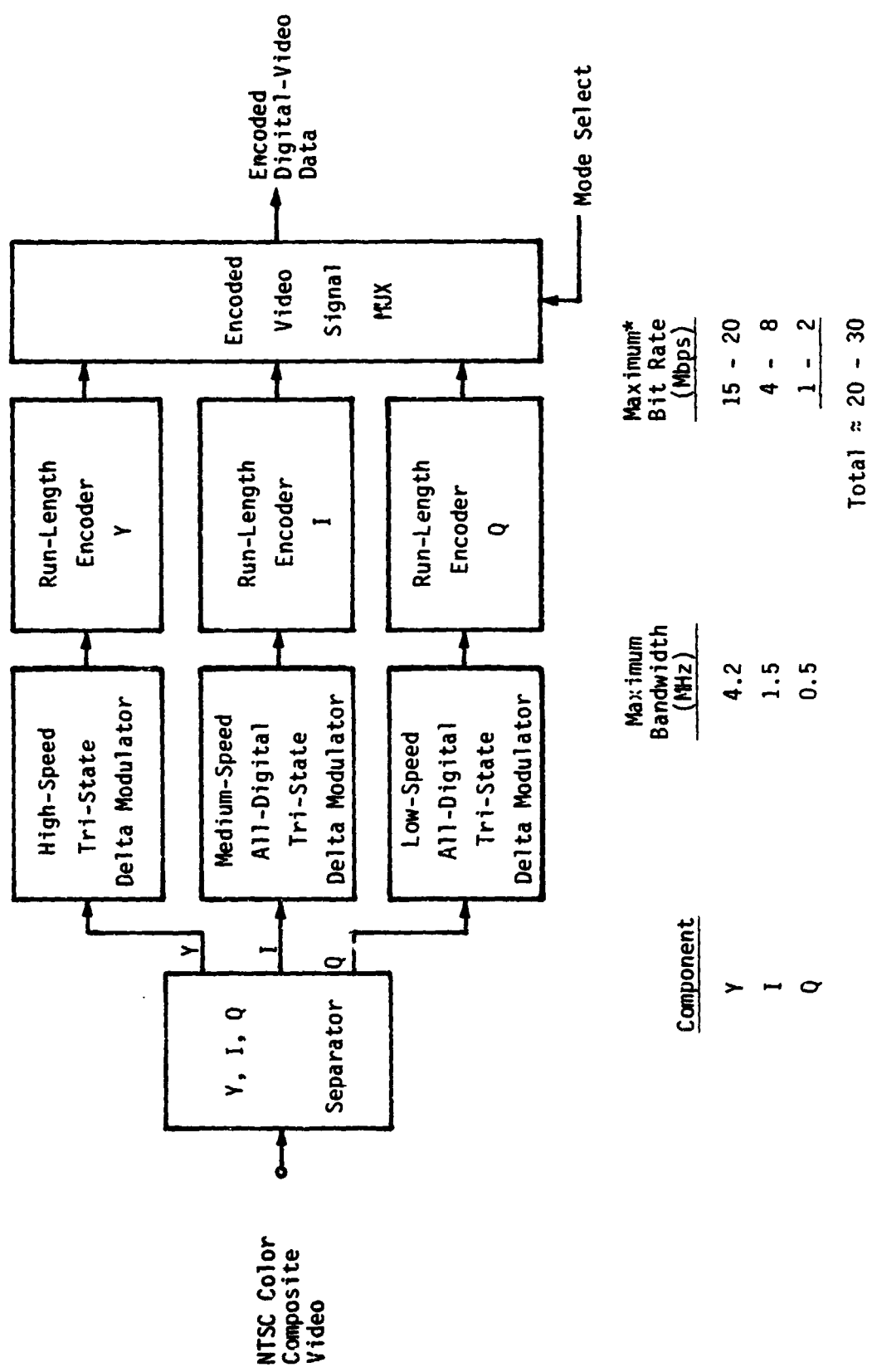


Figure 2.21. Run-Length Decoder (Receiver Side)



* After coding.

Figure 2.22. NTSC Color TV Component Digitization

2.4 VLSI Utilization Potential

2.4.1 Capabilities and Limitations of VLSI Applications to Bandwidth-Reduction Systems

VLSI (very large-scale integration) techniques are being applied to more electronic systems every day. The computer field, in particular, is amenable to their application, and many devices have already been developed. For example, 64k RAM chips are now on the market, with a number of alternative manufacturers. Other examples of products already developed in VLSI include a two-chip, 32-bit generalized data processor by Intel and a 32-bit CPU chip by Hewlett Packard which is capable of operating with an 18-MHz clock. These chips were developed several years ago, so VLSI is clearly a practical technology whose "time has come."

Packaging of more circuitry on one chip has more than one advantage. In addition to reducing the volume required to perform a given system function, the overall system reliability is improved. Specifically, because there are fewer chips in the system, reduced interconnections between chips increase reliability. However, in terms of the ultimate size reduction possible through VLSI techniques, no absolute value exists for the ratio of volume between VLSI and previously developed systems employing SSI and MSI.

The actual size reduction depends on many details of the system being redesigned and how well the functions to be implemented will mesh in a few VLSI chips. If the number of gates on a chip is used as the criteria, ratios of 10 or more are obtainable. The dividing line between LSI and VLSI is generally taken to be somewhere around 15,000 gates per chip, and some VLSI layouts have realized 150,000 gates on one chip. A new system under development, however, would not be amenable to the regularity of patterns, such as those in a CPU and memory chips. Therefore, 80,000 gates per chip should be a good average, and the ratio of chip-count reduction for motion compensation or interframe encoding should be about 10:1. Also, since the VLSI chip will generally require a larger package due to the greater number of inputs and outputs to each chip, the total volume reduction will be significantly less than the 10:1 ratio.

Since the package for a VLSI chip could easily be twice as large as the presently used SSI/SMI/LSI chip, a rough estimate of the overall volume reduction would be 4:1. This estimate may seem quite conservative considering the potential gate-density increase, but a number of limiting factors combine to lessen the potential volume reduction.

These limiting factors include thermal and geometrical considerations as well as propagation times. Reference [14] addresses these problems; Figure 2.23 is from that reference. The idea represented in Figure 2.23 is that several factors converge at approximately the same practical limit to the realizable density of the VLSI implementation. The process of "breaking through" this density limit will therefore require solving several problems at once. However, it must be noted that [14] does not claim that VLSI gate densities will not improve in the future but, rather, that a natural limit exists which, as it is approached, will reduce the rate of progress.

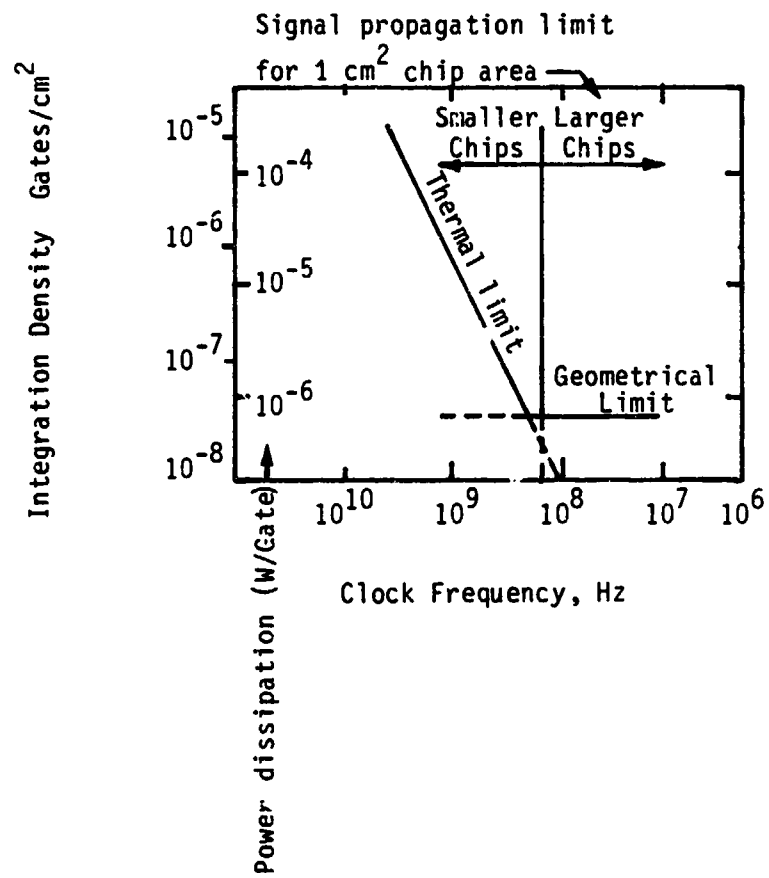


Figure 2.23. Speed-Power-Density Diagram

2.4.2 Specific Systems to be Potentially Reduced Through VLSI

In this section, we make estimates of the potential size reduction to be realized if some of the existing systems were reduced by means of VLSI for SS application. The two systems we consider here are motion-compensated, video-conferencing types of systems which are compatible with our baseline data rate of 2.048 Mbps or less. We picked these systems because they typify a rather complex real-time video-processing system, yet processing has been reduced to operational levels in the field.

We cannot say that the processing algorithms are final for these systems. In fact, Nippon Electric Co. (NEC) feels that the potential limit of the motion-compensation interframe encoding has not yet been reached and, therefore, it is too early (at least for them) to go to custom-made VLSI. Such thinking is understandable because, once an investment is made in custom-made VLSI, the design is essentially "frozen", and no further improvements can be realized.

Both systems to be discussed with respect to size reduction via VLSI were developed for commercial use. They were packaged for low-cost fabrication, ease of maintenance, and with relatively low-density packaging in order to ease field modifications. A thorough review of each system would be required to produce a very accurate estimate of the final package size. The following estimates were made with a rough description of the systems involved; they do not represent the most accurate size estimate possible, given enough time and complete data on the present system.

2.4.2.1 VTS 1.5E System made by Compression Labs, Inc.*

The present system weighs 460 pounds, is 25" wide by 24" deep by 51" high and contains approximately 3,000 integrated circuits. Based on a picture of the unit, a rough estimate is that one-third of the volume is used up by the power supply, base and top of the cabinet, which leaves 25" x 24" x 34" for the actual circuitry. Again judging by the picture, not all of that volume has cards plugged in so that, after repackaging, the system ought to fit in a space 2.4 ft³. It is very conceivable that the volume could drop further if all the blank spaces in the picture are not, in fact, used. Since the system is a two-way system, a one-way system for the SS would fit, after LSI'ing, in a space of about 1.0 ft³.

* See Appendix A for data sheets.

2.4.2.2 NETEC-X1TV Codec, made by Nippon Elec Co., Ltd.*

The Nippon system is 42" high by 22" wide by 24" deep and weighs about 350 pounds. It has approximately 10,000 chips. Once again, it is a two-way system, so only about one-half of it needs to be flown into space for SS use. Using the same ground rules as the previous system, it should require about 1.5 ft³ once it has been repackaged and LSI'ed.

* See Appendix A for data sheets.

3.0 RELATED VIDEO-TECHNOLOGY DEVELOPMENTS

In addition to the application of VLSI to SS TV bandwidth compression, several technological developments have taken place. Although perhaps not directly identifiable with bandwidth compression, these developments can be of great value in assembling an efficient system. Some of these innovations are described below.

3.1 CCD Cameras

The charge-coupled devices (CCD's) have progressed sufficiently to yield extremely small and lightweight CCD cameras. However, information available to us so far indicates that only black-and-white cameras are available in CCD implementations. In addition to being small and lightweight, CCD cameras are compatible, at least in principle, with discrete-sample types of signal processing. In essence, the CCD camera sensor consists of an array of multiple light-sensitive elements arranged in rows and columns in the focal plane of the lens. Each CCD element consists of an analog storage device which develops and stores a voltage proportional to the light impinging on the element. Thus, the video-image readout is performed on a dot-by-dot basis and is controlled by "clocking" the analog information along the horizontal and vertical axes. This clocking determines the sampled nature of the output video signal.

The grid structure of the CCD camera mosaic appears to be ideally suited for implementing video-image transforms directly onto the image sensor. Information available to us, however, indicates that such a transform implementation is rather difficult to manufacture, particularly when compared to CMOS technology. Consequently, it appears that an approach which uses A/D conversion of the discrete readout of a CCD camera, with subsequent digital signal processing and storage using CMOS devices, is more feasible despite the initial attractiveness of using CCD signals directly for video bandwidth-compression processing.

3.2 Digital TV Devices Applicability

The application of VLSI to commercial television may provide a technology which can be of potential use for SS bandwidth-compression techniques. For example, International Telephone and Telegraph Corp. (IT&T) has introduced several VLSI chips which will replace most of the circuits in modern-day color TV sets [15]. These chips are designed for implementing "digital television." In this case, the word "digital" is not to be confused with digital transmission

such as that considered in this report for SS link applications. Specifically, in a digital TV set, the received video signal is A/D converted at the output of the analog IF, and all of the functions presently performed in an analog fashion are then performed in a digital format. This provides for superior color and luminescence signal processing. Signal averaging on an interframe basis is also realizable with the appropriate memory capability. Although not immediately applicable to our requirements, the development of these chips will synergistically affect the bandwidth-compression technology.

4.0 SUMMARY AND CONCLUSIONS

Various existing video data-compression techniques have been considered from the standpoint of their applicability to space station (SS) digital data links. The emphasis was made on these techniques which are either operational or have been tested and verified in real-time. As the result of this study, the following findings can be summarized:

- Good-quality, moderate-motion TV color pictures can be transmitted at a rate of 2.048 Mbps using interframe encoding with motion compensation. The video processor for this transmission can be packaged to within 1 ft³ using VLSI.

- For channel rates much lower than 2.048 Mbps, low-frame rate, black-and-white pictures can be transmitted using hybrid coding. The processor value for this type of transmission is about 25 in³ using LSI.

- For requirements where a lot of picture motion has to be accommodated, delta modulation can be used provided that a channel capacity of 15-30 Mbps is available. Depending on the requirements (i.e., color versus black and white, resolution, etc.), the processor volume may range from 25 in³ to 0.5 ft³.

One can conclude, therefore, that a number of verified techniques are available for potential SS application. Implementation of these techniques for space application will be greatly facilitated by utilization of LSI/VLSI technologies.

REFERENCES

1. H. Kaneko, and T. Ishiguro, "Digital Television Transmission Using Bandwidth-Compression Techniques," IEEE Communications Magazine, July 1980, pp. 14-22.
2. T. Ishiguro, and K. Iinuma, "Television Bandwidth-Compression Transmission by Motion-Compensated Interframe Coding," IEEE Communications Magazine, November 1982.
3. A.N. Natrevali, and Y.O. Limb, "Picture Coding: A Review," Proceedings of the IEEE, Volume 68, No. 3. March 1980, pp. 366-406.
4. L.C. Chan, P. Whiteman, "Hardware-Constrained Hybrid Coding of Video Imagery," IEEE Transactions on Aerospace and Electronic Systems, Volume AES-19, No. 1, January 1983, pp. 71-84.
5. P. Camana, "Video Bandwidth Compression: A Study in Trade-offs," IEEE Spectrum, June 1979, pp. 24-29.
6. J.E. Abate, "Linear and Adaptive Delta Modulation," Proceedings of IEEE, Volume 55, March 1967.
7. C. L. Song, J. Garodnick and D. L. Schilling, "A Variable-Step-Size Robust Delta Modulator," IEEE Transactions on Communications, Volume COM-19, December 1971, pp. 1033-1044.
8. M. Oliver, "An Adaptive Delta Modulator with Overshoot Suppression with Video Signals," IEEE Transactions on Communications Technology, Volume COM-21, March 1973, pp. 243-247.
9. L. Weiss, I.M. Paz, and D.L. Schilling, "Video Encoding Using an Adaptive Digital Delta Modulator with Overshoot Suppression," IEEE Transactions on Communications, Volume COM-23, September 1975, pp. 905-920.
10. D. L. Schilling, N. Scheinberg and J. Garodnick, "Video Encoding Using Adaptive Delta Modulation," IEEE Transactions on Communications, Volume COM-26, No. 11, November 1978, pp. 1682-1689.
11. N. Scheinberg, Y. Barbara and D. L. Schilling, "One-Dimensional, Composite Coding of NTSC Signals Using Adaptive Predictors and Quantizers," Proceedings of the National TeleSystems Conference, Galveston, Texas, pp. 1107-1110.
12. I. M. Paz, G. C. Collins and B. H. Batson, "A Tri-State Delta Modulator for Run-Length Encoding of Video," Proceedings of NTC'76, Dallas, Texas, November 29 - December 1, 1976, pp. 6.3-1 and 6.3-6.
13. I. M. Paz, G. C. Collins and B. H. Batson, "Overshoot Suppression in Tri-State Delta Modulation Channels," 1976 Region V, IEEE Conference Digest, pp. 177-180.
14. O. G. Folberth, "The Interdependence of Geometrical, Thermal and Electrical Limitations for VLSI Logic," IEEE Journal of Solid-State Circuits, Volume SC-16, No. 1, February 1981, pp. 51-53.
15. E. J. Lerner, "Digital TV: Makers' Bet on VLSI," IEEE Spectrum, February 1983, pp. 39-43.